Development of Bi-metallic Catalysts for Multi-electron Chemistry: of Consequence to Sustainable Energy

STACEY CAROLINE LINDSAY

How to cite:

LINDSAY, STACEY CAROLINE (2016) Development of Bi-metallic Catalysts for Multi-electron Chemistry: of Consequence to Sustainable Energy. Doctoral thesis, Durham University.

Development of Bi-metallic Catalysts for Multi-electron Chemistry:

of Consequence to Sustainable Energy

Stacey Caroline Lindsay

The new ligand L^1 (21), 1-*N*,1-*N*-bis(pyridine-2-ylmethyl)-3-*N*-(pyridine-2-ylmethylidene)benzene-1,3-diamine, was synthesised as a platform to study bi-metallic first row transition complexes containing redox-active ligands. The asymmetric ligand L^1 (21) contains a redox-active α-iminopyridine unit bridged to redox-inert or "innocent" bis(2-pyridylmethyl)amino counterpart and offers two distinct co-ordination sites. The co-ordination chemistry of L^1 (21) with Fe^{2+}, Cu^{2+}, and Zn^{2+} was examined. Reaction with Zn^{2+} afforded the asymmetric binuclear complex $[(L^1)Zn_2Cl_4]$ (**C1**), whereas the symmetric $[(L^1)_2Fe_2(OTf)_2](OTf)_2$ (**C2**), $[(L^1)_2Fe_2(CH_3CN)_2](PF_6)_4$ (**C3**) and $[(L^1)_2Cu_2](OTf)_4$ (**C4**) complexes were isolated in reactions with iron and copper salts. Both metal- and ligand-centered redox processes are available to complexes **C2**, **C3** and **C4** and were investigated by cyclic voltammetry. Complexes **C2** and **C3** favor ligand-centered reduction while **C4** favors metal-centered reduction. EPR, Mössbauer spectroscopy and magnetic susceptibility studies establish that complexes **C2**, **C3** and **C4** are paramagnetic.

Ferrous complexes **C2** and **C3** were studied as potential C-H oxidation catalysts. Difficult C-H oxidation transformations are known to be facilitated by synthetic and biomimetic iron species. The **C2** and **C3** complexes provide a unique contrast non-heme enzyme active sites and biomimetic complexes due to the large Fe···Fe inter-nuclear distances of > 7Å. Complexes **C2** and **C3** provided evidence of moderate catalytic activity toward a range of substrates of varying bond strengths including cyclohexene (80 kcal mol^{-1}), 9,10-dihydroanthracene (76 kcal mol^{-1}), xanthene (75.5 kcal mol^{-1}) and triphenylmethane (81 kcal mol^{-1}). The oxidising strength of complexes **C2** and **C3** toward C-H bonds were found to be limited by bond strength with both **C2** and **C3** proving to be incapable of oxidising cyclohexane (99 kcal mol^{-1}) and adamantane (96 kcal mol^{-1}). The oxidation pathway was investigated by employing deuterated substrates in place of cyclohexene, DHA and xanthene. The increased strength of the C-D bond over a C-H bond (1.4 kcal mol^{-1}) should induce decreased reactivity and hence product formation if the hydrogen abstraction pathway is being accessed. Decreased reactivity was observed when the deuterated versions of cyclohexene, DHA and xanthene were employed illustrating the hydrogen abstraction pathway is indeed the mechanistic means by which complexes **C2** and **C3** oxidise C-H bonds.

The structural identity of the active species formed by **C3** during C-H oxidation, was investigated in the absence of substrate which exposed the formation of a transient species identified by λ_{max} 430 nm in the UV-Vis spectrum - labelled **C7**. Complex **C7** decays to the di-ferric species **C8**. Spectroscopic studies in the presence of substrate uncovered the existence of two active species with two distinct rates of oxidation. Exposing complexes **C7** and **C8** to DHA unveiled complex **C7** as the lesser active species, while complex **C8** was unreactive toward DHA oxidation. The structural identity of the more reactive species has been elusive to the studies presented herein.

A new bi-macrocyclic ligand scaffold which might more readily favour the formation of two-electron mixed valence species was designed. A series of five structures with varying M···M inter-nuclear distances were designed and the synthetic routes toward their formation are discussed accompanied by calculated geometry optimised structures as full characterisation of the final complexes are yet to be obtained.

Development of Bi-metallic Catalysts for Multi-electron Chemistry:

of Consequence to Sustainable Energy

Stacey Caroline Lindsay

A thesis presented in partial fulfilment of the
requirements for the degree of Doctor of Philosophy
in Chemistry.

Department of Chemistry
Durham University

2015

DECLARATION

The material contained in this thesis, unless stated otherwise through cited reference, is the result of the author's work at the University of Durham, Department of Chemistry, between October 2011 and July 2015 and it has not been submitted for a degree at this or any other institution.

STATEMENT OF COPYRIGHT

The copyright of this thesis rests with the author. No quotation from it should be published without the author's prior written consent and information derived from it should be acknowledged.

ACKNOWLEDGEMENTS

First I would like to begin by thanking Dr. Corinna Hess for her continued support and guidance during this project, both during her time at Durham University and particularly after her re-location to Munich, Germany. The project has been full of highs and lows, but whatever the situation the solution was always "beer?"

I would like to go on to thank those at Durham University who have personally taken the time to guide me along the way including Dr. Ross Davidson and Dr. Helen Hsu who, over the last year, have been a constant support both in and out of the lab always listening to my grievances when my chemistry "isn't doing what it's supposed to!" with plenty of suggestions.

Thank you to Emma Puttock for always taking time out for me, you're always the first person I run down to tell when things finally work (a rarity) and the first one to complain to when they're not (frequently).

To my family, who still don't understand what I've been doing for the last few years - sorry Mum that I didn't make that anti-aging cream you were wanting me to whip up on the weekends. You have been an immense support over the last few years, I truly wouldn't have made it without you.

I have saved my final thanks for my Fiancé, Daniel Stark. I'm lucky enough that you are in the same boat also doing a Chemistry PhD and so you understand everything I have been through over the last few years. Your support has been unmeasurable so much so that a simple acknowledgement is very inadequate but here it is!

“But I don’t want to go among mad people,” Alice remarked.

“Oh, you can’t help that,” said the Cat: “we’re all mad here. I’m mad. You’re mad.”

“How do you know I’m mad?” said Alice.

“You must be,” said the Cat, “or you wouldn’t have come here.”

Lewis Carroll

Alice’s Adventures in Wonderland

TABLE OF CONTENTS

LIST OF FIGURES

LIST OF SCHEMES

LIST OF TABLES

NUMBERED LIST

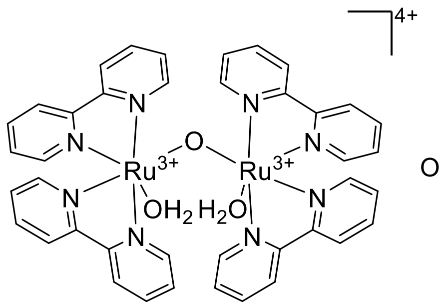

1

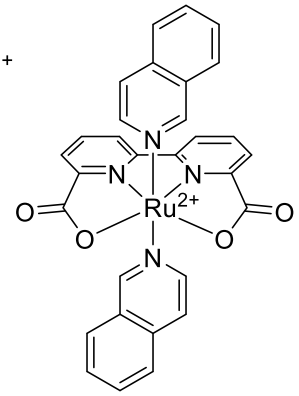

2

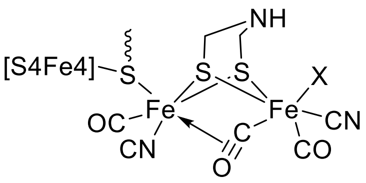

X = OH_2, H^-, H_2

3

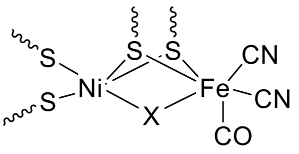

X = O^{2-}, OH^-, OH_2, H^-

4

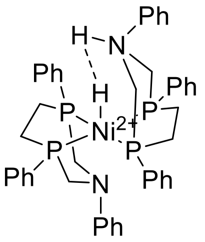

5

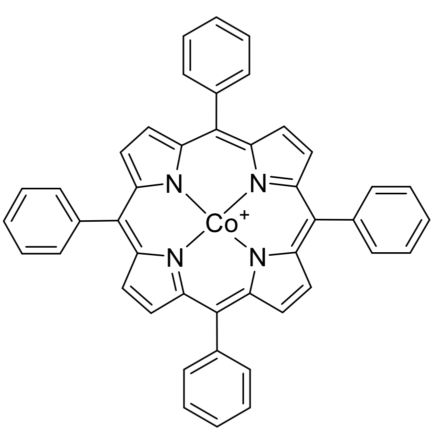

6

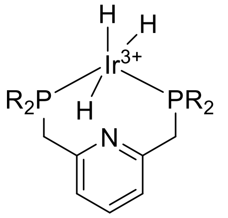

7

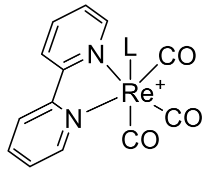

8

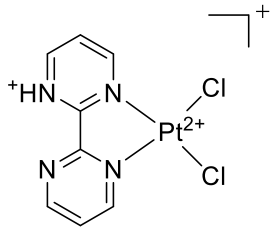

9

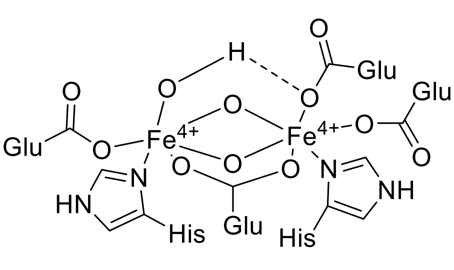

10

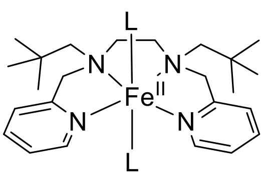

11

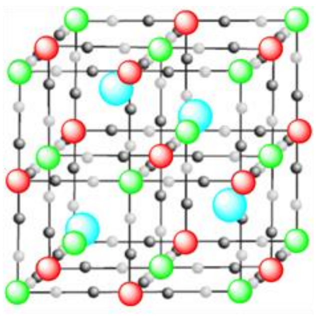

12

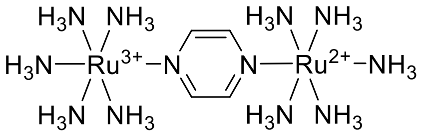

13

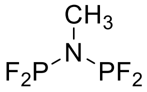

$F_2P{-}N(CH_3){-}PF_2$

14

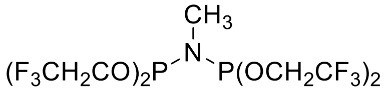

$(F_3CH_2CO)_2P{-}N(CH_3){-}P(OCH_2CF_3)_2$

15

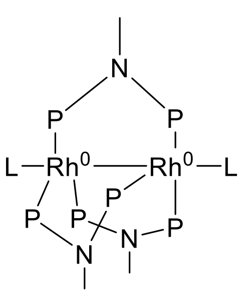

16

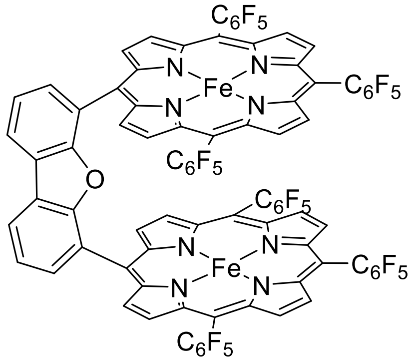

17

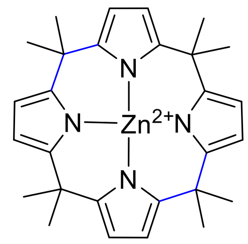

18

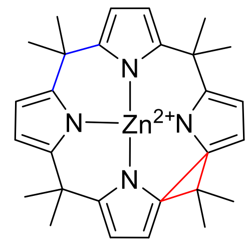

19

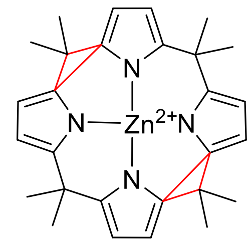

20

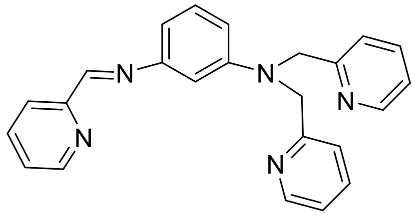

21

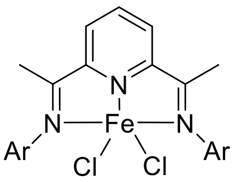

22

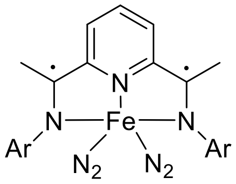

23

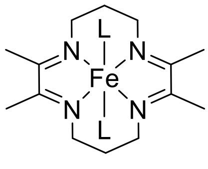

24

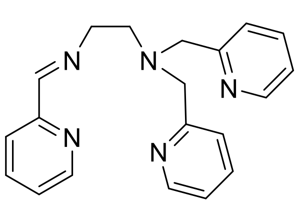

25

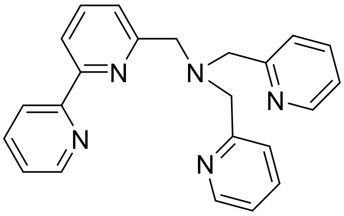

26

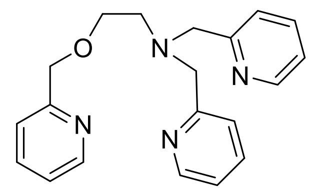

27

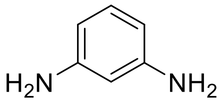

28

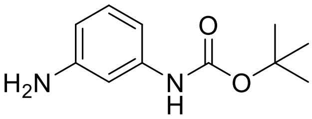

29

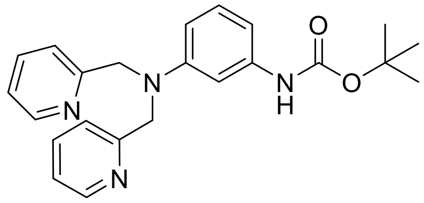

30

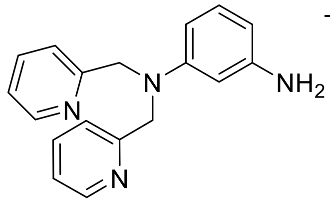

31

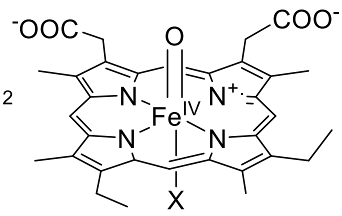

32

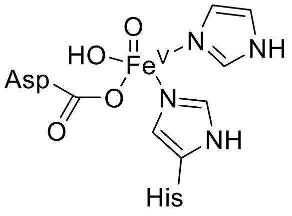

33

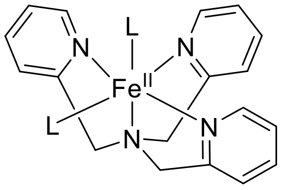

34

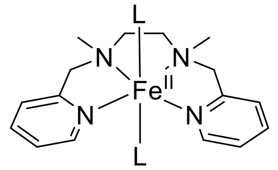

35

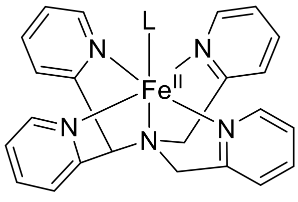

36

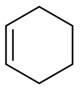

37

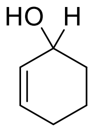

38

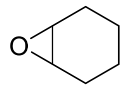

39

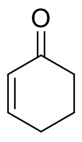

40

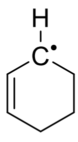

41

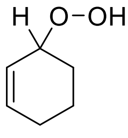

42

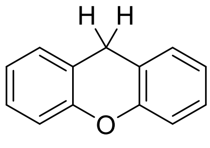

43

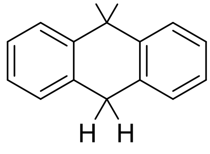

44

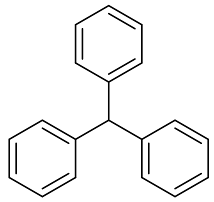

45

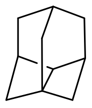

46

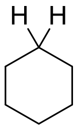

47

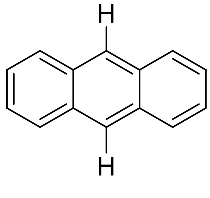

48

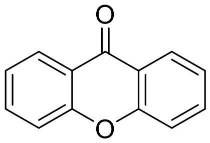

49

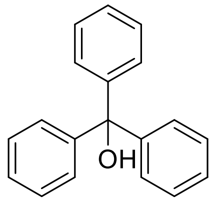

50

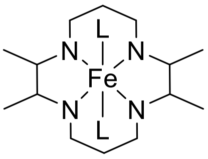

51

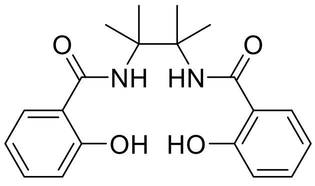

52

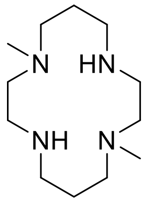

53

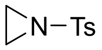

54

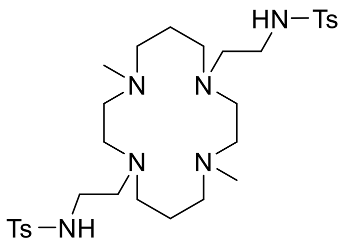

55

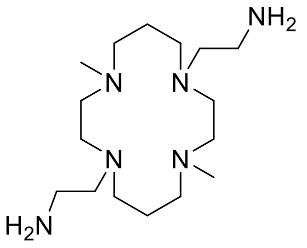

56

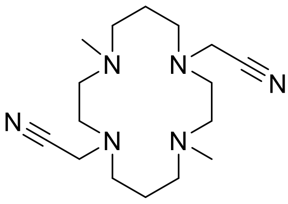

57

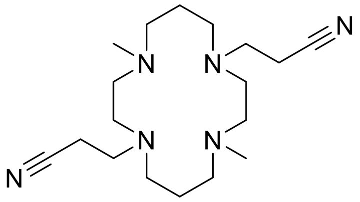

58

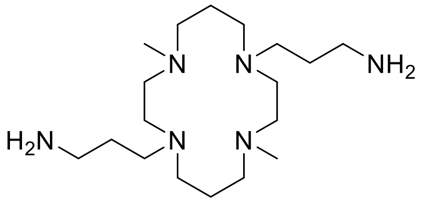

59

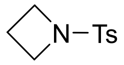

60

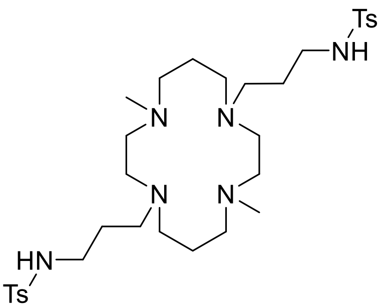

61

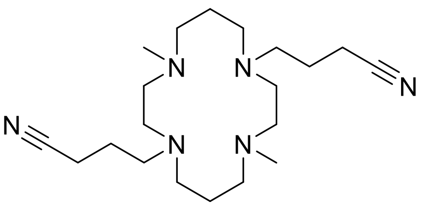

62

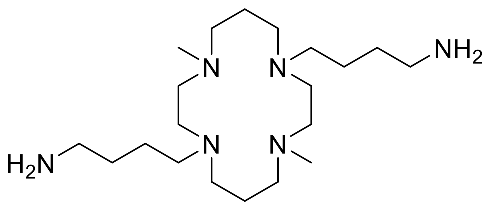

63

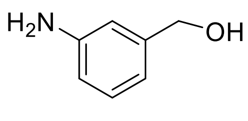

64

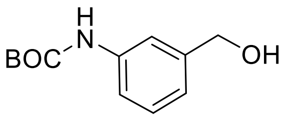

65

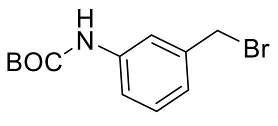

66

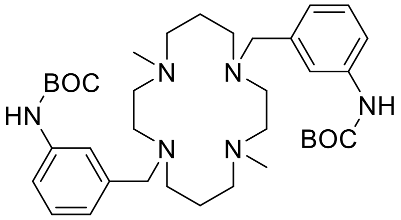

67

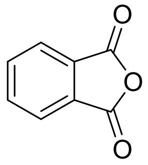

68

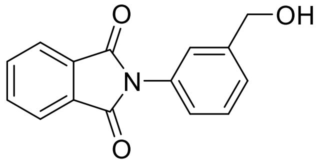

69

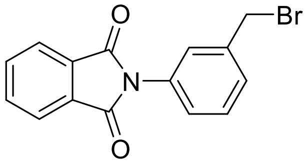

70

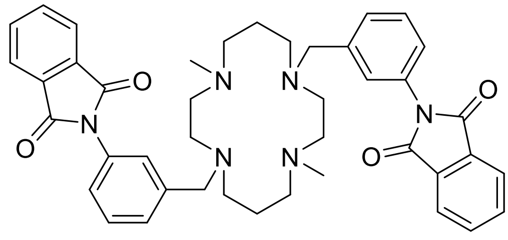

71

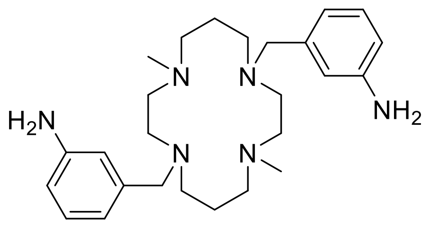

72

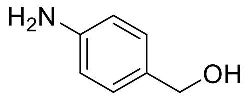

73

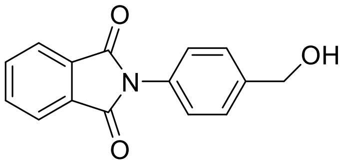

74

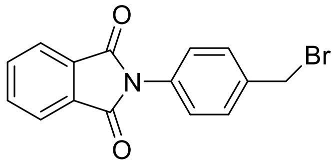

75

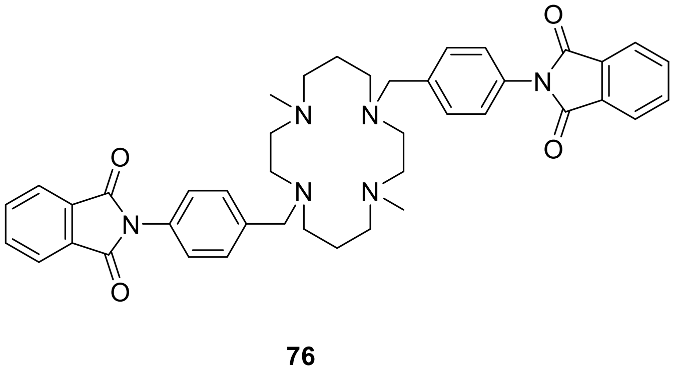

76

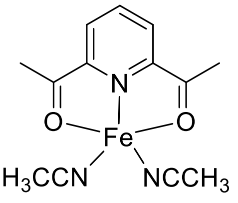

77

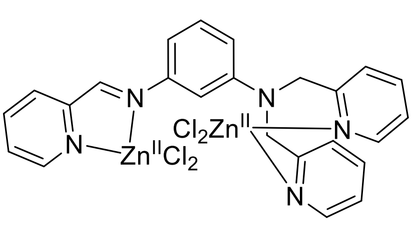

C1

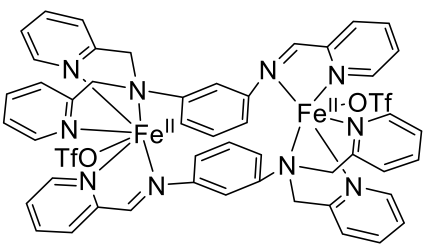

C2

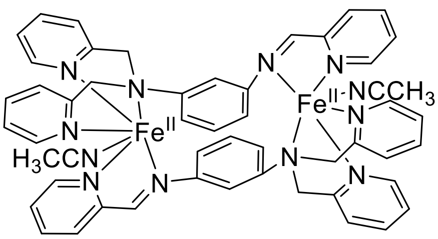

C3

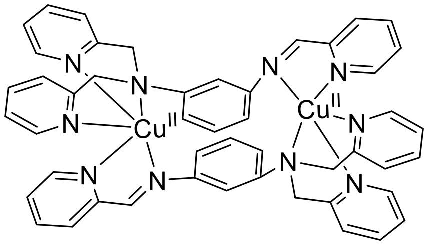

C4

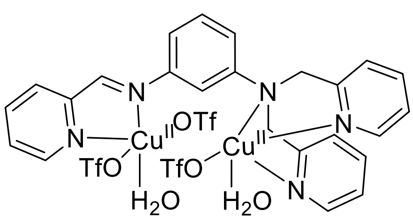

C5

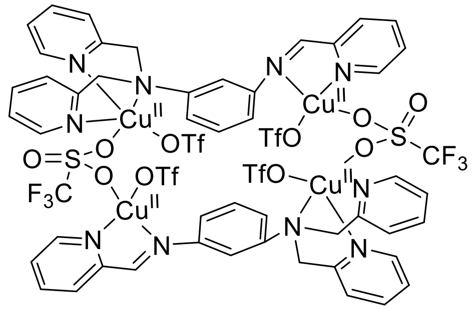

C6

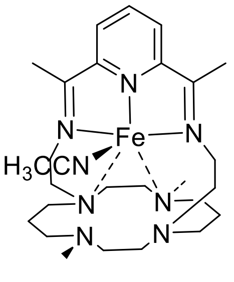

C9

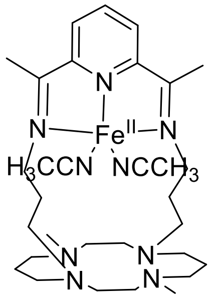

C10

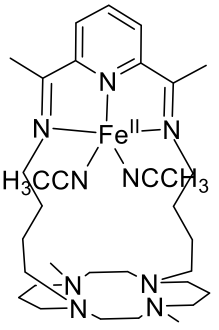

C11

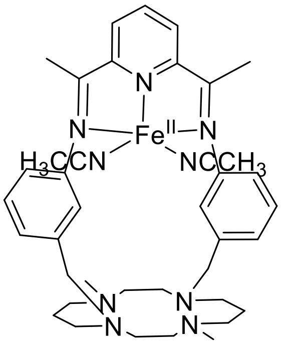

C12

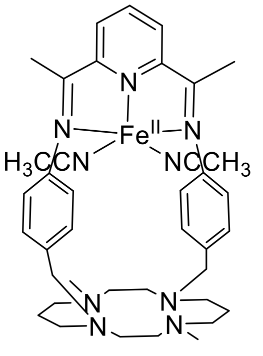

C13

ABBREVIATIONS

ASAP	Atmospheric Solids Analysis Probe
Atm.	Atmosphere
ATP	Adenosine Triphosphate
B3LYP	Becke, three-parameter, Lee-Yang-Parr – Basis Set for DFT
BDE	Bond Dissociation Energy
Bipy	Bipyridine
BOC	tert-Butyloxycarbonyl
BP86	Becke, Perdew 86 – Basis Set for DFT
BPABipy	Bis(pyridylmethyl)(bipyridylmethyl)amine
BPMEN	N,N’-dimethyl-N,N’-bis(2-pyridylmethyl)ethylene-1,2-diamine
Cat.	Catalyst
Conc.	Concentrated
COSY	Correlation Spectroscopy
CP450	Cytochrome P450
CT	Charge Transfer
CV	Cyclic Voltammetry

DCM	Dichloromethane
DHA	9,10-dihydroanthracene
DMF	Dimethylformamide
DMS	Dimethylsulfide
dnpbn	*N*,*N′*-dineopentyl-*N*,*N′*-bis(2-pyridylmethyl)-1,2-ethanediamine
EC	Electronic Process Coupled to a Chemical Reaction
E_{pa}	Anodic Potential at which an Oxidation Occurs in CV
E_{pc}	Cathodic Potential at which a Reduction Occurs in CV
EPR	Electron Paramagnetic Resonance
Eq.	Molar Equivalents
ESI	Electrospray Ionisation
GC-MS	Gas Chromatography – Mass Spectrometry
HAB	Hydrogen Abstraction
HOMO	Highest Occupied Molecular Orbital
HRMS	High Resolution Mass Spectrometry

I_{pa}	Anodic Current of an Oxidation in CV
I_{pc}	Cathodic Current of a Reduction in CV
IR	Infrared
IRF	Internal Response Factor
KIE	Kinetic Isotope Effect
k_{obs}	Observed Rate Constant
L^1	1-*N*,1-*N*-bis(pyridine-2-ylmethyl)-3-*N*-(pyridine-2-ylmethylidene)benzene-1,3-diamine
LC-MS	Liquid Chromatography – Mass Spectrometry
LMCT	Ligand to Metal Charge Transfer
LRMS	Low Resolution Mass Spectrometry
LUMO	Lowest Occupied Molecular Orbital
m-	Meta substituted
MALDI	Matrix Assisted Laser Desorption Ionisation
MCPBA	Meta-Chloroperoxybenzoic Acid
MLCT	Metal to Ligand Charge Transfer
MMO	Methane Monooxygenase
MO	Molecular Orbital

N4Py	N,N-bis(2-pyridylmethyl)-N-(bis-2-pyridylmethyl)amine
NADPH	Nicotinamide Adenine Dinucleotide Phosphate
NBS	*N*-Bromosuccinimide
NHE	Normal Hydrogen Electrode
NIR	Near Infrared
NMR	Nuclear Magnetic Resonance
o-	Ortho substituted
OAT	Oxygen Atom Transfer
Ox.	Oxidant
p-	Para substituted
PCET	Proton-Coupled Electron Transfer
PEC	Photoelectrochemical Cell
PhIO	Iodosylbenzene
PDI	Pyridine diimine
PIE	Product Isotope Effect
PSI	Photosystem 1
PSII	Photosystem 2

RBF	Round Bottom Flask
RT	Room Temperature
SBPy3	*N*,*N*-bis(2-pyridylmethyl)amine-*N*-ethyl-2-pyridine-2-aldimine
SHE	Standard Hydrogen Electrode
SOMO	Singly Occupied Molecular Orbital
SQUID	Superconducting Quantum Interference Device
STD	Standard
Sub.	Substrate
THF	Tetrahydrofuran
TIM	2,3,9,10-tetramethyl-1,4,8,11-tetraazacyclotetradeca-1,3,8,10-tetraene
TMC	1,4,8,11-tetramethyl-1,4,8,11-tetraazacyclotetradecene
TOF	Turnover Frequency
TON	Turnover Number
TPA	Tris(2-pyridylmethyl)amine
TPDB	*N*,*N*,*N′*,*N′*-tetrakis(pyridine-2-ylmethyl)benzene-1,3-diamine

TPOEN	N-(2-pyridylmethoxyethyl)-N,N-bis(2-pyridylmethyl)amine
UK	United Kingdom
UV	Ultra-Violet
WOC	Water Oxidation Catalyst
δ	Isomer Shift Mössbauer / Shift ^{1}H NMR
ΔEQ	Quadrupole Splitting
ε	Molar Extinction Coefficient

Chapter 1 – Bio-inspired Catalysis: Functionalisation of Small Molecules of Consequence to Energy Production

1.1 The Global Energy Problem

The world is facing a potential energy crisis that is directing a transition in the methods and resources employed to produce energy. A rapidly increasing global population alongside the continued technological advancement of current developed and developing countries mean the global demand for energy has never been higher. It is predicted that the world's population will increase by a further 3.2 billion people by 2050 bringing with it the need to accommodate vast additional energy demands.[1] Reliance on fossil fuels cannot be maintained as they being depleted at an unsustainable rate. Furthermore, the by-products of fossil fuel consumption have detrimental effects on the environment and are proposed to be the key contributors to global warming. The ever increasing fossil fuel combustion to meet demands has increased atmospheric CO_2 concentrations to levels exceeding that which can be managed naturally *via* photosynthesis. Therefore, the replacement of fossil fuels by clean, renewable energy sources is one of the most urgent issues society is facing today.

Wind power, hydroelectric power, nuclear and solar energy are some of the technologies that have been proposed and implemented as alternative energy sources, but all have drawbacks deeming them unsuitable as the sole replacement for fossil fuels. The UK is one of the largest generators in the world for offshore wind power. The primary weakness of wind power is intermittency resulting in variable production levels and inadequacy to meet demand; only ~ 4.9 % of UK electricity consumption was supplied by wind power in the first quarter of this year (Figure 1).[2] Hydroelectric power currently provides ~ 2.1 % of electricity consumed in the UK, expansion potential is very limited as the implementation of new systems is extremely costly (Figure 1).[2] The nine nuclear power stations in the UK currently supply ~ 19.1 % of electricity consumption (Figure 1).[2] Negative public perception of nuclear energy that has arisen from highly publicised disasters such as Chernobyl, Ukraine in 1986 and most recently Fukushima, Japan in 2011, limit expansion opportunities. In fact, one plant in the UK, Wylfa, is to be decommissioned in December 2015 and so the contribution of nuclear energy is decreasing in the UK in the short term. Solar energy holds the most potential of the list; energy from the sun reaches the earth's surface at $\sim 3 \times 10^{24}$ J year^{-1}, 10^4 times more energy than is globally consumed.[3] A vast expanse of research is on-going toward efficient solar light capture. There is currently a trade-off between production cost and light capture efficiency with the highest efficiency currently at 15 % for commercially available dye-sensitised solar cells.[4] All the technologies listed have the mutual disadvantage of providing the converted energy in the form of electricity, which is difficult to store and transport. Therefore, the development of alternative chemical energy carriers, performing the same role as fossil fuels, is highly desirable. One approach to address both the development of alternative chemical energy carriers and the reduction of greenhouse gas emissions is *via* small molecule activation and catalysis. CO_2, H_2 and CH_4 are all candidates as alternative chemical energy carriers.

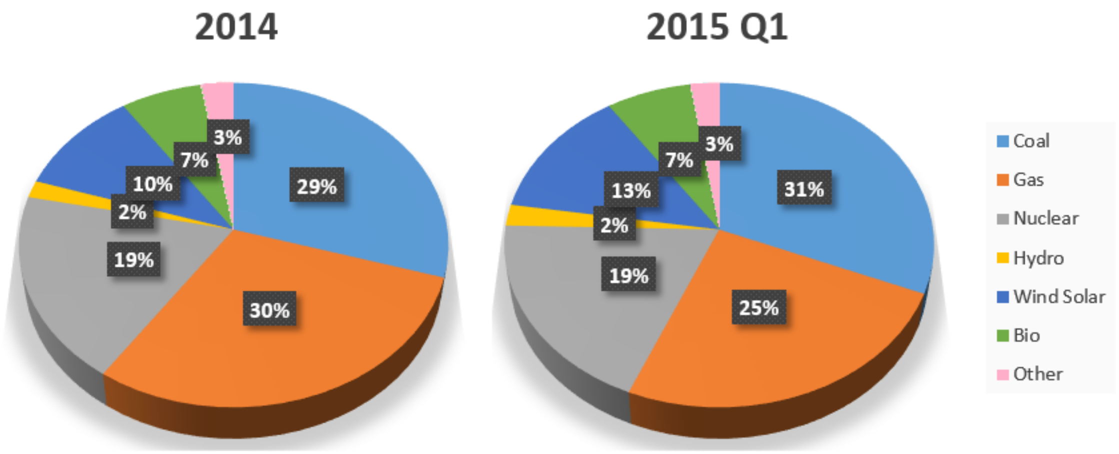

Figure 1. Breakdown of Energy Source Contribution in the UK for 2014 and the First Quarter of 2015.[2]

1.2 Alternative Energy Sources: Inspiration From Nature

We can look to nature for inspiration when developing alternative energy strategies. Nature creates fuel *via* photosynthesis, storing energy within the bonds of carbohydrates such as glucose. Photosynthesis is a complex system requiring synchronised behaviour of several components. Photosystem II (PSII) absorbs photons into chlorophyll molecules resulting in photo-ionisation of two electrons. The oxidised chlorophyll molecules induce oxidation of water molecules forming molecular oxygen, four protons and four electrons (Scheme 1).[4, 5] Two electrons are transferred back to the oxidised chlorophyll molecule while the remaining two electrons pass through photosystem I (PSI) producing energetically enriched reducing agents NADPH and ATP that are employed in the Calvin cycle to reduce atmospheric CO_2 to a variety of carbohydrates.[4] The carbohydrates have all the properties required for a chemical fuel; they can be stored, transported and burned to release energy (higher energetic content than the starting materials). The photosynthesis system is perfectly cycled and sustainable.

Achieving artificial photosynthesis is the ‘Holy Grail’ solution to the energy issue, but is far from becoming a realisation. To achieve artificial photosynthesis three different components are required to perform the individual steps of the reaction; the absorption of light, the oxidation of water and the reduction of either CO_2 or protons (H^+). The reduction of protons to form H_2, which can also serve as a fuel or chemical energy carrier, is an alternative approach over CO_2 reduction. H_2 is desirable as it has zero carbon content and so releases zero carbon emissions. Since artificial photosynthesis is complex a useful strategy is to divide the overall process into its two half reactions; water oxidation and proton reduction or CO_2 reduction (Scheme 1). Each reaction needs to be optimised, after which point they can be combined in a full catalytic system such as a photoelectrochemical cell (PEC).[4]

$$2H_2O \longrightarrow 4H^+ + O_2 + \mathbf{4e^-}$$ Water Oxidation

---

$$4H^+ + \mathbf{4e^-} \longrightarrow 2H_2$$ Proton Reduction

$$CO_2 + 2H^+ + \mathbf{2e^-} \longrightarrow HCO_2H$$ Carbon Dioxide Reduction

Scheme 1. Artificial Photosynthesis System Individual Processes.

Accomplishing each half reaction is difficult as there are large thermodynamic or kinetic barriers impeding each. The activation of small molecules of energy consequence including H_2O, H_2, CO_2, O_2, CH_4 and N_2 all share the fundamental challenge; manipulating multi-electron processes (Scheme 1). Full understanding and management of multi-electron transformations is yet to be realised opening a vast scope of research in the design and synthesis of potential catalysts. The function of a multi-electron catalyst is to act as a charge pool, acquiring electrons (or holes) from one-electron reducing (or oxidising) agents in a stepwise process, then delivering the electrons (or holes) to the substrate in a concerted process to avoid the formation of high energy intermediates, thus lowering the large energy barriers in place. The multi-electron transformations of artificial photosynthesis and of other consequence to energy production are discussed herein along with current molecular catalysts for each and their mechanistic function, with the purpose to gain insight to allow the systematic design of new multi-electron catalysts.

1.3 Water Oxidation

Water oxidation is a four electron transformation (Scheme 1). In 1982 the first molecular catalyst to facilitate water oxidation was reported, named the blue dimer; *cis*,*cis*-$[(bpy)_2(H_2O)Ru^{III}ORu^{III}(H_2O)(bpy)_2]^{4+}$ **(1)** (Figure 2).[6, 7] Complex **1** is made up of two ruthenium ions capable of facilitating the four electron oxidation by adopting different oxidation states. Since 1982 a significant number of water oxidation catalysts have been successfully established. Common features have been recognised allowing for the systematic design of further catalysts. Firstly, the metal centre must be able to access high oxidation states, aided by the ligand scaffold. Stabilisation of high oxidation states is generally achieved by proton-coupled electron transfer (PCET) by avoiding highly charged intermediates.[4] A water ligand, or an available coordination site to bind a water molecule, is essential to generate the M–O group responsible for the O–O bond formation step.[4] The high thermodynamic energy associated with water oxidation (0.81 V vs. NHE) means it is important that the ligand scaffold used is robust and should not be easily substituted or altered under the working conditions.[4]

Water oxidation has been ascertained to proceed through two alternative mechanisms (Scheme 2).[4, 8, 6] Common to both, the first step is the activation of the reactive species. This can be done chemically, electrochemically or photochemically with the photochemical process being the most desirable due to the close relationship to photosynthesis. In the first mechanism the O-O bond is formed through nucleophilic attack of a water molecule to the oxo group of M-O (Scheme 2; Top). In the second mechanism the interaction between two M-O molecules followed by either radical coupling or reductive elimination forms the O-O bond (Scheme 2; Bottom). The most notable water oxidation catalyst to date is the mono-ruthenium catalyst **2** displaying a turnover frequency (TOF) of 300 s^{-1} when Ce(IV) is used as a chemical oxidant in the first activation step (Figure 2).[9] The reactivity of **2** is comparable to PSII which produces oxygen at TOFs of 100 – 400 s^{-1}. The ruthenium catalyst, **2** operates *via* the second mechanism described forming Ru^{IV}-O-O-Ru^{IV} that further oxidises to Ru^{V}-O-O-Ru^{IV}, both of which release dioxygen.[9]

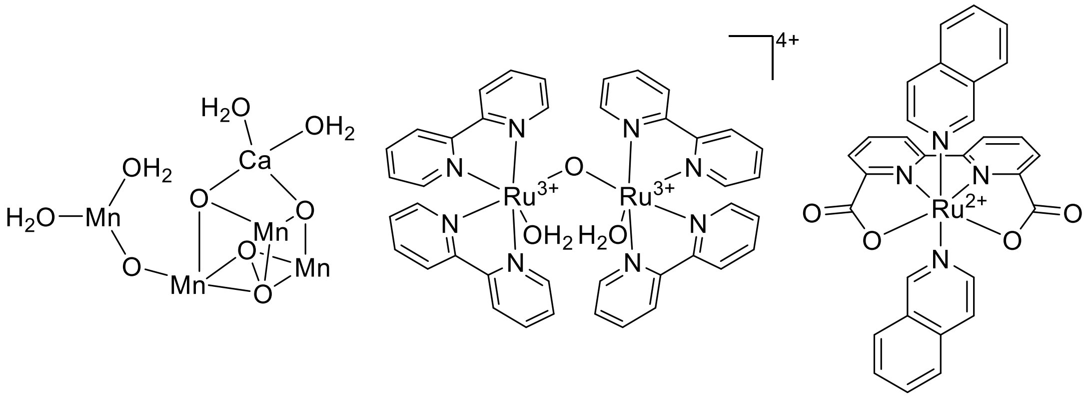

PSII Mn_4Ca Cluster

Blue Dimer

1

2

Figure 2. Notable Water Oxidation Catalysts (WOC). Left; Active Site of PSII. Middle; Blue Dimer (1) the First Molecular WOC. Right; 2 Best WOC to Date.[6, 9, 5]

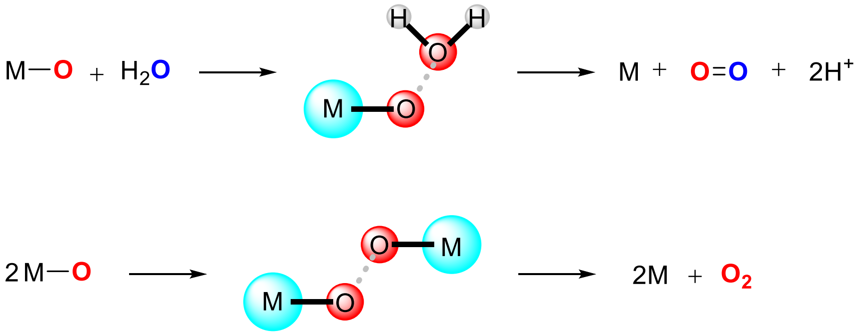

Scheme 2. Alternative Mechanisms for Water Oxidation after Activation of Molecular Catalyst. Top; Nucleophilic Attack of H_2O Molecule. Bottom; M-O Interaction.[4, 8]

1.4 Proton Reduction

Dihydrogen has the potential to act as a clean alternative to fossil fuels and an alternative over CO_2 reduced products. Hydrogen is one of the most abundant elements on earth but molecular hydrogen is not readily available, only 0.5ppm of H_2 is present in the atmosphere.[10] Hydrogen exists in the form of hydrocarbons and H_2O on earth. Currently 95 % of molecular hydrogen is produced from fossil fuels, such as methane, in conjunction with the formation of CO_2/CO.[10] Hydrogen production from fossil fuels offers no advantage over using the fossil fuels directly. Proton reduction coupled to water oxidation is the most desired route for hydrogen formation. The oxidation of dihydrogen, either electrochemically or *via* combustion, results in the reformation of water as the sole by-product making the cycle renewable and with zero emissions.

The reduction of protons to form molecular hydrogen is a two electron process. The addition of one electron has a large energy barrier requiring a very negative potential; -2.29 V/SHE.[11, 1, 12] The combination of hydrogen radicals and thus the formation of dihydrogen expels energy equivalent to 2.29 V/SHE so the overall reaction is thermo-neutral. The addition of two electrons instantaneously to a proton to form a hydride (H^-) has a much lower energy barrier; -1.05 V/SHE.[11, 1, 12] Addition of a proton and thus the formation of dihydrogen expels energy equivalent to 1.05 V/SHE, again resulting in a thermo-neutral overall reaction. The two electron concerted reduction is the favoured reaction pathway due to the lower energy barrier and therefore the development of catalysts that allows the direct two-electron reduction of H^+ is desired.

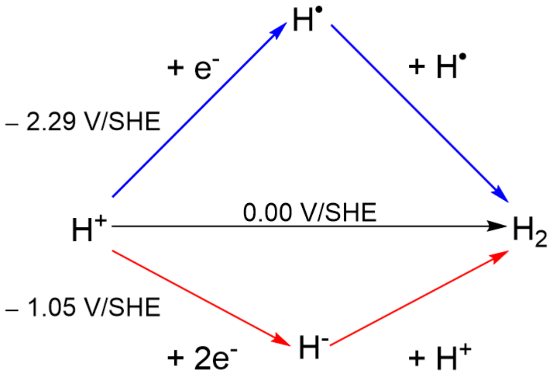

Figure 3. Energetic Pathways of Proton Reduction to Form Dihydrogen.

Nature utilises the hydrogenase metalloenzymes to produce dihydrogen. Hydrogenases have an inorganic bi-metallic active site situated deep within a protein environment. There are two distinct types of hydrogenases based on their active sites, Fe-Fe **(3)** and Ni-Fe **(4)** (Figure 4).[12] Both are capable of reversible proton reduction. The multi-electron nature of proton reduction is accommodated by an electron relay system. Electrons are shuttled to the active site using [FeS] cluster chains, the [FeS] clusters are ligated in the case of **3** and situated within the protein environment for **4**.[13] [4Fe4S] as present in **3** exists in four oxidation states, $[4Fe4S]^0$, $[4Fe4S]^+$, $[4Fe4S]^{2+}$ and $[4Fe4S]^{3+}$enabling their use as an electron relay system.[13] Hydrogen can travel toward or away from the active site, depending on which process is occurring, *via* a hydrophobic channel within the protein environment.[14] Fe-Fe hydrogenases are 50-100 times more active than Ni-Fe.[12] However, Fe-Fe hydrogenases function only under anaerobic conditions whereas Ni-Fe hydrogenases can catalyse hydrogen production in oxygen levels up to 1 %.[15] Replicating the active site and applying the molecules toward proton reduction has proved unsuccessful; of fifty model Ni-

Fe complexes synthesised only two were reported to demonstrate catalytic proton reduction.[1] The lack of functioning hydrogenase mimics suggest the large protein environment in which the active site is situated plays a primary role in activity and therefore simply replicating the active site will not succeed in producing proton reduction catalysts, also known as hydrogen evolution catalysts. A different approach is therefore required.

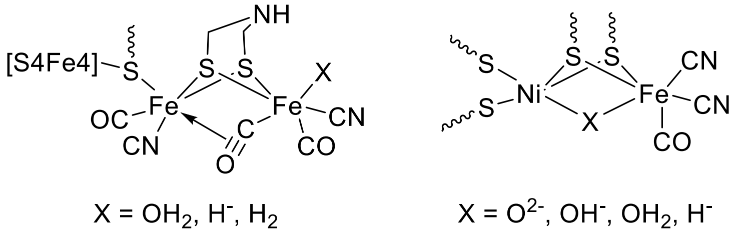

3 **4**

Figure 4. The Bi-metallic Active Sites of FeFe (3) and NiFe (4) Hydrogenases.

One approach is the use of solid state electrocatalysts. The mechanism of hydrogen evolution at metal electrodes in aqueous media consists of a sequence of three processes.[16] The initial process is the adsorption of H· to the surface of the electrode by coupling a single electron transfer with a proton transfer. Hydrogen evolution can occur *via* the interaction of two adsorbed hydrogen radicals combining and desorbing as H_2 or alternatively *via* protonation of an absorbed H· coupled to another single electron transfer evolving H_2. The efficiency of dihydrogen formation depends upon the strength of the M-H adsorption bond. A representation of hydrogen evolution rate against M-H bond strength is shown in Figure 5.[16] Metals that lie on the left-hand side of the volcano peak form relatively weak M-H bonds so the adsorption process is slow, thus causing hydrogen evolution to be slow. The metals situated on the right-hand side of the volcano peak form strong M-H bonds so desorption and evolution of hydrogen is hindered, reducing efficiency. The metals situated at the peak of the volcano plot have the optimum M-H interaction strength for efficient adsorption and desorption and therefore are the most accomplished hydrogen evolution catalysts. These metals are expensive, rare metals and so implementation is not a viable concept for affordable energy production.

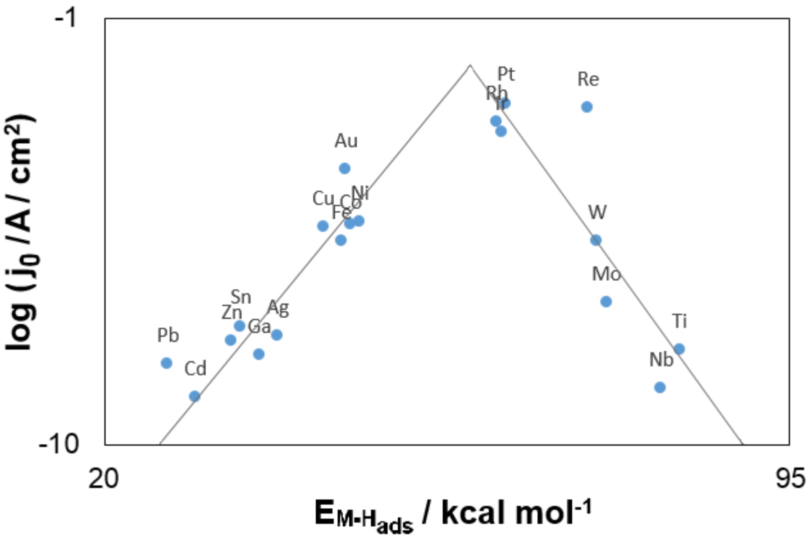

Figure 5. Representative Plot of Hydrogen Evolution Rates of Various Metals (in Terms of Dependence of Log Jo values) over M-H Bond Energy *via* Electrocatalysis. Representative Plot Adapted From Ref [16].

Another approach is the development of molecular catalysts incorporating inexpensive, earth abundant metals, but moving away from the hydrogenase mimic approach. Transition metals can store electrons *via* multiple redox states and are therefore suitable candidates to catalyse proton reduction.[17, 18] DuBois and co-workers developed diphosphine nickel complexes (including **5**) capable of proton reduction in organic solvents (Figure 6).[19, 17, 18] DuBois' catalysts have strategically positioned amine groups that are believed to be responsible for the high catalytic rates of the catalysis by serving as proton relays.[19, 17] The presence of proton relays in the second coordination sphere of the metal catalyst can favour PCET processes and facilitate the formation of the H–M^{n+} hydride intermediate which in turn facilitates the formation of the H–H bond. Application within water was unsuccessful do to solubility issues. In 1984 Spiro and co-workers demonstrated hydrogen production from water using cobalt porphyrins; **6** (Figure 6).[20] A Co^{III}-H$^-$ is formed from the Co^I porphyrin, this species can either undergo protonation to form H_2 and Co^{III} porphyrin or alternatively two hydride species can come together to form H_2 and two Co^{II} porphyrins. Gray and co-workers also defined these two mechanisms during their work on cobaloximes.[21] Both mechanisms rely on bi-molecular diffusion which limits rate.

A generic mechanistic scheme for proton reduction at a mono-metallic centre, M^{n+}, is given in Scheme 3. The two electron reduction of M^{n+} followed by protonation affords the key hydride intermediate, H–M^{n+}; this species can proceed to the products through two alternative pathways.[4] In the first, protonation of the hydride species results in hydrogen evolution and the regeneration of the starting catalyst; this pathway is labelled as the heterolytic pathway (Scheme 3, blue arrow).[4] Alternatively, reaction of the hydride species with a second hydride molecule releases hydrogen and forms M$^{(n-1)+}$; this is labelled as the homolytic pathway (Scheme 3, red arrow).[4] Heterolytic and homolytic pathways are competing mechanisms that can proceed exclusively or simultaneously, depending on the experimental conditions, such as the catalyst concentration or pH.

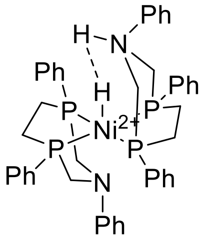

5

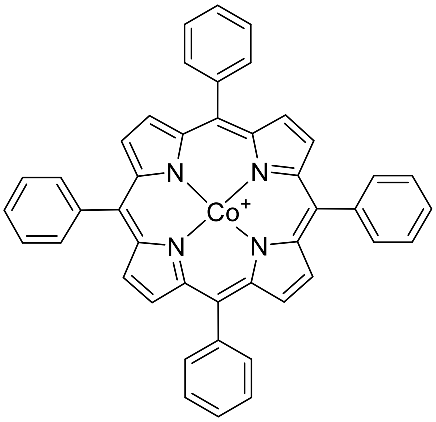

6

Figure 6. The Molecular Structure of Notable Proton Reduction Catalysts Employing First Row Transition Metals. Left; DuBois Catalyst. Right; Spiro Co^{I} porphyrin.[20, 22, 19]

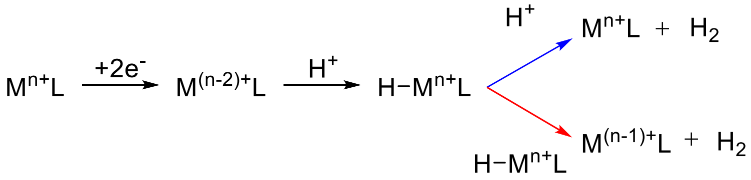

Scheme 3. Mechanistic Pathways of Proton Reduction by Mono-metallic Catalyst.[4]

1.5 Carbon Dioxide Reduction

The reduction of CO_2 to compounds of higher energy is the second process coupled to water oxidation by which nature creates fuel. Reduced CO_2 products have all the requirements for a chemical energy carrier as demonstrated by photosynthesis. Replicating the process industrially has additional benefits to the environment as it recycles carbon and reduces emissions. The current route to reduced carbon-based products used industrially is the production of syngas, which requires very high temperatures, ~ 900 °C. A more direct synthetic route to these industrial products may coincide in an overall reduction in energy consumption. CO_2 can be extracted from natural wells, but it is more beneficial to recover CO_2 from power station flue gases and other industrial sources. The structural stability of CO_2 makes reduction difficult. The one electron reduction of CO_2 has a highly negative redox potential (-1.9 V vs. NHE) (Scheme 4).[23] Alternatively, proton-coupled multi-electron transfer pathways are generally more favourable as thermodynamically stable molecules are produced avoiding high energy barriers (Scheme 4).[23]

$$CO_2 + e^- \longrightarrow CO_2^{\bullet -} \qquad E^0 = -1.90\ V$$

$$CO_2 + \mathbf{2e^-} + 2H^+ \longrightarrow H_2CO_2 \qquad E^0 = -0.61\ V$$

$$CO_2 + \mathbf{6e^-} + 6H^+ \longrightarrow CH_3OH + H_2O \qquad E^0 = -0.38\ V$$

Scheme 4. A Selection of CO_2 Reduction Processes and the Associated Energy of Each.

There are different methods of reducing CO_2; electrochemically, photochemically or *via* the use of chemical reducing agents such as hydrogen. All three methods require the employment of a catalyst to avoid the formation of the CO_2 radical anion and minimise the energy barrier. Using hydrogen is favourable as it allows access to the lower energy PCET pathways. The most efficient molecular catalysts for CO_2 reduction are based on noble metals such as iridium, ruthenium or rhodium. One of the most active catalysts reported to date for CO_2 reduction in the presence of hydrogen is the iridium pincer complex **7**, capable of 3.5×10^6 TON with a TOF of 40 s^{-1} (Figure 7).[24] Photocatalytic reduction using solar energy is desirable as it decreases input energy. $[Re(bpy)(CO)_3Cl]$, **8**, has demonstrated photocatalytic ability with a $Ø_{CO} = 0.14$ and good selectivity (Figure 7).[23] The rhenium complex performs dual roles in the reaction; it both absorbs the light and performs the catalytic reduction.

The first step toward CO_2 reduction is the two electron reduction of the metallic centre (Scheme 5).[4] In the presence of hydrogen a metal hydride is formed oxidising the metal centre by two electrons; $H\text{-}M^{n+}L$. From this point two pathways are available; hydride transfer from the metal complex to a coordinated CO_2 molecule forming a carboxylate anion that is released and protonated to form formic acid, in turn recycling the initial complex.[4] Alternatively H_2 coordination occurs preceding release, again recycling to the original complex.[4]

The primary drawbacks of each molecular catalyst is the incorporation of expensive metal centres meaning they cannot be implemented into a commercially viable large scale CO_2 reduction process.

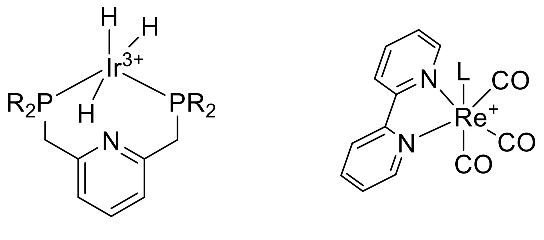

7 **8**

Figure 7. The Structure of Notable Carbon Dioxide Reduction Catalysts.[24, 23]

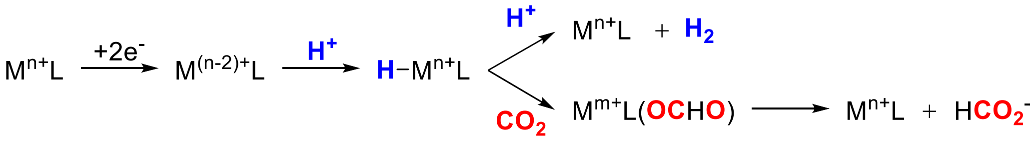

Scheme 5. Mechanism of Carbon Dioxide Reduction in the Presence of Hydrogen.[4]

1.6 Methane Oxidation

Methane oxidation does not play a role in the artificial photosynthesis system, but provides another alternative chemical energy carrier. Methane is the major component of natural gas (75 – 90 %) and is one of the most abundant hydrocarbons in the world.[25] Current estimates of natural gas reserves are ~ 6100 trillion cubic feet, comparable with oil on an energy content basis.[25] Given the abundance, wide global distribution and low carbon and sulphur content compared to oil and coal, methane is an ideal candidate to replace fossil fuels. One of the main reasons that methane cannot replace oil and coal is that it cannot be economically transported due its low boiling point and the low energy density. Commercially available technologies for the conversion of methane to liquids that can be efficiently transported, such as methanol or liquid paraffins *via* the Fischer-Tropsch process, are too expensive to compete with petroleum.[26] To exploit the abundance of methane reserves new processes need to be developed for low cost and efficient conversion to methanol. Methanol is a convenient liquid fuel with a safe boiling point, 64.7 °C, low carbon content and the liquid state means current fuel infrastructures do not need to be replaced (as would be required for a gaseous fuel such as CH_4 and H_2).[27] At present, methanol is mass produced from syngas, which is obtained from reforming fossil fuels requiring very high temperatures.[27, 26] The selective hydroxylation of methane to methanol employing atmospheric oxygen is another 'Holy Grail' transformation for energy production but the process is challenging due to the large C-H bond strength of methane; 105 $kcalmol^{-1}$.[25]

Commercial catalysts used for generic alkane oxidations typically take the form of solid metal oxides and have been insufficient toward methane oxidation without employing high temperatures and pressures that lead to low reaction selectivity and inefficient chemistry. The development of new catalysts to facilitate the selective oxidation of methane at low temperatures and pressures are required to realise a 'methanol economy'. The modified Shilov system, $Pt(bpym)Cl_2/H_2SO_4$ (bpym = 2,2'-bipyrimidyl) **(9)**, demonstrated conversion of methane to methanol in yields of over 70 %, selectivity > 90 % and turnovers ~ 1000 (Figure 8).[28, 29] However, a platinum based catalyst is not commercially viable for large scale methanol production. This method of methanol production also produces equimolar amounts of sulphur dioxide, which is toxic.

Another approach is C-H activation using homogeneous catalysts consisting of transition metals. The methane monooxygenases (MMO) are an extensively studied family of oxidative metalloenzymes. MMO is a versatile catalyst, but is renowned for its ability to oxidise methane bonds, producing methanol, by activating dioxygen, a feat unmatched by synthetic systems. MMO is a bi-metallic iron complex existing within the di-nuclear non-heme classification **(10)** (Figure 8). While MMO mimics have not been able to replicate the strong oxidation power of the metalloenzyme a vast amount of research into C-H oxidation with ferrous complexes *via* the activation of atmospheric O_2 is underway and discussed further in Chapter 3 – Oxidation of Hydrocarbon by Di-ferrous C3. Ferrous ions can reach the high valence IV and sometimes V oxidation states supplying the electrons required to activate dioxygen. The typical mechanism for oxygen activation and subsequent C-H oxidation by mono-metallic ferrous complexes is shown in Figure 9. The ferrous centre binds dioxygen and is oxidised by one electron to form a ferric-superoxo, homolytic cleavage of the O-O bond results in the formation of an $Fe^{IV}=O$ species capable of C-H oxidation *via* hydrogen abstraction and oxygen rebound. $[Fe(dnpbn)(L)_2]^{2+}$ is one of many mono-nuclear ferrous complexes employed as catalysts for C-H oxidation by activating dioxygen.[30] The complex is cheap and readily synthesised making it an ideal candidate as a catalyst.

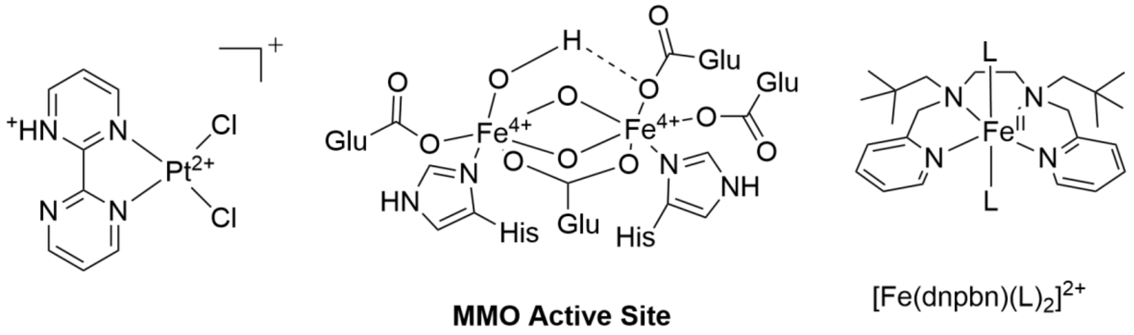

9 **10** **11**

Figure 8. Notable Methane Oxidation Catalysts. Left; Modified Shilov System, 9. Middle; Active Site of MMO Metalloenzymes, 10. Right; Synthetic C-H Oxidation Catalyst 11.

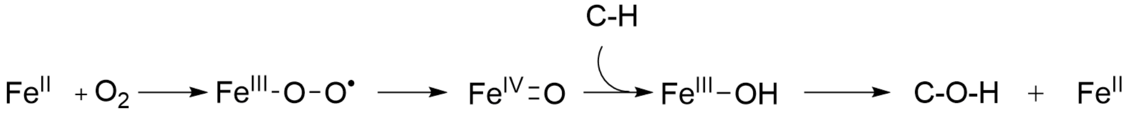

$$Fe^{II} + O_2 \longrightarrow Fe^{III}\text{-}O\text{-}O^{\bullet} \longrightarrow Fe^{IV}=O \xrightarrow{C\text{-}H} Fe^{III}\text{-}OH \longrightarrow C\text{-}O\text{-}H + Fe^{II}$$

Figure 9. Mechanism of C-H Oxidation *via* Activation of Dioxygen by Ferrous Mono-nuclear Complexes.

1.7 Two Electron Mixed Valence Strategy For Facilitating Multi-Electron Reactions

In the development of multi-electron catalysts many approaches have been taken including solid state electrocatalysts, metalloenzyme mimics and first row transition metal molecular catalysts, another approach is two-electron mixed valence complexes. Nocera proposed that bi-metallic two-electron mixed-valence systems are ideally suited to accommodate multi-electron reactions, just as single electron mixed-valence compounds react in one electron steps it is proposed that two-electron mixed valence compounds will react in two electron steps thus supplying the electrons required for proton reduction and other multi-electron reactions *via* the lowest energy pathway.

Mixed valence complexes are commonly made up of two or more metal centres of different oxidation states leading to a disproportionation of charge throughout the molecule. Robin and Day formed a classification system for bridged bi-metallic mixed valence complexes based on charge delocalisation.[31] When the charge is held independently on each metal atom it is categorised as a class I system. Conversely, when the charge is delocalised over both metal atoms such that the charge is shared equally, it is categorised as a class III system. A range of complexes demonstrating characteristics between class I and III, in which coupling between the metal centres is moderate, are categorised as class II. The earliest report of a mixed valence complex is Prussian Blue **(12)** (Figure 10, Top).[32] **12** has a basic cubic structure consisting of alternating ferrous and ferric ions. The distinctive blue colour that led to the name is caused by intervalence charge transfer between the chemically inequivalent iron ions.[33, 34] The presence of intervalence charge transfer bands are a means of confirming the formation of a mixed valence complex. In 1969 an intervalence charge transfer band at 1570 nm after the addition of $[(NH_3)_5RuOH_2]^{2+}$ to a solution of pyrazine confirmed the formation of a new mixed valence complex later characterised as the Creutz-Taube ion **(13)** (Figure 10, Bottom).[35] The structure of **13** is such that one ruthenium ions exists in the 2+ oxidation state while the other exists in the 3+ state. The formation of this complex pioneered extensive study of one-electron mixed valence systems and intervalence electron transfer.

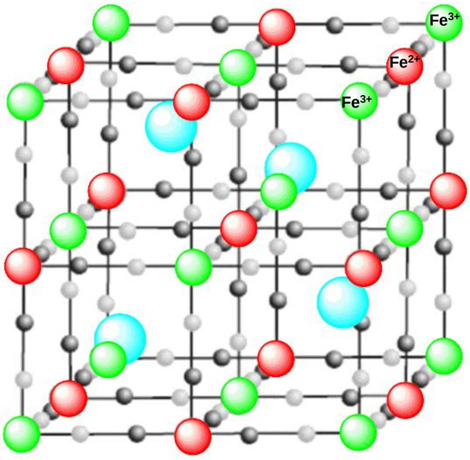

12

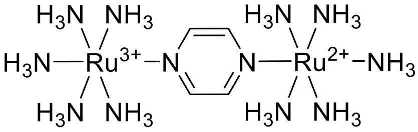

13

Figure 10. The First One-Electron Mixed Valence Complexes Discovered. Top; Prussian Blue, 12. Bottom; Creutz-Taube ion, 13.[34, 35]

The development of two-electron mixed valence complexes is more challenging as it is chemically difficult to maintain the two electron difference in oxidation state and prevent the symmetric M^{n+}-M^{n+} species being reformed. Nocera and co-workers discovered two-electron mixed-valence complexes could be generated from internal disproportionation of the metal centres of a symmetric bi-metallic core.[36, 37] For M^{n+}-M^{n+}, with weakly coupled valence electrons, disproportionation could be accomplished by exciting metal-to-metal charge transfer transitions to give $M^{(n+1)+}$-$M^{(n-1)+}$. They found the two-electron mixed valence state could be maintained by tuning the coordinating ligands.[38, 37] Stable two-electron mixed valence complexes were obtained using ligands comprising of an amine bridgehead between two electron deficient phosphines or phosphites such as $CH_3N(PF_2)_2$ (dfpma) **(14)** and $CH_3N[P(OCH_2CF_3)_2]_2$ (tfepma) **(15)** (Figure 11).[38, 39, 40] The structure of these ligands has been labelled as an *A-D-A* system (acceptor – donor – acceptor) due to the π-accepting character of the electron deficient phosphines situated either side of the π-donating amine bridge.[38, 41, 42]

The phosphine/phosphite groups can accept electrons from either the metal ions or nitrogen group. The amine bridgehead donates a lone pair of electrons to the phosphine group bonded to the electron deficient $M^{(n+2)+}$ centre. With $M^{(n+2)+}$ – phosphine π-back bonding absent the phosphine group acts solely as a σ-donor maintaining the n+2 charge of the metal centre. The phosphine bonded to the electron rich M^{n+} centre maintains π-accepting character and stabilises the M^{n+} centre. The *A-D-A* system was demonstrated to be essential for stabilisation of two-electron mixed valency when contrast to $CH_2(PR_2)_2$ ligands; without the donating amine bridgehead the two-electron mixed-valence state could not be stabilised and the symmetric M^{n+}-M^{n+} complex resulted.[43]

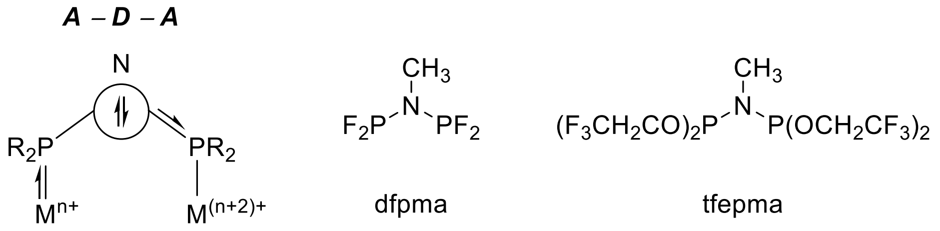

dfpma

14

tfepma

15

Figure 11. Nocera *A-D-A* Ligand Scaffold Structure which Supports Stabilisation of Bi-metallic Two-Electron Mixed Valence Complexes and Two Exemplary Structures; 14 and 15.

In 2000 Nocera and co-workers synthesised a stable two-electron mixed-valence di-iridium complex with ligand scaffold **15**, capable of reversible hydrogen binding; this was particularly significant as reversible H_2 addition across a preserved M-M bond had not been seen previously.[39] The mechanism is illustrated in Scheme 6.[44, 45] Addition of H_2 to Ir^0 – $Ir^{II}(X)_2$ occurred at the Ir^{II} site mediated by a bridging hydride that must be supplied by the reactant. A halogen must swing from the equatorial position to allow an entering hydrogen atom to access the bridge position.[39] The macroscopic reverse of hydrogen binding is reductive elimination (Scheme 6, Bottom). The $H^{\bullet}$ must migrate back to the M^{n+2} site to form the H-H bond prior to release of H_2.[42] The ability of the hydrogen atom to migrate across metal centres while the asymmetric mixed-valence state is maintained is essential for catalytic function.

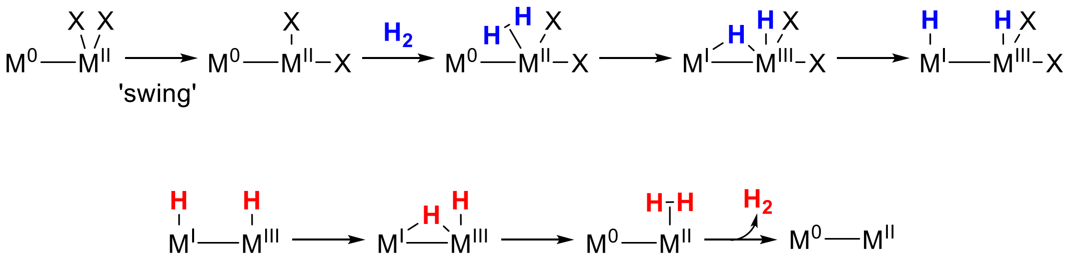

Scheme 6. Mechanism of Hydrogen Addition (Top) and Reductive Elimination (Bottom) by Bi-metallic Two-Electron Mixed Valence Complexes.

In 2001 Nocera and co-workers successfully achieved proton reduction to evolve hydrogen *via* a di-rhodium complex with ligand scaffold **14**.[46] Rh-H bonds are weaker than Ir-H bonds and hence should facilitate hydrogen migration and elimination with greater ease. The precursor to the reaction was $Rh_2^{0,0}(dfpma)_3(PPh_3)(CO)$, **16** (Scheme 7).[46, 47] The CO ligand bound to one rhodium centre is photolabile whereas the PPh_3 ligand bound to the other rhodium centre is photoinert. Irradiation of the complex in CH_2Cl_2 at $\lambda_{exc} \geq 338$ nm led to the dissociation of the photolabile CO ligand creating a vacant axial coordination site. The subsequent reaction with HX (X = Cl or Br) led to the formation of an equivalent of H_2 and a blue intermediate that could not be structurally characterised. It was originally proposed that the blue intermediate was a tetra-nuclear complex formed from the reaction of two PPh_3-Rh^0-Rh^{II}-HX molecules coming together and releasing the first equivalent of H_2. The mechanism was proposed on the basis of similarities between the blue intermediates spectral profile and that of a tetra-nuclear rhodium cluster with mixed valence character found by Gray and co-workers.[48] However, further work disproved the proposed mechanism.[47] It is now known the reaction of $Rh_2^{0,0}(dfpma)_3(PPh_3)(CO)$ with hydrohalic acid yields a $Rh^{II,II}$ dihydride dihalide product that photoeliminates an equivalent of H_2 leading to the characterisation of the blue intermediate as a $Rh^{I,I}$ dihalide complex (Scheme 7).[47, 42]

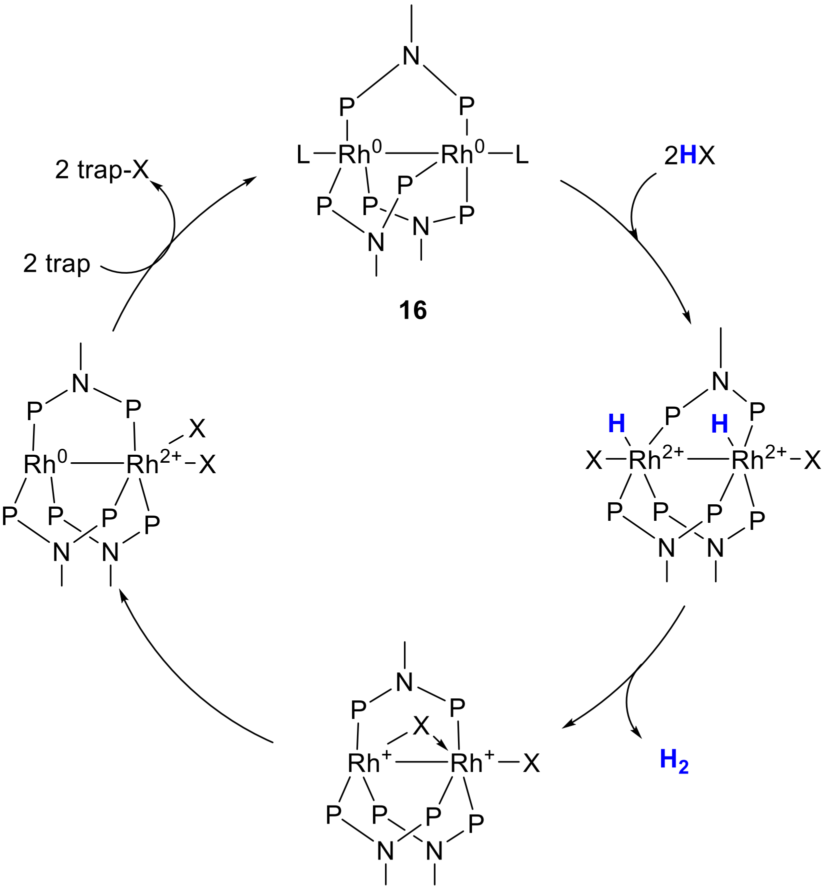

Scheme 7. Photocatalytic Cycle of Proton Reduction Facilitated by Dirhodium Complex Supported by *A-D-A* Ligand Scaffold 15.

The mixed valence approach is not restricted to reduction reactions. Oxygen can be activated *via* the two-electron mixed-valence strategy using co-facial porphyrins, given the name "Pacman porphyrins", as photocatalysts.[41] The di-ferrous "Pacman" binds molecular oxygen to form a di-ferric μ-oxo porphyrin, light excitation breaks the Fe^{III}–O–Fe^{III} bond to produce a two electron mixed valence $Fe^{II}\cdots Fe^{IV}=O$ intermediate capable of oxidising simple electron-rich substrates such as phosphines and sulphides (Figure 12).

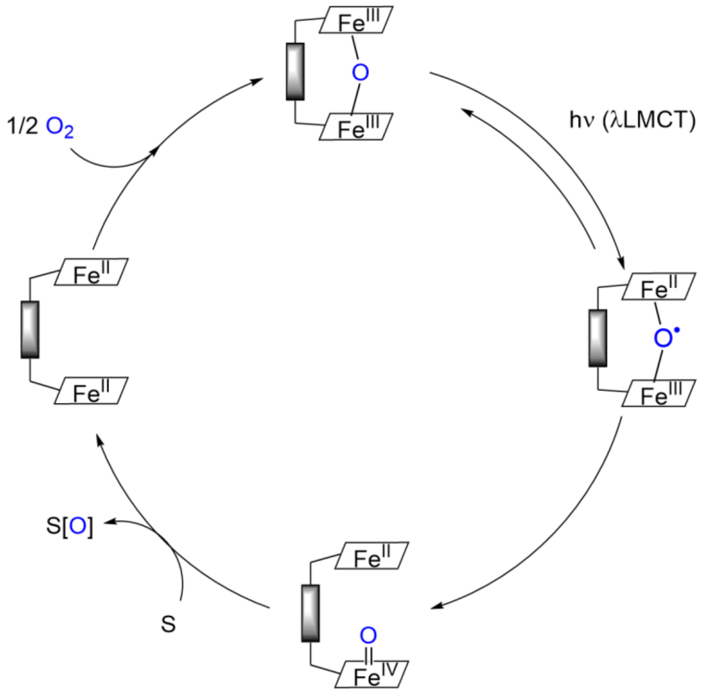

Figure 12. Catalytic Cycle of "Pacman porphyrins" Toward Oxygen Activation and Substrate Oxidation. [41]

Although Nocera has developed a novel means of facilitating multi-electron reactions *via* the successful synthesis and characterisation of elusive two-electron mixed-valence complexes, the incorporation of iridium or rhodium catalysts as a viable, affordable means of energy production is not realistic as they are not abundant elements and therefore the demand would exceed resources. Therefore the scope of two-electron mixed-valence research expanded to ligand-based mixed valence complexes.

As with the metal-based complexes, ligand-based two-electron mixed valence complexes contain an unequal distribution of two electrons, but the inequality of charge is situated on the ligand rather than the bi-metallic core which can achieved by the utilisation of redox active ligands. Ligands are usually thought of as spectators or with influence by tuning reactions but not as reaction centres, however a number of ligands can display redox activity when in certain environments (further discussion can be found in Chapter 2 – Asymmetric Ligand L^1 and Bi-metallic Complexes Thereof). The redox active ligand can serve as an electron reservoir, storing and releasing electrons when required throughout the reaction.[49]

Nocera and co-workers used porphyrinogens as the basis for their ligand-based mixed valence complex investigation.[49] Upon oxidation of the tetrapyrrole one or two cyclopropane rings are formed, which can act as hole reservoirs. Two or four oxidation equivalents can therefore be stored within the macrocycle (Scheme 8).[49] Nocera and co-workers investigated the redox activity of Zn-containing porphyrinogens **(18)** as the redox inert behaviour of zinc allows for characterisation of ligand radicals. Starting from **18**, two oxidation processes were detected using differential pulse voltammetry (products; **19** and **20**). The voltammogram obtained provided evidence that the intermediate two-electron mixed-valence complex **(19)** is a stable entity (Scheme 8. Middle).[49] Obtaining the stable intermediate demonstrates ground state ligand-based two-electron mixed-valence complexes can be achieved and could realistically play a key role in facilitating multi-electron reactions.

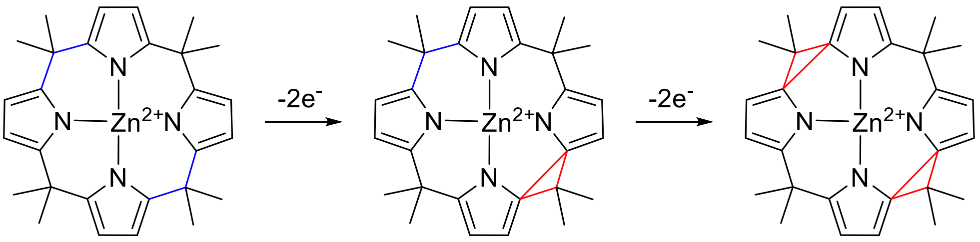

18 **19** **20**

Scheme 8. Nocera Ligand-based Two-Electron Complex Based on Zinc Porphyrinogen.

1.8 Conceptual Design of Molecular Catalysts In This Thesis and Aims

The initial aim of this project was to address the critical energy situation through the development of first row transition metal molecular catalysts capable of facilitating multi-electron reactions. Reactivity with respect to H_2 formation, as an initial target, was considered in the design of the system.

The first characteristic thought to beneficial for multi-electron catalysis design, based on the review of current multi-electron transformations and catalysts, was the incorporation of bi-metallic structures. The oxidation of water *via* the M-O interaction pathway relies upon M-O bi-molecular diffusion. Proton reduction to molecular hydrogen can also occur through a similar bi-molecular mechanism. Bi-metallic complexes offer enhanced catalytic rates offer mono-nuclear complexes as the two sites are already within close proximity and do not rely upon diffusion.

The second attribute desired was the ability of the complex to access multiple oxidation states allowing for the storage and distribution of electrons, specifically for proton reduction the accommodation of two electrons for distribution during the reaction. This was typically achieved by current molecular catalysts through employment of transition metals such as Ir, Rh and Ru, but can be addressed by the utilisation of a ligand-based redox active unit. The employment of redox active ligands allows for the incorporation of low cost, abundant metals while retaining the same activity. Nocera’s work on two-electron mixed valence complexes has shown particular success in the two electron reduction of protons. Just as single electron mixed-valence compounds react in one electron steps it is proposed that two-electron mixed valence compounds will react in two electron steps thus supplying the electrons required for proton reduction and other multi-electron reactions *via* the lowest energy pathway. An asymmetric ligand scaffold design was chosen to enable the formation of two-electron mixed valence species.

Finally, commonly metal hydride species are formed as the active intermediates in CO_2 reduction and proton reduction. PCET pathways provide lower energy barriers so the formation of complexes with metals known to bind hydrides are important. Nocera's work with di-iridium and di-rhenium complexes unveiled the mechanism by which hydrogen is formed is through migration of a hydrogen atom from one metal centre to the second so the distance between the metal sites needs to be close enough to allow this. A spacer that allows the coordination of two metal ions within close proximity is required.

The conceptual design taking into account all these features is illustrated in Figure 13. The first ligand scaffold design is shown in Figure 13 and was named L^1 (**21**).

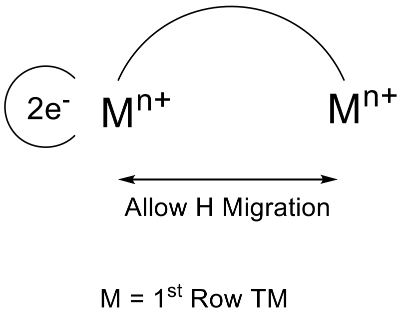

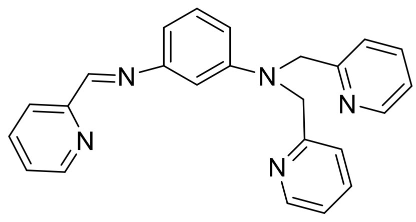

L^1

21

Figure 13. Ligand Scaffold Concept to Facilitate Multi-electron Transformations and Initial Scaffold L^1, 21.

L^1 has the potential to bind two metal ions through *N*-donors of the α-diimine unit and bis(pyridylmethyl)amino groups. The bis(pyridylmethyl)amino group is redox inactive and selected due to the chelate ability and saturated character. The α-diimine group is redox active and can theoretically be reduced twice to store two electrons. The use of a ligand-based electron pool allows cheap and abundant first row transition metals to be used. The asymmetric design of the ligand should allow for the formation of two-electron, mixed valence complexes. The *meta* bridging benzene group was chosen as an initial spacer as it should favour the coordination of two metal ions in close proximity, required for processes such as proton migration.

The complexes formed using L^1 and late first row transition metals were synthesised, characterised and assessed with respect to suitability for multi-electron reactions. These studies are presented in Chapter 2 – Asymmetric Ligand L^1 and Bi-metallic Complexes Thereof. The L^1 scaffold originally designed for reduction processes, initially proton reduction, proved to be most suitable for oxygen transfer. Based on this realisation, C-H oxidation reactivity studies were undertaken and are discussed in Chapter 3 – Oxidation of Hydrocarbons by Di-ferrous **C2** and **C3**. Detailed spectroscopic studies were undertaken in attempt to expose the active species formed during C-H oxidation by the di-ferrous **C3,** and are discussed in Chapter 4 – Spectroscopic

Investigation into the Active Species Facilitating Hydrocarbon Oxidation using **C3**. The studies of L^1 with first row transition metals highlighted limitations for use in redox processes therefore a new series of improved ligand scaffolds, which might more readily favour the desired two electron mixed valence form were designed. Structures and synthetic routes developed are described in the final Chapter of this work; Chapter 5 – Synthesis of a New Generation Series of Aza-macrobicyclic Ligand Scaffolds for use in Multi-electron Reactions.

1.9 References

(1) Cook, T. R.; Dogutan, D. K.; Reece, S. Y.; Surendranath, Y.; Teets, T. S.; Nocera, D. G. *Chem. Rev.* **2010**, *110*, 6474.

(2) Gov. UK *Energy Trends Section 5: Electricity;* **2015**.

(3) Grätzel, M. *Inorg. Chem.* **2005**, *44*, 6841.

(4) Berardi, S.; Drouet, S.; Francas, L.; Gimbert-Surinach, C.; Guttentag, M.; Richmond, C.; Stoll, T.; Llobet, A. *Chem. Soc. Rev.* **2014**, *43*, 7501.

(5) Vrettos, J. S.; Brudvig, G. W. *Philos. Trans. R. Soc. London, Ser. B* **2002**, *357*, 1395.

(6) Liu, F.; Concepcion, J. J.; Jurss, J. W.; Cardolaccia, T.; Templeton, J. L.; Meyer, T. J. *Inorg. Chem.* **2008**, *47*, 1727.

(7) Gersten, S. W.; Samuels, G. J.; Meyer, T. J. *J. Am. Chem. Soc.* **1982**, *104*, 4029.

(8) Pokhrel, R.; Brudvig, G. W.; Poeppelmeier, J. R. In *Comprehensive Coordination Chemistry II;* Elsevier: Amsterdam, 2013, p 385.

(9) Duan, L.; Bozoglian, F.; Mandal, S.; Stewart, B.; Privalov, T.; Llobet, A.; Sun, L. *Nat. Chem.* **2012**, *4*, 418.

(10) Armaroli, N.; Balzani, V. In *Energy for a Sustainable World*; Wiley-VCH Verlag: 2010, p 279.

(11) Parker, V. D. *J. Am. Chem. Soc.* **1992**, *114*, 7458.

(12) Artero, V.; Fontecave, M. *Coord. Chem. Rev.* **2005**, *249*, 1518.

(13) Johnson, D. C.; Dean, D. R.; Smith, A. D.; Johnson, M. K. *Annu. Rev. Biochem.* **2005**, *74*, 247.

(14) Tamagnini, P.; Axelsson, R.; Lindberg, P.; Oxelfelt, F.; Wünschiers, R.; Lindblad, P. *Microbio. Mol. Biol. Rev.* **2002**, *66*, 1.

(15) Reisner, E.; Fontecilla-Camps, J. C.; Armstrong, F. A. *Chem. Commun.* **2009**, 550.

(16) Conway, B. E.; Tilak, B. V. *Electrochim. Acta* **2002**, *47*, 3571.

(17) Wang, M.; Chen, L.; Sun, L. *Energy Environ. Sci.* **2012**, *5*, 6763.

(18) Thoi, V. S.; Sun, Y.; Long, J. R.; Chang, C. J. *Chem. Soc. Rev.* **2013**, *42*, 2388.

(19) Helm, M. L.; Stewart, M. P.; Bullock, R. M.; DuBois, M. R.; DuBois, D. L. *Science* **2011**, *333*, 863.

(20) Kellett, R. M.; Spiro, T. G. *Inorg. Chem.* **1985**, *24*, 2373.

(21) Dempsey, J. L.; Brunschwig, B. S.; Winkler, J. R.; Gray, H. B. *Acc. Chem. Res.* **2009**, *42*, 1995.

(22) Eckenhoff, W. T.; Eisenberg, R. *Dalton Trans.* **2012**, *41*, 13004.

(23) Benson, E. E.; Kubiak, C. P.; Sathrum, A. J.; Smieja, J. M. *Chem. Soc. Rev.* **2009**, *38*, 89.

(24) Wang, W.; Wang, S.; Ma, X.; Gong, J. *Chem. Soc. Rev.* **2011**, *40*, 3703.

(25) Conley, B. L.; Tenn, W. J.; Young, K. J. H.; Ganesh, S.; Meier, S.; Ziatdinov, V.; Mironov, O.; Oxgaard, J.; Gonzales, J.; Goddard, W. A.; Periana, R. A. In *Activation of Small Molecules*; Wiley-VCH Verlag: 2006, p 235.

(26) Armaroli, N.; Balzani, V. In *Energy for a Sustainable World*; Wiley-VCH Verlag: 2010, p 69.

(27) Olah, G. A. *Angew. Chem. Int. Ed.* **2005**, *44*, 2636.

(28) Kushch, K. A.; Lavrushko, V. V.; Misharin, Y. S.; Moravsky, A. P.; Shilov, A. E. *New. J. Chem.* **1983**, *7*, 729.

(29) Periana, R. A.; Taube, D. J.; Gamble, S.; Taube, H.; Satoh, T.; Fujii, H. *Science* **1998**, *280*, 560.

(30) Zhang, Q.; Gorden, J. D.; Goldsmith, C. R. *Inorg. Chem.* **2013**, *52*, 13546.

(31) Robin, M. B.; Day, P. In *Adv. Inorg. Chem. Radiochem.*; Sharpe, Academic Press: 1968; Vol. 10, p 247.

(32) Buser, H. J.; Schwarzenbach, D.; Petter, W.; Ludi, A. *Inorg. Chem.* **1977**, *16*, 2704.

(33) Day, P.; Herren, F.; Ludi, A.; Güdel, H. U.; Hulliger, F.; Givord, D. *Helv. Chim. Acta* **1980**, *63*, 148.

(34) Robin, M. B. *Inorg. Chem.* **1962**, *1*, 337.

(35) Creutz, C.; Taube, H. *J. Am. Chem. Soc.* **1969**, *91*, 3988.

(36) Dulebohn, J. I.; Ward, D. L.; Nocera, D. G. *J. Am. Chem. Soc.* **1988**, *110*, 4054.

(37) F. Heyduk, A.; G. Nocera, D. *Chem. Commun.* **1999**, 1519.

(38) Heyduk, A. F.; Macintosh, A. M.; Nocera, D. G. *J. Am. Chem. Soc.* **1999**, *121*, 5023.

(39) Heyduk, A. F.; Nocera, D. G. *J. Am. Chem. Soc.* **2000**, *122*, 9415.

(40) Odom, A. L.; Heyduk, A. F.; Nocera, D. G. *Inorg. Chim. Acta* **2000**, *297*, 330.
(41) Rosenthal, J.; Bachman, J.; Dempsey, J. L.; Esswein, A. J.; Gray, T. G.; Hodgkiss, J. M.; Manke, D. R.; Luckett, T. D.; Pistorio, B. J.; Veige, A. S.; Nocera, D. G. *Coord. Chem. Rev.* **2005**, *249*, 1316.
(42) Dempsey, J. L.; Esswein, A. J.; Manke, D. R.; Rosenthal, J.; Soper, J. D.; Nocera, D. G. *Inorg. Chem.* **2005**, *44*, 6879.
(43) Gray, T. G.; Nocera, D. G. *Chem. Commun.* **2005**, 1540.
(44) Gray, T. G.; Veige, A. S.; Nocera, D. G. *J. Am. Chem. Soc.* **2004**, *126*, 9760.
(45) Veige, A. S.; Gray, T. G.; Nocera, D. G. *Inorg. Chem.* **2005**, *44*, 17.
(46) Heyduk, A. F.; Nocera, D. G. *Science* **2001**, *293*, 1639.
(47) Esswein, A. J.; Veige, A. S.; Nocera, D. G. *J. Am. Chem. Soc.* **2005**, *127*, 16641.
(48) Sigal, I. S.; Mann, K. R.; Gray, H. B. *J. Am. Chem. Soc.* **1980**, *102*, 7252.
(49) Bachmann, J.; Nocera, D. G. *J. Am. Chem. Soc.* **2004**, *126*, 2829.

Chapter 2 – Asymmetric Ligand L^1 and Bi-metallic Complexes Thereof

The asymmetric ligand L^1 **(21)** was designed with two distinct coordination sites, supplied by an α-iminopyridine and a bis(2-pyridylmethyl)amino group. The two-electron redox series available to α-iminopyridines, as a consequence of low-lying π* orbitals, has been previously established, whereas the bis(2-pyridylmethyl)amino group serves as an innocent counterpart. The divergent nature of the two functional groups offers a strategy for the selective reduction of one side of a bi-metallic complex, thus, permitting mixed valency unconstrained by the accessibility of a particular metal oxidation state. The coordination chemistry of L^1 with Fe, Cu and Zn is described herein. The series of metal complexes includes both symmetric and asymmetric bi-metallic complexes. Electrochemical studies provide an indication of the nature of the redox processes available to these complexes. Both metal- and ligand-centred redox processes are available to the series of metal compounds. The Cu and Fe complexes were further characterised by spectroscopic, magnetic susceptibility and DFT computational studies, which unveiled weak ferromagnetic coupling between the metal centres of the dimers.

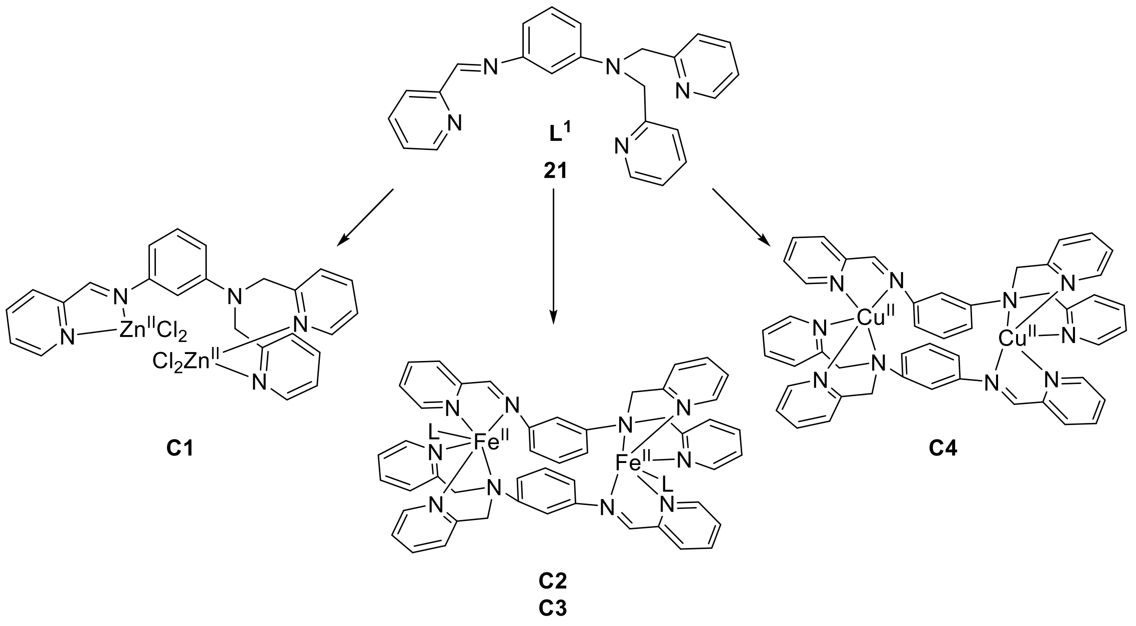

Scheme 9. The Structure of Asymmetric Ligand L^1 and Subsequent Bi-metallic Complexes Studied in this Chapter. Where L = OTf$^-$ for C2 and L = CH_3CN for C3.

2.1 Introduction

The development of alternative chemical energy carriers to replace fossil fuels is highly desirable given the high global energy demand and depleting resources. The transformation of small molecules (e.g. N_2, H_2O, CO_2, CH_4) to energy rich fuels is one bio-inspired approach, but involves energetically costly multi-electron processes. Nature has developed metalloenzymes to facilitate these transformations which make use of multiple redox sites to overcome the large energy barriers. Multi-electron reactions can be achieved synthetically by noble metals such as Pt, Ir and Rh, but the application of such metal catalysts is not cost effective. To create catalysts using cheap, abundant, first row transition metals non-innocent ligands can be incorporated. The coordination chemistry of non-innocent ligands has received considerable attention over the last decade.[50, 51, 52, 53, 54] Metal complexes containing non-innocent coordinating ligands have been shown to not only defy conventional oxidation state assignments, but exhibit unique electronic structures and a rich chemistry.[55, 56] The non-innocent behaviour has proven advantageous for reactivity: among the examples, ligand-centred redox processes have been implicated in C-C bond formation, alkene addition and nitrene transfer reactions by transition metal and actinide complexes containing the aforementioned non-innocent moieties.[57, 58, 59, 60, 61, 62, 63]

The non-innocent terminology was first introduced by Jörgensen in 1966.[64] Innocence is the classification given to ligands that "allow oxidation states of the central atom to be defined".[50] Conversely, the presence of non-innocent ligands stipulates a discrepancy of the oxidation state assignment of the central atom; the formal oxidation state differs from that found experimentally. The formal oxidation state of a metal ion in a complex is not a measurable quantity, but is determined from the charge of the metal ion after the closed shell ligands have been removed.[65] The number of *d* electrons present is a measureable quantity interpreted from spectroscopic data. An illustrative example of non-innocence is $Fe^{III} – O^{\bullet} – Ph$; the formal oxidation state after removing the closed shell ligand, $[O –Ph]^{-}$, assigns the iron ion as Fe^{IV}, but Mössbauer and Raman spectroscopy indicate the physical oxidation state of the iron ion is Fe^{III}.[65] The discrepancy can arise from the presence of electron rich and/or highly conjugated ligands with a raised HOMO level which overlaps with the metal frontier orbitals. This is called inverted bonding and allows the ligand to delocalise electron density and behave non-innocently (Figure 14).[66]

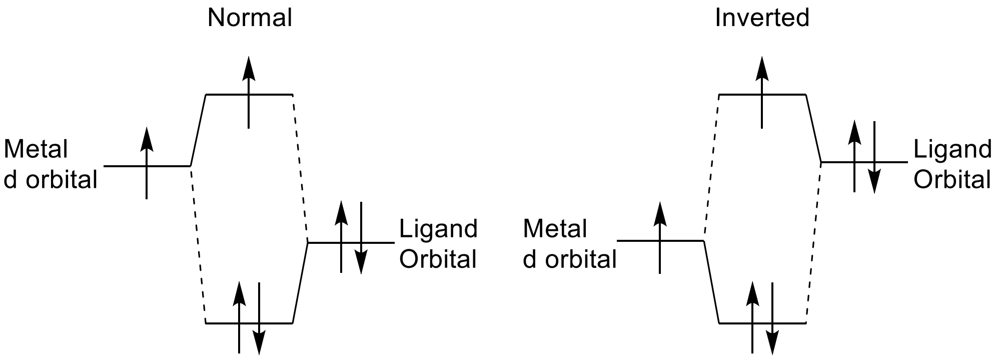

Figure 14. Normal and Inverted Bonding Orbital Energy Level Diagram.[66]

One of the first discovered examples of non-innocent ligand behaviour was by Holm and co-workers in 1966.[67] Holm and co-workers found that complexes comprised of dithiolate ligands could undergo reversible chemical and electrochemical redox processes. They demonstrated the two successive, reversible, one-electron redox reactions between the di-anionic dithiolate complex

$Ni(S_2C_2R_2)_2^{2-}$ and the neutral complex $Ni(S_2C_2R_2)_2$.[67] Although the structures could not be established at the time of publishing, these redox reactions are now known to be ligand-based as illustrated in Scheme 10.[53] The same two electron redox series has since been revealed for α-dicarbonyl compounds, including the extensively studied *o*-quinones, and α-diimines, by accepting electron density into the lowest unoccupied molecular orbital (LUMO).

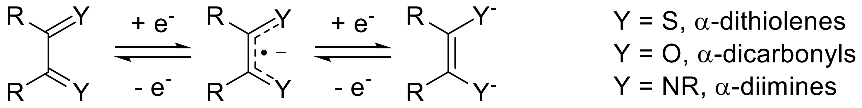

Scheme 10. Two Electron Redox Series of Organic Groups.[53]

During reactions non-innocent ligands can cooperate with the metal centre reacting synergistically to facilitate chemical processes *via* several different mechanisms. Four mechanisms are outlined as follows:[54]

1. Redox activity of the ligand modifies the Lewis acidity of the metal centre.
2. Ligands can accept or donate electron density avoiding uncommon oxidation states of the metal.
3. Reactive ligand radicals actively partake in the chemical reaction.
4. Radical reactivity is induced on the substrate ligand.

One example of a successful catalyst facilitating multi-electron reactions *via* mechanism two is Chirik's $[Fe^{II}(PDI)]^{2-}$ **(22)**.[51, 68, 69, 52] The bis(imino)pyridine ligand has four theoretical oxidation states.[70] Reduction of the ferrous $Fe^{II}(PDI)Cl_2$ with a sodium amalgam affords the di-radical species **(23)** capable of the [2+2] cycloaddition of dienes and terminal alkene hydrosilylation (Scheme 11).[51, 68, 71] The iron ion remains in the ferrous oxidation state throughout the catalytic cycles with the charge localised on the PDI ligand.

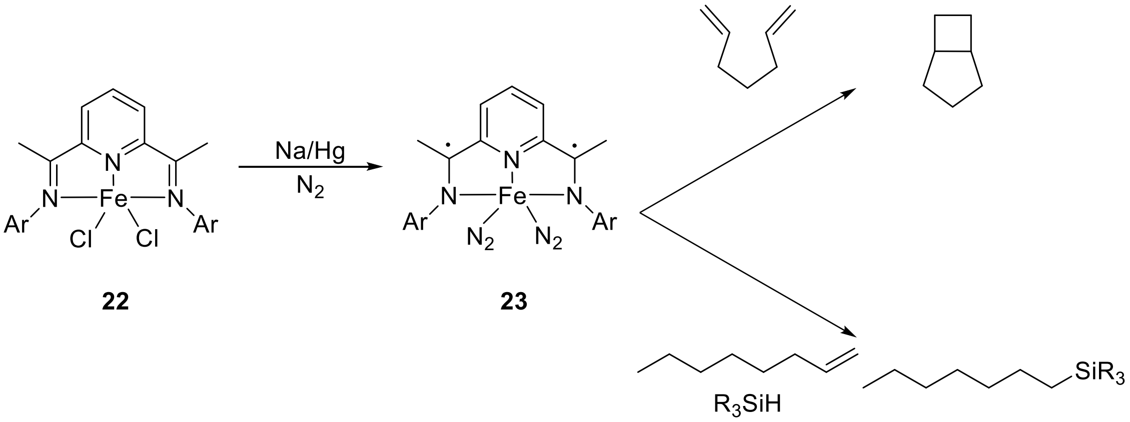

Scheme 11. Chirik [Fe^{II}(PDI)]²⁻ Reduction with Na/Hg and Subsequent Reactivity.

Although non-innocent ligands have been studied extensively in recent years in mono-metallic complexes, examples of bi-metallic complexes containing redox-active ligands are few. The most common bi-metallic motif consists of two metal ions connected by a redox-active bridge that directly moderates exchange interactions between the sites.[72, 73, 74] These, predominantly symmetric, compounds have attracted attention due to their relevance for molecular electronics. Examples include the dimeric $[Fe(TIM)]_2$ complex (TIM = 2,3,9,10-tetramethyl-1,4,8,11-tetraazacyclotetradeca-1,3,8,10-tetraene) **(24)** in which ligand radicals contribute to metal-metal bond formation and mixed valency.[75] Imido-bridged Zr and Ta dimers containing redox-active [NNN] and [ONO] pincer-type ligands have also been isolated where the ligands play a key role in oxidative formation of di-azenes.[63, 76, 77] The latter example illustrates how the electron storage capabilities of non-innocent ligands can be a powerful tool for facilitating multi-electron transformations. However, the reactivity of bi-metallic compounds containing organic cofactors have yet to be fully explored.

2.2 Asymmetric Ligand L^1 (21)

The asymmetric ligand, L^1, was designed as a bi-metallic scaffold. The asymmetry of the molecule is imposed by the distinct set of *N*-donor groups. Ligand-centred redox processes are available at the iminopyridine coordination site while the redox innocent bis(2-pyridylmethyl)amino group supplies the second coordination site. The two electron redox series available to α-iminopyridines imply that both one and two electron charge separated bi-metallic complexes could theoretically be accessed. Thus, L^1 offers an alternative strategy to the rare metal-based two electron mixed valence complexes. The *meta*-disposition of the bridging benzene moiety disfavours the formation of a mono-nuclear complex, exhibited by similar ligand scaffolds SBPy$_3$ **(25)**, BPAbipy **(26)** and TPOEN **(27)**.[78, 79, 80, 81] The *meta*-substituted benzene provides a large enough spacer distance to bind two metal ions in distinctive pockets.

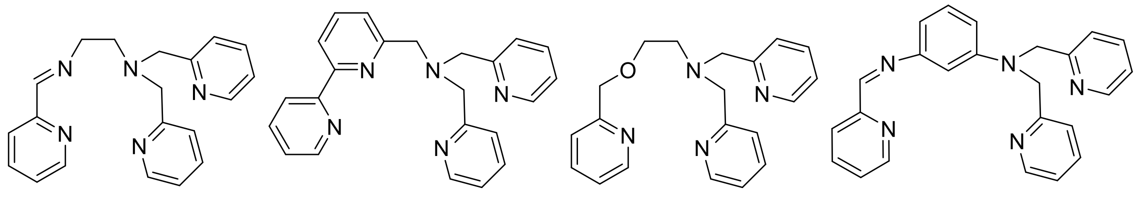

SBPy$_3$ BPAbipy TPOEN L^1

25 **26** **27** **21**

Scheme 12. Related Ligand Scaffolds All of Which Form Mono-Nuclear Iron Complexes in Contrast to L^1 Which Achieves Bi-metallic Complexes.

L^1 was synthesised in four steps starting from the commercially available *m*-phenylenediamine **(28)** illustrated in Scheme 13. The reaction of the (3-aminophenyl)carbamic acid tert-butyl ester **(29)** with 2-(chloromethyl)pyridine affords a mixture of both the mono- and bis-[(pyridin-2-ylmethyl)amino]phenyl carbamate **(30)**, which are readily separated by column chromatography.

Deprotection of **30** followed by reaction with 2-pyridinecarboxaldehyde cleanly generates the target molecule, L^1 **(21)**. [82] [83]

The synthesis of L^1 has been studied by former students of the Hess group; for this reason no further discussion will follow. The synthetic routes were in place prior to my PhD studies however I made improvements increasing yields for each step. The overall yield is 26 %. The finalised synthetic routes can be found in this chapter and in publication.[83]

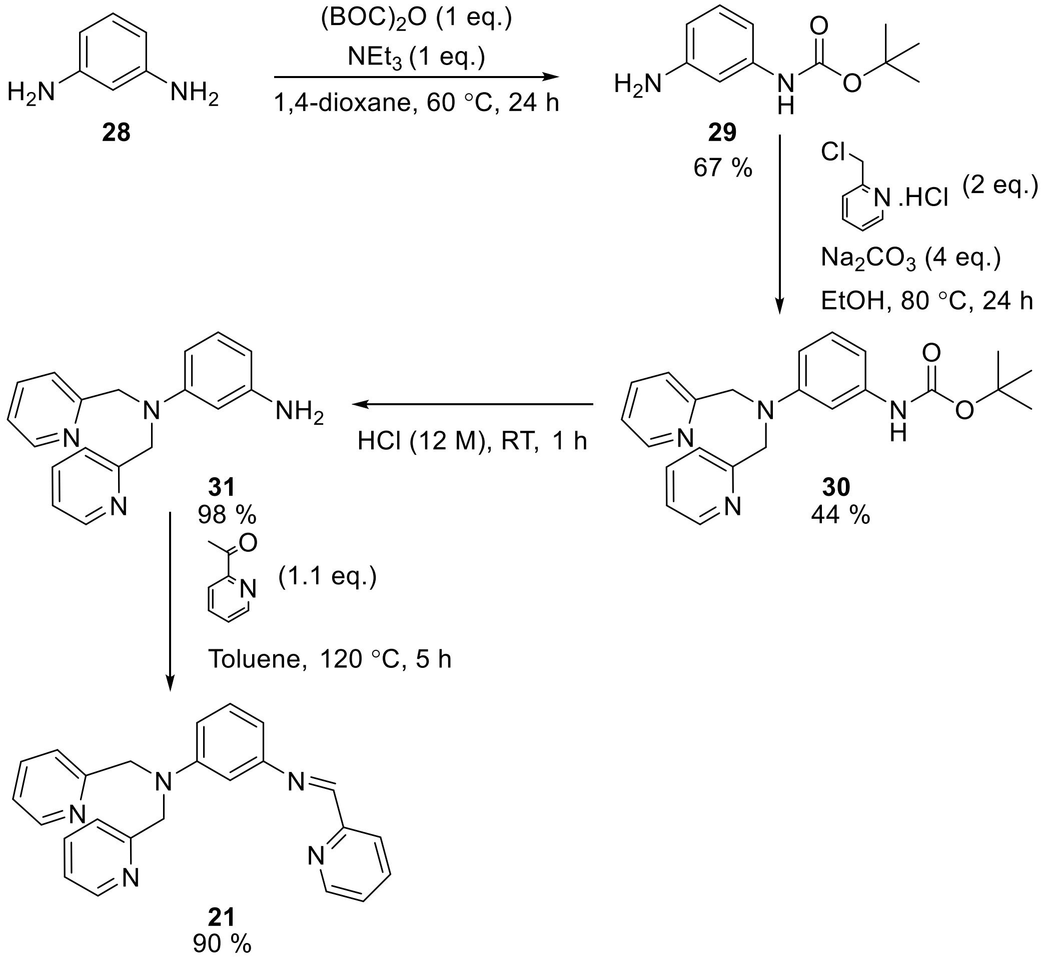

Scheme 13. Synthesis of Asymmetric Ligand L^1 from Commercially Available *m*-phenylenediamine.[83]

Solid State Analysis

2.2.1 Vibrational Spectroscopic Analysis at 298 K

L^1 was analysed by infrared spectroscopy (IR). The distinctive C=N imine stretch of the α-diimine group is expected between 1610 – 1630 cm^{-1}.[84] A medium stretch is observed at 1600 cm^{-1} assigned to this group. IR is a good technique for monitoring the oxidation state of this group. The one and two electron reductions would result in a shift of the imine stretch to a lower wavenumber as the bond order of C-N decreases; a singly bonded C-N stretch is typically observed at 1350 – 1000 cm^{-1}.[85] Pyridyl and benzyl stretches dominate the IR spectrum of L^1 overlapping at 1590 cm^{-1} and

1570 cm^{-1} with the C-H out of plane deformation of the *meta*-disubstituted benzene observed as a very strong peak at 766 cm^{-1}.[85]

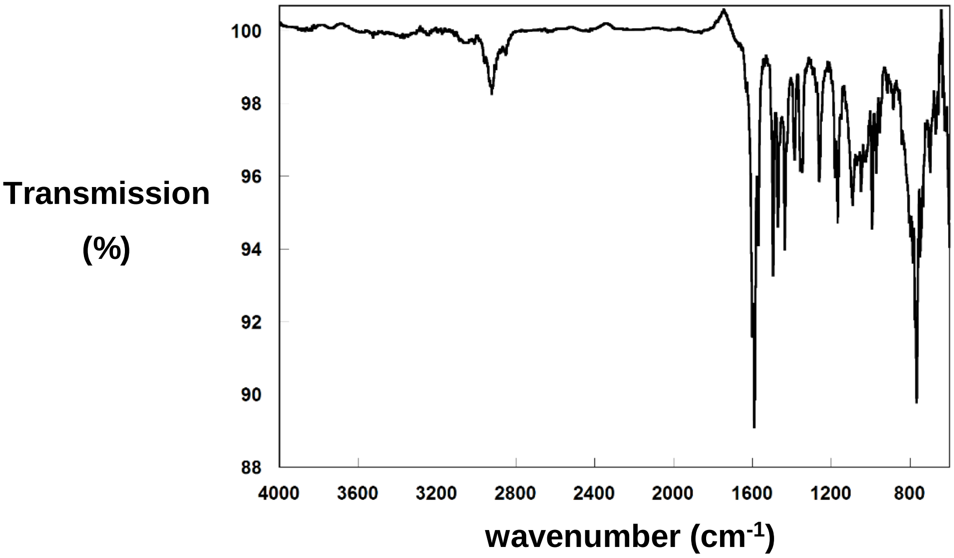

Figure 15. Vibrational Spectrum of L^1 Determined by Infrared Spectroscopy. The Infrared Spectrum was Collected using a Diamond ATR (Attenuated Total Reflection) Accessory (Golden Gate) for Solids; No Sample Preparation was Required.

Solution State Analysis

2.2.2 Electronic Absorption Spectroscopic Analysis at 298 K

The electronic absorption spectrum of L^1 was examined in CH_3CN. A prominent transition peak was observed at λ_{max} (M^{-1} cm^{-1}) ~ 253 nm (12 ×10^4), assigned as $\pi \rightarrow \pi^*$ transitions due to the high molar extinction coefficient (Figure 16). This broad, shouldered peak is common for highly conjugated systems due to the number of vibrational and rotational sub-levels within this transition energy. High energy, large molar extinction coefficient transitions are observed ≤ 200 nm, assigned as $\sigma \rightarrow \sigma^*$ transitions, which are commonly observed below 200 nm.[86] Weaker transitions are observed between 300 – 425 nm, assigned as $n \rightarrow \pi^*$ transitions of the five nitrogen lone pairs within the molecule and the unsaturated α-diimine.

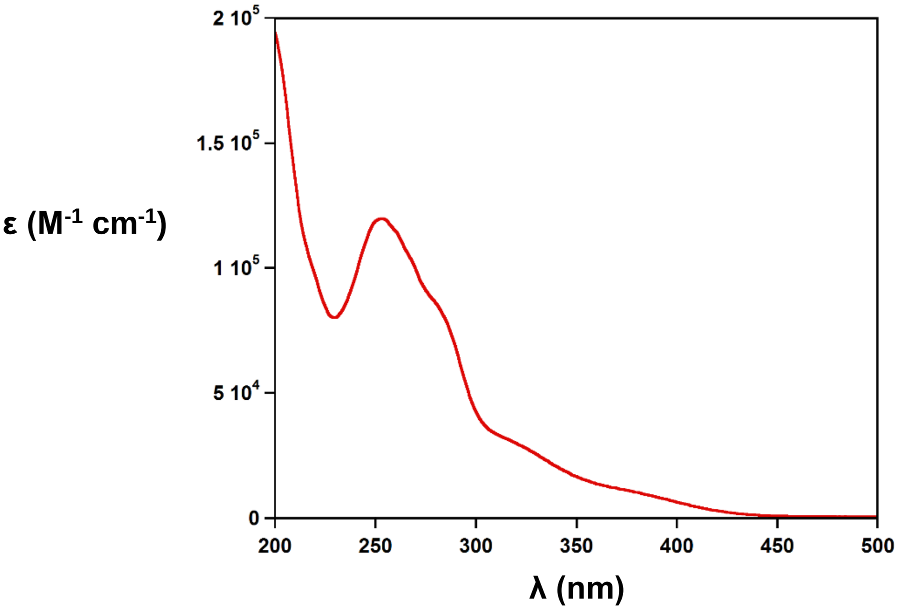

Figure 16. Absorption Spectrum of L^1. Solvent = CH_3CN.

2.2.3 Electrochemical Analysis at 298 K

The ability to perform multi-electron reactions, such as proton reduction, relies upon L^1 serving as an electron storage site. Cyclic voltammetry (CV) is a convenient tool for gathering qualitative information about electron transfer processes. It is a quick means of obtaining good estimates of formal reduction potentials and the number of electrons transferred per reactant molecule.

CV was employed to investigate the redox properties of L^1 and confirm the redox activity of the α-diimine unit. The voltammogram shows one quasi-reversible reduction process at E_{pc} = -0.95 V with a return oxidation at E_{pa} = -0.71 V, thus $E^{\circ\prime}$ = -0.83 V (Figure 17). The peak separation between forward and return wave is 0.24 V, a fully reversible redox process is defined as having a peak separation < 0.059 V, hence the reason for the "quasi" classification.[87] The large peak separation may be the result of structural rearrangement upon reduction. The reduction is assigned as the one electron reduction of the α-diimine group; [L^1]/[L$^{1\cdot}$]$^-$. Free 2,2'-bipyridine (bipy), a comparable α-diimine, exhibits a one electron reduction at $E^{\circ\prime}$ = -2.05 V assigned as the one electron reduction of the α-diimine group; [bipy]/[bipy$^\cdot$]$^-$. The second electron reduction of bipy is not observed, evidence that the theoretical two electron reduction series for the α-diimine group is not always accessible depending on the surrounding environment.[88] Substitution of bipy with one and two NO_2 groups in various positions shifts the reduction potential to between $E^{\circ\prime}$ = -0.61 V and -0.98 V demonstrating the structural environment around the α-diimine group plays a large part in determining the potential at which the reduction occurs.[88]

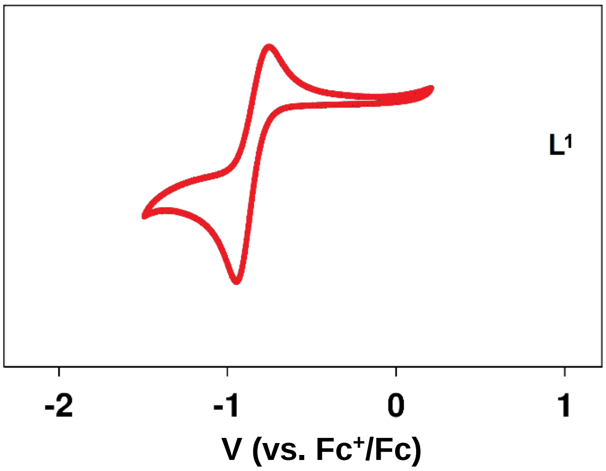

Figure 17. Electrochemical Studies of L^1 by Cyclic Voltammetry. Solvent = CH_3CN. Scan Rate = 0.2 V/s. Electrolyte = 0.1 M $TBAPF_6$.

2.3 Reaction of L^1 with Zinc (C1)

The di-nuclear zinc complex, $[(L^1)Zn_2Cl_4]$ **(C1)**, is obtained upon reaction of L^1 with two molar equivalents of $ZnCl_2$ in THF or CH_3CN (Scheme 14). **C1** is obtained as a yellow precipitate under both reaction conditions.

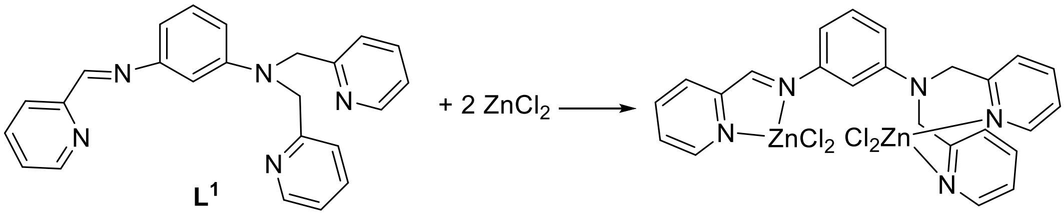

21

C1

Scheme 14. Synthetic Scheme for Formation of Di-nuclear $[(L^1)Zn_2Cl_4]$ Complex C1.

Solid State Analysis

2.3.1 Crystallographic Analysis

The structure of **C1** substantiates the ability of L^1 to provide two distinct metal coordination sites. The two zinc ions are held in a distorted tetrahedral configuration, with a constrained 80° bite angle imposed by the α-iminopyridine at Zn(1) (Figure 18). The coordination geometry at the Zn(2) site is analogous to a related symmetric di-nuclear zinc complex, $[Zn_2(1,3\text{-tpbd})Cl_4]$ (1,3-tpbd = *N*,*N*,*N'*,*N'*-tetrakis(pyridine-2-ylmethyl)benzene-1,3-diamine),[89] with only a weak interaction between Zn(2) and the amino nitrogen; Zn(2)-N(3) = 2.6237(16). The bound chloride ligands prohibit close approach of the two zinc ions, leading to a Zn···Zn separation of ~ 5.7 Å. Full crystallographic details can be found in the Appendix.

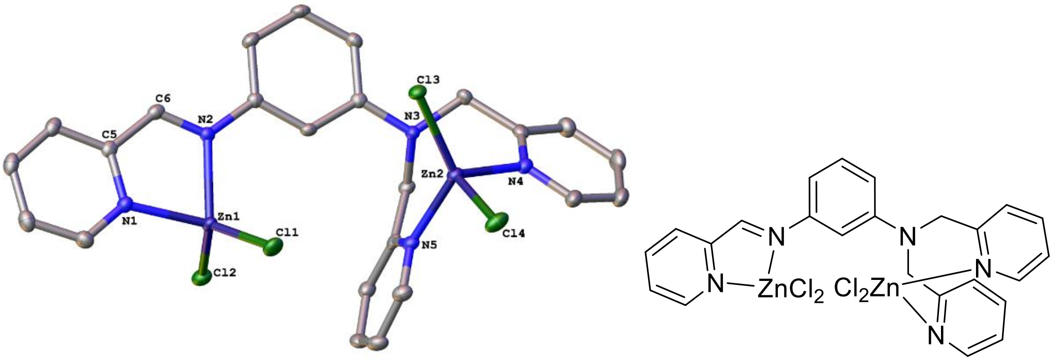

Figure 18. Left: Molecular Structure of C1; 50 % Probability Ellipsoids. Hydrogens Omitted for Clarity. Selected Bond Lengths (Å) and Angles (deg): Zn1-Cl1 2.1917(5), Zn2-Cl3 2.2499(5), Zn1-Cl2 2.2176(6), Zn2-Cl4 2.2866(5), Zn1-N1 2.0714(16), Zn2-N3 2.6237(16), Zn1-N2 2.0880(17), Zn2-N4 2.0667(16), Zn2-N5 2.0695(17), N1-C5 1.352(3), C5-C6 1.468(3), N2-C6 1.287(3) N1-Zn1-N2 80.77(6), N4-Zn2-N5 99.23(7), Cl1-Zn1-Cl2 121.46(2), Cl3-Zn2-Cl4 103.56(2), Zn1--Zn2 5.6978(3) Determined by X-Ray Crystallography. Right: ChemDraw Structural Representation of C1.

Solution State Analysis

2.3.2 Electronic Absorption Spectroscopic Analysis at 298 K

Compound **C1** is moderately soluble in CH_2Cl_2. The electronic absorption spectra of L[1] and **C1** in CH_2Cl_2 are clearly dissimilar, with distinct absorption bands λ_{max} (M^{-1} cm^{-1}) ~ 262 (9000) and ~ 331 nm (7000) apparent in the spectrum of **C1** (Figure 19). The new bands are assigned as π-π* shifts indicative of metal coordination.

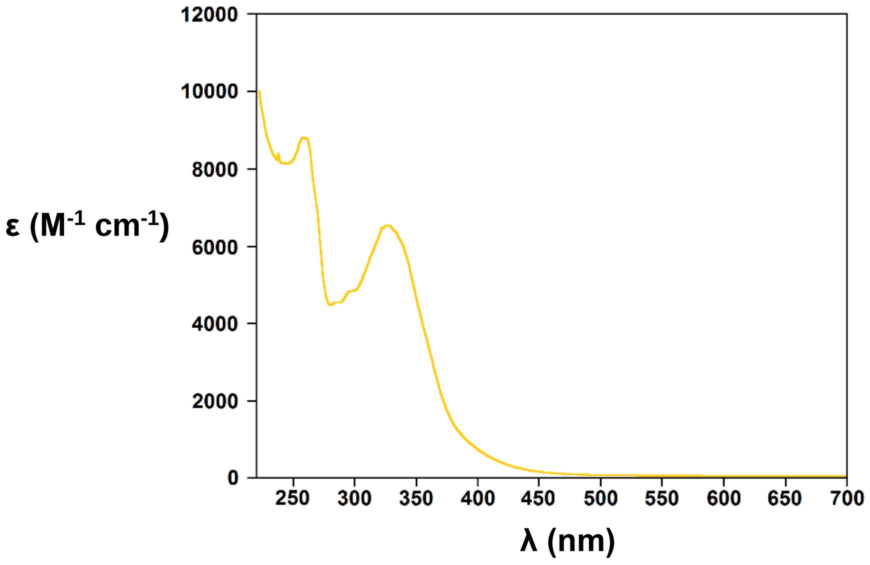

Figure 19. Absorption Spectrum of C1. Solvent = CH_2Cl_2.

2.3.3 ^{1}H Nuclear Magnetic Resonance Spectroscopic Analysis

The full *d*-shell of Zn^{2+} results in the diamagnetism of **C1** allowing it to be structurally analysed by ^{1}H NMR spectroscopy. The proton resonances in the aryl region of the ^{1}H NMR spectrum of **C1** in CD_2Cl_2 are shifted to higher frequency significantly in comparison to the L^1 spectrum (Figure 20). Protons in environments H_p, H_f and H_k, are shifted to higher frequency considerably due to their proximity to the coordinated zinc ion with H_k shifted the most as it experiences the effects of both coordinated zinc ions. The aliphatic H_L remains at the same shift in the spectra of both L^1 and **C1** confirming the adjacent amine nitrogen is not bound to the Zn ion, as also determined from X-ray diffraction.

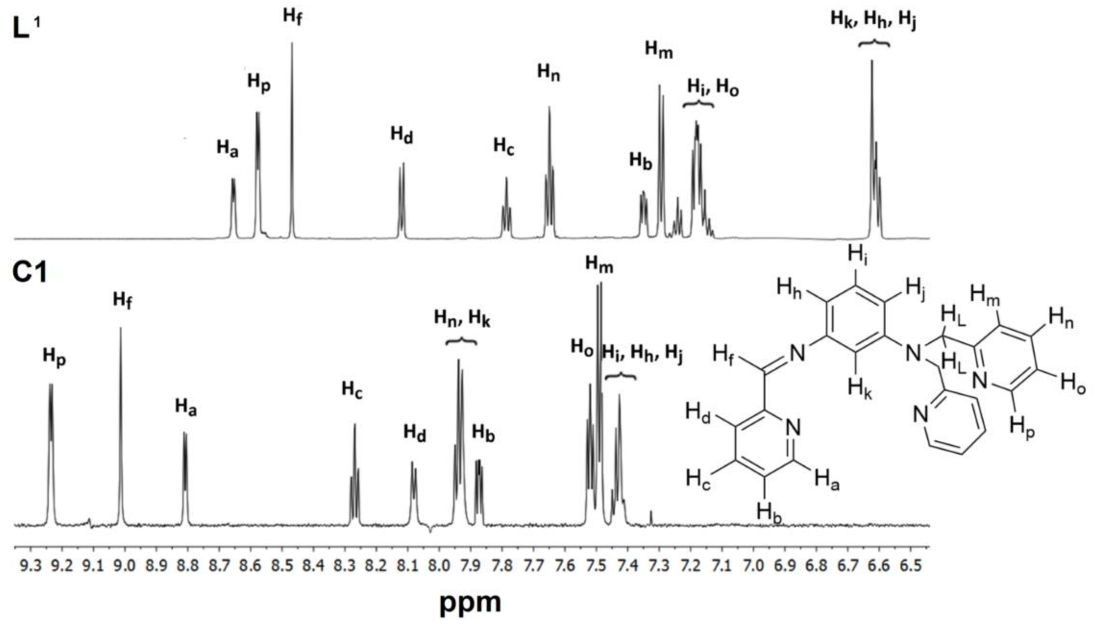

Figure 20. Overlay of Aromatic Region of the ^1H NMR Spectrum (700 MHz, CD_2Cl_2) of L^1 (Top) and C1 (Bottom). Assignments Based on COSY Spectra.

2.3.4 Electrochemical Analysis at 298 K

CV was employed to investigate the electrochemistry of **C1**. Zn^{2+} is not redox active due to the full *d*-shell configuration and therefore the only reduction available to **C1** is that of the α-diimine unit of L^1. A reduction is observed at $E_{pc} = -1.31$ V in the voltammogram of **C1**, assigned as the one electron ligand-centred reduction of the α-diimine group (Figure 21). The reduction of **C1** is observed at a more negative potential than L^1, to be expected due to the electronic contribution from the Zn^{2+} ions. The reduction of **C1** is assigned as irreversible as the i_{pa} is insignificant in comparison to the i_{pc}. Irreversibility may be due to structural rearrangement after reduction.[90]

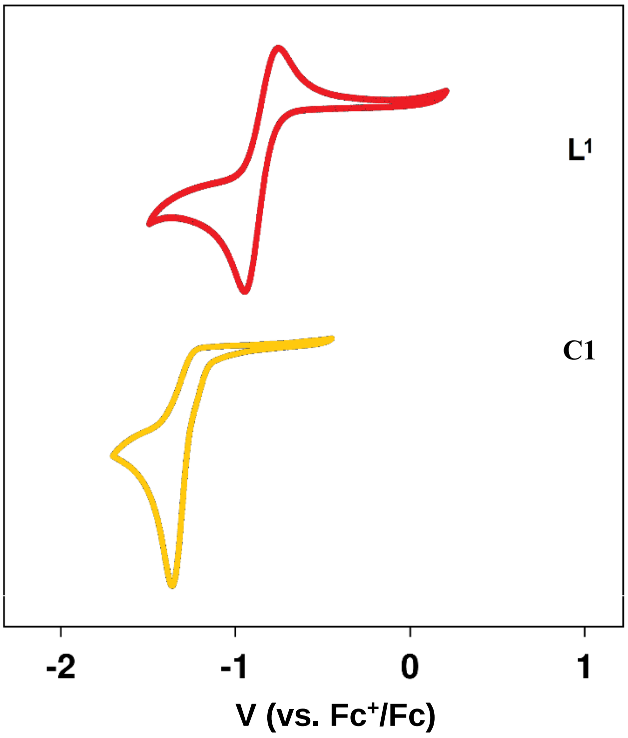

Figure 21. Electrochemical Studies of L^1 **and C1 by Cyclic Voltammetry. Solvent for L**^{1} **=** CH_3CN**. Solvent for C1 =** CH_2Cl_2**. Scan Rate = 0.2 V/s. Electrolyte = 0.1 M** $TBAPF_6$**.**

2.4 Reactions of L^1 with Ferrous Salts (C2 and C3)

Products obtained from the reactions of L^1 with $FeCl_2$ proved highly insoluble, which prevented characterisation. Therefore, alternative starting reagents were used to further investigate the ligand coordination chemistry. The addition of two molar equivalents of $Fe(OTf)_2$ to a solution of L^1 in THF resulted in the precipitation of a pink solid corresponding to dimeric $[(L^1)_2Fe_2(OTf)_2](OTf)_2$ **(C2)** in addition to a blue solution after transition through an initial forest green suspension (Scheme 15). Initial reaction conditions for **C2** and the initial crystal structure were obtained by Oliver Maguire. The colour changes throughout the reaction and low yield of **C2**, 54 %, suggest the formation of various intermediates *en route* to, or products in addition to, **C2**. We have not identified any other products, and dimeric compound **C2** was isolated in all reactions irrespective of the Fe:ligand stoichiometry (2:1, 1:1, 1:2 examined). The sister complex **C3**, structurally analogous to **C2**, is obtained on addition of one molar equivalent of $[Fe(CH_3CN)_6](PF_6)_2$ to a solution of L^1 in CH_3CN. A pink solution is observed immediately upon addition from which **C3** is directly recrystallised (Scheme 15). No intermediate colour changes are observed in addition to the higher yield of 75 % suggesting no additional products are made through this route. Again, the dimeric compound, **C3**, was isolated in all reactions irrespective of the Fe:ligand stoichiometry (2:1, 1:1, 1:2 examined). The bi-metallic complexes obtained do not hold the desired asymmetry with one redox active component coordinated to one metal ion with the second metal ion held by the innocent counterpart. Each metal ion is coordinated by both redox active and innocent groups.

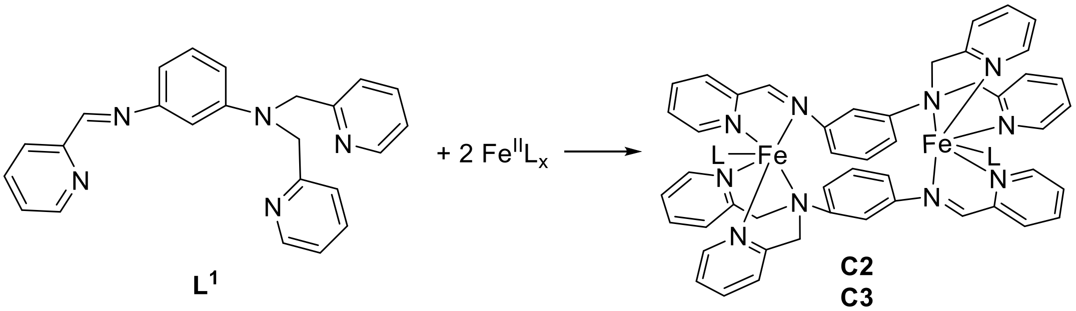

L^1

21

C2
C3

Scheme 15. Synthetic Route for Formation of Ferrous L^1 Complexes. Ferrous Salts Studied in this Chapter; Fe(OTf)$_2$ and [Fe(CH$_3$CN)$_6$](PF$_6$)$_2$. Where L = OTf$^-$ for C2 and L = CH$_3$CN for C3.

Solid State Analysis

2.4.1 Crystallographic Analysis

C2 and **C3** are structurally analogous. The iron ions in both **C2** and **C3** structures are held in an octahedral configuration (Figure 22, Figure 23). The *N*-atoms of the bis(pyridylmethyl)amino groups adopt a facial arrangement around each iron ion, while the opposing face comprises the α-iminopyridine unit and a coordinated labile ligand (Figure 22, Figure 23). The labile ligand in **C2** is a triflate anion while for **C3** it is a neutral CH$_3$CN ligand. The triflate ligand is held at 2.101(2) Å, a slightly shorter bond length than the CH$_3$CN ligand of **C3**, 2.134(3) Å. The two substitutionally labile ligands of **C2** and **C3** are antiparallel with respect to the Fe···Fe axis. The Fe–N bond distances of **C2** and **C3** (~ 2.1 – 2.3 Å) are indicative of high-spin Fe^{II} ions. From the bond lengths of the diimine unit, 1.273(4) Å and 1.459(5) Å for **C2** and 1.283(4) Å and 1.460(4) Å for **C3**, it is determined that L^1 is in the neutral form.[91] The coordination geometry at the iron centre coincides with the 'slipped' arrangement of the L^1 bridging benzenes and of a 7.5 – 7.7 Å separation between the two metal sites of **C2**. The Fe···Fe distance of **C3** is slightly shorter than **C2** at 7.403 Å. The crystal system of **C2** includes two unbound triflate anions and five CH$_3$CN solvent molecules. The crystal system of **C3** includes four unbound hexafluorophosphate anions and two unbound CH$_3$CN solvent molecules. Full crystallographic details for both **C2** and **C3** can be found in the Appendix.

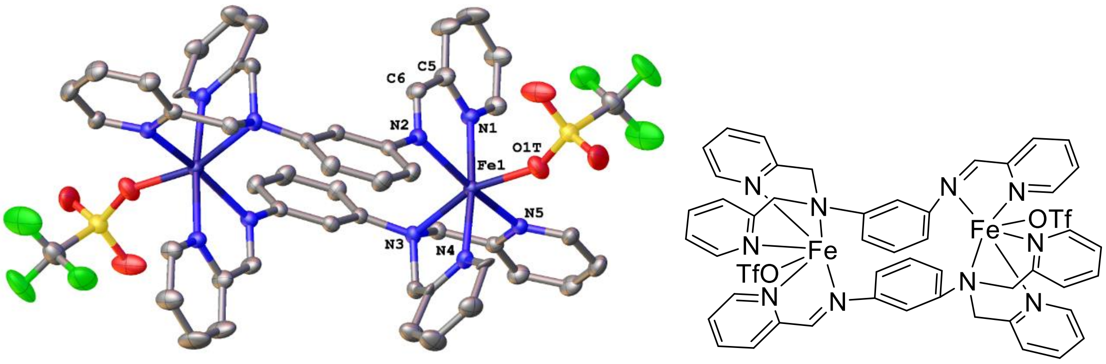

Figure 22. Left: Molecular Structure of C2; 50 % Probability Ellipsoids. Hydrogen Atoms and the Triflate Counteranions have been Omitted for Clarity. Selected Bond Lengths (Å) and Angles (deg): Fe-

N1 2.177(3), Fe-N2 2.214(3), Fe-N3 2.321(2), Fe-N4 2.141(3), Fe-N5 2.161(3), Fe-O1T 2.101(2) N1-C5 1.352(4), N2-C6 1.273(4), C5-C6 1.459(5), N1-Fe-N2 75.98(9), N3-Fe-N4 78.61(9), N3-Fe-N5 76.17(9), N4-Fe-N5 91.22(10) N1-Fe-N4 174.35(9), N2-Fe-N5 166.81(10), N3-Fe-O1 162.16(10), Fe--Fe 7.4782(5). Determined by X-Ray Crystallography. Right: ChemDraw Structural Representation of C2.

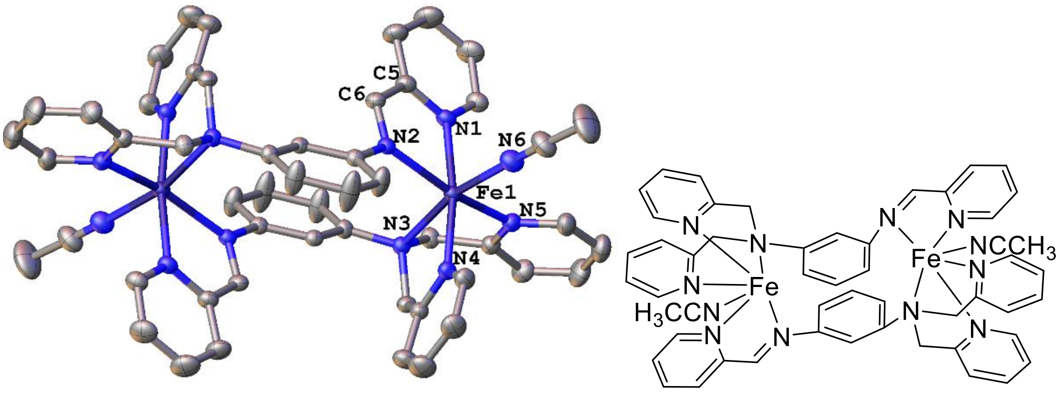

Figure 23. Left: Molecular Structure of C3; 50 % Probability Ellipsoids. Hydrogen Atoms and the Hexafluorophosphate Counteranions have been Omitted for Clarity. Selected Bond Lengths (Å) and Angles (deg): Fe-N1 2.195(3), Fe-N2 2.236(3), Fe-N3 2.296(2), Fe-N4 2.158(3), Fe-N5 2.140(3), Fe-N6 2.133(3) N1-C5 1.356(4), N2-C6 1.283(4), C5-C6 1.462(4), N1-Fe-N2 75.41(10), N3-Fe-N4 77.96(10), N3-Fe-N5 76.97(10), N4-Fe-N5 94.94(10) N1-Fe-N4 171.16(10), N2-Fe-N5 162.95(10), N3-Fe-N6 167.64(11), Fe--Fe 7.403(3) Determined by X-Ray Crystallography. Right: ChemDraw Structural Representation of C3.

2.4.2 Vibrational Spectroscopic Analysis at 298 K

C2 and **C3** were analysed by IR spectroscopy. The α-diimine stretch is observed at 1590 cm^{-1} for **C2** and 1588 cm^{-1} for **C3**, in the typical range for the neutral form. The spectrum of **C2** is otherwise dominated by the triflate group, which exhibits SO_3 and CF_3 stretches between 760 – 1280 cm^{-1} and a C-S stretch at 648 cm^{-1}. **C3** is dominated by the PF_6 stretch of the counteranions at 824 cm^{-1}.

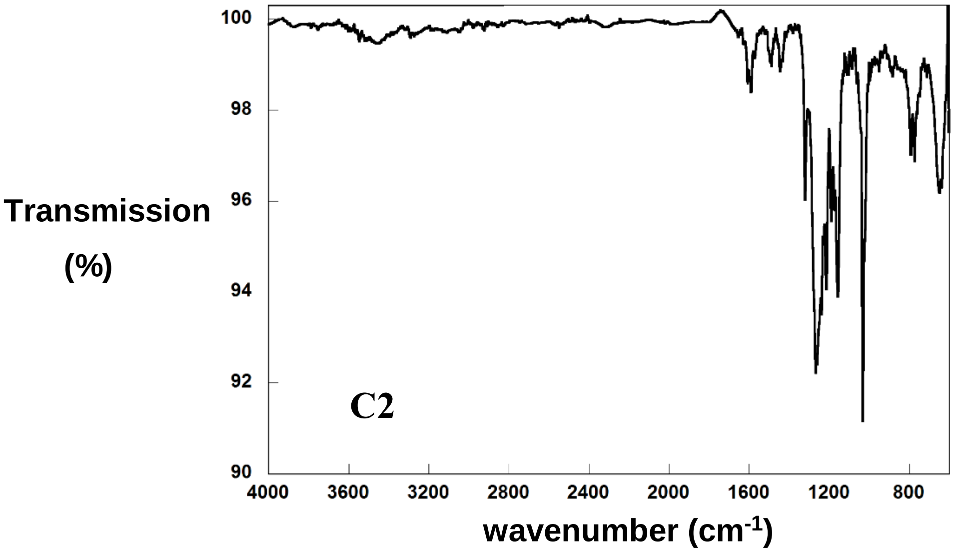

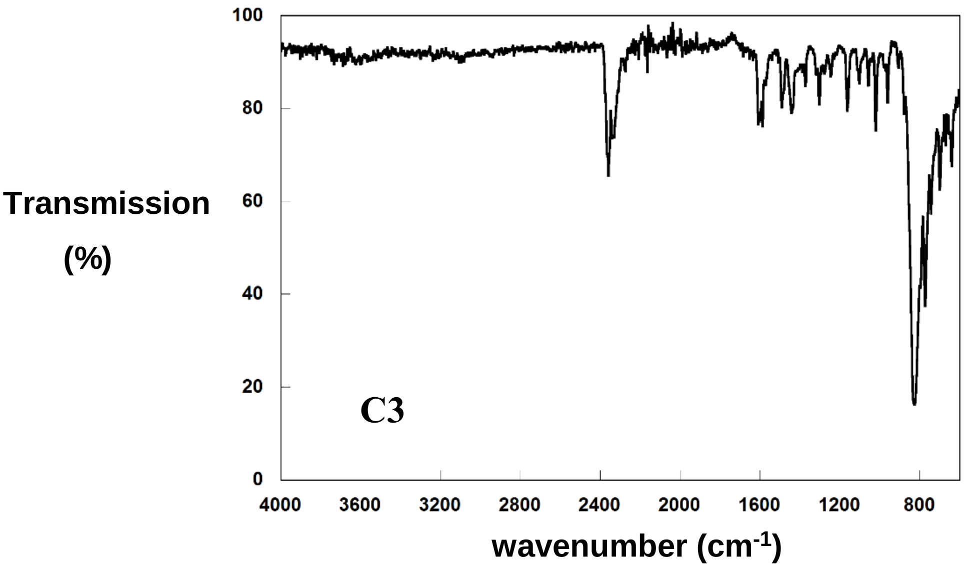

Figure 24. Top: Vibrational Spectrum of C2 Determined by Infrared Spectroscopy. Bottom: Vibrational Spectrum of C3 Determined by Infrared Spectroscopy. The Infrared Spectra Were Collected using a Diamond ATR (Attenuated Total Reflection) Accessory (Golden Gate) for Solids; No Sample Preparation was Required.

2.4.3 Mössbauer Analysis

Mössbauer spectroscopy is a very valuable technique when studying iron complexes, divulging information on the electronic configuration of the ions present. This technique uses γ-radiation to excite the nucleus of the iron atom.[92] In order to achieve measurable results a fluorescence resonance must be achieved. The energies required to measure the hyperfine interactions are so small they can be achieved using the Doppler effect. Two key features that can be obtained from the Mössbauer spectrum are the isomer shift (δ) and the quadrupole splitting (ΔEQ).[92]

The isomer shift is proportional to the electron density at the nucleus and can be used to distinguish between oxidation states. Although the electron density at the nucleus is dictated by the *s*-electrons, the *d*-electrons influence through shielding of the nuclear charge from the *s*-electrons. An increase in the number of 3*d* electrons reduces the *s*-electron density at the iron nucleus and causes a more positive isomer shift.

ΔEQ occurs in nuclei with an angular momentum quantum number I > ½ which produces a non-spherical charge distribution resulting in a nuclear quadrupole moment. In the presence of an asymmetric electric field (produced by a ligand arrangement) the nuclear energy levels are split. In the case of iron-57 (I = 3/2) the excited state splits into two: m_I ± ½ and m_I ± 3/2.

C2 crystals gave Mössbauer parameters of δ (|ΔEQ|): 1.12 (1.93) mm s^{-1} confirming the presence of high-spin ferrous ions, *S* = 2, already deduced from the crystal structure (Figure 25). One quadrupole doublet indicates both iron ions exist in an identical environment. **C3** crystals gave Mössbauer parameters of δ (|ΔEQ|): 1.09 (2.17) mm s^{-1} again representative of a high-spin ferrous ion, *S* = 2 (Figure 25). Again, one quadrupole doublet indicates both iron ions exist in an identical environment.

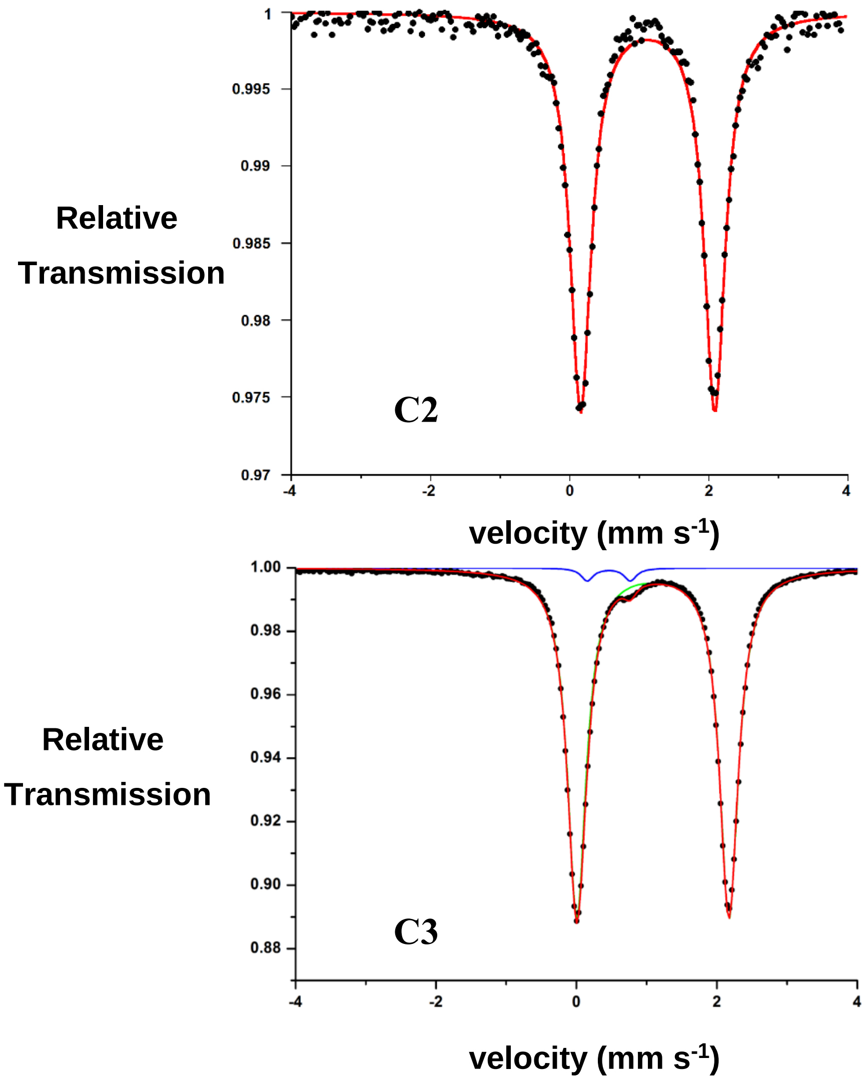

Figure 25. Top: Zero-Field Mössbauer Spectrum (80 K) of C2. Experimental Data Shown as Solid Circles. The Primary Component (Solid Red Line) Affords δ (|ΔEQ|): 1.12 (1.93) mm s^{-1}. Bottom: Zero-Field Mössbauer Spectrum (80 K) of C3. Experimental Data Shown as Solid Circles. The Primary Component (Solid Green Line) Affords δ (|ΔEQ|): 1.09 (2.17) mm s^{-1}. The Combined Fit (Solid Red Line) Includes a Minor Impurity Present in the Crystalline Solid (Solid Blue Line, 2.56 %, δ (|ΔEQ|): 0.46 (0.59 mm s^{-1})).

2.4.4 Magnetic Susceptibility Analysis

The superconducting quantum interference device (SQUID) is the most sensitive and versatile magnetometer. SQUIDs are based on Josephson junctions, which are formed by two superconductors separated by a non-conducting barrier.[93] In the absence of magnetic flux the current is distributed equally between two superconductors, if a magnetic force is present the current between each of the superconductors varies. The difference can be used to determine the magnetic flux as a function of temperature.[93]

Magnetic susceptibility measurements using SQUID were carried out on **C2** and **C3** to determine metal-metal interactions and investigate the magnetic properties of the complexes. Magnetic susceptibility measurements of **C2** indicated a temperature independent magnetic moment in the range of 50 – 290 K, decreasing below 50 K to a value of ~4.8 μ_B (Figure 26). The effective magnetic moment of 7.9 μ_B at room temperature is higher than the spin-only value for two uncoupled $S = 2$ iron ions ($\mu_{eff} = 6.9$ μ_B for $g = 2$), but below the spin-only values of 8.9 μ_B for an $S = 4$ ground state arising from two strongly ferromagnetically coupled high-spin ferrous ions, thus weak ferromagnetic coupling is assigned. The data were fitted according to the following spin-Hamiltonian including exchange coupling and zero-field splitting terms with $S_1 = S_2 = 2$:

$$H = -2J\hat{S}_1 \cdot \hat{S}_2 + g\beta(\hat{S}_1 + \hat{S}_2) \cdot \vec{B} + \sum_{i=1,2} D\left[\hat{S}^2_{z,i} - \tfrac{1}{3} S_i(S_i + 1) + \tfrac{E}{D}(\hat{S}^2_{x,i} - \hat{S}^2_{y,i})\right]$$

Fits with either J or D fixed at zero were included, to assess the relative contribution of each parameter, and yielded values for $J = 0 - 0.2$ cm^{-1} and $|D| = 14 - 22$ cm^{-1}. The best fit was obtained with $g = 2.2$, $J = 0.04$ cm^{-1}, $|D| = 19.7$ cm^{-1} and $E/D = 0.26$, denoting negligible interaction between the two iron ions of **C2**.

Magnetic susceptibility measurements of **C3** also indicate a temperature independent magnetic moment in the range of 50 – 290 K, increasing to a maximum of 9.4 μ_B at 15 K, decreasing to a final value of 6.7 μ_B at 2 K (Figure 26). The effective magnetic moment of 7.7 μ_B at room temperature is higher than the spin-only value for two uncoupled $S = 2$ iron ions ($\mu_{eff} = 6.9$ μ_B for $g = 2$), but below the spin-only values of 8.9 μ_B for an $S = 4$ ground state arising from two strongly ferromagnetically coupled high-spin ferrous ions, again allowing for weak ferromagnetic coupling assignment. The best fit of the data was obtained with $g = 2.16$, $J = 3.2$ cm^{-1}, $|D| = 12.0$ cm^{-1}, and $E/D = 0.30$. The exchange coupling is significantly larger than previously determined for **C2**, although weak for both.

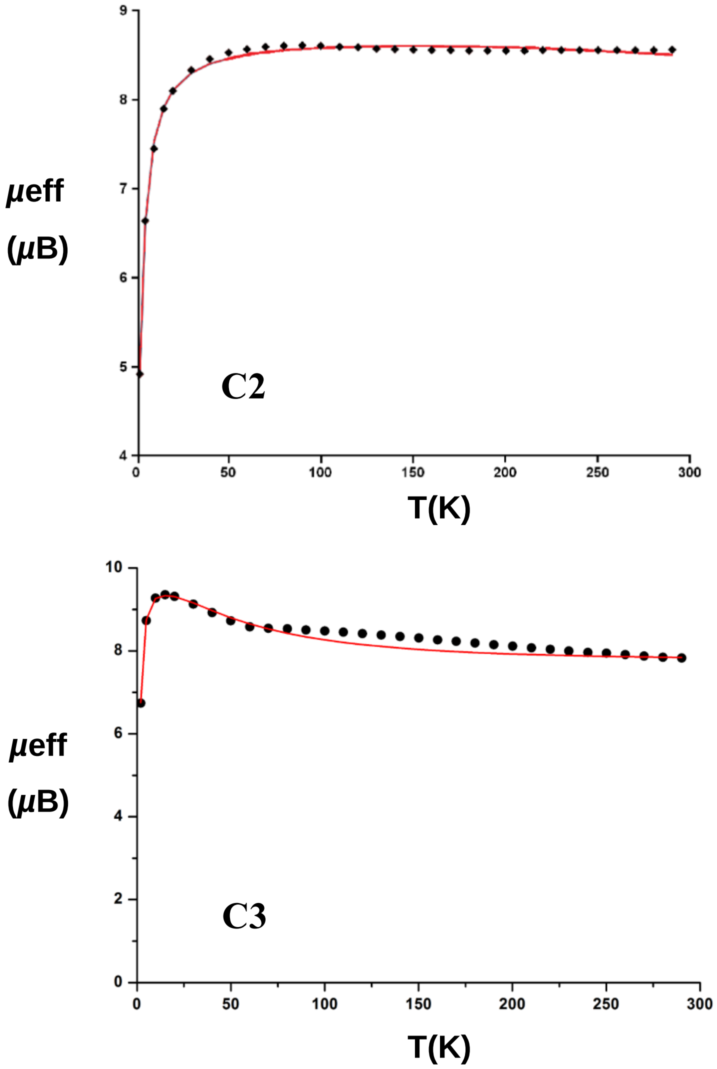

Figure 26. Top: Magnetic Susceptibility Data (1 T, 2 – 290 K) for C2; Experimental = Diamonds, Simulation = Solid Line. Best Fit of Data for C2 with: $S_1 = S_2 = 2$, $g_1 = g_2 = 2.2$, $J = 0.043$ cm^{-1}, $|D_1| = |D_2| = 19.7$ cm^{-1}, $E/D_1 = E/D_2 = 0.26$, TIP = 27 x 10^{-3} emu. Bottom: Magnetic Susceptibility Data (1 T, 2 – 290 K) for C3; Experimental = Circles, Simulation = Solid Line. Best Fit of Data for C3 with: $S_1 = S_2 = 2$, $g_1 = g_2 = 2.16$, $J = 3.20$ cm^{-1}, $|D_1| = |D_2| = 12.0$ cm^{-1}, $E/D_1 = E/D_2 = 0.30$, TIP = 7 x 10^{-4} emu.

2.4.5 Computational Density Function Theory Analysis

The iron ions in **C2** and **C3** are weakly ferromagnetically coupled. Ferromagnetic coupling is expected for systems containing an odd number of bridging atoms between two paramagnetic centres (e.g. *meta*-substituted benzene linkers), while an even number of bridging atoms promotes antiferromagnetic interactions (Figure 27). Spectroscopic, magnetic and DFT computational studies demonstrated that the coupling is orchestrated by spin polarisation through the aromatic bridge.[94, 95] Overlap between the Fe d_{z^2} orbitals and the extended N_{im}-C-C-C-N_{am} π-system provides a possible exchange pathway between the iron ions. Ferromagnetic coupling is observed when the interacting SOMOs are orthogonal to one another, where the larger the overlap the larger the coupling.[95]

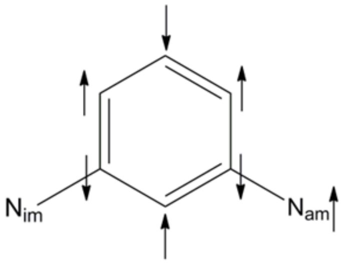

Figure 27. Alternating Spin of Bridging Benzyl and Effects on Neighbouring Ions.

Several factors impede strong communication between the iron sites, illustrated both by the molecular structure and density function theory (DFT) calculations. The large Fe···Fe distances for **C2** and **C3** (7.4 – 7.7 Å) and the α-iminopyridine canted at 52° (**C2**) and 61° (**C3**), with respect to the plane of the benzene bridge, result in poor overlap with the aromatic π-system. The DFT-derived spin density map for **C2** and **C3** depict negligible spin density on the phenylenediamine unit (Figure 28). All singularly occupied molecular orbitals (SOMOs) of **C2** and **C3** are strongly metal-based (Figure 29, Figure 30). The benzene π-system contributes minimally to these d_{z^2}-based SOMOs.

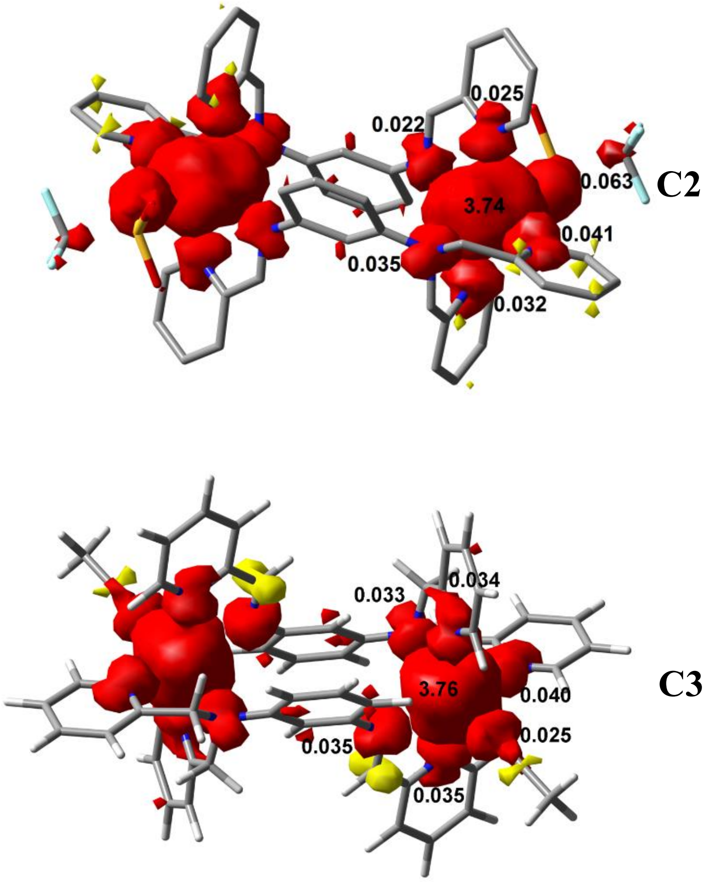

Figure 28. Top: DFT-Derived (B3LYP) Spin Density Plot for C2 Based on Loewdin Population Analysis. Bottom: DFT-Derived (B3LYP) Spin Density Plot for C3 Based on Loewdin Population Analysis.

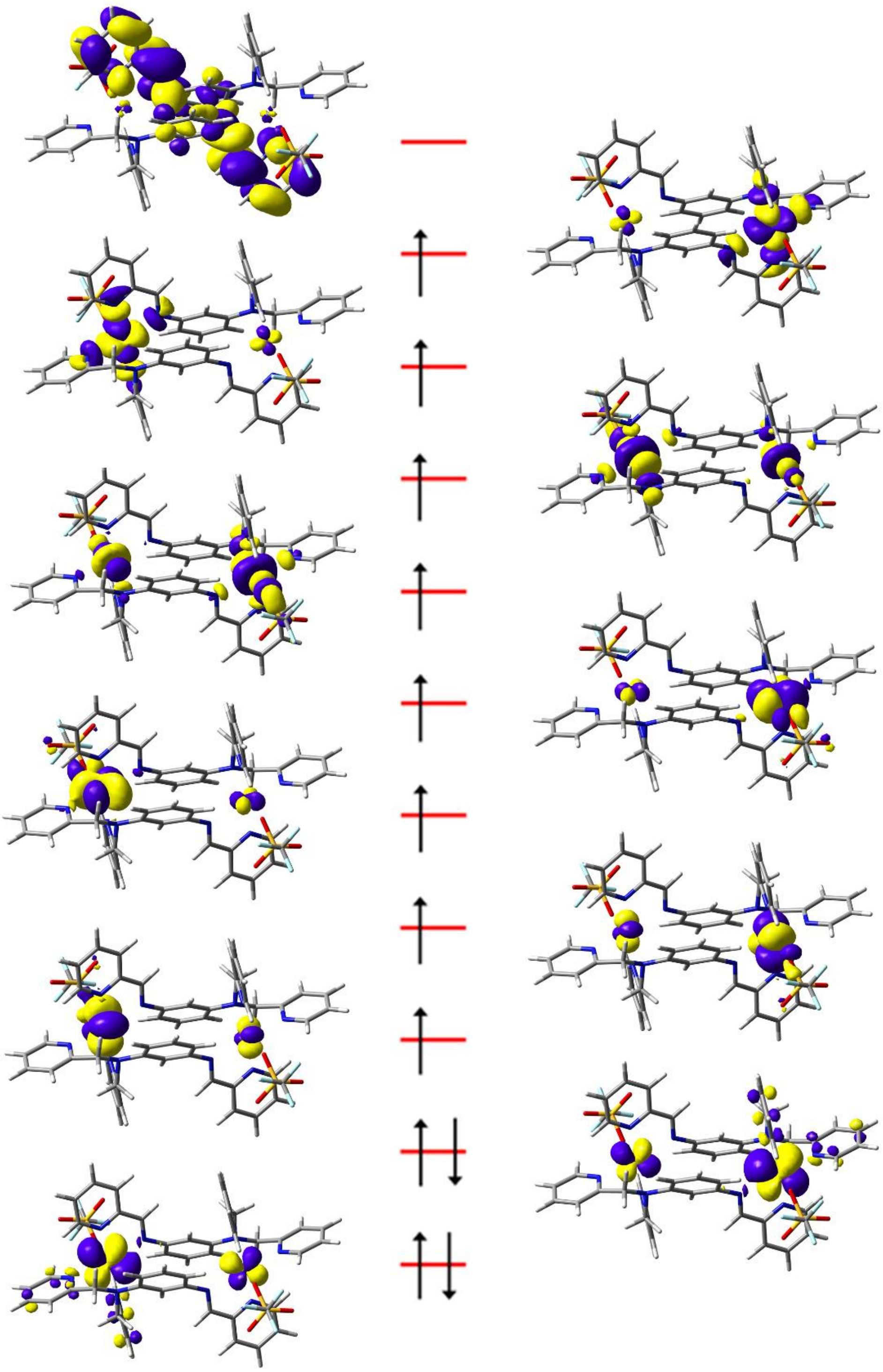

Figure 29. DFT-derived (B3LYP) Molecular Orbital Diagram for C2.

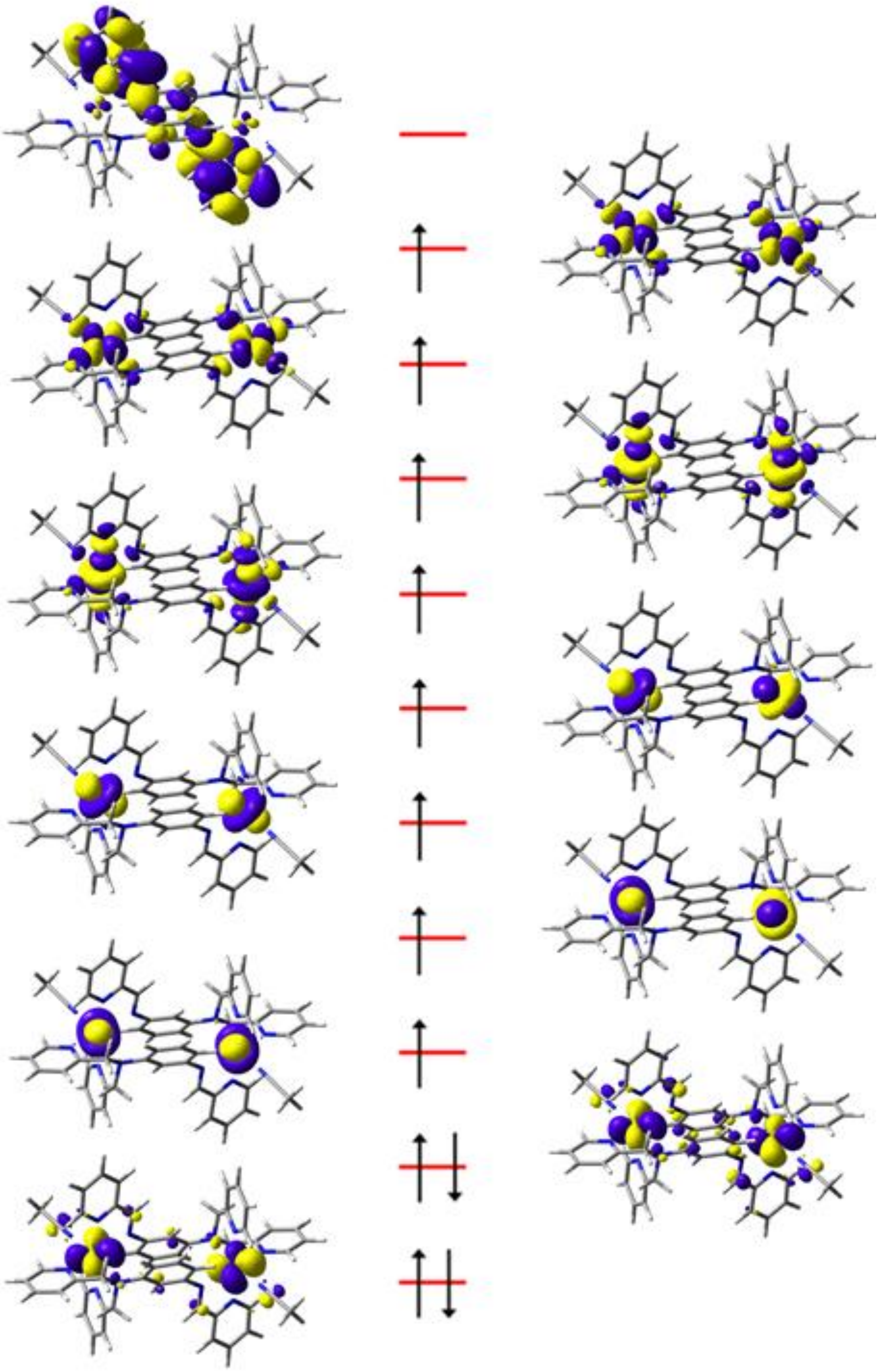

Figure 30. DFT-derived (B3LYP) Molecular Orbital Diagram for C3.

Solution State Analysis

2.4.6 Electronic Absorption Spectroscopic Analysis at 298 K

The electronic absorption spectra of **C2** and **C3** have been studied in CH_3CN. A prominent transition peak λ_{max} (M^{-1} cm^{-1}) ~ 505 nm (796) is observed for **C2**, assigned as a charge transfer (CT) band due to the high molar coefficient, which differentiates it from *d-d* transitions (Figure 31). Due to the octahedral environment of the ferrous ions the *d-d* transitions are expected to be much lower in intensity as they are formally Laporte forbidden. Conversely CT is both spin and Laporte allowed resulting in a high intensity. The CT band is more specifically assigned as metal-to-ligand charge transfer (MLCT). L^1 is more readily reduced than the ferrous ion as observed by CV (see electrochemical analysis) and MLCT is consistent with the aromaticity of the ligand; the low lying π^* orbitals accommodate the reception of electron density. **C3** exhibits a very similar absorption spectrum to **C2**. The MLCT band is slightly red-shifted and exhibits a larger molar extinction coefficient; λ_{max} (M^{-1} cm^{-1}) 510 nm (1060).

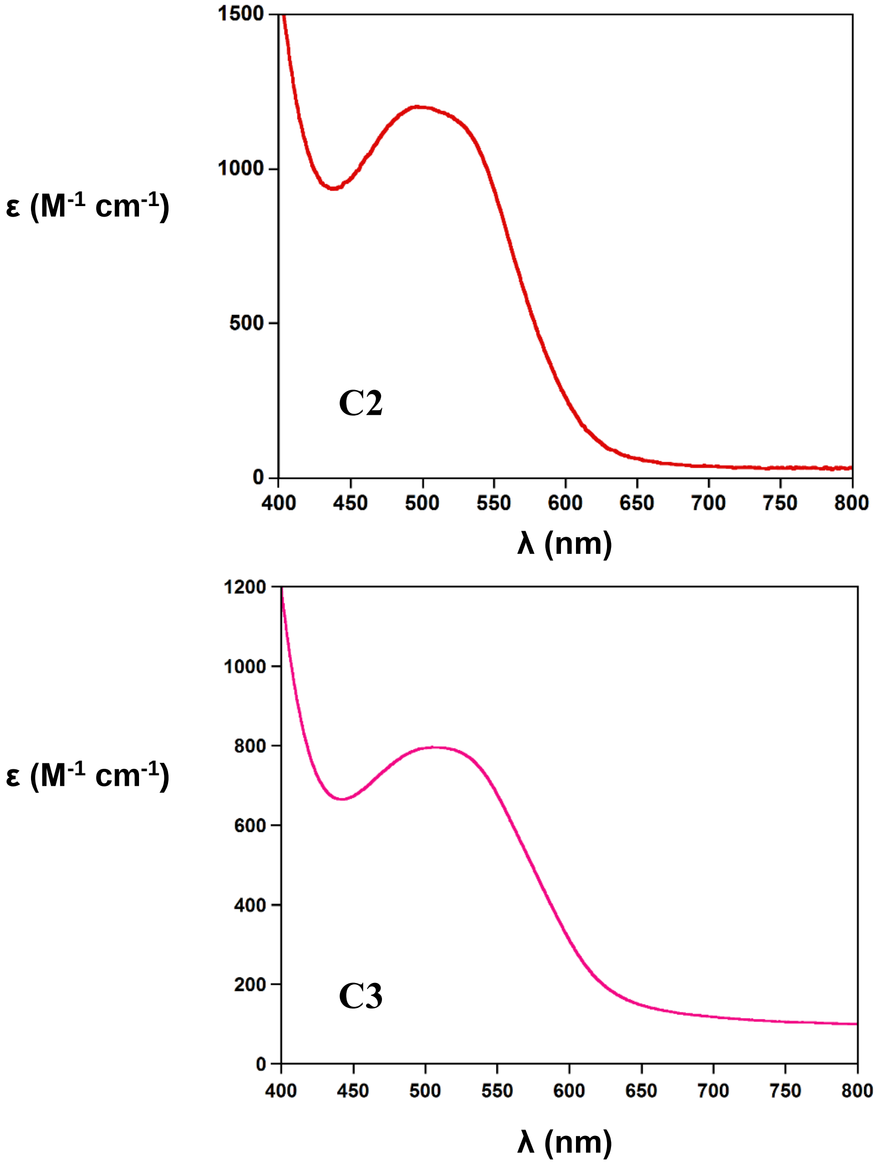

Figure 31. Top: Absorption Spectrum of C2. Solvent = CH_3CN. Bottom: Absorption Spectrum of C3. Solvent = CH_3CN.

2.4.7 Nuclear Magnetic Resonance Spectroscopic Analysis

Evans' method ^{1}H NMR studies in CD_3CN were undertaken to determine the magnetic susceptibility of the iron ions in solution and allows for comparison to solid state analysis.[96] The equations used for Evans' method ^{1}H NMR studies can be found in the Appendix. An observed frequency difference of $\Delta f = 175$ Hz was exhibited, which calculated as a $\mu_{\text{eff}} = 4.4$ per iron ion indicative of $S = 2$ configuration and $\mu_{\text{eff}} = 6.2$ for the complex, comparable to $\mu_{\text{eff}} = 6.9$ determined by SQUID analysis. The iron ions of **C2** and **C3** exist in the same electronic configuration in solid and solution state.

The ^{19}F NMR of **C2** shows a single, broad response at -76 ppm indicative of non-coordinated triflate anions; the signal broadening is a result of fast exchange of the triflate ions.[97, 98] Thus, in CH_3CN solutions **C2** exists in a dynamic equilibrium with bound triflate and CH_3CN ligands. The ^{19}F NMR spectrum can be found in the Appendix.

2.4.8 Electrochemical Analysis at 298 K

In contrast to the di-zinc complex, both metal-centred and ligand-centred redox processes are feasible for **C2** and **C3**. Literature studies of iron complexes containing diimine ligands have demonstrated that reduction of the ligand is commonly favoured over the formation of low-valent metal oxidation states.[91, 99, 100] However, numerous intriguing possibilities exist with respect to the nature of the $[(L^1)_2Fe_2]^{4+/3+}$ and $[(L^1)_2Fe_2]^{3+/2+}$ couples and the distribution of two additional electrons among the four redox-active centres of **C2** and **C3**. **C2** and **C3** were investigated by CV to determine the nature of the redox processes available.

Two closely spaced reduction events at E_{pc} = -1.23 V and -1.34 V are observed for **C2** (Figure 32). Reduction of the di-iron complex occurs at a more negative potential than observed for L^1. The oxidative currents for these processes are ill-resolved at all scan rates examined (10 – 800 mV s^{-1}). For a reversible reduction process the modulus ratio of i_{pa} (anodic peak potential) over i_{pc} (cathodic peak potential) should be equal or close to 1. This is not the case for either reduction processes displayed in Figure 32, there are no defined return waves, E_{pa}, thus both processes are considered irreversible. An irreversible redox process can be due to an electrochemical reaction proceeded by a chemical reaction, labelled an EC mechanism, possibly due to structural rearrangement. The reduction processes are assigned as the one electron reductions of each of the α-diimine units. A comparison to the redox activity of $[Fe(bipy)_3]^{2+}$ supports this assignment; the voltammogram exhibits three individual reductions at E°' = -1.54 V, -1.72 V and -1.90 V assigned as ligand-based one electron reductions of each of the bipy ligands.[101] Comparison to work by Hess and co-workers also supports this assignment as $[Fe(TIM)(CH_3CN)]^{2+}$ exhibits two one electron processes at $E_{1/2}$ = -1.13 V and -1.60 V in which each α-diimine group is reduced by one electron.[99] The potential at which the reductions of **C2** occur are similar to L^1, slightly more negative due to the electron density at the iron ions.

The **C3** voltammogram was a duplicate of **C2**; again two reduction processes were observed, at E_{pc} = -1.26 V and -1.36 V, therefore assigned as one electron reductions of each α-diimine ligands.

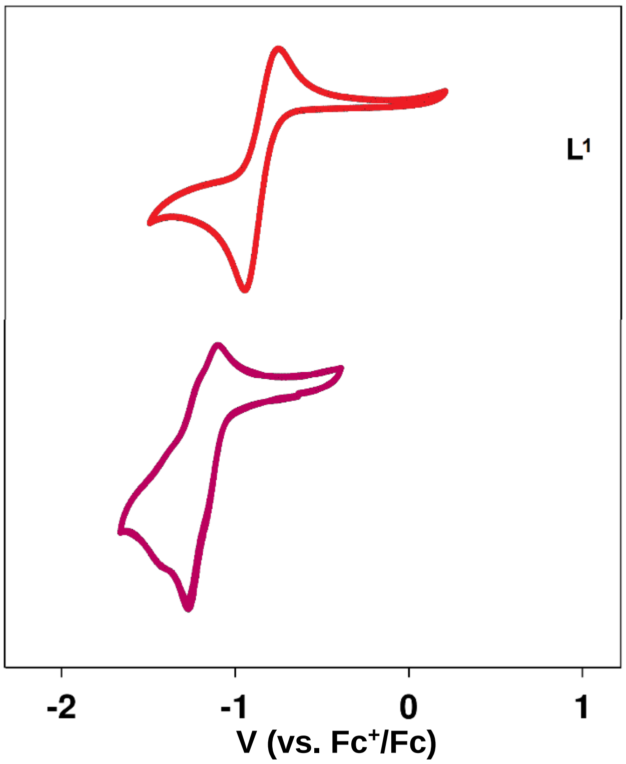

Figure 32. Electrochemical Studies of L^1 and C2 by Cyclic Voltammetry. Solvent = CH_3CN. Scan Rate = 0.2 V/s. Electrolyte for L^1 = 0.1 M TBAPF6. Electrolyte for C2 = 0.1 M TBAOTf.

2.4.9 Chemical Reduction of C2

The isolation and characterisation of reduced forms of **C2** were attempted employing a series of chemical reductants. The reduced form of the α-diimine ligand unit can be distinguished from the neutral form by analysing the bond lengths of the structure (Scheme 16). Four molar equivalents of $CoCp^*_2$ were added to a solution of **C2** in THF, CH_3CN, DCM or Ether. $CoCp^*_2$ was selected as the reductant as the $CoCp^*_2/CoCp^*_2{}^+$ couple is at -1.91 V (CH_3CN) and the CV studies illustrated the **C2** reduction potentials are at E_{pc} = -1.23 V and -1.34 V. Four molar equivalents were added in attempt to achieve the one electron reduction of both α-diimine units and allow an excess. A colour change to orange/brown was observed in all solvents. The pink colour of **C2** is due to MLCT transitions, so reduction of the ligand would affect the energy of this transition as the low lying π accepting orbitals would now exist as partially filled and hence a colour change would be expected. No compounds were successfully isolated from the reaction mixture. The addition of Na/Hg beads (-3.04 V THF) or Na^0 to a solution of **C2** in THF or CH_3CN resulted in a black suspension. No compounds were successfully isolated from the black suspension, thus, this reaction was considered unsuccessful.

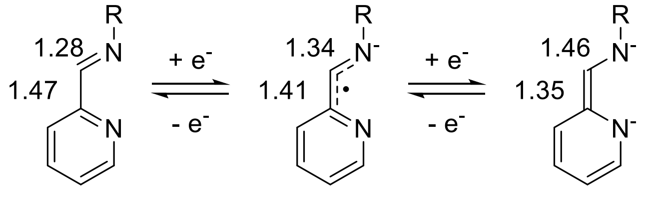

Scheme 16. Two-Electron Redox Series for the α-Iminopyridine Group, With Characteristic Bond Lengths (Å)

2.5 Reaction of L^1 with Copper Salts (C4)

The copper dimer, $[(L^1)_2Cu_2](OTf)_4$ **(C4)**, was synthesised in reactions with equimolar amounts of $Cu(OTf)_2$ and L^1 in THF (Scheme 17). The yellow L^1 solution turned to a dark green suspension immediately upon addition. After filtration of the green precipitate the filtrate had a slight green colouring suggesting some form of copper remains in solution. However, given the high yield of solid **C4** no further analysis of the faintly green coloured solution was carried out.

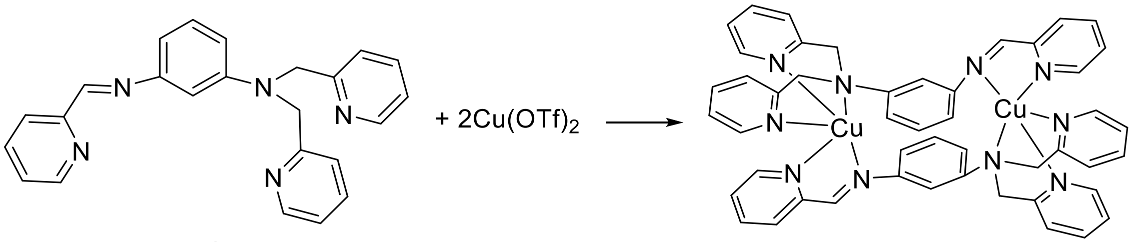

L¹
21
C4

Scheme 17. Synthetic Scheme of Cupric Complex of L^1, C4.

Solid State Analysis

2.5.1 Crystallographic Analysis

Each copper ion in **C4** adopts a distorted square pyramidal geometry (τ = 0.06 – 0.12)[102], with lengthening of the Cu–N_{im} bond (2.25 Å) along the Jahn-Teller axis. The bis(pyridylmethyl)amino group assumes a pincer-like arrangement, with two short Cu–N_{py} (~1.97 Å) bonds and one slightly longer Cu–N_{am} (~2.10 Å) bond. The pyridyl-nitrogen of the α-iminopyridine supplies the fourth ligand of the square planar base (Cu–N_4 plane = 0.21 Å), which constrains the weakly coordinated axial imine-nitrogen at a 76° N_{py}–Cu–N_{im} angle. The two L^1 benzene rings of the di-copper complex are nearly superimposed and within π-stacking distance (3.4 – 3.7 Å). From the bond lengths of the α-diimine unit, 1.27 Å and 1.47 Å, it is determined that L^1 is in the neutral form. The crystal system includes four unbound triflate anions. The Cu···Cu distance is smaller than the metal separation found for **C1, C2 and C3** at 6.928 Å illustrating the flexibility of L^1. Further crystallographic details can be found in the Appendix.

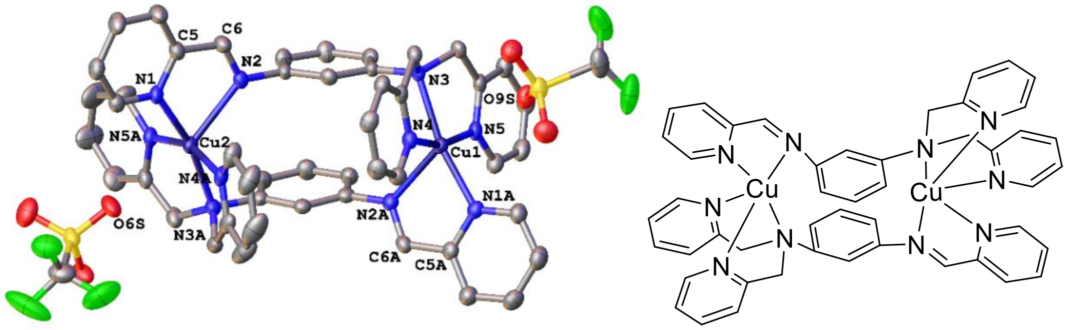

Figure 33. Left: Molecular Structure of C4 (50 % Probability Ellipsoids). Hydrogen Atoms Have Been Omitted and Only Two Triflate Counteranions are shown for Clarity. Selected Bond Lengths (Å) and Angles (deg): Cu1-N1A 2.075(3), Cu1-N2A 2.247(3), Cu1-N3 2.105(3), Cu1-N4 1.977(3), Cu1-N5 1.968(3), Cu2-N1 2.042(3), Cu2-N2 2.284(3), Cu2-N3A 2.086(3), Cu2-N4A 1.975(3), Cu2-N5Aavg 1.945(9), N1-C5 1.348(5), C5-C6 1.475(6), N2-C6 1.263(5), N1A-Cu1-N2A 76.72(13), N3-Cu1-N4 83.14(13), N3-Cu1-N5 82.86(13), N1A-Cu1-N3 166.70(13), N4-Cu1-N5 163.12(14), N1-Cu2-N2 76.87(12), N3A-Cu2-N4A 83.36(14), N3A-Cu2-N5A 83.5(5), N1-Cu2-N3A 166.33(14), N4A-Cu2-N5Aavg 161.9(6), Cu1--Cu2 6.9283(8) Determined by X-Ray Crystallography. Right: ChemDraw Structural Representation of C4.

2.5.2 Magnetic Susceptibility Analysis

Magnetic susceptibility measurements using SQUID were carried out on **C4** to determine metal-metal interactions and investigate the magnetic properties of the complex. Magnetic susceptibility measurements of **C4** indicated a temperature independent magnetic moment in the range of 20 – 290 K, decreasing below 20 K to a value of ~2.4 μ_B (Figure 34). The effective magnetic moment of 2.6 μ_B at room temperature matches the expected value for two uncoupled cupric centres with the hallmark $g \sim 2.1$. The data were fit for $g = 2.12$ and $J = -0.2$ cm^{-1}.

The magnetic susceptibility of **C4** was also investigated by electron paramagnetic resonance (EPR) by our collaborator Dr. Stephen Sproules. The X-band EPR spectrum recorded in CH_3CN/CH_2Cl_2 displayed a signal consistent with two weakly coupled Cu^{II} (S = $^1/_2$) ions. EPR spectra and further details can be found in the Appendix.

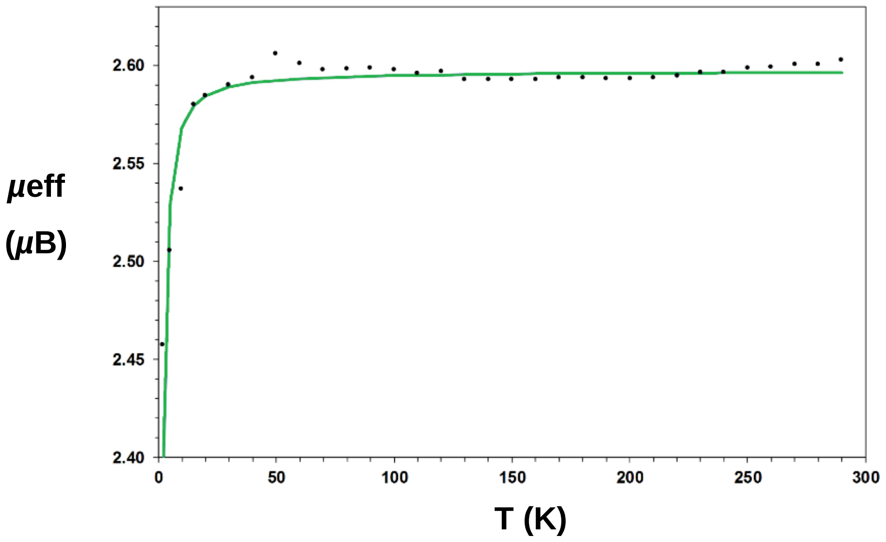

Figure 34. Magnetic Susceptibility Data of C4 (1 T, 2 – 290 K); Experimental = Circles, Simulation = Solid Line. Simulation of Data for C4 with $S_1 = S_2 = ½$, $g_1 = g_2 = 2.12$ (fixed), $J = -0.241$ cm^{-1}, TIP = 50 x10^{-6} emu.

2.5.3 Computational Analysis by Density Function Theory

The copper ions in **C4** are weakly ferromagnetically coupled. As discussed in Section 2.4.5 ferromagnetic coupling is expected for 1,3-phenyldiamine bridged complexes where there is an odd number of atoms separating the metal ions, which leads to spin polarisation.[94, 95] DFT calculations of **C4** illustrate the spin polarisation of the 1,3-phenylenediamine system of L^1.[95] The DFT-derived spin density map depicts alternating spin densities on the carbon atoms of the central aromatic ring, with delocalisation of the metal spin towards the amino-nitrogen of the bis(pyridylmethyl) group (Figure 35). Spin polarisation was hard to observe for **C2** and **C3** as there was very little charge density on the phenyl bridge. The SOMOs of **C4** consist of the in-phase and out of phase σ* orbitals, comprising ~ 34 % Cu $d_{x^2-y^2}$ character with minor contributions from the delocalised π-system of the benzene ring. Due to the orientation of the α-iminopyridine ligands the N_{im} *p* orbitals lie orthogonal to the $d_{x^2-y^2}$ –based σ* orbitals, severing the conventional pathway for π-type exchange through the N_{im}-C-C-C-N_{am} bridge. As mentioned previously the better the orbital overlap between metal and bridge orbitals the stronger the coupling. Efficient π-type overlap of the copper SOMOs with both N *p* orbitals in the related 1,3-phenylenediamine bridged cupric metallocyclophane (Cu···Cu = 6.8 Å)[103] and 1,3-[bis(2-pyridylmethyl)amino]benzene complexes (Cu···Cu = 5.87 Å)[104] led to substantial coupling of the two metal centres, with measured exchange constants of 8.4 and 4.6 cm^{-1}, respectively, obtained from magnetic susceptibility measurements. Weak interactions between the copper ions in **C4** can thus be attributed to the poor overlap of the Cu $d_{x^2-y^2}$ orbitals to the bridge. Interactions between the stacked benzene rings of L^1 might provide an alternate pathway for communication between the two copper ions.[105] Further inspection of the remaining metal-based MOs of **C4** also reveals pervasive covalency, with contributions from the ligand π-system and admixture of the copper *d* orbitals. There is then a greater chance of spin-orbit coupling contributions accounting for the weak coupling in **C4** in contrast to **C2** and **C3** were studies of the MOs showed only metal character.

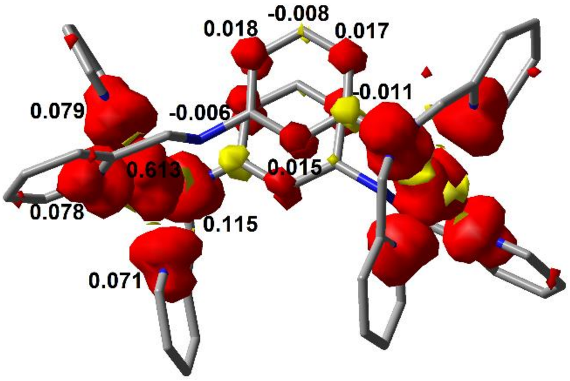

Figure 35. DFT-derived (B3LYP) Spin Density Plot for C4 Based on Loewdin Population Analysis.

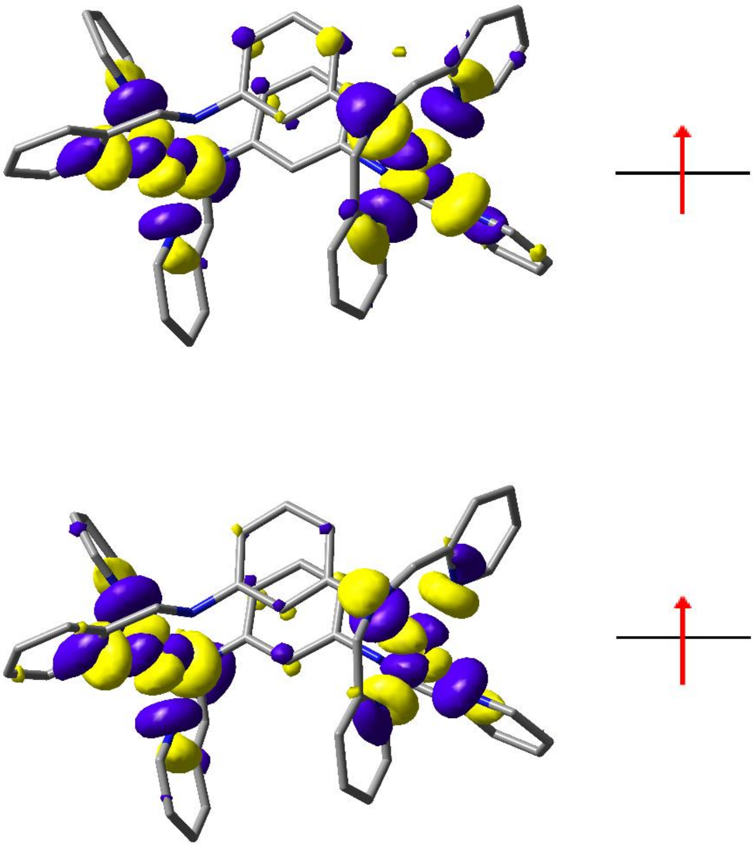

Figure 36. DFT-derived (B3LYP) SOMOs for C4.

Solution State Analysis

2.5.4 Electronic Absorption Spectroscopic Analysis at 298 K

The electronic spectrum of **C4** was studied in CH_3CN. A prominent absorption band is observed at λ_{max} (M^{-1} cm^{-1}) ~ 579 nm assigned as Cu^{II} *d-d* transitions (ε = 520 M^{-1} cm^{-1} ⇒ 260 M^{-1} cm^{-1} per Cu). The energy and intensity of the transition is within the typical range observed for *d-d* bands in related tetragonal Cu^{II}-pyridine compounds.[102, 106] Furthermore, an MLCT transition would be expected to occur at higher energy than for the corresponding di-iron complexes.

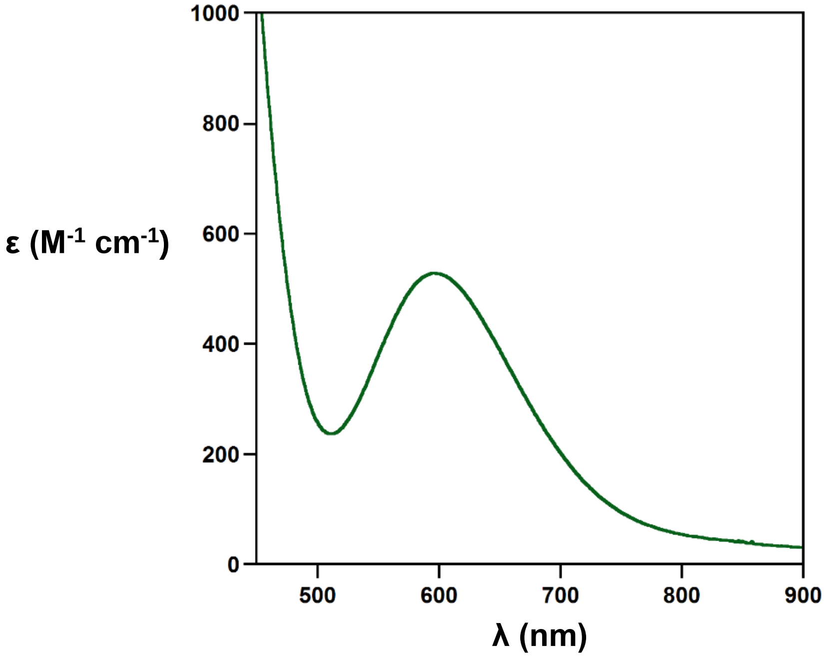

Figure 37. Absorption Spectrum of C4. Solvent = CH_3CN.

2.5.5 Electrochemical Analysis at 298 K

Cyclic voltammetry was employed to investigate the redox properties of **C4**. The voltammogram displays two individual redox processes. The first is a quasi-reversible reduction at E_{pc} = -0.44 V with a return E_{pa} = -0.25 V (Figure 38, Left). The process is classified as quasi-reversible as the peak separation is 0.19 V and the $|i_{pa}/i_{pc}|$ ratio = 0.36. The free ligand L^1 does not exhibit redox activity at this voltage and because of this and the comparison to redox potentials exhibited by **C1**, **C2** and **C3** the reduction process can be assigned as a metal-based reduction of Cu^{2+}/Cu^{+}. This assignment is in agreement with the observed trend of increasing metal character in a series of first row bis(iminopyridine) complexes, across the period from Cr to Ni.[91] The lack of reversibility of this process can be rationalised by the expected structural changes in coordination geometry that typically accompany Cu^{I} formation. Further reduction of the di-copper complex is obscured by copper stripping beyond -0.75 V. The second redox process occurs at E_{pc} = -1.28 V, a similar redox potential as the free L^1 and related complexes. However, it is the reverse wave which is indicative of the type of process occurring; a large i_{pa} of 2.5 ×10^{-5} A at E_{pa} = -0.87 V. This process is assigned as a stripping peak and therefore assigns the reduction at E_{pc} = -1.28 V as the metal-centred reduction of Cu^+/Cu^0. ‘Stripping’ involves the deposition of the M^0 onto the working electrode over a period of time. As the M^0 builds on the electrode over time, it essentially concentrates the metal, this concentration of the M^0 is followed by the dissolution of the deposit on the reverse cycle. For this complex Cu^0 is deposited on the electrode between ~ - 1.15 V and -1.45 V. The large i_{pa} which follows is due to the direct relationship between concentration and current according to the Randle-Sevcik equation.

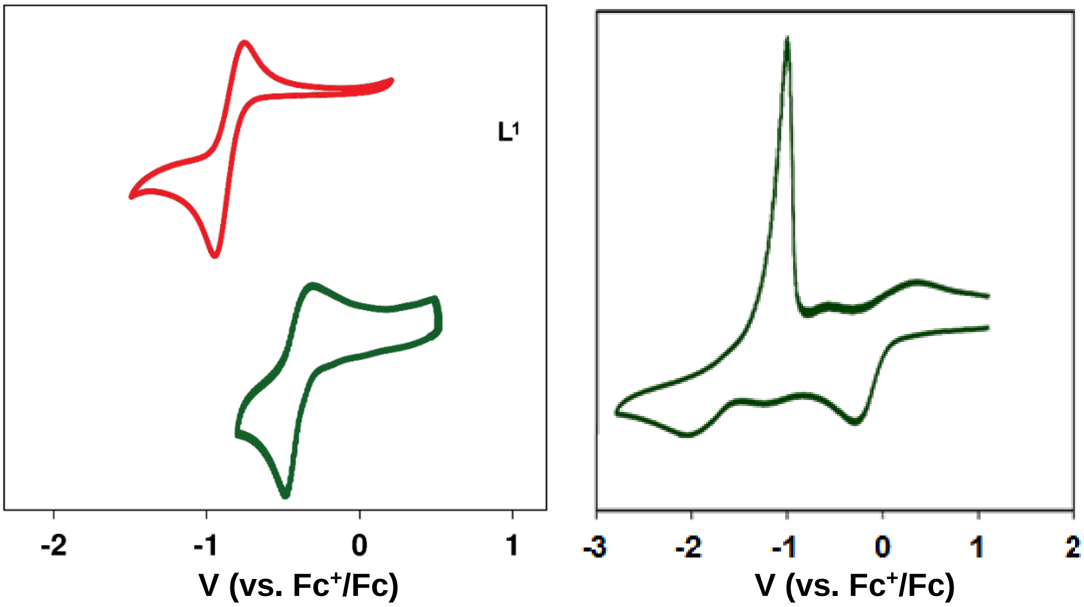

Figure 38. Left; Electrochemical Studies of L^1 and C4 by Cyclic Voltammetry. Solvent for C4= CH_3CN. Scan Rate = 0.2 V/s. Electrolyte for L^1 = 0.1 M TBAPF6. Electrolyte for C4 = 0.1 M TBAOTf. Right; Stripping exhibited by C4. Scan Rate = 0.2 V/s. Electrolyte = 0.1 M TBAOTf.

2.5.6 Chemical Reductions of C4

From the electrochemical studies the reduction processes of **C4** have been assigned as metal-based Cu^{2+}/Cu^+, Cu^+/Cu^0. To isolate and characterise possible reduced forms, **C4** was chemically reduced with $CoCp_2$ (-1.33 V in CH_2Cl_2). One method employed to monitor the reaction was UV-Vis spectroscopy. Cu^+ cannot exhibit *d-d* transitions as the electronic configuration of Cu^+ is $[Ar]3d^{10}$, a full *d* shell. The reduction from Cu^{2+} to Cu^+ should coincide with the depletion of the prominent *d-d* transition observed for **C4**. The *d-d* transition at 579 nm is significantly reduced after reduction with cobaltocene, approximately by half (Figure 39). This is consistent with the reduction of one of the copper sites to Cu^+. Two new overlapping transitions from ~ 550 - 400 nm are seen in the reduced spectra. These could be CT transitions due to their higher energy and large molar coefficients, but further assignment has not been made as isolation of this compound was not achieved.

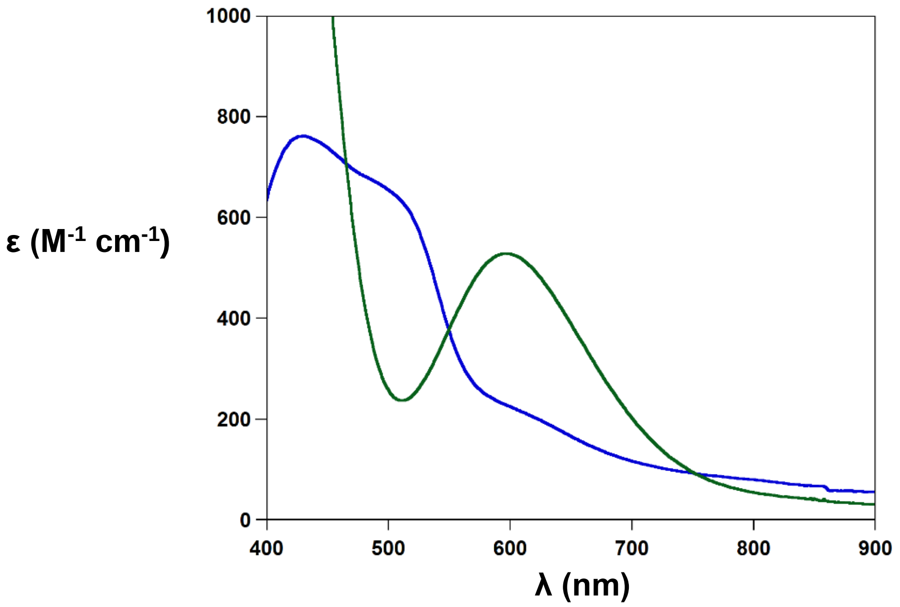

Figure 39. Electronic Absorption Spectra of C4 (Green) and After Reduction with Cobaltocene (Blue). Solvent = CH_3CN.

2.5.7 Other Copper Systems

By altering the reaction conditions between L^1 and $Cu(OTf)_2$ two further copper structures were obtained. By changing the reaction solvent from THF to DCM and to a Cu:ligand 2:1 stoichiometry, the asymmetric $[L^1Cu_2(OTf)_3(H_2O)_2](OTf)$, **C5**, complex was obtained. The reaction in CH_2Cl_2 was slower than in THF and required 5 hours until a persistent green suspension was obtained. Upon filtration a small amount of blue precipitate and green solution were obtained. From the green solution crystals were readily grown, *via* vapour diffusion with toluene, which were characterised as **C5** (Figure 40). Each copper ion is in a pentadentate, square pyramidal configuration. The iminopyridine unit makes up half of the square base around Cu(1); the base is completed with a coordinated triflate and water ligand, a further triflate ligand makes up the pyramidal peak. Cu(2) is coordinated by all three nitrogen atoms of the innocent coordination site of L^1, unlike **C1** which is only coordinated by the pyridyl nitrogen atoms. The almost planar arrangement of the tridentate innocent coordination site constructs the square base, which is completed by a water ligand. A triflate ligand occupies the pyramidal apex of the coordination sphere. The apical triflate ligands are facially opposing, which could be beneficial to further reactivity. **C5** retains the desired asymmetry originally designed for the bi-metallic complexes employing L^1.

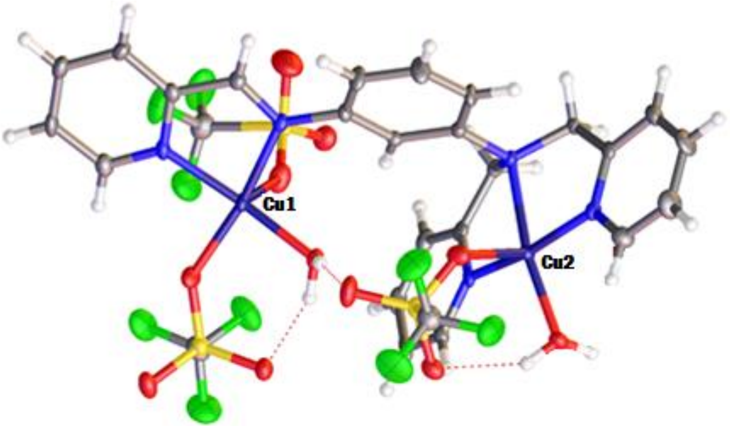

Figure 40. Molecular Structure of Asymmetric Bi-metallic Copper mono-L^1 Complex C5; 50 % Probability Ellipsoids. Triflate Counteranions have been omitted for Clarity.

The drawback of the aforementioned synthetic route to obtaining **C5** is purity. A second crystal was isolated from the same green solution under identical conditions. The second crystal was blue and was characterised as [L$^1_2$Cu$_4$(OTf)$_6$](OTf)$_2$, **C6** (Figure 41). **C6** is tetra-metallic with two L^1 molecules. Unlike **C2**, **C3** and **C4** where the dimeric species is formed from two L^1 molecules coordinating around each metal centre, the two L^1 molecules of **C6** are connected through copper ions bridged by triflate ligands. Cu(1) coordinated by the iminopyridine unit is held in a distorted tetrahedral configuration with one terminal triflate ligand and one bridging triflate ligand. Cu(2) is coordinated by all three nitrogen atoms of the innocent coordination site and by one terminal and one bridging triflate ligand, completing the pentadentate coordination sphere. The desired asymmetry across the molecule is lost as each iminopyridine unit is bridged to an innocent bis(2-pyridylmethyl)amino group. The bridging triflate may hold the sites far enough apart to allow for electron localisation within the iminopyridine unit. **C6** may reveal some interesting reactivity based on this tetra-metallic bridging structure and the proximity of the copper ions to one another. The challenge before exploring the catalytic potential of these copper complexes is the development of a synthetic route in which each species is formed exclusively. The above synthetic route resulted in a mixture of crystals such that achieving a solely pure sample even by separating crystals by hand would be unreliable. For this reason no further bulk analysis could be carried out.

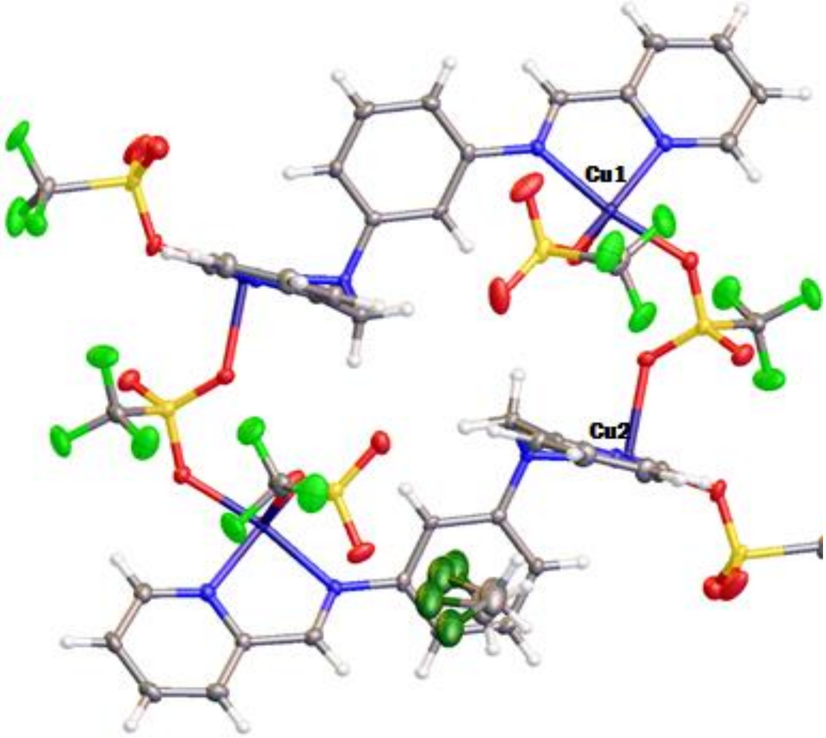

Figure 41. Molecular Structure of Bi-metallic Complex C6; 50 % Probability Ellipsoids. Triflate Counteranions have been Omitted for Clarity.

2.6 Hetero bi-metallic Complexes

Hetero bi-metallic systems are another interest of this research, due to the possibility that the different metal centres could exhibit cooperative behaviour during catalysis. Each metal could play a unique mechanistic role and influence the behaviour of the other. This is termed synergism and can lead to increased catalytic behaviour.[107] Successful hetero bi-metallic catalysts found in nature include the active sites of Ni-Fe hydrogenases, as previously discussed, human calcineurin; FeZn, human protein phosphatase 1; MnFe and superoxide dismutase; CuZn.[108] PtRu clusters have proven to exhibit a higher level of catalytic activity for hydrogenation than the homo bi-metallic metal analogues and RuPd, RuPt and RuAu bi-metallic complexes have exhibited higher activity for alcohol oxidation than their homo bi-metallic complexes.[109] Initial attempts at synthesising hetero bi-metallic complexes were undertaken by adding 1.0 molar equivalent of two different metals to a solution of L^1. From the reaction with 50:50 $Fe(OTf)_2$ and $Cu(OTf)_2$ evidence came that only one metal was being bound by L^1 when crystals of **C4** were solely obtained. This outcome was rationalised as the result of the copper ions affinity to bind with ligands; an extract of the Irving-Williams series for the metal ions studied in this research is shown below.

$$\mathbf{Fe^{2+} < Co^{2+} < Ni^{2+} < Cu^{2+}}$$

Scheme 18. Extract of Irving-Williams Series

The next approach at synthesising hetero bi-metallic complexes took consideration of the Irving-Williams series; synthesising the bi-metallic complexes with weakly bound metal ions first proceeded by the addition of 1.0 molar equivalent of the stronger metal ion in attempt to substitute only one of the weaker metal ions. This approach gave some promising UV-Vis spectroscopic results (Figure 42). The reaction between L^1 and $CoCl_2$ yields $(L^1)_2Co_4Cl_8$, (synthesised and studied by Hannah Blackburn). 1 molar equivalent of $Ni(OTf)_2$ and $Cu(OTf)_2$ were each added to a solution of $(L^1)_2Co_4Cl_8$ and the reaction monitored by UV-Vis. The electronic absorption spectra show distinctive differences after the addition of the second metal which is a promising result toward achieving hetero bi-metallic complexes.

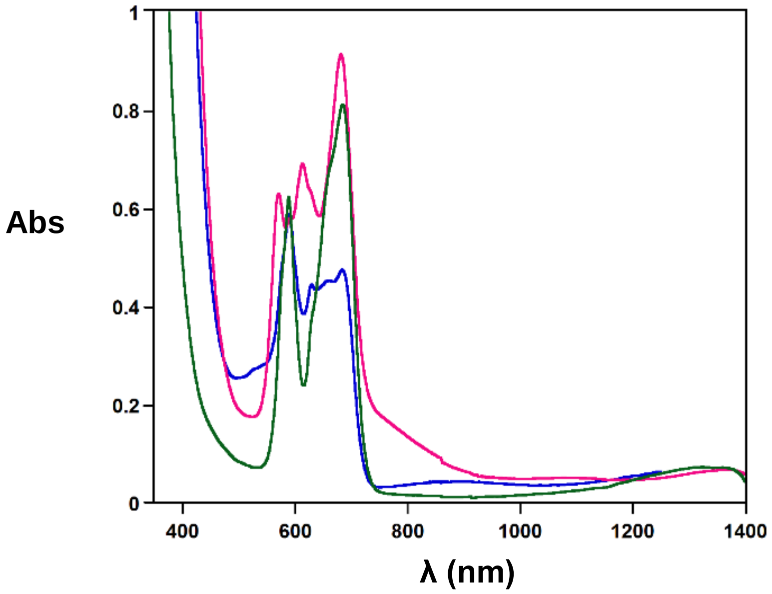

Figure 42. Hetero Bi-metallic Complexes Monitored by Absorption Spectroscopy. Blue Trace; $(L^1)_2Co_4Cl_8$ in CH_3CN (1mM). Pink Trace: After Addition of $Cu(OTf)_2$ to $(L^1)_2Co_4Cl_8$ in CH_3CN (1mM). Green Trace: After Addition of $NiCl_2$ to $(L^1)_2Co_4Cl_8$ in CH_3CN (1mM).

2.7 Conclusions

The synthesis of a novel complex with the potential to facilitate multi-electron reactions was the long-term focus of this project. The task was approached by the development of the redox active ligand L^1 with the aim of its use to generate a ligand-based two-electron mixed valence complex. The design of L^1 is such that it possible to bind two metal ions through *N*-donors of the α-diimine group and bis(pyridylmethyl)amino groups, the α-diimine group is theoretically capable of a two-electron reduction which is to be the source of mixed valency. The high flexibility of the ligand accommodates the coordination geometry preferences of various metal ions and the formation of both symmetric and asymmetric bi-metallic complexes.

Electrochemical studies confirm the redox activity of L^1, but is indicative of a one electron reduction rather than the two electron reduction series theoretically possible for the α-diimine group. The redox behaviour of **C1, C2, C3 and C4** follows the anticipated trend for the series of metals examined in this study. A one-electron reduction is observed for compound **C1**, due to the inert nature of Zn^{2+} this reduction can be assigned as ligand-based. The reduction occurs at a slightly more negative potential than L^1 and in contrast to L^1 loses all reversibility, suggesting structural rearrangement upon reduction. At the opposite end of our series the dimeric copper complex, **C4**, displayed two successive one-electron reductions likely attributed to the $Cu^{II/I}$ $Cu^{I/0}$ couples due to the observation of a distinctive stripping peak and the more positive potential of the first reduction against the CV of L^1. Therefore no ligand-based reduction was exhibited by **C4**. Compounds **C2** and **C3** offers the option of both metal- and ligand-centred redox processes. Two very close one electron reductions were observed assigned as ligand-based one electron reductions of each of the α-diimine groups present. Both reductions were irreversible, again suggesting structural rearrangement upon reduction.

Both the copper and iron dimers are paramagnetic. **C2** and **C3** exist as high-spin ferrous ions in both solid and solution state. While studies have shown that 1,3-phenylenediamine bridges in related bi-metallic compounds can provide an efficient route for exchange interactions between two metal centres, the metal ions in both **C2, C3** and **C4** are only very weakly ferromagnetically coupled.[94, 95] An inspection of the molecular structures and DFT computational results reveal that the communication pathway between the metal sites is dismantled by the orientation of the *m*-phenylenediamine groups and the coordination geometry adopted by the metal leading to weak coupling.

The desired asymmetry, and thus the potential to form a two electron mixed valence complex, is maintained by **C1** but lost in the formation of the dimeric **C2, C3** and **C4**. The asymmetric **C5** complex can be obtained by altering the reaction conditions of **C4**, but it is imagined this complex will favour metal-centred reduction over ligand-based as demonstrated by **C4**. The facially opposing labile triflate ligands and weakly bound water molecules of **C5** still offers plenty of scope for reactivity. A better synthetic route needs to be developed as **C5** is made in parallel with **C6**; a tetra-metallic complex with bridging triflate ligands. Each needs to be exclusively isolated to allow for full characterisation and reactivity studies.

The synthesis of hetero bi-metallic complexes was attempted taking into consideration the Irving-Williams series which yielding promising absorption spectroscopy results and so perusal of this route is recommended.

Bi-metallic complexes of L^1 have displayed several shortcomings for application as multi-electron catalysts. Firstly, L^1 is highly flexible preferentially forming an L^1 dimer for **C2**, **C3** and **C4** and forming some unexpected tri-metallic and tetra-metallic structures, as seen by other members of the Hess group investigating the coordination of different first row transition metals. The original design of an asymmetric mixed valence complex cannot be achieved with these structures. The second pitfall are the large M···M distances found which incapable of holding the metal ions closely enough for processes such as hydrogen migration, required for proton reduction. Thirdly, from CV studies, only the one electron reduced form of L^1, **C1**, **C2** and **C3** was accessible, these complexes could not be used to generate a two-electron mixed valence state while the cuprous complex **C4** displayed only metal-centred reduction. Finally, the stability of L^1 and subsequent bi-metallic complexes has been found to be problematic in aqueous and acidic media. A new ligand scaffold design based on the original two-electron ligand-based mixed valence concept is required to develop multi-electron catalysts and is discussed in Chapter 5 – Synthesis of a New Generation Series of Aza-Macrobicyclic Ligand Scaffold for use in Multi-electron Reactions.

2.8 Experimental

(3-Aminophenyl)carbamic acid *tert*-butyl ester (29). The synthesis of the BOC-protected 1,3-benzenediamine was analogous to procedures previously described.[82] A solution of di-*tert*-butyl-dicarbonate (10.6 mL; 0.046 mol) in 1,4-dioxane (15 mL) was added dropwise to a solution of *m*-phenylenediamine **(28)** (5.00g; 0.046 mol) in 1,4-dioxane (15 mL). Triethylamine (6.4 mL; 0.046 mol) was then added to the reaction mixture and the solution was heated at 60 °C for 24 h. The solvent was removed *in vacuo* to yield a red-brown oil. The crude product was purified *via* flash column chromatography (2:3 ethyl acetate/hexanes, R_f = 0.2) to give the desired product, (3-aminobenzyl)carbamic acid *tert*-butyl ester (6.5 g, 67 % yield). ^{1}H NMR (400 MHz, $CDCl_3$): δ 7.04 (t, J = 8.0 Hz, 1H), 6.97 (s, 1H), 6.55 (ddd, J = 8.0, 2.0, 0.8 Hz, 1H), 6.47 (br s, $\nu_{1/2}$ = 9.9 Hz, 1H), 6.37 (ddd, J = 8.0, 2.0, 0.8 Hz, 1H), 3.67 (br s, $\nu_{1/2}$ = 8.8 Hz, 2H), 1.51 (s, 9H). ^{13}C NMR (100 MHz, $CDCl_3$): δ 152.8, 147.4, 139.5, 129.8, 110.0, 108.8, 105.3, 80.5, 28.5. The ^{1}H NMR data obtained is in agreement with that reported in literature.[82]

[3-[bis(pyridine-2-ylmethyl)amino]phenyl]amino-2,2-dimethylpropanoate (30). To a solution of **29** (4.00 g; 0.019 mol) in anhydrous ethanol (60 mL) was added Na_2CO_3 (8.14 g; 0.077 mol). 2-(chloromethyl)pyridine hydrochloride (6.3 g, 0.038 mol) was then added and the mixture was heated to reflux at 80 °C for 24 h. The resulting brown suspension was filtered and the solvent removed *in vacuo* to yield a brown oil. The brown oil was diluted with CH_2Cl_2 (40 mL) and treated with 2 M NaOH (50 mL). The product was extracted with CH_2Cl_2 (3 × 50 mL), then the organic layer was washed with brine (2 × 50 mL), dried over $MgSO_4$ and the CH_2Cl_2 removed under vacuum. The crude product was run through a silica plug (125 cm^3 silica; ethyl acetate; R_f = 0.2) to give the desired product **30** (4.1 g, 44 % yield). ^{1}H NMR (400 MHz, $CDCl_3$); δ 8.58 (d, J = 4.7 Hz, 2H), 7.62 (td, J = 7.7, 1.9 Hz, 2H), 7.25 (d, J = 7.9 Hz, 2H), 7.16 (dd, J = 7.7, 4.8 Hz, 2H), 7.07 (t, J = 8.2 Hz, 1H), 6.89 (br s, $\nu_{1/2}$ = 17.6 Hz, 1H), 6.58 (t, J = 2.2 Hz, 1H), 6.38 (dd, J = 8.4, 2.4 Hz, 1H), 6.35 (br s, $\nu_{1/2}$ = 4.2 Hz, 1H), 4.79 (s, 4H), 1.46 (s, 9H). ^{13}C NMR (100 MHz, $CDCl_3$): δ 158.9, 152.8, 149.8, 149.1, 139.6, 137.0, 130.0, 122.2, 121.1, 108.1, 107.8, 102.8, 80.42, 57.31, 28.46. MS (LRMS$^+$; ESI; *m/z*): 391.4 [M+H], 185.2 [M$^+$-2×Me-Py], 102.2 [M$^+$-(BOC + 2×Me-Py)]. IR; 2976 (w), 2940 (w), 1720 (m), 1608 (m), 1591 (m), 1544 (m), 1500 (m), 1473 (m), 1433 (m), 1390 (m), 1365 (m), 1319 (m), 1237 (m), 1157 (s), 1049 (m), 992 (m), 755 (s), 729 (s), 690 (m), 618 (m).

1-*N*, 1-*N*-bis(pyridin-2-ylmethyl)benzene-1,3-diamine (31). **30** (1.00 g; 2.56 mmol) was dissolved in ethyl acetate (30 mL) and then treated dropwise with 12 M HCl (10 mL). The reaction mixture was left to stir for 1 h. The resultant solution was combined with 5 M NaOH (50 mL) and the organic layer was extracted with CH_2Cl_2 (3 × 50 mL). The solvent was removed *in vacuo* to yield **31** (0.7 g, 98 % yield). ^{1}H NMR (400 MHz, $CDCl_3$): δ 8.58 (ddd, J = 4.9, 1.8, 0.9 Hz, 2H), 7.62 (td, J = 7.7, 1.8 Hz, 2H), 7.28 (d, J = 8.0 Hz, 2H), 7.16 (dd, J = 7.4, 4.9 Hz, 2H), 6.95 (t, J = 8.0 Hz, 1H), 6.14 (dd, J = 8.3, 2.4 Hz, 1H), 6.09 (dd, J = 7.9, 2.0 Hz, 1H), 6.02 (t, J = 2.4 Hz, 1H), 4.78 (s, 4H), 3.51 (s, 2H). ^{13}C NMR (100 MHz, $CDCl_3$): δ 159.2, 149.8, 149.6, 147.7, 137.0, 130.3, 122.1, 121.0,

104.9, 103.7, 99.49, 57.38. MS (LRMS$^+$; ESI; *m/z*): 291.3 [M+H], 200.2 [M$^+$-Me-Py], 109.2 [M$^+$-2Me-Py]. IR; 3427 (m), 3350 (m), 3012 (w), 2960 (w), 1606 (m), 1590 (s), 1570 (s), 1470 (m), 1439 (m), 1391 (m), 1352 (s), 1260 (m), 1204 (m), 1180 (s), 1094 (m), 1046 (m), 991 (m), 970 (m), 943 (m), 818 (s), 758 (s), 716 (m), 690 (s), 663 (m), 616 (s).

1-*N*,1-*N*-bis(pyridine-2-ylmethyl)-3-*N*-(pyridine-2-ylmethylidene)benzene-1,3-diamine (L^1, 21). A solution of 2-pyridinecarboxaldehyde (180 µL; 1.89 mmol) and **31** (0.50 g; 1.72 mmol) in dry toluene (90 mL) was heated to reflux at 120 °C, over molecular sieves, under an argon atmosphere for 5 h. The solvent was removed *in vacuo* to give L^1 **(21)** (0.60 g, 90 % yield). ^{1}H NMR (400MHz, $CDCl_3$) δ 8.68 (d, *J* = 4.8 Hz, 1H), 8.59 (d, *J* = 4.8 Hz, 2H), 8.51 (s, 1H), 8.11 (d, *J* = 8.0 Hz, 1H), 7.78 (td, *J* = 7.7, 1.7 Hz, 1H), 7.63 (td, *J* = 7.7, 1.8 Hz, 2H), 7.34 (ddd, *J* = 7.7, 4.9, 1.2 Hz, 1H), 7.29 (d, *J* = 8.0 Hz, 2H), 7.21 – 7.16 (m, 3H), 6.68 – 6.61 (m, 3H), 4.85 (s, 4H). ^{13}C NMR (700 MHz, $CDCl_3$): δ160.29, 158.51, 154.49, 152.30, 149.74, 149.65, 149.25, 136.83, 136.58, 130.00, 124.99, 122.06, 121.98, 120.75, 110.94, 109.23, 105.86, 57.07. MS (LRMS$^+$, ESI; *m/z*): 380.6 [M+H]. HRMS (ASAP; *m/z*: 380.1898 [M+H]). IR; 2919 (w), 2830 (w), 1632 (w), 1588 (s), 1569 (m), 1491 (m), 1468 (m), 1434 (m), 1383 (m), 1344 (m), 1258 (m), 1180 (m), 1166 (m), 1088 (m), 1048 (m), 991 (m), 971 (m), 798 (m), 776 (m), 766 (s), 700 (m), 662 (m), 616 (m). UV-vis: λ_{max}, nm (ε, $M^{-1}cm^{-1}$) in DCM: 254 (2.7 ×10^4).

[L^{1}Zn$_2$Cl$_4$] (C1). Colorless $ZnCl_2$ (26 mg; 0.19 mmol) was added to a solution of L^1 (36 mg; 0.09 mmol) in THF or MeCN (10 mL). The mixture was stirred overnight and the resultant yellow precipitate was filtered to give **C1** (43 mg, 70 % yield). Diffraction quality single crystals were obtained by slow evaporation of a concentrated solution of **C1** in CH_3CN. ^{1}H NMR (700MHz, CD_2Cl_2) δ 9.24 (d, *J* = 5.0 Hz, 2H), 9.01 (s, 1H), 8.81 (d, *J* = 5.1 Hz, 1H), 8.27 (td, *J* = 7.7, 1.6 Hz, 1H), 8.08 (d, *J* = 7.7 Hz, 1H), 7.96 – 7.91 (m, 3H), 7.87 (ddd, *J* = 7.7, 5.0, 1.2 Hz, 1H), 7.52 (t, *J* = 6.1 Hz, 2H), 7.51 (d, *J* = 7.7 Hz, 2H), 7.45 – 7.40 (m, 3H), 4.85 (s, 4H). IR; 2930 (s), 2924 (s), 2900 (s), 1729 (s), 1590 (m), 1443 (s), 1382 (m), 1285 (m), 1240 (s), 1103 (s), 1052 (s), 1023 (s), 967 (m), 886 (m), 865 (m), 784 (s), 766 (s), 686 (m), 646 (m) 630 (m), 607 (m). Anal Calcd for $C_{24}H_{21}Cl_4N_5Zn_2$: C, 44.21; H, 3.25; N, 10.74. Found: C, 43.99; H, 3.25; N, 10.80. UV-vis: λ_{max}, nm (ε, M^{-1} cm^{-1}) in DCM: 262 (~1.6 ×10^4), 331 (~1.6 ×10^4).

[(L^1)$_2$Fe$_2$(OTf)$_2$](OTf)$_2$ (C2). A suspension of Fe(OTf)$_2$ (23 mg, 0.065 mmol) in THF (5 mL) was added to a solution of L^1 (25 mg, 0.066 mmol) in THF (5 mL; THF was stored over Na – the yield of product obtained was highly dependent on the quality of the reagents and solvent) upon which the mixture immediately turned green. The reaction mixture was stirred for 72 h, during which time a series of colour changes was observed, from green to blue to black, with the appearance of a pink solid. The pink solid **C2** was collected by filtration (26 g, 54 % yield), leaving a charcoal grey filtrate. Additional products of this reaction were not identified. Single crystals were obtained by slow diffusion of diethyl ether into a solution of **C2** in CH_3CN. IR; 3074 (w), 1597 (m), 1490 (m), 1446 (m), 1376 (w), 1313 (m), 1281 (s), 1256 (s), 1234 (s), 1210 (s), 1164 (s), 1108 (m), 1060 (m), 1029 (s), 972 (m), 948 (m), 881 (m), 860 (m), 790 (m), 764 (m), 690 (m), 635 (s). Anal Calcd for $C_{52}H_{42}N_{10}O_{12}S_4F_{12}Fe_2$: C, 42.58; H, 2.89; N, 9.55. Found: C, 42.37; H, 2.96; N, 9.61. UV-vis: λ_{max}, nm (ε, M^{-1} cm^{-1}) in MeCN: 515 (750).

$[L^1{}_2Fe_2(CH_3CN)_2](PF_6)_4$ (C3). A solution of $[Fe(CH_3CN)_6](PF_6)_2$ (78 mg; 0.13 mmol) in CH_3CN (5 mL) was added to a solution of L^1 (50 mg, 0.13 mmol) in CH_3CN (5 mL), upon which the mixture immediately turned ruby pink. The reaction mixture was stirred for at least 1 h. Single crystals were obtained by slow diffusion of diethyl ether into an acetonitrile solution of **C3** (76 mg, 0.05 mmol, 75 %). IR; 2385 (m), 2332 (m), 1608 (m), 1588 (m), 1490 (m), 1442 (m), 1372 (m), 1307 (m), 1246 (w), 1162 (m), 1102 (w), 1056 (w), 1020 (m), 960 (m), 906 (w), 864 (m), 824 (s), 772 (s), 742 (s), 700 (s), 640 (m). Anal Calcd for $C_{52}H_{48}N_{12}P_4F_{24}Fe_2$: C, 40.75; H, 3.16; N, 10.97. Found: C, 40.82; H, 3.20; N, 11.12. UV-vis: λ_{max}, nm (ε, M^{-1} cm^{-1}) in CH_3CN: 510 (1060), CH_3CN/CH_3OH (10/1): 578 (2433), 528 (2146).

$[(L^1)_2Cu_2](OTf)_4$ (C4). In THF (5 mL) was dissolved L^1 (25 mg; 0.066 mmol) and $Cu(OTf)_2$ (25 mg, 0.066 mmol). The solution was stirred overnight resulting in a forest green suspension, which was filtered to give the green solid **C4** (36 mg, 74 % yield). Single crystals were obtained by slow diffusion of diethyl ether into an acetonitrile solution of **C4**. IR; 3084 (w), 1639 (w), 1600 (m), 1489 (m), 1449 (m), 1314 (m), 1246 (s), 1223 (s), 1150 (s), 1110 (m), 1062 (m), 1028 (s), 964 (w), 934 (w), 878 (m), 777 (s), 690 (m), 634 (s). Anal Calcd for $C_{52}H_{42}N_{10}O_{12}S_4F_{12}Cu_2$: C, 42.13; H, 2.86; N, 9.45. Found: C, 42.20; H, 3.01; N, 9.46. UV-vis: λ_{max}, nm (ε, M^{-1} cm^{-1}) in MeCN: 596 (520). MS (LRMS$^+$, ESI; *m/z*): 1333.3 [M-OTf], 592.2 [M-2OTf], 221.2 [M-4OTf].

Hetero Bi-metallic General Reaction and Combinations Attempted

A suspension of metal salt 1 (2 eq.) in THF or CH_3CN (3 mL) was added to a solution of L^1 (25 mg, 0.066 mmol) in THF or CH_3CN (5 mL). The reaction mixture was stirred for overnight to allow formation of initial dimeric complex. Solid metal salt 2 (1 eq.) was added to reaction mixture. An immediate colour change was usually observed.

Metal Salt 1	Metal Salt 2	Colour 1	Colour 2
$Ni(OTf)_2$	$Cu(OTf)_2$	Orange	Military Green
$CoCl_2$	$Cu(OTf)_2$	Blue	Green
$CoCl_2$	$NiCl_2$	Blue	Blue
$Fe(OTf)_2$	$Cu(OTf)_2$	Navy/Pink Suspension	Green
$Fe(OTf)_2$	$Ni(OTf)_2$	Navy/Pink Suspension	Navy/Pink Suspension

2.9 References

(50) Chirik, P. J. *Inorg. Chem.* **2011**, *50*, 9737.

(51) Praneeth, V. K. K.; Ringenberg, M. R.; Ward, T. R. *Angew. Chem. Int. Ed.* **2012**, *51*, 10228.

(52) van der Vlugt, J. I. *Eur. J. Inorg. Chem.***2012**, *2012*, 363.

(53) Kaim, W.; Schwederski, B. *Coord. Chem. Rev.* **2010**, *254*, 1580.

(54) Lyaskovskyy, V.; de Bruin, B. *ACS Catalysis* **2012**, *2*, 270.

(55) Sproules, S.; Wieghardt, K. *Coord. Chem. Rev.* **2011**, *255*, 837.

(56) Kaim, W. *Eur. J. Inorg. Chem.* **2012**, 343.

(57) Hindson, K.; de Bruin, B. *Eur. J. Inorg. Chem.* **2012**, 340.

(58) Haneline, M.; Heyduk, A. F. *J. Am. Chem. Soc.* **2006**, *128*, 8410.

(59) Sylvester, K. T.; Chirik, P. J. *J. Am. Chem. Soc.* **2009**, *131*, 9772.

(60) Tondreau, A. M.; Milsmann, C.; Patrick, A. D.; Hoyt, H. M.; Lobkovsky, E.; Wieghardt, K.; Chirik, P. J. *J. Am. Chem. Soc.* **2010**, *132*, 15046.

(61) Kraft, S. J.; Williams, U. J.; Daly, S. R.; Schelter, E. J.; Kozimor, S. A.; Boland, K. S.; Kikkawa, J. M.; Forrest, W. P.; Christensen, C. N.; Schwarz, D. E.; Fanwick, P. E.; Clark, D. L.; Conradson, S. D.; Bart, S. C. *Inorg. Chem.* **2011**, *50*, 9838.

(62) Ouch, K.; Mashuta, M. S.; Grapperhaus, C. A. *Inorg. Chem.* **2011**, *50*, 9904.

(63) Nguyen, A. I.; Zarkesh, R. A.; Lacy, D. C.; Thorson, M. K.; Heyduk, A. F. *Chem. Sci.* **2011**, *2*, 166.

(64) Jørgensen, C. K. *Coord. Chem. Rev.* **1966**, *1*, 164.

(65) Chaudhuri, P.; Verani, C. N.; Bill, E.; Bothe, E.; Weyhermüller, T.; Wieghardt, K. *J. Am. Chem. Soc.* **2001**, *123*, 2213.

(66) Szilagyi, R. K.; Lim, B. S.; Glaser, T.; Holm, R. H.; Hedman, B.; Hodgson, K. O.; Solomon, E. I. *J. Am. Chem. Soc.* **2003**, *125*, 9158.

(67) Holm, R. H.; Balch, A. L.; Davison, A.; Maki, A. H.; Berry, T. E. *J. Am. Chem. Soc.* **1967**, *89*, 2866.

(68) Bouwkamp, M. W.; Bowman, A. C.; Lobkovsky, E.; Chirik, P. J. *J. Am. Chem. Soc.* **2006**, *128*, 13340.

(69) Tondreau, A. M.; Atienza, C. C. H.; Weller, K. J.; Nye, S. A.; Lewis, K. M.; Delis, J. G. P.; Chirik, P. J. *Science* **2012,** *335*, 567.

(70) Bart, S. C.; Chłopek, K.; Bill, E.; Bouwkamp, M. W.; Lobkovsky, E.; Neese, F.; Wieghardt, K.; Chirik, P. J. *J. Am. Chem. Soc.* **2006**, *128*, 13901.

(71) Tondreau, A. M.; Atienza, C. C. H.; Weller, K. J.; Nye, S. A.; Lewis, K. M.; Delis, J. G. P.; Chirik, P. J. *Science* **2012**, *335*, 567.

(72) Kaim, W. *Inorg. Chem.* **2011**, *50*, 9752.

(73) Nawn, G.; Waldie, K. M.; Oakley, S. R.; Peters, B. D.; Mandel, D.; Patrick, B. O.; McDonald, R.; Hicks, R. G. *Inorg. Chem.* **2011**, *50*, 9826.

(74) Arumugam, K.; Shaw, M. C.; Chandrasekaran, P.; Villagran, D.; Gray, T. G.; Mague, J. T.; Donahue, J. P. *Inorg. Chem.* **2009**, *48*, 10591.

(75) Hess, C. R.; Weyhermüller, T.; Bill, E.; Wieghardt, T. *Angew. Chem. Int. Ed.* **2009**, *48*, 3703.

(76) Szigethy, G.; Heyduk, A. F. *Inorg. Chem.* **2011**, *50*, 125.

(77) Zarkesh, R. A.; Ziller, J. W.; Heyduk, A. F. *Angew. Chem. Int. Ed.* **2008**, *47*, 4715.

(78) E. Wong, J. J., M. Grau, A. J. P. White, G. J. P. Britovsek *Catal. Sci. Technol.* **2013**, 1116.

(79) A. K. Patra, M. M. O., P. K. Mascharak *Inorg. Chem.* **2002**, *41*, 5403.

(80) F. Li, M. W., C. Ma, A. Gao, H. Chen, L. Sun *Dalton Trans.* **2006**, *20*, 2427.

(81) G. Roelfes, M. L., K. Chen, R. Y. N. Ho, A. Meetsma, S. Genseberger, R. M. Hermant, R. Hage, S. K. Mandal, V. G. Young, Jr., Y. Zang, H. Kooijman, A. L. Spek, L. Que, Jr., B. L. Feringa *Inorg. Chem.* **1999**, *38*, 1929.

(82) Hah, J.-M.; Martásek, P.; Roman, L. J.; Silverman, R. B. *J. Med. Chem.* **2003**, *46*, 1661.

(83) Lindsay, S.; Lo, S. K.; Maguire, O. R.; Bill, E.; Probert, M. R.; Sproules, S.; Hess, C. R. *Inorg. Chem.* **2013**, *52*, 898.

(84) Britovsek, G. J. P.; Gibson, V. C.; Spitzmesser, S. K.; Tellmann, K. P.; White, A. J. P.; Williams, D. J. *Dalton Trans.* **2002**, 1159.

(85) Lambert, B. J. In *Introduction to Organic Spectroscopy*; Macmillam: New York, 1987; Vol. 1.

(86) Eaton, S. S.; More, K. M.; Sawant, B. M.; Eaton, G. R. *J. Am. Chem. Soc.* **1983**, *105*, 6560.

(87) Kissinger, P. T.; Heineman, W. R. *J. Chem. Educ.* **1983**, *60*, 702.

(88) Murray, P. R.; Crawford, S.; Dawson, A.; Delf, A.; Findlay, C.; Jack, L.; McInnes, E. J. L.; Al-Musharafi, S.; Nichol, G. S.; Oswald, I.; Yellowlees, L. J. *Dalton Trans.* **2012**, *41*, 201.

(89) Foxon, S.; Xu, J.-Y.; Turba, S.; Leibold, M.; Hampel, F.; Heinemann, F. W.; Walter, O.; Würtele, C.; Holthausen, M.; Schindler, S. *Eur. J. Inorg. Chem.* **2007**, 429.

(90) Mabbott, G. A. *J. Chem. Educ.* **1983**, *60*, 697.

(91) Lu, C. C.; Bill, E.; Weyhermuller, T.; Bothe, E.; Wieghardt, K. *J. Am. Chem. Soc.* **2008**, *130*, 3181.

(92) Herber, R. H. *J. Chem. Educ.* **1965**, *42*, 180.

(93) Kirschvink, J.; Jones, D.; MacFadden, B.; Fuller, M.; Goree, W. S.; Goodman, W. L. In *Magnetite Biomineralization and Magnetoreception in Organisms*; Springer US: 1985; Vol. 5, p 103.

(94) Mataga, N. *Theoret. Chim. Acta* **1968**, *10*, 372.

(95) Foxon, Simon P.; Torres, Gemma R.; Walter, O.; Pedersen, Jens Z.; Toftlund, H.; Hüber, M.; Falk, K.; Haase, W.; Cano, J.; Lloret, F.; Julve, M.; Schindler, S. *Eur. J. Inorg. Chem.* **2004**, *2004*, 335.

(96) Schubert, E. M. *J. Chem. Educ.* **1992**, *69*, 62.

(97) Ward, A. L.; Elbaz, L.; Kerr, J. B.; Arnold, J. *Inorg. Chem.* **2012**, *51*, 4694.

(98) Börzel, H.; Comba, P.; Hagen, K. S.; Lampeka, Y. D.; Lienke, A.; Linti, G.; Merz, M.; Pritzkow, H.; Tsymbal, L. V. *Inorg. Chim. Acta* **2002**, *337*, 407.

(99) Hess, C. R.; Weyhermüller, T.; Bill, E.; Wieghardt, T. *Inorg. Chem.* **2010**, *49*, 5686.

(100) Muresan, N.; Lu, C. C.; Ghosh, M.; Peters, J. P.; Abe, M.; Henling, L. M.; Weyhermüller, T.; Bill, E.; Wieghardt, K. *Inorg. Chem.* **2008**, *47*, 4579.

(101) Braterman, P. S.; Song, J. I.; Peacock, R. D. *Inorg. Chem.* **1992**, *31*, 555.

(102) Addison, A. W.; Rao, T. N.; Reedijk, J.; Rijn, J. v.; Verschoor, G. C. *Dalton Trans.* **1984**, 1349.

(103) Fernández, I.; Ruiz, R.; Faus, J.; Julve, M.; Lloret, F.; Cano, J.; Ottenwaelder, X.; Journaux, Y.; Muñoz, M. C. *Angew. Chem. Int. Ed.* **2001**, *40*, 3039.

(104) Foxon, S. P.; Torres, G. R.; Walter, O.; Pedersen, J. Z.; Toftlund, H.; Hüber, M.; Falk, K.; Haase, W.; Cano, J.; Lloret, F.; Julve, M.; Schindler, S. *Eur. J. Inorg. Chem.* **2004**, 335.

(105) Martín, S.; Grace, I.; Bryce, M. R.; Wang, C.; Jitchati, R.; Batsanov, A. S.; Higgins, S. J.; Lambert, C. J.; Nichols, R. J. *J. Am. Chem. Soc.* **2010**, *132*, 9157.

(106) Murthy, N. N.; Mahroof-Tahir, M.; Karlin, K. D. *Inorg. Chem.* **2001**, *40*, 628.

(107) Adams, R. D.; Barnard, T. S. *Organometallics* **1998**, *17*, 2885.

(108) Golchoubian, H.; Waltz, W. L.; Quail, J. W. *Can. J. Chem.* **1999**, *77*, 37.

(109) Adams, R. D.; Barnard, T. S.; Li, Z.; Wu, W.; Yamamoto, J. *J. Am. Chem. Soc.* **1994**, *116*, 9103.

Chapter 3 – Oxidation of Hydrocarbons by Di-ferrous C2 and C3

In this chapter the di-ferrous complexes **C2** and **C3** are reviewed as C-H oxidation catalysts. The functionalisation of unactivated C-H bonds presents a real challenge to synthetic chemists. In contrast, nature has a host of metalloenzymes at its disposal able to efficiently, and selectively, catalyse oxidation under mild conditions employing molecular oxygen. Di-ferrous **C2/C3** is a dimer of the asymmetric ligand L^1. Each iron ion is held in a pentadentate configuration by the L^1 dimer and the sixth coordination site is occupied by a labile ligand; CH_3CN for **C3** and OTf^- for **C2**. The oxidative capability of **C2/3** toward hydrocarbons of varying bond strengths has been examined in the presence of a variety of common oxidants; iodosylbenzene (PhIO), peroxides (ROOH, R = ^{t}Bu or H), and O_2 (Scheme 19). Complex **C3** proved to be a succesful catalyst toward unactivated hydrocarbon substrates of C-H bond dissociation energy (BDE) $\leq$ 81 kcal mol^{-1}. Complex **C3** exhibited limitations as a catalyst, failing to oxidise cyclohexane and adamantane with C-H BDE ~ 100 kcal mol^{-1}. The use of mechanistic probes indicated metal-centred oxidation by **C3**, over radical-based mechanisms. The use of isotopically labelled substrates demonstrated that **C3** oxidised substrates *via* a hydrogen abstraction mechanism.

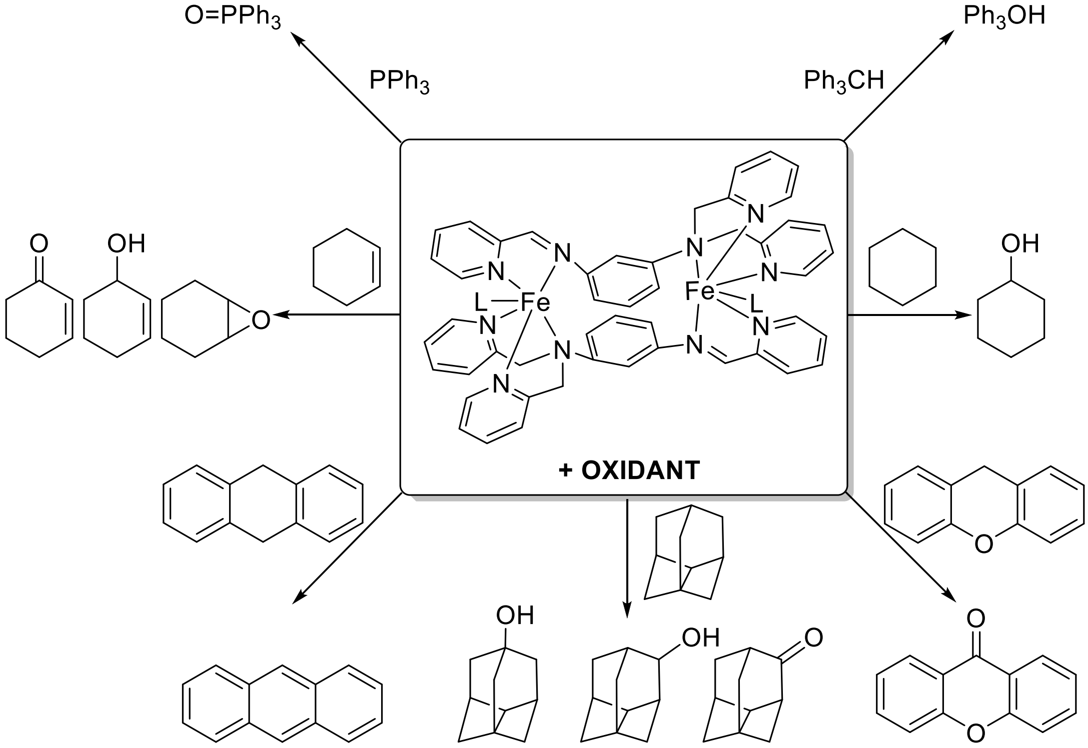

Scheme 19. Oxidation Reactions Examined in this Chapter. Where L = CH_3CN for C3 or L = OTf^- for C2. Oxidant = $PhIO/H_2O_2/^tBuOOH/O_2$.

3.1 Introduction

Efficient, selective and low cost hydrocarbon oxidation is fundamental to industry; alkanes, both abundant and inexpensive, are an attractive feedstock for more valuable oxygenated compounds including alcohols, epoxides and aldehydes.[110] However, achieving these transformations by environmentally sustainable and cost effective means is a challenge for synthetic chemists. In contrast, in nature there is a myriad of metalloenzymes able to efficiently and selectively catalyse oxidations, such as the hydroxylation of unactivated C-H bonds and epoxidation of C=C bonds, at mild temperatures and pressures.[111-113] The active sites of metalloenzymes are comprised of a single, or multiple, transition metal(s). The redox properties of the transition metal are vital to the success of metalloenzyme activity. The transition metal can cycle between numerous oxidation states throughout the catalytic cycle (Scheme 20). Iron ions, for example, commonly exist in two stable oxidation states, 2+ and 3+, but have been characterised in the 4+ and 5+ oxidation states during catalytic cycles of oxidising metalloenzymes (Scheme 21). The iron ions act as a reductant, supplying the electrons required to activate dioxygen by adopting high valence states.

While metalloenzymes are excellent catalysts in biological systems they cannot be employed in a large scale industrial setting due to the sensitive nature of the protein environment. Therefore, they cannot be the means by which industry produces valuable oxygenated products from low cost feedstock. Studying how metalloenzymes operate, although providing valuable information in its own right, can be used as a tool to guide research efforts toward developing successful synthetic catalysts. Bio-mimetic complexes, which replicate the active sites of metalloenzymes exactly, do not exhibit the same reactivity as their enzyme counterparts. The metalloenzymes are successful due to contributions from both the active site and the protein environment. Bio-inspired complexes, which take key features from the metalloenzymes active sites but change other structural features, have shown greater success. Structural fine-tuning of bio-inspired catalysts can expand the substrate scope and increase reactivity or selectivity toward a specific substrate.

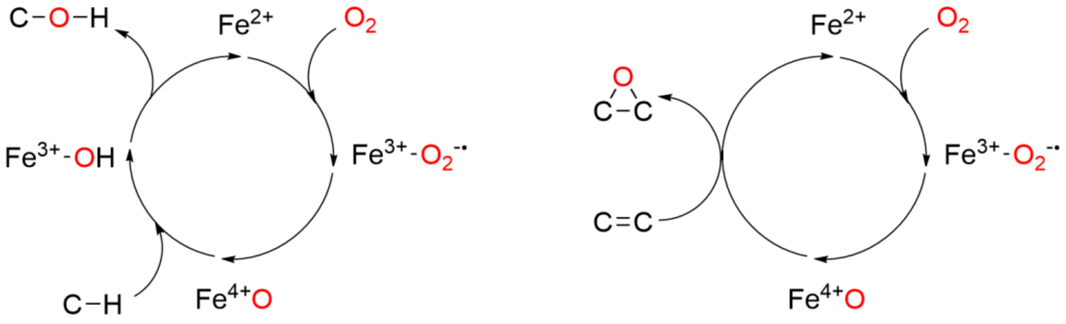

Scheme 20. General Scheme for C-H and C=C Oxidation by Iron Metalloenzymes.

3.1.1 The Study of Biological Precedents to Aid Development of Bio-inspired Oxidation Catalysts

Iron metalloenzymes are particularly prevalent in the performance of biological oxidative transformations and can be classified into three groups by structure: heme, mono-nuclear non-heme and di-nuclear non-heme motifs.[114, 115] Extensive studies of oxidative iron metalloenzymes, across all three classifications, have revealed the active species to be high-valent Fe-oxygen forms.[112, 116] The most extensively studied oxygen-activating family of metalloenzymes are the cytochromes P450 (CP450).[117-119] CP450s exist within the heme classification containing an iron porphyrin cofactor within the protein backbone. The porphyrin unit is tetradentate with four planar nitrogen donors surrounding the ferrous ion **(32)** (Scheme 21). Two facially opposing labile sites complete the coordination sphere of the ferrous ion. CP450s are exceptionally versatile catalysts facilitating the hydroxylation of aliphatic C-H bonds and the epoxidation of C=C bonds with high selectivity and efficiency. Additionally CP450s facilitate *N*-, *S*-, *O*-dealkylations, *N*-, *S*-oxidations and dehalogenation reactions.[117, 119] Dioxygen is initially activated by CP450 *via* coordination to the ferrous centre resulting in the formation of a ferric-superoxo species (Scheme 21). The superoxo is reduced to a peroxo species, upon addition of a proton, which undergoes O-O bond cleavage to generate a formally Fe^{V}oxo species that is the active species which carries out two-electron oxidations. Although formally an Fe^{V} the porphyrin unit donates an electron to support the iron ion so the formally Fe^{V}oxo is generally described as an Fe^{IV}=O-(oxidised porphyrin radical = $\mathbf{P}^{\cdot+}$) species.[120] It is because of the ability to delocalise electrons that the otherwise difficult to reach, but competent, Fe^{V} species can be accessed.

The methane monooxygenase (MMO) family is another extensively studied oxidative metalloenzyme. MMO exists within the di-nuclear non-heme classification. The MMO active site consists of two ferrous ions, each in a tetradentate configuration bridged by a carboxylate unit **(10)**. MMO is a versatile catalyst renowned for its ability to oxidise strong methane bonds (C-H BDE= 105 kcal mol^{-1}), producing methanol, by activating dioxygen, a feat unmatched by synthetic systems.[114, 121, 122] Dioxygen is initially activated by MMO *via* coordination to one of the ferrous centres resulting in the formation of an $Fe^{II}\cdots Fe^{III}$-superoxo species (Scheme 21). Extensive studies of MMO have identified two active interchangeable bridged species; (μ-1,2-peroxo)$Fe^{III}Fe^{III}$ species (commonly referred to as **P**) and $(\mu\text{-O})_2Fe^{IV}Fe^{IV}$ species (commonly referred to as **Q**).[114, 123, 124]

The Rieske dioxygenases exist in the third classification of iron metalloenzymes; mono-nuclear non-heme. Rieske dioxygenases are the only iron metalloenzymes among all three classes that can accomplish enantioselective *cis*-dihydroxylation of arenes, a transformation not observed in synthetic organic chemistry.[125-127] Rieske dioxygenases are versatile and in addition to *cis*-dihydroxylation can catalyse benzylic hydroxylation, desaturation, *O*-, *N*-dealkylation and *S*-oxidation.[127] Dioxygen is initially activated by the Rieske dioxygenases *via* coordination to the ferrous centre resulting in the formation of a ferric-superoxo species (Scheme 21). The superoxo species reduces to the peroxo species which is postulated to isomerise to an Fe^{V}=O(OH) active species **(33)**.[128, 129] The high valence Fe^{V} state is hard to achieve synthetically. The $Fe^{IV}=O$ species has demonstrated high activity toward a range of substrates performing a variety of transformations, with the exception of *cis*-diol oxidation of alkenes. *Cis*-diol formation from alkenes has been achieved by the more active $Fe^{V}=O$ species so differences in reactivity can indicate which species is present.

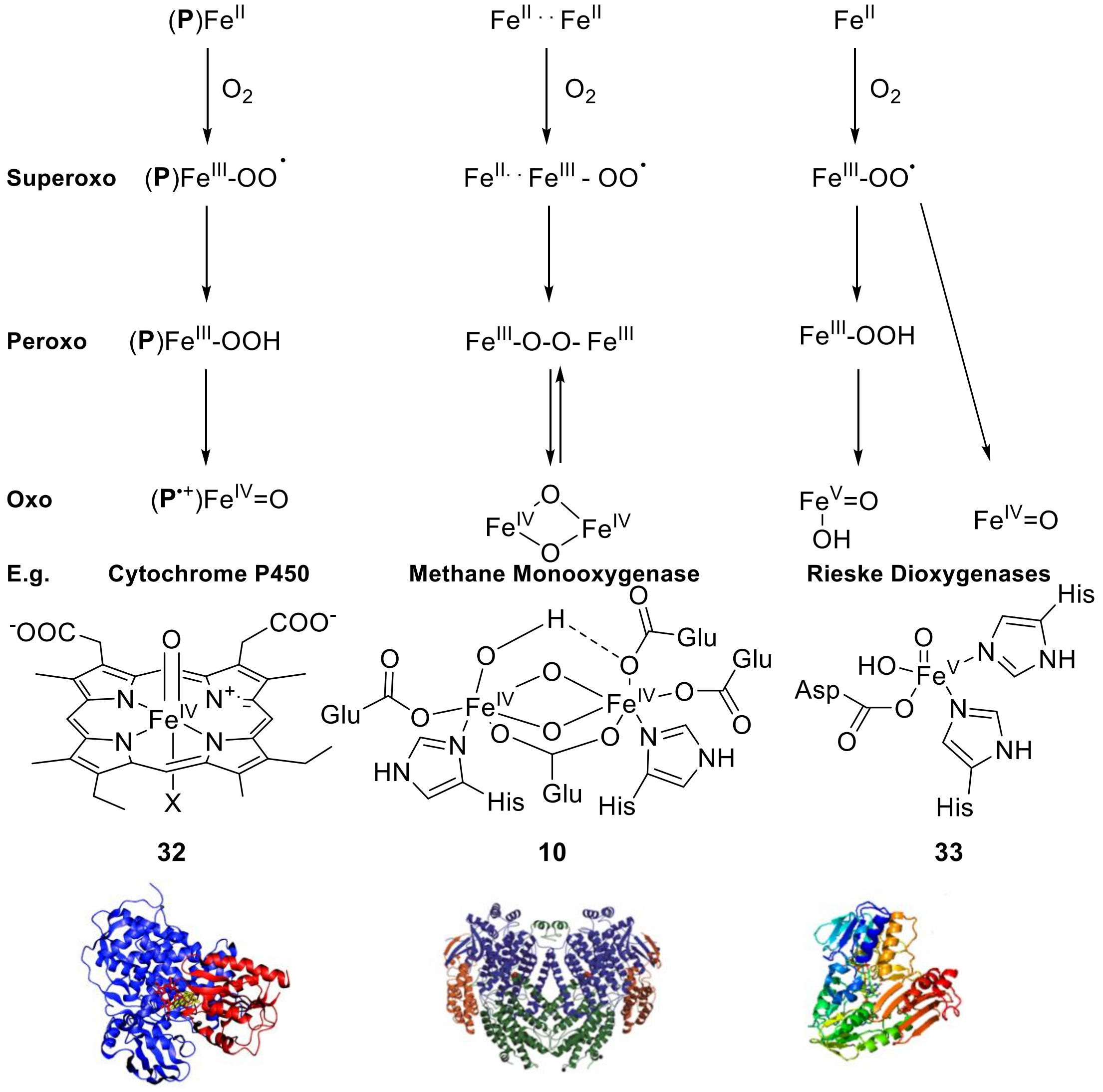

Scheme 21. High Valence Iron Oxygen Species Generated by Notable Metalloenzymes.[112]

From the study of the aforementioned notable metalloenzymes key structural features can be identified. The main structural features found across each category of iron metalloenzyme is a ferrous resting state ion, required to facilitate the two electron reduction of dioxygen during the catalytic cycle. A typically tetradentate nitrogen and/or oxygen rich coordination environment, which supports the Fe-oxygen intermediates formed, and one or two labile ligands to allow dioxygen binding. These features can be applied in the design of bio-inspired complexes.

3.1.2 The Study of Benchmark Bio-inspired Synthetic Systems and Structural Contributions to Reactivity

Catalytic C-H hydroxylation and C=C epoxidation has been successfully achieved by numerous bio-inspired non-heme complexes.[130-132] The diverse array of synthetic bio-inspired complexes has allowed for evaluation of structure contributions to reactivity.[133, 134] The structural support around the ferrous ion dictates the type of Fe-oxygen species formed. Studies have revealed that the metal electronic configuration and coordination environment have significant effects upon the reactivity of the species.[135-137] Identifying correlations between reactivity and structure allows for systematic design of bio-inspired catalysts. Investigating novel structures and looking at the contribution to reactivity allows for the advancement of bio-inspired catalysts.

The vast majority of synthetic bio-inspired iron catalysts for C-H oxidation consist of a mono-nuclear ferrous centre and a tetradentate *N*-rich ligand scaffold.[116, 138] For these complexes the six coordinate ferrous centre has two vacant sites occupied by labile ligands such as CH_3CN, OTf^- and H_2O. The two most extensively studied families of tetradentate ligands for C-H oxidation are the tripodal TPA (tris(2-pyridylmethyl)amine) **(34)** and linear BPMEN (N,N'-dimethyl-N,N'-bis(2-pyridylmethyl)ethylene-1,2-diamine) **(35)** (Scheme 22).[132, 139, 140] Mechanistic probes confirm metal-centred oxidation by these ferrous complexes, supported by the isolation and characterisation of high-valent $Fe^{IV}=O$ species, the active species identified for many metalloenzymes.[141] Ferrous complexes containing TPA and BPMEN ligands have displayed high hydrocarbon oxidation efficiency setting the benchmark for bio-inspired complexes. **C2/3** structurally compares to these complexes in the *N*-rich coordination environment enveloping the ferrous ion, with the presence of both heterocyclic pyridine and aliphatic amine *N*-donors. The main structural differences between the two benchmark ferrous complexes and **C2/3** is that **C2/3** has two iron ions each held in a pentadentate configuration by L^1 and with only one labile ligand. The highest reactivity for tetradentate complexes has been observed when the two vacant sites are in a *cis* disposition.[142] The reactivity dependence on labile ligand disposition demonstrates both sites have a role to play in hydrocarbon oxidation, therefore reducing to only one labile site is expected to have an effect on reactivity.

Iron complexes containing pentadentate ligands have been explored less than their tetradentate counterparts toward hydrocarbon oxidation catalysis as they are found fewer in biological systems. Complexes with pentadentate ligands have been examined as structural and functional models of Fe-bleomycin, which is one example found in nature. Fe-bleomycin is an anti-tumour antibiotic.[143-146] One pentadentate ligand examined toward C-H oxidation is N4Py (N4Py = N,N-bis(2-pyridylmethyl)-N-(bis-2-pyridylmethyl)amine) (Scheme 22).[81] $[Fe(N4Py)L]^{2+}$ has demonstrated reasonable reactivity toward hydrocarbon oxidation reactions **(36)**. Mechanistic probes confirm metal-centred oxidation, supported by the isolation and characterisation of high-valent $Fe^{IV}=O$ species. **C2/3** structurally compares closely to **36** in the *N*-rich pentadentate coordination environment, the presence of both heterocyclic pyridine and aliphatic amine *N*-donors and the existence of one labile ligand in the ferrous coordination sphere. The main structural difference between **C2/3** and **36** is that **C2/3** has two iron sites. Comparison of reactivity to **36** will be interesting given the similarity in ferrous environments and dissimilarity in reactivity must then arise from the presence of the second iron site.

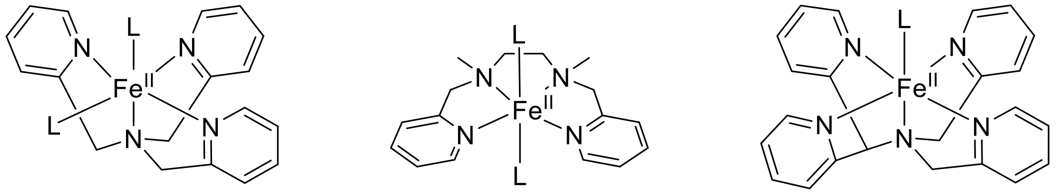

[Fe(TPA)(L)$_2$]$^{2+}$ [Fe(BPMEN)(L)$_2$]$^{2+}$ [Fe(N4Py)L]$^{2+}$

34 **35** **36**

Scheme 22. Benchmark Bio-inspired Ferrous Complexes.

The development of functional di-nuclear non-heme bio-inspired complexes has proven more challenging than mono-nuclear systems. Synergistic effects and exchange interactions between the two metal centres are additional factors to be manipulated and cause increased complication. Biological systems activate dioxygen by bridging oxygen, in peroxo, oxo or hydroxo forms, between the two iron ions. The inter-nuclear iron distance and electronic configuration dictates the likelihood of the formation of a bridging Fe-oxygen species. Attempts to synthetically replicate the (μ-O)$_2$Fe^{IV}Fe^{IV} active species (**Q**) of MMO have proven difficult due to instability at room temperature, making trapping and characterisation problematic. One of the few examples of a characterised synthetic (μ-O)$_2$Fe^{IV}Fe^{IV} species has been established when supported by a dimer of modified TPA ligands.[147-150] The diamond core model complex exhibits C-H oxidation reactivity 2-3 orders of magnitude lower than that of the related mono-nuclear Fe^{IV}=O complex raising interesting questions as to precisely what mechanisms may be involved in C-H oxidation by high-valent enzymatic vs. synthetic bridging species.

Complexes **C2** and **C3** offer two adjacent iron sites but precludes intramolecular bridging due to the large Fe···Fe distances; > 7 Å.[83] The **C2/3** complexes thus provide a unique structural disparity to both mono-nuclear and di-nuclear non-heme enzyme active sites and bio-inspired complexes. Diimine groups offer additional redox sites surrounding each ferrous centre which may play a notable role in reactivity of **C2/3.** The oxidative reactivity of **C2/3** was investigated in comparison to the benchmark ferrous complexes and similar pentadentate complex. Studies endeavoured to unveil mechanistic details regarding the behaviour of the multiple redox sites within this unique structure and how the unique structure contributes to reactivity.

3.2 Oxidation of Cyclohexene

Initial hydrocarbon oxidation studies were carried out using cyclohexene (**37**) as the substrate. Cyclohexene oxidation allows for an assessment of two oxidative pathways: allylic C-H hydroxylation and C=C epoxidation, leading to the formation of 2-cyclohexen-1-ol **(38)** and cyclohexene oxide **(39)**, respectively.[135] Cyclohexene oxidation has been studied by a wide range of related ferrous complexes, including the benchmark complexes outlined in the introduction of this chapter, therefore there is a wealth of data for reactivity and selectivity comparison.[132] A range of common oxidants were employed during these studies; PhIO, H_2O_2, ^tBuOOH and O_2. Information accrued from literature studies suggest each oxidant can react with **C2** and **C3** differently to form different active species, which may exhibit different reactivities toward cyclohexene oxidation. Final reaction mixtures were analysed by GC-MS (Gas Chromatography Mass Spectrometry). Reaction products were identified by comparison to GC retention times and mass spectra of commercial samples. Products were quantified using a single point internal standard method, with the addition of fluorene as the standard which did not interfere or overlap with any of the reaction products. Reactions were analysed after a 30 min period. The analysis of control reactions of each oxidant (PhIO, H_2O_2, ^tBuOOH and O_2) with cyclohexene verified no cyclohexene oxidation had occured after a 30 min reaction period in both air and Ar atmospheres. After a 45 min period, analysis of the control reaction of PhIO with cyclohexene, under an aerated atmosphere, revealed the formation of cyclohexene oxidised products. The reaction time was therefore capped to 30 min to allow comparisons to be drawn between oxidant and atmospheric environment with no risk of unwanted oxidation.

Under all conditions examined, cyclohexene oxidation by **C2** and **C3** yielded a mixture of epoxide and allylic oxidation products; cyclohexene oxide **(39)**, 2-cyclohexen-1-ol **(38)** and 2-cyclohexen-1-one **(40)**. The presence of both cyclohexene oxide and 2-cyclohexen-1-ol highlights the competing reaction pathways and demonstrates the ability of **C2** and **C3** to facilitate both C=C epoxidation and C-H hydroxylation reactions. The results of cyclohexene oxidation by **C2** and **C3** are displayed in Table 1. The data in Table 1 and possible reaction pathways of each oxidant are discussed herein.

Table 1. Catalytic Oxidation of Cyclohexene by C2/3 at 298 K as Quantified by GC-MS.[a]

Entry	Cat.	Oxidant	Atm.	Mol Epoxide[b] (+/-)[c]	Mol En-ol[b] (+/-)[c]	Mol En-one[b] (+/-)[c]	TON[d]	TOF[e] (min^{-1})
1	**C2**	PhIO	Air	2.15×10^{-6}	2.18×10^{-5}	1.01×10^{-5}	10.5	0.35
				(1.73×10^{-7})	(4.11×10^{-7})	(9.94×10^{-7})		
2	**C3**	PhIO	Air	2.74×10^{-6}	2.21×10^{-5}	2.00×10^{-5}	13.8	0.46

				(3.61×10^{-7})	(7.32×10^{-7})	(9.09×10^{-7})		
3	**C3**	PhIO	Ar	3.82×10^{-6}	1.47×10^{-5}	4.33×10^{-6}	7.0	0.23
				(5.34×10^{-7})	(3.93×10^{-7})	(3.85×10^{-7})		
4	**C2**	H_2O_2	Air	5.98×10^{-8}	6.05×10^{-6}	3.44×10^{-6}	2.9	0.10
				(1.12×10^{-8})	(7.64×10^{-7})	(6.45×10^{-7})		
5	**C3**	H_2O_2	Air	4.77×10^{-7}	7.67×10^{-6}	5.47×10^{-6}	4.2	0.14
				(5.44×10^{-8})	(3.04×10^{-7})	(9.68×10^{-7})		
6	**C3**	H_2O_2	Ar	8.27×10^{-7}	2.70×10^{-5}	2.42×10^{-6}	9.3	0.31
				(2.88×10^{-8})	(5.00×10^{-7})	(2.14×10^{-7})		
7	**C2**	^{t}BuOOH	Air	1.62×10^{-6}	5.09×10^{-5}	1.91×10^{-5}	22.0	0.73
				(1.39×10^{-7})	(5.56×10^{-6})	(3.37×10^{-6})		
8	**C3**	^{t}BuOOH	Air	3.60×10^{-6}	5.94×10^{-5}	4.41×10^{-5}	32.8	1.09
				(1.75×10^{-7})	(6.21×10^{-6})	(2.26×10^{-6})		
9	**C3**	^{t}BuOOH	Ar	8.59×10^{-7}	6.08×10^{-5}	5.03×10^{-6}	20.5	0.68
				(2.95×10^{-8})	(3.16×10^{-6})	(1.85×10^{-7})		
10	**C2**	O_2	Air	1.15×10^{-7}	4.94×10^{-6}	1.05×10^{-6}	1.9	0.06
				(4.10×10^{-8})	(8.78×10^{-7})	(2.12×10^{-7})		
11	**C3**	O_2	Air	2.55×10^{-7}	5.34×10^{-6}	2.54×10^{-6}	2.5	0.08
				(1.08×10^{-8})	(3.18×10^{-7})	(1.70×10^{-7})		

[a] Cat./Oxidant/Cyclohexene = 1:10:300. Mol Cat. = 3.24×10^{-6}. Solvent = CH_3CN. [b] Epoxide Denotes Cyclohexene Oxide; En-ol, 2-Cyclohexen-1-ol; En-one, 2-Cyclohexen-1-one. [c] Error = One Standard Deviation of Three Runs. [d] Turnover Number (TON) = Total Moles of Oxidised Products / Moles of Catalyst. [e] Turnover Frequency (TOF) min^{-1} = (Total Moles of Oxidised Product / Moles of Catalyst) / 30.

3.2.1 Reactivity of the C2/3/PhIO system

The Fe^{IV}=O species, proposed as the active species for hydrocarbon oxidation in both metalloenzyme and bio-inspired systems, has been successfully isolated among related ferrous complexes upon reaction with PhIO. The Fe^{IV}=O species has demonstrated reactivity toward both C=C epoxidation and C-H hydroxylation. After the formation of the Fe^{IV}=O species two reaction pathways can ensue in the presence of cyclohexene, identified by literature studies (Scheme 23).[141] The first reaction pathway yields cyclohexene oxide (**39**) as the result of direct oxygen atom transfer (OAT). The second reaction pathway is available owing to the ability of the Fe^{IV}=O species to perform hydrogen abstraction (HAB). An allylic hydrogen of cyclohexene (bond dissociation energy, BDE = 80 kcal mol^{-1}) is abstracted resulting in the formation of an Fe^{III}-OH species and a cyclohexene organic radial (**41**). HAB is generally followed by oxygen rebound from the Fe^{III}-OH species to the cyclohexene radical (**41**) forming the allylic product 2-cyclohexen-1-ol (**38**) and recycling the ferrous complex.

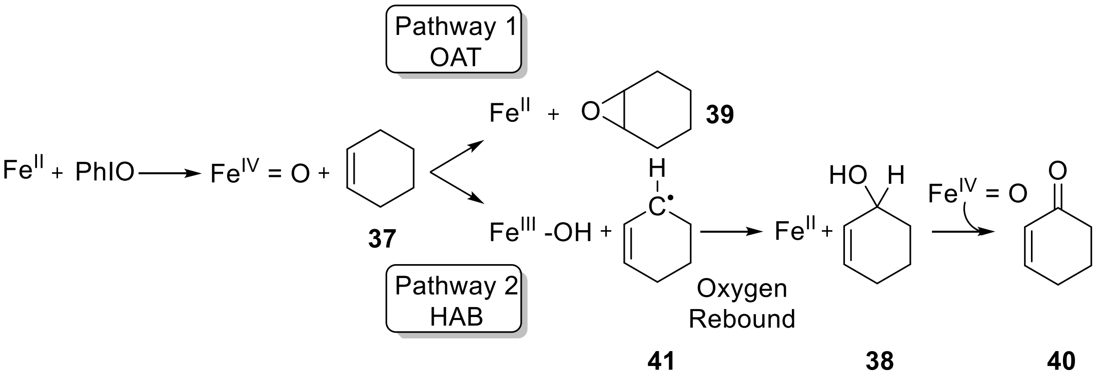

Scheme 23. Common Cyclohexene Oxidation Pathways, and the Resultant Products, Obtained in the Reaction of Various Non-Heme Iron Complexes with PhIO.

When cyclohexene oxidation is executed in the presence of dioxygen an additional reaction pathway is accessible. If mono-radical **41** is long lived, due to a slow oxygen rebound step, dioxygen can alternatively trap the radical forming the peroxide intermediate **42** and results in the formation of equimolar amounts of 2-cyclohexen-1-ol **(38)** and 2-cyclohexen-1-one **(40)**, *via* a process known as Russell-type termination (Scheme 24).[141] The occurrence of Russell-type termination can lead to high product yields exceeding the amount of oxidant employed as dioxygen serves as a secondary oxygen source. Russell-type termination leads to low selectivity of allylic oxidation products.

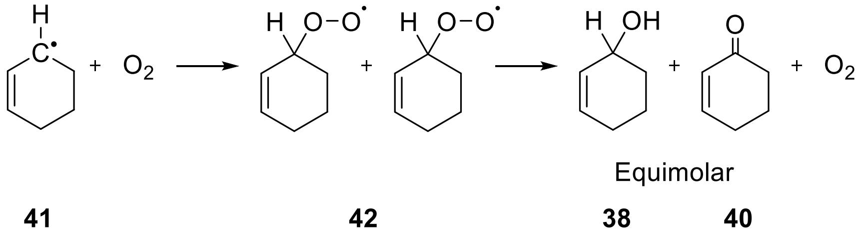

Scheme 24. Russell-type Termination Reaction of Cyclohexene in the Presence of Oxygen.

When cyclohexene oxidation was executed employing the **C2**/PhIO and **C3**/PhIO systems in the presence of dioxygen (reactions in a capped vessel to ensure no evaporation, but vessel filled with air) the dominant product was 2-cyclohexen-1-ol (**38**) alongside a considerable amount of 2-cyclohexen-1-one (**40**); approx. 2 : 1 ratio of 2-cyclohexen-1-ol to 2-cyclohexen-1-one for **C2**/PhIO and approx. 1 : 1 ratio of 2-cyclohexen-1-ol to 2-cyclohexen-1-one for **C3**/PhIO (Table 1, entry 1 and 2). Cyclohexene oxide (**39**) made up only 6 % of the total oxidised products for both **C2**/PhIO and **C3**/PhIO systems suggesting the OAT pathway is least favourable. The low selectivity between 2-cyclohexen-1-ol and 2-cyclohexen-1-one formation can be indicative of the aforementioned

Russell-type termination over the HAB pathway. Both **C2** and **C3** performed comparatively under these conditions.

Reactions were repeated under an Ar atmosphere, thereby eliminating the Russell-type pathway, to investigate if/what proportion of products are formed from a Russell-type termination pathway (reactions in an Ar filled glovebox in a capped vessel to ensure no evaporation, but vessel filled with Ar; all solvents and reagents were thoroughly degassed *via* freeze pump method). It should be noted that further studies under an Ar atmosphere were carried out with **C3** only, rapid exchange of the coordinated OTf anions with acetonitrile solvent molecules, as determined from ^{19}F NMR, adds further complexity to the reaction mechanisms with **C2**.[83] It can be assumed that **C2** and **C3** would provide comparable results in an Ar atmosphere as was found from the reactions in air. The removal of dioxygen from the reaction resulted in a large reduction in the amount of 2-cyclohexen-1-one (**40**) formed, by approx. 4/5, and reduced the amount of 2-cyclohexen-1-ol (**38**) formed by approx. 1/3. The change in product formation increased product selectivity of 2-cyclohexen-1-ol to 2-cyclohexen-1-one from 1 : 1 to 7 : 2 (Table 1, entry 3), suggesting the Russell-type termination pathway is active when dioxygen is present during cyclohexene oxidation. The occurrence of Russell-type reactions infer the oxygen rebound step is slow compared to the rate of dioxygen trapping.[141]

Performing the reactions under an Ar atmosphere did not completely diminish the formation of 2-cyclohexen-1-one (**40**). 2-Cyclohexen-1-one (**40**) formation is suggested as the result of over-oxidation of 2-cyclohexen-1-ol (**38**) in literature (Scheme 23). We probed this possibility by employing 2-cyclohexen-1-ol as the starting substrate using the **C3**/PhIO system. 2-Cyclohexen-1-ol was indeed oxidised to 2-cyclohexen-1-one, under analogous reaction conditions, with a turnover number (TON) of 1.1 within a 30 min reaction period, which is in good agreement with the amount of 2-cyclohexen-1-one formed when cyclohexene is the starting substrate, TON of 1.3. Therefore we can affirm that 2-cyclohexen-1-one formed under an Ar atmosphere is the result of 2-cyclohexen-1-ol over-oxidation (Scheme 23). The **C3**/PhIO system, under Ar, kinetically favours the hydrogen abstraction pathway over direct OAT with the dominating product being 2-cyclohexen-1-ol; ratio of allylic products/epoxide of 5.0. In comparison to the other **C3**/oxidant systems under Ar, **C3**/PhIO produced the largest proportion of cyclohexene oxide (**39**) despite it being a relatively low 17 % of the total oxidised products. The amount of cyclohexene oxide formed is relatively consistent under both air and Ar atmospheres suggesting the presence of air does not affect the OAT pathway.

3.2.2 Reactivity of the C3/H_2O_2 System

The initial species generated by the **C2/3**/H_2O_2 catalyst system is likely an Fe^{III}-OOH, as has been determined with related ferrous complexes upon addition of H_2O_2.[151] In literature studies the Fe^{III}-OOH species has demonstrated low oxidation reactivity toward unactivated hydrocarbons.[151] However, the Fe^{III}-OOH species can convert, *via* several alternative pathways, to other species more active toward hydrocarbon oxidation. The first is *via* O-O bond cleavage to form an Fe^{IV}=O species

(Scheme 25).[141] The $Fe^{IV}=O$ species will follow the reaction pathways as described for the **C2/3**/PhIO system. The Fe^{III}-OOH species can alternatively decompose to a ferrous ion and a hydroperoxide radical (Scheme 25). The hydroperoxide radical can in turn convert to the highly reactive hydroxide radical, which can attack cyclohexene directly to form the allylic 2-cyclohexen-1-ol (**38**) product. 2-Cyclohexen-1-ol is still susceptible to over oxidation. Russell type termination is again accessible under an aerated atmosphere as mono-radical **41** is formed after HAB and upon initial attack of cyclohexene by OH radicals.

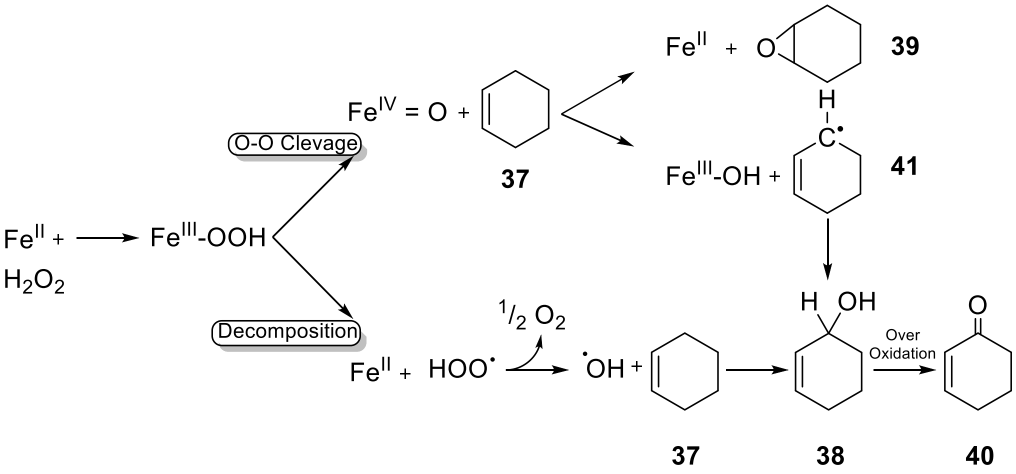

Scheme 25. Common Cyclohexene Oxidation Pathways, and the Resultant Products, Obtained in the Reaction of Various Non-Heme Iron Complexes with H_2O_2.

Fenton type chemistry must also be considered for the **C2/3**/H_2O_2 system (Scheme 26). Fenton ascertained the reaction of iron salts (Fe^{2+}, Fe^{3+}) with H_2O_2 and alkanes produces equimolar amounts of alcohols and ketones.[152, 153] In Fenton type oxidation the ferrous species directly decomposes H_2O_2 to a hydroxide radical, as opposed to the formation of an Fe^{III}-OOH species.[152] Fenton reactions have poor yields and poor selectivity due to the difficulty in controlling radical reactions.

$$Fe^{II} + HO{-}OH \longrightarrow Fe^{III} + {}^{\bullet}OH + {}^{-}OH$$

Scheme 26. Fenton Type Decomposition of H_2O_2.

When cyclohexene oxidation was executed employing the **C2**/H_2O_2 and **C3**/H_2O_2 systems in the presence of dioxygen reactivity toward cyclohexene oxidation was poor displaying the lowest product formation of the **C2/3**/oxidant systems with a notable lack of cyclohexene oxide formation (Table 1, entry 4 and 5). One possibility for the low reactivity could be problematic independent disproportionation of H_2O_2 to H_2O and O_2, reported as a common issue in literature.[150] Precautions were taken in attempt to prevent disproportionation; the H_2O_2 was added as a CH_3CN diluted solution (0.1 mL, 0.3 M) over a period of 25 min to avoid build-up of H_2O_2, but it cannot be guaranteed these precautions prevented all disproportionation. If disproportionation is occurring a much smaller % of H_2O_2 is available for use within the system than thought. Another consideration for the low reactivity is the possibility of intramolecular oxidation of the L^1 ligand scaffold by H_2O_2. The oxidation of α-diimine moieties, in ligand scaffolds similar to L^1, to corresponding amides and/or hydroxylation of aromatic groups have been observed upon exposure of metal complexes to H_2O_2 in literature .[154-156] Oxidative modification of the L^1 scaffold of **C2/3** could lead to a change in reactivity as the mechanistic details of oxidation by **C2/3** are not yet known and the L^1 scaffold may play a key role. Additionally, alteration of the scaffold could consume the H_2O_2 from the system leaving less to partake in cyclohexene oxidation. To investigate possible intramolecular oxidation of **C2/3**, H_2O_2 was added as a CH_3CN solution (0.1 mL, 0.3 M) to a solution of **C3** (1.1 mL, 2.95 mM in CH_3CN) over 25 mins under an Ar atmosphere. The mixture was then evaporated to dryness and the subsequent solid was analysed by infrared spectroscopy (IR) to determine whether modifications to the L^1 backbone had occurred. The IR spectrum was collected using a diamond ATR (Attenuated Total Reflection) accessory (golden gate) for solids; no sample preparation was required. The lack of any discernible features in the region associated with C=O (1650 – 1760 cm^{-1}) or OH (3200 – 3600 cm^{-1}) stretches suggest the L^1 ligand scaffold remains intact and thus intramolecular oxidation is not the cause of the low reactivity.

When cyclohexene oxidation was executed employing the **C2**/H_2O_2 and **C3**/H_2O_2 systems in the presence of dioxygen, the dominant product was 2-cyclohexen-1-ol (**38**) alongside a considerable amount of 2-cyclohexen-1-one (**40**); approx. 2 : 1 ratio of 2-cyclohexen-1-ol to 2-cyclohexen-1-one for **C2**/H_2O_2 and approx. 3 : 2 ratio of 2-cyclohexen-1-ol to 2-cyclohexen-1-one for **C3**/H_2O_2 (Table 1, entry 4 and 5). Cyclohexene oxide (**39**) made up only 0.6 % of the total oxidised products when employing **C2** and 3.5 % when employing **C3**. The low selectivity between 2-cyclohexen-1-ol and 2-cyclohexen-1-one formation can be indicative of Russell-type termination, as was found for **C2**/**C3**/PhIO, therefore reactions were repeated under an Ar atmosphere.

When the reaction was repeated under an Ar atmosphere 2-cyclohexen-1-one formation decreased by approx. 1/2 suggesting Russell-type termination is present in the aerated system (Table 1, entry 6). Contrary to what was expected, after eliminating the Russell-type termination pathway a three-fold increase in 2-cyclohexen-1-ol formation was quantified as opposed to the expected decrease in formation (Table 1, entry 6). The reaction employing **C3**/H_2O_2 under an Ar atmosphere was repeated several times after degassing a fresh CH_3CN solution of H_2O_2 and fresh cyclohexene to ensure the increase in 2-cyclohexen-1-ol is a true trend and not the result of handling errors. The same product amount and distribution were obtained upon repetition. The three-fold increase in 2-cyclohexen-1-ol contributes to the increased average TON from 4.2 to 9.3 when changing from air to Ar atmospheres (Table 1, entry 5 and 6). Overall lower reactivity in air suggests the presence of dioxygen in the system contributes to deactivation in some way, possibly effecting how the Fe^{III}-OOH species converts to more active species. No further information can provided at this time, further insight is hoped to be obtained upon investigation of the active species formed found in the next chapter. Under both Ar and air atmospheres the OAT pathway is the least prevalent for the

C3/H_2O_2 system with a similar amount of cyclohexene oxide (**39**) formed; 4.77 $\times 10^{-7}$ and 8.27 $\times 10^{-7}$ mol, respectively (Table 1, entry 6).

3.2.3 Reactivity of the C2/3/^{t}BuOOH System

The same reaction pathways which are outlined for the **C2/3**/H_2O_2 system are applicable to the **C2/3**/^{t}BuOOH system with the initial formation of a Fe^{III}-OO^tBu species (Scheme 25).[141] The **C2/3**/^{t}BuOOH system exhibited the highest overall turnover numbers of the **C2**/**3**/oxidant systems (Table 1, entry 7 - 9). One advantage of using ^{t}BuOOH over H_2O_2 is that ^{t}BuOOH does not disproportionate as H_2O_2 does and therefore does not risk decreasing in reactivity. When cyclohexene oxidation was employed in the **C2**/^{t}BuOOH and **C3**/^{t}BuOOH systems in the presence of dioxygen, the dominant product was 2-cyclohexen-1-ol (**38**) alongside a considerable amount of 2-cyclohexen-1-one (**40**); approx. 5 : 2 ratio of 2-cyclohexen-1-ol to 2-cyclohexen-1-one for **C2**/^{t}BuOOH and approx. 3 : 2 ratio of 2-cyclohexen-1-ol to 2-cyclohexen-1-one for **C3**/^{t}BuOOH (Table 1, entry 7 and 8). Cyclohexene oxide (**39**) made up only 2.3 % of the total oxidised products when employing **C2** and 3.4 % when employing **C3**. The low selectivity between 2-cyclohexen-1-ol and 2-cyclohexen-1-one formation can once again be indicative of Russell-type termination. Another indication of the occurrence of the Russell-type termination reaction are the large TONs exceeding the amount of oxidant employed; ten equivalents of oxidant were employed with respect to catalyst therefore TONs should be limited to 10. The **C2**/^{t}BuOOH and **C3**/^{t}BuOOH systems achieved 22.0 and 32.8 TONs respectively; there must then be a secondary source of oxygen present. Reactions were repeated under an Ar atmosphere.

As expected, the amount of 2-cyclohexen-1-one was significantly reduced, by approx. 9/10 when the reaction was repeated under an Ar atmosphere (Table 1, entry 9). In contrast to what was expected, the amount of 2-cyclohexen-1-ol remained consistent, which resulted in an average TON of 20.4, still exceeding the amount of oxidant employed suggesting a secondary oxygen source remains. To eliminate the secondary oxygen source and get a true representation of the reaction products reactions were repeated after degassing a fresh CH_3CN solution of ^{t}BuOOH, degassing fresh cyclohexene and obtaining a different source of dry CH_3CN. The data remained consistent. These results are flawed. The TON of the system cannot theoretically exceed 10 without a secondary oxygen source. The steps taken to eliminate the secondary oxygen sources of air and moisture have not been successful. Mechanistic information or comparisons to literature cannot be drawn based on these data. One suggestion is to repeat the experiment with the addition of staggered standard samples. Standards were run at frequent intervals (approx. weekly) to ensure the processing of the data was accurate. Running a standard every three samples or so would rule out any erroneous results from instrumentation error, which may have occurred at time these experiments were run or eliminate this as a potential source of error.

3.2.4 Reactivity of C2/3 with Dioxygen

Solutions of **C2/C3** in CH_3CN are stable when exposed to air over a period of several days when monitored by UV-Vis spectroscopy. However, in the presence of cyclohexene **C2** activates dioxygen generating a mixture of the cyclohexene oxide (1 %), 2-cyclohexen-1-ol (33 %), and 2-cyclohexen-1-one (5 %) over a 30 min reaction period (Table 1, entry 10). Comparable product yields and ratios were obtained with **C3**/O_2 (Table 1, entry 11). Ferrous complexes are proposed to activate dioxygen as illustrated in Scheme 27 to form the active Fe^{IV}=O species or Fe^{V}=O species.[157] Cyclohexene oxidation by **C2**/O_2 and **C3**/O_2 achieved 1.9 and 2.5 TONs respectively; TOF = 0.06 and 0.08 min^{-1}. The TON is approx. stoichiometric with respect to iron. One explanation for this level of reactivity is non-catalytic oxidation whereby each iron site may have the capability of activing dioxygen once without regenerating the original ferrous species producing one equivalent of oxidised species each resulting in a TON of 2. Another possibility is that the rate of dioxygen activation is slow and the reaction has not reached an endpoint after 30 min. The reaction was only studied for 30 min to allow comparison to all other cyclohexene oxidation reactions. Further work in the Hess group would involve the study of this reaction for a longer period of time to investigate the endpoint of the reaction and the maximum TON achievable by the system. The allylic oxidation products are favoured for **C2** and **C3** with cyclohexene oxide making up only 1.9 % and 3.1 % of the total oxidised products respectively.

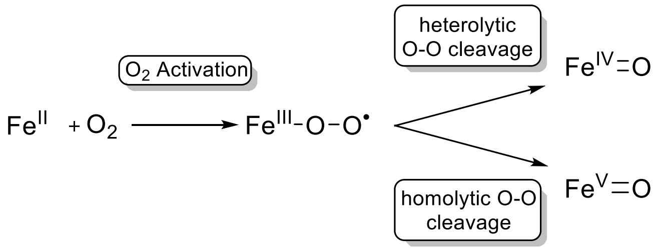

Scheme 27. Activation of Dioxygen by Ferrous Complexes to Form Active Iron-Oxo Species.

3.2.5 Radical-Based Mechanistic Considerations

Several radical-based reaction pathways are available during the oxidation of cyclohexene by **C2/3** which need to be considered when discussing the performance of **C2/3** as an oxidation catalyst. Two radical-based pathways have already been described; Russell-type termination radical reactions and Fenton oxidations. Russell-type termination reactions are considered operational in all aerated reactions by the **C2**/**3**/oxidant systems. Fenton oxidation reactions were investigated by substituting **C2/3** for another ferrous salt, $[Fe(CH_3CN)_6](PF_6)_2$ and examining differences in reactivity. Similar reactivity may suggest the structure of the iron complex and hence the formation of an Fe-O species does not contribute to performance and only the presence of Fe^{2+} is important such as is found for Fenton oxidations. When the oxidation of cyclohexene was carried out using the ferrous salt $[Fe(CH_3CN)_6](PF_6)_2$, in place of **C2/3**, insignificant amounts of oxidation products were obtained, thus Fenton oxidation reactions can be considered negligible for all **C2/3**/oxidant systems.[141, 153]

Reactivity must therefore be due to the interaction between **C2**/**3** and the oxidants employed. The results of $[Fe(CH_3CN)_6](PF_6)_2$ cyclohexene oxidation can be found in the Appendix.

The **C2**/**3**/ROOH systems can additionally yield peroxide/hydroxide free radicals which can directly oxidise the cyclohexene molecule (Scheme 25). To probe hydroxide radical pathways the reactions were repeated in the presence of pyridine. Pyridine can be used as a hydroxide radical trap forming hydroxypyridines and bipyridine (Scheme 28).[153, 158] When cyclohexene oxidation reactions were repeated under analogous conditions, but with the addition of pyridine, no quantifiable 2-/4-hydroxypyridine or bipyridine was identified for any **C2**/**3**/oxidant system, nor was a reduction in product yields observed.

Another means of determining the participation of radical-based oxidation mechanisms is the nature of the lifetime of the organic radical generated. Organic radicals produced by metal-centred oxidants *via* the HAB pathway are short lived, in comparison to those formed by $OH^{\cdot}/{}^{t}BuO^{\cdot}$, due to their proximity to the metal centre, which performs the next step in the oxidation mechanism; oxygen rebound. Longer lived radicals, produced by $OH^{\cdot}/{}^{t}BuO^{\cdot}$ radicals, have time to diffuse freely in solution and are therefore susceptible to radical chain oxidations, which result in an equal formation of alcohol and ketone products.[141, 153] The ratio of alcohol to ketone products (A/K) is therefore a simple test of the organic radical lifetime. A high A/K ratio is indicative of short lived radicals likely formed by metal based oxidants, whereas a low A/K is indicative of longer lived radicals typically formed by $OH^{\cdot}/{}^{t}BuO^{\cdot}$ radicals, which are prone to radical chain reactions. Cyclohexene oxidations by the **C2**/**3**/oxidant systems, in air, produced low average A/K ratios of 1 – 2, which can be attributed to the presence of Russell-type radical reactions. When the reactions were repeated under Ar an average A/K of 3.4 was obtained for the **C3**/PhIO system, 11.2 for the **C3**/H_2O_2 system and 12.1 for the **C3**/tBuOOH indicative of short lived radicals and hence metal-centred oxidation *via* the HAB pathway.

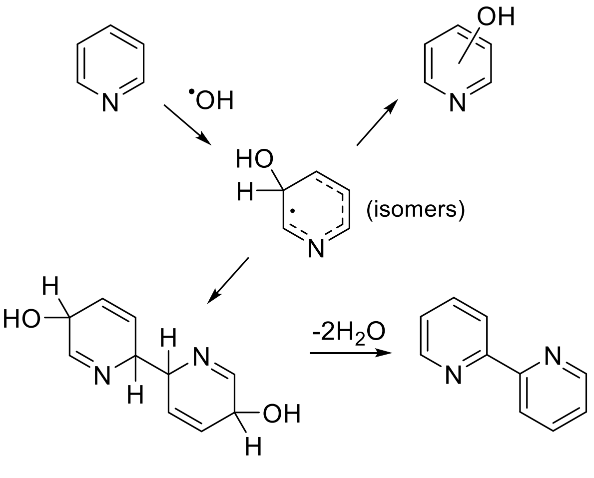

Scheme 28. Mechanisms, and Resultant Products, of Pyridine as a Hydroxide Radical Trap.[158]

3.2.6 Mechanistic Pathways

To further probe the two competing oxidation pathways, OAT and HAB, cyclohexene was replaced with deuterium labelled cyclohexene-d_{10}. The increased strength of the C-D bond over the C-H bond (1.4 kcalmol^{-1}) makes the HAB pathway harder to facilitate and should coincide with a decreased rate of allylic product formation. An approximately four-fold decrease in the yields of 2-cyclohexen-1-ol and 2-cyclohexen-1-one were observed in the reactions of the **C3**/PhIO system when cyclohexene-d_{10} was employed in place of cyclohexene, alongside a two-fold increase in the amount of epoxide (Table 3, entry 1). The same trend was established for the peroxide systems with a five-fold decrease in the yields of 2-cyclohexen-1-ol and 2-cyclohexen-1-one and a three-fold increase in the amount of epoxide for both **C3**/H_2O_2 and **C3**/^{t}BuOOH systems (Table 3, entry 2 and 3). The effect on reactivity of this isotopic substitution can be represented as a product isotope effect (PIE) where PIE = moles of product formed using protiated substrate/ moles of product formed using deuterated substrate.

PIE is a parallel measurement to a kinetic isotope effect (KIE). KIEs represent the competition between substrates when both protio- and deutero- substrates are present. A mixture of protio- and deutero- cyclohexene oxidised products are formed and the KIE = moles of protiated product / moles of deuterated product. PIEs, in contrast, compare the final reactivity over a set period of time when only one of the substrates are present at a time. The moles of products formed are compared when only the protio- substrate is employed versus when the deutero- substrate is employed, over a set period of time. The measurement of PIE over KIE was chosen over the KIE measurement as overlapping product peaks were found after GC-MS measurement of the reaction mixture making quantification inaccurate. Small KIEs/PIEs of 1 - 2 are representative of a low discrimination between C-H and C-D bonds common when a strong oxidant is present, like OH radicals.[159] The difference in bond strength is of no consequence to a strong oxidant as it can easily overcome both energy barriers. The ^{t}BuO$^{\cdot}$ radical is not as strong an oxidant as OH$^{\cdot}$ and so slightly higher typical KIEs of 4 - 5 are commonly exhibited when this oxidant is operational.[160] Metal-centred oxidants are weaker than both OH$^{\cdot}$ and ^{t}BuO$^{\cdot}$ radicals so exhibit higher KIE values with a semi-classical limit of 7.[161] Some metal-centred oxidants have exhibited KIE values higher than 7 which have been explained by tunnelling effects. Some metalloenzymes have exhibited extremely high KIE values; CP450s have exhibited KIEs of 11 while MMO has exhibited KIEs of 50 - 100.[120, 162]

Overall PIEs of 2.0, 3.6, 4.1 for the **C3**/PhIO, **C3**/H_2O_2, **C3**/^{t}BuOOH systems, respectively, were calculated (Table 2). The PIE value of 2.0 for the **C3**/PhIO system is low for metal-centred oxidation, but this may be explained by the higher activity of the C=C pathway (two-fold increase when the HAB pathway was impeded. The PIE value of 3.6 for the **C3**/H_2O_2 system is indicative of metal-centred oxidation as OH radicals should produce a lower value of 1-2, 3.6 may be a bit low again due to the higher activity of the C=C pathway. The PIE for **C3**/^{t}BuOOH of 4.1 is within the range of ^{t}BuO$^{\cdot}$ radicals but there is an issue with the **C3**/^{t}BuOOH data presented and so mechanistic conclusions cannot be drawn.

Table 2. Product Isotope Effect of Cyclohexene Oxidation by C3 at 298 K as Quantified by GC-MS.[a]

Entry	Cat.	Oxidant	Atm.	TON_H[b](+/-)[c]	$\mathrm{TOF_H}$ ($\mathrm{min^{-1}}$)	TON_D[b] (+/-)[c]	PIE[d] (+/-)[c]	$\mathrm{TOF_D}$ ($\mathrm{min^{-1}}$)
1	**C3**	PhIO	Ar	7.0 (0.3)	0.23	3.4 (0.4)	2.0 (0.2)	0.07
2	**C3**	H_2O_2	Ar	9.3 (0.2)	0.31	2.6 (0.01)	3.6 (0.07)	0.12
3	**C3**	^{t}BuOOH	Ar	20.5 (1.0)	0.68	5.0 (0.3)	4.1 (0.4)	0.14

[a] Cat./Oxidant/Substrate = 1:10:300. Mol Cat. = 3.24 ×10^{-6}. Solvent = CH_3CN. [b] Turnover Number (TON) = Total Moles of Oxidised Products / Moles of Catalyst. [c] Error = Standard Deviation of At Least Three Runs for TON and Propagated Error for PIE. [d] Product Isotope Effect (PIE) = (Moles of Product using Protiated Substrate/ Moles of Product using Deuterated Substrate).

Table 3. Product Distribution for Cyclohexene Oxidation by C3 at 298 K as Quantified by GC-MS.[a]

Entry	Oxidant	Protio- products (mol)			Deutero – products (mol)		
		Epoxide[b] (+/-)[c]	En-ol[b] (+/-)[c]	En-one[b] (+/-)[c]	Epoxide[b] (+/-)[c]	En-ol[b] (+/-)[c]	En-one[b] (+/-)[c]
1	PhIO	3.8 ×10^{-6} (5.3 ×10^{-7})	1.5 ×10^{-5} (3.9 ×10^{-7})	4.3 ×10^{-6} (3.9 ×10^{-7})	6.2 ×10^{-6} (9.7 ×10^{-7})	3.7 ×10^{-6} (3.4 ×10^{-7})	1.3 ×10^{-6} (2.2 ×10^{-7})
2	H_2O_2	8.3 ×10^{-7} (2.9 ×10^{-8})	2.7 ×10^{-5} (5.0 ×10^{-7})	2.4 ×10^{-6} (2.1 ×10^{-7})	2.5 ×10^{-6} (9.0 ×10^{-8})	5.1 ×10^{-6} (1.6 ×10^{-7})	8.5 ×10^{-7} (3.9 ×10^{-8})
3	^{t}BuOOH	8.6 ×10^{-7} (3.0 ×10^{-8})	6.1 ×10^{-5} (3.2 ×10^{-6})	5.0 ×10^{-6} (1.9 ×10^{-7})	2.9 ×10^{-6} (4.4 ×10^{-7})	1.2 ×10^{-5} (7.0 ×10^{-7})	1.7 ×10^{-5} (3.8 ×10^{-7})

[a] Cat./Oxidant/Cyclohexene = 1:10:300. Mol Cat. = 3.24 ×10^{-6}. Solvent = CH_3CN. [b] Epoxide Denotes Cyclohexene Oxide; En-ol, 2-Cyclohexen-1-ol; En-one, 2-Cyclohexen-1-one. [c] Error = Standard Deviation of At Least Three Runs.

3.3 Further Reactivity Studies

Cyclohexene allowed the initial investigation of HAB and OAT pathways; the OAT reaction was investigated further using triphenylphosphine. PhIO (as a solid) was allowed to react with a solution of **C3** in CH_3CN for a time period of 10 min. The reaction mixture was then filtered to remove any trace of unreacted PhIO. The active species remaining in solution formed from the reaction of **C3** with PhIO was then exposed to triphenylphosphine (PPh_3). The reaction solution was analysed qualitatively by GC-MS and ^{31}P NMR spectroscopy. A complete shift from -6 ppm (PPh_3) to +27 ppm ($OPPh_3$) was observed by ^{31}P NMR spectroscopy and triphenylphosphine oxide ($OPPh_3$) was the sole compound detected in the GC-MS trace, indicating successful OAT.

The HAB reaction was examined further by employing a range of substrates of varying bond dissociation energies (BDE); xanthene (75.5 kcal mol^{-1}) **(43)**, 9-10-dihydroanthracene (DHA, 76 kcal mol^{-1}) **(44)**, triphenylmethane (81 kcal mol^{-1}) **(45)**, adamantane (96 kcal mol-1) **(46)** and cyclohexane (99 kcal mol^{-1}) **(47)**, to examine how C-H bond strength affects reactivity. Reactions were carried out under an Ar atmosphere, using PhIO. PhIO was selected as the oxidant for all further reactions as the cyclohexene oxidation data employing tBuOOH is under dispute due to exceeding product yields and the cyclohexene oxidation reactions employing H_2O_2 showed low reactivity possibly due to disproportionation of H_2O_2.

Aromatisation was probed by employing DHA **(44)** as the substrate. DHA is oxidised to anthracene **(48)** following two successive hydrogen abstraction steps (Scheme 29). The first hydrogen abstraction has a BDE of 76 kcal mol^{-1} while the second has a BDE of 45 kcal mol^{-1}, thus the first hydrogen abstraction is rate limiting.[163, 164] Anthracene (**48**) was the sole product formed in the oxidation of DHA (**44)** by **C3**/PhIO, as determined by GC-MS. Literature studies indicated 9,9'-dianthracene can be generated if the second abstraction is kinetically hindered.[165] The absence of 9,9'-dianthracene, as determined by GC-MS, suggests the second hydrogen abstraction proceeds quickly for this system.

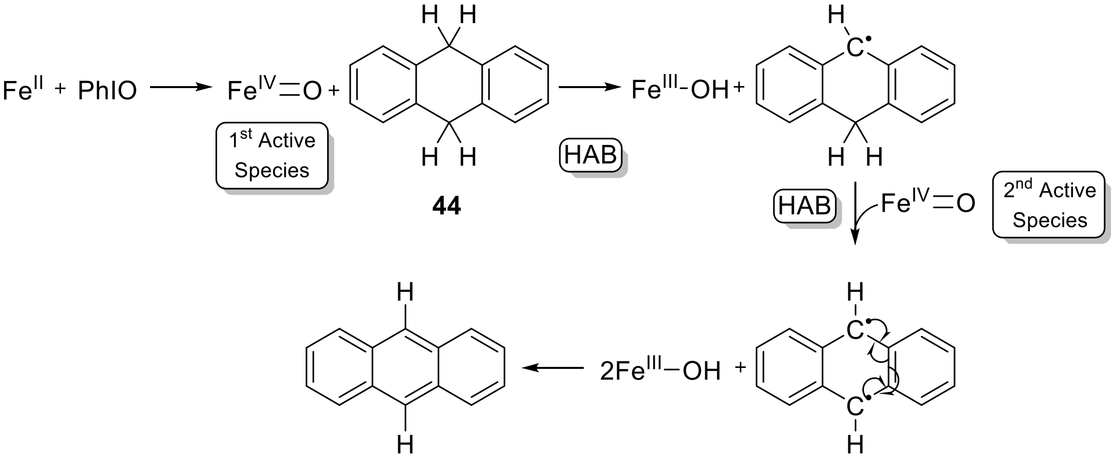

48

Scheme 29. 9,10-Dihydroanthracene Oxidation Pathway, and the Resultant Product, Obtained in the Reaction of Various Non-Heme Iron Complexes with PhIO.

During the 30 min reaction period 3.0 TON were achieved (Table 4, entry 1). Two active iron species are required to facilitate both HAB steps, as shown in Scheme 29, to produce the anthracene product. To allow reactivity comparison to cyclohexene oxidation, where only one active species is required to produce oxidised products, the reactivity of DHA oxidation will be compared in terms of moles of product × no. of active species. DHA oxidation produced 1.80 $\times 10^{-5}$ mol of product in comparison to 2.29 $\times 10^{-5}$ mol by cyclohexene oxidation under analogous conditions. The reactivity of DHA oxidation was expected to be higher due to the lower C-H bond strength in comparison to cyclohexene.

Xanthene (**43**) oxidation proceeds *via* a more complex mechanism than DHA (Scheme 30). Xanthene (**43**) oxidation begins with a HAB step, an oxygen rebound step proceeds to form xanthen-9-ol. A second HAB step forms the ketone product xanthone (**49**). As with DHA, side products such as 9-hydroxyxanthene and 9,9′-bixanthene can be formed in the oxidation of xanthene when the second hydrogen abstraction step is slow.[141, 166, 167] Xanthone (**49**) was the sole product formed, as determined by GC-MS, suggesting the second hydrogen abstraction for this system is fast for this system.

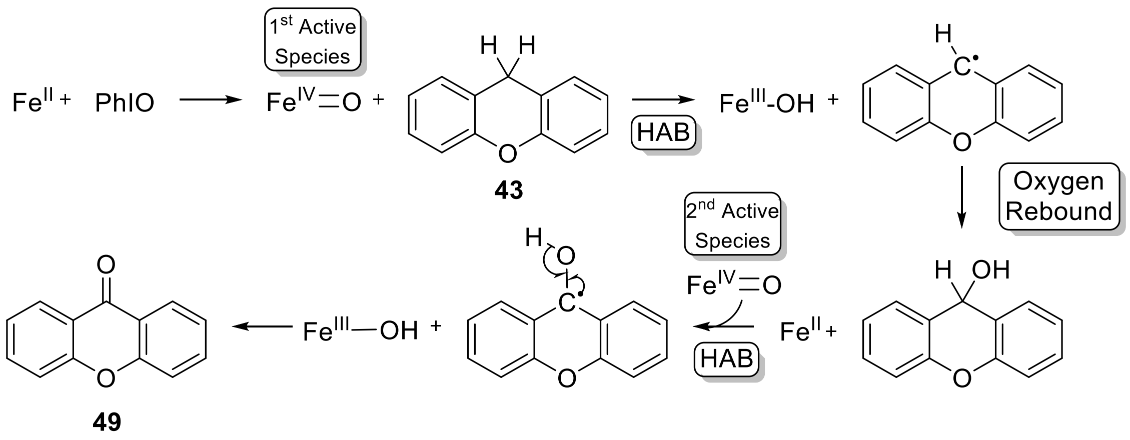

Scheme 30. Xanthene Oxidation Pathway, and the Resultant Product, Obtained in the Reaction of Various Non-Heme Iron Complexes with PhIO.

During the 30 min reaction period a TON of 4.3 was achieved (Table 4, entry 2). Again, as with DHA, two active iron species are required to facilitate both HAB steps, as shown in Scheme 30, to produce the xanthone product. To allow reactivity comparison to cyclohexene oxidation, where only one active species is required to produce oxidised products, the reactivity of xanthene oxidation will be compared in terms of moles of product × no. of active species. Using this means of comparing reactivity xanthene oxidation produced 2.54 $\times 10^{-5}$ mol of product in comparison to 2.29 $\times 10^{-5}$ mol of product by cyclohexene oxidation. Xanthene displayed the highest reactivity exhibited by the **C3**/PhIO system compared to cyclohexene and DHA oxidation. This is as expected as xanthene has the weakest C-H BDE.

Alkane hydroxylation was probed by employing triphenylmethane **(45)** as the substrate. Triphenylmethane oxidation occurs *via* a HAB/oxygen rebound mechanism, just as allylic cyclohexene oxidation (Scheme 31). Triphenylmethanol **(50)** was the sole product formed during this reaction, as determined by GC-MS.

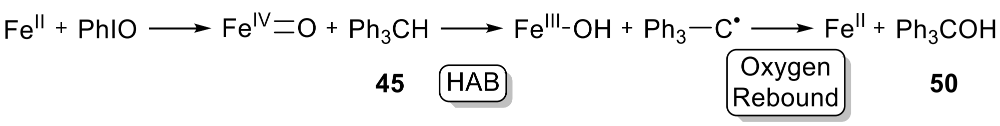

$$\mathrm{Fe^{II} + PhIO \longrightarrow Fe^{IV}{=}O + \underset{\mathbf{45}}{Ph_3CH} \xrightarrow[\boxed{\text{HAB}}]{} Fe^{III}\text{-}OH + Ph_3{-}C^{\bullet} \xrightarrow[\boxed{\text{Oxygen Rebound}}]{} Fe^{II} + \underset{\mathbf{50}}{Ph_3COH}}$$

Scheme 31. Triphenylmethane Oxidation Pathway, and the Resultant Product, Obtained in the Reaction of Various Non-Heme Iron Complexes with PhIO.

During the 30 min reaction period a TON of 6.7 was achieved (Table 4, entry 3). This reactivity is very comparable to cyclohexene oxidation (7.0 TON), which is to be expected as the C-H bond strength is very similar between the two substrates (81 and 80 kcalmol^{-1} for triphenylmethane and cyclohexene respectively).

To probe the hydrogen abstraction pathway further DHA and xanthene were replaced with deuterium labelled DHA-d_4 and xanthene-d_2. The increased strength of the C-D bond over the C-H bond should make the HAB harder to facilitate and coincide with a decrease in product formation, as was observed for cyclohexene. Substituting with DHA-d_4 led to a decrease in product formation to a TON of 0.6. The decrease in reactivity can be represented as a PIE of 4.8 (Table 4, entry 1). Substituting with xanthene-d_2 also led to a decrease in product formation to TON of 0.8, which can be represented as a PIE of 5.7 (Table 4, entry 2). The high PIE values indicate hydrogen abstraction is rate determining for both oxidations by the **C3**/PhIO system. The higher PIE values in comparison to cyclohexene oxidation are because there are no alternative pathways to produce oxidation products but *via* a hydrogen abstraction pathway, unlike cyclohexene oxidation in which the OAT pathway is still operational.

Table 4. Product Amounts Obtained in Catalytic Oxidation of 9,10-Dihydroanthracene, Xanthene, Triphenylmethane and their Deutero-Counterparts by C3 at 298 K as Quantified by GC-MS. [a]

Entry	Substrate	Oxidant	Atm.	Mol Protio - Ox. Product (+/-)[c]	TON_H [b] (+/-)[c]	TOF_H (min^{-1})	Mol Deutero - Ox. Product (+/-)[c]	TON_D [b] (+/-)[c]	TOF_D (min^{-1})	PIE [d] (+/-)[c]
1	**44**	PhIO	N_2	8.99×10^{-6} (8.01×10^{-7})	3.0 (0.3)	0.10	1.89×10^{-6} (2.09×10^{-7})	0.6 (0.04)	0.02	4.8 (0.5)
2	**43**	PhIO	N_2	1.27×10^{-5} (5.44×10^{-7})	4.3 (0.2)	0.14	2.23×10^{-6} (1.14×10^{-7})	0.8 (0.04)	0.03	5.7 (0.4)
3	**45**	PhIO	N_2	1.99×10^{-5} (4.66×10^{-7})	6.7 (0.2)	0.22				

[a] Cat./Oxidant/Substrate = 1:10:300. Mol Cat. = 3.24×10^{-6}. Solvent = CH_3CN. Reactions Carried Out Under Inert Atmosphere. [b] Turnover Number (TON) = Total Moles of Oxidised Products / Moles of Catalyst. [c] Error = Standard Deviation for Moles and TON, Propagated Error for PIE. [d] Product Isotope Effect (PIE) = (Moles of Product Protiated using Substrate/ Moles of Product using Deuterated Substrate).

3.4 Limitations of C3

Complex **C3** has displayed catalytic oxidation capability toward substrates with C-H bonds of BDE ≤ 81 kcal mol^{-1}. Cyclohexane **(47)** has a C-H BDE = 99.3 kcal mol^{-1}. Cyclohexane is oxidised to cyclohexanol *via* a HAB/oxygen rebound mechanism (Scheme 32).[141] Complex **C3** was tested for cyclohexane oxidation under analogous conditions to all other substrates in this chapter with PhIO, H_2O_2 and ^tBuOOH. After a 30 min reaction period the reaction mixture was analysed by GC-MS. No cyclohexanol product, nor cyclohexanone, was detected in reaction mixtures under all conditions. Thus cyclohexane oxidation was considered beyond the capability of **C3**.

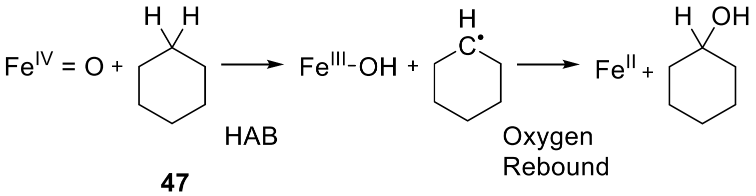

47

Scheme 32. Cyclohexane Oxidation Pathway, and the Resultant Product, Obtained in the Reaction of Fe^{IV}=O Active Species.

Adamantane **(46)** has a slightly weaker BDE of 96.2 kcal mol^{-1}, for the tertiary C-H bonds. Oxidation of adamantane leads to a mixture of 1-adamantanol, 2-adamantanol and 2-adamantanone

(Scheme 33).[168] An intramolecular competition reaction in the oxidation of adamantane, which contains both secondary and tertiary C-H bonds, can reveal mechanistic details of the metal-centred oxidant.[141, 169] Complex **C3** was tested for adamantane oxidation, under analogous conditions to all other substrates discussed in this chapter, with PhIO, H_2O_2 and ^tBuOOH to determine were the limitations of **C3** lay based on C-H bond strength. After a 30 min reaction period the reaction mixture was analysed by GC-MS. No 1-adamantanol, 2-adamantanol nor 2-adamantanone was detected in reaction mixtures under all conditions. Thus adamantane oxidation was also considered beyond the capability of **C3**.

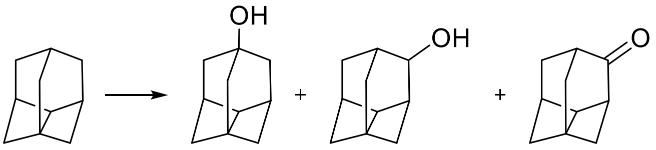

46

Scheme 33. Tertiary vs. Secondary C-H Oxidation of Adamantane.

3.5 Comparison of Reactivity of C3 to Benchmark Bio-inspired Complexes

A comparative analysis between the reactivity of complex **C3** toward hydrocarbon oxidation to the benchmark ferrous complexes, outlined in the introduction section, allows for an analysis of the performance of complex **C3**. A comparison of reactivity and product distribution may give insight into the reaction mechanism of our systems with the known mechanisms of reported non-heme complexes.

3.5.1 Reactivity Toward Cyclohexene with PhIO

The reactivity of the **C3**/PhIO system is comparable to benchmark complex $[Fe(TPA)(CH_3CN)_2](ClO_4)_2$ **(34)**, under analogous conditions under both air and Ar atmospheres (Table 5). In an aerated environment complex **34** exhibited an overall TON of 14.5 in comparison to 13.8 exhibited by **C3**, with a nearly identical distribution of products. In an aerated environment, benchmark complex $[Fe(BPMEN)(CH_3CN)_2](ClO_4)_2$ **(35)**, in contrast, gave a lower TON of 8.3, reflected by a lower overall amount of allylic product formation. Although complex **35** exhibited lower allylic product formation to **34** and **C3**, all three complexes favoured the HAB pathway over OAT. Under an Ar atmosphere all three complexes displayed very similar reactivity and distribution of products. Complexes **34** and **35** exhibited overall TONs of 7.6 and 7.3, in comparison to **C3** which exhibited an overall TON of 7.0 (Table 5).[132] Again all three complexes favoured the formation of allylic oxidation products. As with the **C3**/PhIO system, both complexes **34** and **35** indicated Russell-type termination reactions were present in aerated solutions, as signified by the equimolar amounts of allylic oxidation products formed (Table 5). Overall, the **C3**/PhIO system performed competitively with the benchmark complexes **34** and **35**.

Table 5. Comparison of Reactivity of C3 to Benchmark Ferrous Complexes 34 and 35 with PhIO toward Cyclohexene.[a][130,132]

Entry	Cat.	Oxidant	Atm.	Mol Epoxide[b]	Mol En-ol[b]	Mol En-one[b]	TON[c]	TOF[d] (min^{-1})
1	**34**	PhIO	Air	4.77×10^{-6}	2.20×10^{-5}	2.00×10^{-5}	14.5	0.48
2	**35**	PhIO	Air	5.09×10^{-6}	1.15×10^{-5}	9.86×10^{-6}	8.3	0.28
3	**C3**	PhIO	Air	2.74×10^{-6}	2.21×10^{-5}	2.00×10^{-5}	13.8	0.46
4	**34**	PhIO	Ar	1.27×10^{-6}	1.37×10^{-5}	9.23×10^{-6}	7.6	0.25
5	**35**	PhIO	Ar	4.14×10^{-6}	1.18×10^{-5}	7.32×10^{-6}	7.3	0.24
6	**C3**	PhIO	Ar	3.82×10^{-6}	1.47×10^{-5}	4.33×10^{-6}	7.0	0.23

[a] Cat/Oxidant/Cyclohexene = 1:10:300. Mol Cat = 3.24×10^{-6}. Solvent = CH_3CN. [b] Epoxide Denotes Cyclohexene Oxide; En-ol, 2-Cyclohexen-1-ol; En-one, 2-Cyclohexen-1-one. [c] Turnover Number (TON) = Total Moles of Oxidised Products / Moles of Catalyst. [D] Turnover Frequency (TOF) min^{-1} = (Total Moles of Oxidised Product / Moles of Catalyst) / 30.

3.5.2 Reactivity Toward Cyclohexene with H_2O_2

The reactivity of the **C3**/H_2O_2 system was considerably lower than was found for related ferrous complexes **34** and **35**, which achieved TONs of 16.8 and 14.4, respectively, under analogous conditions in air, in comparison to a TON of 4.2 by complex **C3** (Table 6).[132] Complex **34**, like **C3**, favoured the formation of allylic products but higher yields were obtained for all three products in comparison to **C3** (Table 6, entry 1). Complex **35** performed only moderately better than **C3** in the allylic oxidation of cyclohexene but produced a considerable amount of cyclohexene oxide, 2.51 $\times 10^{-5}$ mol, whereas **C3** produced only 4.77 $\times 10^{-7}$ mol (Table 6, entry 2 and 4). Complex **35** favoured the OAT pathway. Benchmark complex $[Fe(N4Py)(CH_3CN)]^{2+}$ **(36)** displayed an even greater reactivity toward cyclohexene oxidation producing an overall TON of 36.1 (Table 6, entry 3). Complex **36** strongly favoured the formation of allylic oxidation products, but the TON is not directly comparable as modified conditions were used; increased oxidant and substrate were employed (Table 6, entry 3).[130] Overall, the **C3**/H_2O_2 system performed poorly in comparison to the benchmark complexes. The large variations in reactivity and product distribution across all ferrous complexes suggests different active species are formed on reaction of each ferrous complex with H_2O_2 or the Fe-O species originally formed undergo different conversions to different active species. Reactivity comparison of **34**, **35** and **C3** toward cyclohexene under an Ar atmosphere could not be found. This is unfortunate as it would be interesting to see if these systems also saw a decrease in activity in air.

Table 6. Comparison of Reactivity of C3 to Benchmark Ferrous Complexes with H_2O_2 toward Cyclohexene.[a][130,132]

Entry	Cat.	Oxidant	Atm.	Mol Epoxide[b]	Mol En-ol[b]	Mol En-one[b]	TON[c]	TOF[e] (min^{-1})
1	**34**	H_2O_2	Air	7.32×10^{-6}	2.23×10^{-5}	2.39×10^{-5}	16.8	0.56
2	**35**	H_2O_2	Air	2.51×10^{-5}	1.11×10^{-5}	9.55×10^{-6}	14.4	0.48

3 [d]	**36**	H_2O_2	Air	3.42×10^{-6}	9.92×10^{-5}	2.39×10^{-5}	36.1	1.20
4	**C3**	H_2O_2	Air	4.77×10^{-7}	7.67×10^{-6}	5.47×10^{-6}	4.2	0.14

[a] Cat./Oxidant/Cyclohexene = 1:10:300. Mol Cat. = 3.24×10^{-6}. Solvent =CH_3CN. [b] Epoxide Denotes Cyclohexene Oxide; En-ol, 2-Cyclohexen-1-ol; En-one, 2-Cyclohexen-1-one. [c] Turnover Number (TON) = Total Moles of Oxidised Products / Moles of Catalyst. [d] Cat./Oxidant/Cyclohexene = 1:100:1000. Mol Cat. = 3.50×10^{-6}. Mol H_2O_2 = 3.42×10^{-4}. [e] Turnover Frequency (TOF) min^{-1} = (Total Moles of Oxidised Product / Moles of Catalyst) / 30.

3.5.3 Reactivity Toward Cyclohexene with ^{t}BuOOH

The reactivity of the **C3**/^{t}BuOOH system is very comparable to benchmark complex [Fe(TPA)(CH_3CN)$_2$](ClO_4)$_2$ **(34)**, under analogous conditions under an aerated atmosphere (Table 7). In an aerated environment, complex **34** exhibited an overall TON of 35.7 in comparison to 32.8 exhibited by **C3**, with a nearly identical distribution of products. In an aerated environment, benchmark complex [Fe(BPMEN)(CH_3CN)$_2$](ClO_4)$_2$ **(35)**, in contrast, gave a lower TON of 22.9, reflected by a lower overall amount of allylic product formation. (Table 7, entry 1).[132] Equimolar amounts of allylic products were formed during cyclohexene oxidation by **34** and **35** in addition to exhibiting high reactivity exceeding the amount of oxidant employed, suggesting Russell-type termination reactions are operational just as was determined for **C3** (Table 7, entry 2). Overall, in aerated solutions, **C3** performed competitively with the benchmark complexes with a similar TON and distribution of products dominated by Russell-type termination reactions.

When an Ar atmosphere was employed complexes **34** and **35** decreased in reactivity, no longer exceeding the amount of oxidant employed; TONs of 7.9 and 7.5 respectively, due to a considerable decrease in the formation of 2-cyclohexen-1-one and a decrease in 2-cyclohexen-1-ol, as is expected when eliminating the Russell-type termination pathway (Table 7, entry 4 and 5).[132] Complex **35** also yielded a considerable decrease in cyclohexene oxide formation which was at a considerable value of 1.53×10^{-5} mol in air, whereas **34** yielded negligible amounts of cyclohexene oxide in air and Ar. Like **C3**, both **34** and **35** favour the formation of allylic products under Ar with **34** forming no cyclohexene oxide. Under an Ar atmosphere **C3**, in contrast to the benchmark complexes, still exhibited high reactivity with an exceptionally large formation of 2-cyclohexen-1-ol. The catalyst system cannot theoretically exceed 10 TON (equivalents of oxidant added w.r.t. catalyst) without a secondary oxygen source present, therefore the data set employing C3/tBuOOH must be aerated in some way making the results incomparable to the results with 34 and 35.

Table 7. Comparison of Reactivity of C3 to Benchmark Ferrous Complexes with ^{t}BuOOH toward Cyclohexene. [a130,132]

Entry	Cat.	Oxidant	Atm	Mol Epoxide[b]	Mol En-ol[b]	Mol En-one[b]	TON[c]	TOF[d] (min^{-1})
1	**34**	^{t}BuOOH	Air	2.55×10^{-6}	5.76×10^{-5}	5.47×10^{-5}	35.7	1.19
2	**35**	^{t}BuOOH	Air	1.53×10^{-5}	2.45×10^{-5}	3.31×10^{-5}	22.9	0.70
3	**C3**	^{t}BuOOH	Air	3.60×10^{-6}	5.94×10^{-5}	4.41×10^{-5}	32.8	1.09
4	**34**	^{t}BuOOH	Ar	0	2.07×10^{-5}	4.46×10^{-6}	7.9	0.26

5	**35**	^{t}BuOOH	Ar	2.55 ×10^{-6}	1.56 ×10^{-5}	5.73 ×10^{-6}	7.5	0.25
6	**C3**	^{t}BuOOH	Ar	8.59 ×10^{-7}	6.08 ×10^{-5}	5.03 ×10^{-6}	20.4	0.68

[a] Cat./Oxidant/Cyclohexene = 1:10:300. Mol Cat. = 3.24 ×10^{-6}. Solvent = CH_3CN. [b] Epoxide Denotes Cyclohexene Oxide; En-ol, 2-Cyclohexen-1-ol; En-one, 2-Cyclohexen-1-one. [c] Turnover Number (TON) = Total Moles of Oxidised Products / Moles of Catalyst. [d] Turnover Frequency (TOF) min^{-1} = (Total Moles of Oxidised Product / Moles of Catalyst) / 30.

3.5.4 Reactivity Toward Cyclohexene with Dioxygen

Complex **34** and $[Fe(TPA)(CH_3CN)_2](OTf)_2$ exist as low spin ferrous complexes in CH_3CN and as high spin ferrous complexes in $(CH_3)_2CO$; both complexes displayed no cyclohexene oxidation in aerated CH_3CN solutions but did show reactivity in aerated $(CH_3)_2CO$.[170] The high spin state of ferrous **C2/C3** is then assumed to encourage oxygen activation. In aerated $(CH_3)_2CO$, both complexes oxidised cyclohexene to a mixture of cyclohexene oxide, 2-cyclohexen-1-ol and 2-cyclohexen-1-one. Complex **34** favoured allylic product formation with a ratio of products allylic products/epoxide of 29.6 within a 1 h reaction period. Equimolar amounts of alcohol and ketone products were formed, indicative of radical-based mechanisms. Comparable product amounts were found for $[Fe(TPA)(CH_3CN)_2](OTf)_2$. Cyclohexene oxidation by **C3**/**2**/O_2 also favoured allylic product formation with only a small amount of cyclohexene oxide formed represented by a similar ratio of products to **34**; allylic products/epoxide of 36.0 for **C2** and 30.0 for **C3**. Tanaka and co-workers proposed that the $[Fe(TPA)(CH_3CN)_2]^{2+}$ complexes activate dioxygen forming an Fe^{III}-$OO^{\cdot}$ species. The superoxo species is capable of hydrogen abstraction leading to the formation of the cyclohexene organic radial (**41**) and a Fe^{II}-OOH. Radical mechanisms ensue from this point causing the equimolar amount of allylic products as the Fe^{II}-OOH species is sluggish toward further oxidation steps. The $[Fe(TPA)(CH_3CN)_2]^{2+}$ complexes were tested toward the oxidation of cyclohexene over a 24 h time period; product yields were reported after this time and so direct product reactivity to **C2**/**C3** cannot be compared. Equimolar product distribution of 2-cyclohexen-1-ol to 2-cyclohexen-1-one suggest **C3** and **C2** could also be reacting via the mechanism proposed by Tanaka. Labile ligands also play an important role in dioxygen activation as proven by the $Fe(TPA)Cl_2$ complex which is high spin in both CH_3CN and $(CH_3)_2CO$ but yet showed no oxidation reactivity toward cyclohexene in either aerated solution.[170]

Table 8. Comparison of Reactivity of C2/3 toward Cyclohexene in Aerated Solutions. [a]

Entry	Cat.	Ox.	Atm	Mol Epoxide[b]	Mol En-ol[b]	Mol En-one[b]	TON[c]	TOF[d] (min^{-1})
1	**C2**	O_2	Air	1.15 ×10^{-7}	4.94 ×10^{-6}	1.05 ×10^{-6}	1.9	0.06
2	**C3**	O_2	Air	2.55 ×10^{-7}	5.34 ×10^{-6}	2.54 ×10^{-6}	2.5	0.08

[a] Cat./Oxidant/Cyclohexene = 1:10:300. Mol Cat. = 3.24 ×10^{-6}. Solvent = CH_3CN. [b] Epoxide Denotes Cyclohexene Oxide; En-ol, 2-Cyclohexen-1-ol; En-one, 2-Cyclohexen-1-one. [c] Turnover Number (TON) = Total Moles of Oxidised Products / Moles of Catalyst. [d] Turnover Frequency (TOF) min^{-1} = (Total Moles of Oxidised Product / Moles of Catalyst) / 30.

3.5.5 Limitations of C2/3

In contrast to **C2/3**, the benchmark non-heme ferrous bio-inspired complexes **34**, **35** and pentadentate ligand complex **36** all demonstrated reactivity toward cyclohexane oxidation forming cyclohexanol and cyclohexanone products in the presence of H_2O_2. Complex **35** demonstrated the highest reactivity with a total product yield of 63 % and a high A/K ratio of products of 8.0 signifying metal-centred oxidation.[141, 171] Both **34** and **36** displayed comparable reactivity giving total product yields of 37 % and 31 % respectively.[141, 172] Complex **34** gave an A/K ratio of products of 4.3, again signifying metal-centred oxidation whereas **36** gave a low A/K of 1.4 leaving some uncertainty about radical vs. metal-centred oxidations for this system.[130] KIEs of 3.5 and 3.2 were calculated for **34** and **35** indicative of metal-centred oxidation. Fe(TPA)Cl_2 oxidised cyclohexane in the presence of ^{t}BuOOH with a total product yield of 23 %.[173, 174] A mixture of cyclohexanol and cyclohexanone was formed with a low A/K ratio of 1.3 and a KIE value of 5.4, typical of ^{t}BuO$^\cdot$ mechanisms.

Again, in contrast to **C2/3**, the benchmark non-heme ferrous bio-inspired complexes **34**, **35** and pentadentate ligand complex **36** all demonstrated oxidative reactivity toward adamantane forming 1-adamantanol, 2-adamantanol and 2-adamantanone products in the presence of H_2O_2. Complexes **34** and **35** again signified the oxidation of these strong C-H bonds by metal-centred oxidation as represented by the large 3°/2° ratio of products of 17 and 15, respectively. A large 3°/2° ratio of products signifies metal-centred oxidation according to literature studies. [141, 171, 172]

3.6 Conclusions

The oxidative reactivity of complexes **C2/3** were investigated in an endeavour to assess their performance as hydrocarbon oxidation catalysts and in hope of revealing mechanistic details of the behaviour of the multiple redox sites within these unique structures during hydrocarbon oxidation. Complexes **C2/3** have exhibited capability of facilitating multiple hydrocarbon oxidation pathways, C-H hydroxylation and C=C epoxidation, during the study of cyclohexene oxidation (BDE = 80 kcal mol^{-1}) generating both cyclohexene oxide (**39**) and 2-cyclohexen-1-ol (**38**), in the presence of common oxidants and alone in air.

The **C3**/PhIO system displayed comparable reactivity toward the oxidation of cyclohexene and with a similar distribution of products to the benchmark ferrous complexes $[Fe(TPA)(CH_3CN)_2](ClO_4)_2$ (**34**) and $[Fe(BPMEN)(CH_3CN)_2](ClO_4)_2$ (**35**), under analogous conditions.[132] All three systems favour allylic oxidation products over the formation of cyclohexene oxide. Que Jr. stated the choice to attack either the allylic C-H bond or C=C bond of cyclohexene is dependent on the electronic properties of the active species.[135] The reactivity studies completed by Que Jr. of several isolated active Fe-oxygen species toward cyclohexene oxidation found the preference to form allylic oxidation products, over OAT products, was characteristic of the $Fe^{IV}O$ $S=1$ species. An alcohol to ketone product ratio of 3.4 was obtained for the **C3**/PhIO system indicative of a short lived organic radical like due to metal-centred oxidation, supported by a PIE of 2.0. The similarity in reactivity and selectivity suggests a similar metal-centred active species is formed by all three systems on addition of PhIO. Complexes $[Fe(TPA)(CH_3CN)_2](ClO_4)_2$ and $[Fe(BPMEN)(CH_3CN)_2](ClO_4)_2$ form $Fe^{IV}=O$ $S=1$ species on reaction with PhIO, so the assumption is that **C3** also forms a $Fe^{IV}=O$ $S=1$ species on reaction with PhIO. Complex **C3** in contrast to $[Fe(TPA)(CH_3CN)_2](ClO_4)_2$ and $[Fe(BPMEN)(CH_3CN)_2](ClO_4)_2$ is a bi-metallic system and the effects of the second site are still unknown for this system with regard to oxidative mechanism.

The **C3**/H_2O_2 system demonstrated poor reactivity toward cyclohexene oxidation compared to related ferrous complexes. The **C3**/H_2O_2 system favoured allylic oxidation products with a notable lack of cyclohexene oxide formation. $[Fe(TPA)(CH_3CN)_2](ClO_4)_2$ favoured allylic oxidation products while $[Fe(BPMEN)(CH_3CN)_2](ClO_4)_2$, in contrast, formed a large amount of cyclohexene oxide.[132] The difference in product reactivity and selectivity across all three systems suggests different active species are present. A metal-centred oxidation species is assumed to be formed upon reaction of **C3** and H_2O_2 based on the calculated PIE and A/K values of 3.6 and 11.2, respectively. The species formed may lack oxidising power leading to low reactivity or high disproportionation of H_2O_2 may result in only a small percentage of **C3** reacting with H_2O_2 to form the active species. $[Fe(TPA)(CH_3CN)_2](ClO_4)_2$ and $[Fe(BPMEN)(CH_3CN)_2](ClO_4)_2$ initially form Fe^{III}-OOH $S=5/2$ species upon addition with H_2O_2, which has been shown to be a sluggish oxidant and so conversion to $Fe^{IV}=O$ species, of higher activity, was determined. Complex **C3** may form the initial Fe^{III}-OOH species but conversion to a more active species may be hindered. The main structural difference between **C3** and $[Fe(TPA)(CH_3CN)_2](ClO_4)_2$, $[Fe(BPMEN)(CH_3CN)_2](ClO_4)_2$ is the second iron site, the effects of which are still unclear. One scenario is that the second site has a negative effect on reactivity by impeding conversion of the sluggish Fe^{III}-OOH species to other of higher activity.

The **C3**/^{t}BuOOH system exhibited the highest reactivity toward cyclohexene oxidation, exhibiting comparable reactivity to $[Fe(TPA)(CH_3CN)_2](ClO_4)_2$ and $[Fe(BPMEN)(CH_3CN)_2](ClO_4)_2$ in air.[132] Under an Ar atmosphere **C3**, in contrast to the benchmark complexes, still exhibited high reactivity with an exceptionally large formation of 2-cyclohexen-1-ol. These results have been deemed flawed as the TON of the system cannot theoretically exceed 10 (equivalents of oxidant added w.r.t. catalyst) without a secondary oxygen source. Mechanistic information or comparisons to literature cannot be drawn based on these data. This data set should be repeated by other members of the group if this data is to be reported.

Complex **C3/2** has demonstrated the ability to activate dioxygen to oxidise cyclohexene. Within a 30 min reaction period a TON of ~ 2 was achieved. Similar distribution of products to Tanaka's literature study suggest **C2/3** may follow the same oxygen activation pathway beginning with the formation of an Fe^{III}-superoxo. The superoxo species is capable of HAB leading to the formation of the cyclohexene organic radial and a Fe^{II}-OOH. The stoichiometry between iron sites and product formation can be explained if **C3**, as $[Fe(TPA)(CH_3CN)_2](ClO_4)_2$, activates dioxygen to form an Fe^{III}-$OO^{\cdot}$ species at each site.[170] Each superoxo species can perform one HAB resulting in the formation of two cyclohexene organic radicals. Trapping by O_2 would lead to the formation of equimolar allylic oxidation products with an overall TON of 2.0 if the iron complex did not regenerate. This is not the only suggestion for reactivity in air, the oxidative species may be slow and the complex may not have reached the end point within the 30 min reaction period.

Metal-centred oxidants formed by **C3** in the presence of common oxidants have proven to be limited by C-H bond strength. The metal-centred oxidants are limited to substrates of BDE ≤ 81 kcal mol^{-1} presenting no oxidative reactivity toward cyclohexane or adamantane. $[Fe(TPA)(CH_3CN)_2](ClO_4)_2$ and $[Fe(BPMEN)(CH_3CN)_2](ClO_4)_2$ form metal-centred oxidants in the presence of H_2O_2 strong enough to facilitate oxidation of substrates with challenging C-H bonds of strengths ~ 100 kcal mol^{-1}.[141, 171, 172]

Oxidation of further substrates was undertaken to expand understanding on the capability of **C3** to perform OAT and HAB reactions. The **C3**/PhIO system was chosen to proceed with further studies as it gave the best evidence toward metal-centred oxidations. The stoichiometric reaction between **C3**/PhIO and PPh_3 yielded 100 % $OPPh_3$. $OPPh_3$ formation supports the ability of **C3** to perform OAT. Hydrogen abstraction reactions were probed by employing xanthene, DHA and triphenylmethane. Reactivity was found to be dependent on BDE, with a general trend of higher reactivity for substrates of lower BDE, when taking into account the number of actives species required per final product (Figure 43). The exception to the trend was DHA. Oxidation of DHA is the result of two HAB steps with no oxygen transfer step. This may make it longer for the **C3** active species to recycle as it is left in the Fe^{III}-OH state and hence may result in reduced reactivity.

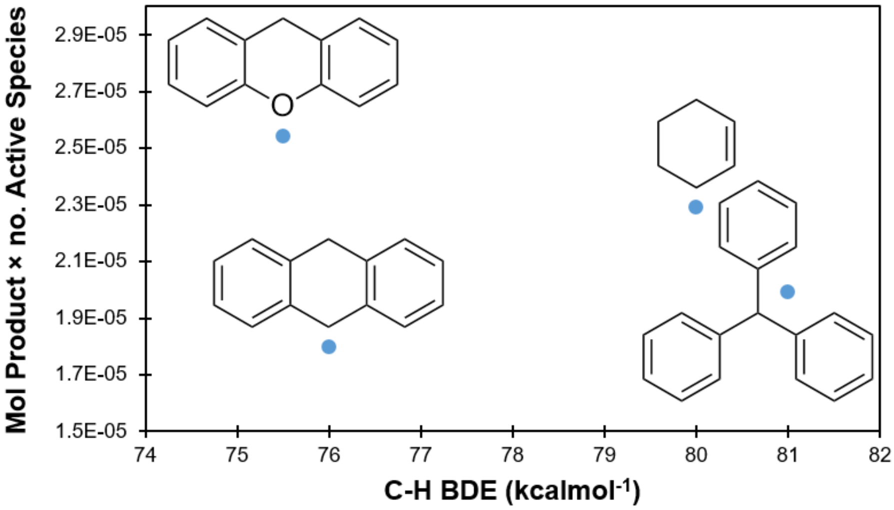

Figure 43. Correlation between Bond Dissociation Energy and Overall Reactivity per Oxidising Species.

Isotopic substitution of substrates to their deutero- counterparts provided evidence that **C3** operated *via* a hydrogen abstraction. The collated results of the reactivity studies demonstrate that the selectivity of **C3** is comparable to that of the aforementioned mono-nuclear complexes in oxidation of cyclohexene with the exception of the H_2O_2/**C2**/**C3** system. The second site does not appear to enhance activity as no increase in reactivity or selectivity is exhibited. There is a possibility that the second site may cause an inhibitory effect as poor results were obtained with H_2O_2. At this stage it is unclear how the two sites interact, independently or co-operatively, and so further spectroscopic studies to identify active species formed were undertaken and discussed in the following chapter; Chapter 4 – Spectroscopic Investigation into the Active Species facilitating Hydrocarbon Oxidation Using **C3**.

3.7 Experimental

Catalytic Oxidation Reactions of Hydrocarbons

In a typical reaction a CH_3CN solution (1.1 mL) containing **C2**, **C3** or $[Fe(CH_3CN)_6](PF_6)_2$ (2.7 mM) and substrate (0.9 M) was stirred briefly at room temperature followed by the addition of 0.1 mL of oxidant (CH_3CN, 0.3 M) added over 25 min. The reaction solution was stirred for a further 5 min. The exception to this was iodosylbenzene, which was added at once and allowed to stir for 30 min after which the reaction mixture was filtered through celite to remove any trace of unreacted solid PhIO, and the solution was subjected to GC-MS analysis. Reaction time was limited to 30 min as, after this stage, PhIO oxidises cyclohexene in the absence of **C2/3** (under analogous conditions). Products were identified by comparison to GC retention times and mass spectra of commercial samples. Products were quantified using a single point internal standard method, with fluorene as the standard. An internal response factor (IRF) was calculated in triplicate for each observed product, (2-cyclohexen-1-ol, 2-cyclohexen-1-one, cyclohexene oxide, anthracene and xanthone), using the formula:

IRFP = (AreaSTD × AmountP)/(AmountSTD × AreaP)

(P is the compound of interest and STD is the internal standard). Amounts of products in each reaction sample could then be calculated using the formula:

AmountP = (AreaP × AmountSTD × IRFP)/(AreaSTD)

Product yields represent the average of at least three repetitions.

Stoichiometric Oxidation Reaction with Triphenylphosphine

Iodosylbenzene (1.4 mg) was added to a CH_3CN solution of **C2/3** (1 mL, 2.7 mM). The mixture was stirred for 10 min, during which an observable colour change from pink to orange-brown was observed. The mixture was filtered to remove any trace unreacted PhIO and an aliquot subjected to GC-MS to confirm the presence of PhI vs. PhIO. Triphenylphosphine (1.6 mg) was then added to the mixture and allowed to stir for 1 hour. The reaction solution was analysed qualitatively by GC-MS and ^{31}P NMR spectroscopy; a complete shift from -6 ppm (PPh_3) to +27 ppm ($POPh_3$) was observed by ^{31}P NMR and only $POPh_3$ was detected in the GC-MS trace.

Synthesis of Deuterated Substrates

9,10-Dihydroanthracene-d_4 and xanthene-d_2 were prepared as per literature procedures.[116] 9,10-dihydroanthracene-*d4* was recrystallised twice from EtOH; 98 % deuterium incorporation was established based on ^1H NMR spectrum signal intensity of benzylic hydrogens at the C-9 and C-10 positions of DHA compared to aromatic hydrogens. A small amount of anthracene-*d2* was also present after this synthesis, as quantified by GC-MS; the amount of anthracene-*d2* originally present in samples of DHA-*d4* was considered in calculating the final amount of anthracene-*d2* generated in the reactions of **C3** with DHA-*d4*. Xanthene-*d2* was recrystallised twice from EtOH; 98 % deuterium incorporation was established based on the ^{1}H NMR spectrum signal intensity of the aliphatic hydrogens of xanthene compared to that of the aromatic hydrogens.

Synthesis of Reactants

Iodosylbenzene[226] and $[Fe(CH_3CN)_6](PF_6)_2$[227] were prepared as per literature procedures. The purity of $[Fe(CH_3CN)_6](PF_6)_2$ was confirmed by elemental analysis: Anal. Calcd for $C_{12}H_{18}N_6F_{12}P_2Fe_2$: C, 24.34; H, 3.06; N, 14.19. Found: C, 24.31; H, 3.04; N, 14.16. Iodosylbenzene purity was confirmed by elemental analysis (Anal. Calcd for C_6H_5IO C, 32.76; H, 2.29. Found: C, 32.88; H, 2.29) and by ^{1}H NMR (400 MHz, C_2D_6SO: δ 7.68 (d, *J* = 8.4 Hz, 2H), 7.34 (tt, *J* = 7.4, 1.2 Hz, 1H), 7.16 (td, *J* = 7.7, 1.7 Hz, 2H)).

3.8 References

(81) Roelfes, G.; Lubben, M.; Chen, K.; Ho, R. Y. N.; Meetsma, A.; Genseberger, S.; Hermant, R. M.; Hage, R.; Mandal, S. K.; Young, V. G. Jr.; Zang, Y.; Kooijman, H.; Spek, A. L.; Que, L. Jr.; Feringa B. L. *Inorg. Chem.* **1999**, *38*, 1929.

(83) Lindsay, S.; Lo, S. K.; Maguire, O. R.; Bill, E.; Probert, M. R.; Sproules, S.; Hess, C. R. *Inorg. Chem.* **2013**, *52*, 898.

(110) Arakawa, H.; Aresta, M.; Armor, J. N.; Barteau, M. A.; Beckman, E. J.; Bell, A. T.; Bercaw, J. E.; Creutz, C.; Dinjus, E.; Dixon, D. A.; Domen, K.; DuBois, D. L.; Eckert, J.; Fujita, E.; Gibson, D. H.; Goddard, W. A.; Goodman, D. W.; Keller, J.; Kubas, G. J.; Kung, H. H.; Lyons, J. E.; Manzer, L. E.; Marks, T. J.; Morokuma, K.; Nicholas, K. M.; Periana, R.; Que, L.; Rostrup-Nielson, J.; Sachtler, W. M. H.; Schmidt, L. D.; Sen, A.; Somorjai, G. A.; Stair, P. C.; Stults, B. R.; Tumas, W. *Chem. Rev.* **2001**, *101*, 953.

(111) Hess, C. R.; Welford, R. W. D.; Klinman, J. P.; Begley, T. P. In *Wiley Encyclopedia of Chemical Biology*; John Wiley & Sons, Inc.: 2007.

(112) Que, L.; Tolman, W. B. *Nature* **2008**, *455*, 333.

(113) Shilov, A. E.; Shulpin, G. B. *Chem. Rev.* **1997**, *97*, 2879.

(114) Wallar, B. J.; Lipscomb, J. D. *Chem. Rev.* **1996**, *96*, 2625.

(115) Lange, S. J.; Jr., L. Q. *Curr. Opinion Chem. Biol.* **1998**, *2*, 159.

(116) McDonald, A. R.; Que, L. *Coord. Chem. Rev.* **2013**, *257*, 414.

(117) Montellano, P. R. In *Cytochrome P450: Structure, Mechanism and Biochemistry*; Kluwer Academic/Plenum Publishers, 2005.

(118) Schlichting, I.; Berendzen, J.; Chu, K.; Stock, A. M.; Maves, S. A.; Benson, D. E.; Sweet, R. M.; Ringe, D.; Petsko, G. A.; Sligar, S. G. *Science* **2000**, *287*, 1615.

(119) Denisov, I. G.; Makris, T. M.; Sligar, S. G.; Schlichting, I. *Chem. Rev.* **2005**, *105*, 2253.

(120) Sono, M.; Roach, M. P.; Coulter, E. D.; Dawson, J. H. *Chem. Rev.* **1996**, *96*, 2841.

(121) Rosenzweig, A. C.; Frederick, C. A.; Lippard, S. J.; Nordlund, P. *Nature* **1993**, *366*, 537.

(122) Elango, N.; Radhakrishnan, R.; Froland, W. A.; Wallar, B. J.; Earhart, C. A.; Lipscomb, J. D.; Ohlendorf, D. H. *Protein Sci.* **1997**, *6*, 556.

(123) Shu, L.; Nesheim, J. C.; Kauffmann, K.; Münck, E.; Lipscomb, J. D.; Que, L. *Science* **1997**, *275*, 515.

(124) Lee, S.; Nesheim, J. C.; Lipscomb, J. D. *J. Biol. Chem.* **1993**, *268*, 21569.

(125) Costas, M.; Mehn, M. P.; Jensen, M. P.; Que, L. Jr. *Chem. Rev.* **2004**, *104*, 939.

(126) Bruijnincx, P. C. A.; van Koten, G.; Klein Gebbink, R. J. M. *Chem. Soc. Rev.* **2008**, *37*, 2716.

(127) Gibson, D. T.; Resnick, S. M.; Lee, K.; Brand, J. M.; Torok, D. S.; Wackett, L. P.; Schocken, M. J.; Haigler, B. E. *J. Bacteriol.* **1995**, *177*, 2615.

(128) Karlsson, A.; Parales, J. V.; Parales, R. E.; Gibson, D. T.; Eklund, H.; Ramaswamy, S. *Science* **2003**, *299*, 1039.

(129) Ferraro, D. J.; Gakhar, L.; Ramaswamy, S. *Biochem. Biophys. Res. Commun.* **2005**, *338*, 175.

(130) Roelfes, G.; Lubben, M.; Hage, R.; Que, L.; Feringa, B. L. *Chem. Eur. J.* **2000**, *6*, 2152.

(131) Lee, Y. M.; Hong, S.; Morimoto, Y.; Shin, W.; Fukuzumi, S.; Nam, W. *J. Am. Chem. Soc.* **2010**, *132*, 10668.

(132) Lyakin, O. Y.; Bryliakov, K.; Talsi, E. P. *Inorg. Chem.* **2011**, *50*, 5526.

(133) Jackson, T. A.; Rohde, J. U.; Seo, M. S.; Sastri, C. V.; DeHont, R.; Stubna, A.; Ohta, T.; Kitagawa, T.; Münck, E.; Nam, W.; Que, L. Jr. *Am. Chem. Soc.* **2008**, *130*, 12394.

(134) Solomon, E. I.; Brunold, T. C.; Davis, M. I.; Kemsley, J. N.; Lee, S.-K.; Lehnert, N.; Neese, F.; Skulan, A. J.; Yang, Y.-S.; Zhou, J. *Chem. Rev.* **2000**, *100*, 235.

(135) Oloo, W. N.; Feng, Y.; Iyer, S.; Parmelee, S.; Xue, G.; Que, L. Jr. *New J. Chem.* **2013**, *37*, 3411.

(136) de Visser, S. P.; Rohde, J. U.; Lee, Y. M.; Cho, J.; Nam, W. *Coord. Chem. Rev.* **2013**, *257*, 381.

(137) Chen, K.; Costas, M.; Que, J. L. *Dalton Trans.* **2002**, 672.

(138) Britovsek, G. J. P.; England, J.; White, A. J. P. *Inorg. Chem.* **2005**, *44*, 8125.

(139) Kim, C.; Dong, Y.; Que, L. *J. Am. Chem. Soc.* **1997**, *119*, 3635.

(140) Chen, K.; Que, L. Jr. *Am. Chem. Soc.* **2001**, *123*, 6327.

(141) Costas, M.; Chen, K.; Que, L. *Coord. Chem. Rev.* **2000**, *200-202*, 517.

(142) Company, A.; Prat, I.; Frisch, J. R.; Mas-Ballesté, D. R.; Güell, M.; Juhász, G.; Ribas, X.; Münck, D. E.; Luis, J. M.; Que, L.; Costas, M. *Chem. Eur. J.* **2011**, *17*, 1622.
(143) Burger, R. M. *Chem. Rev.* **1998**, *98*, 1153.
(144) Burger, R. M.; Peisach, J.; Horwitz, S. B.; *J. Biol. Chem.* **1981**, *256*, 11636.
(145) Sam, J. W.; Tang, X.-J.; Peisach, J. *J. Am. Chem. Soc.* **1994**, *116*, 5250.
(146) Neese, F.; Zaleski, J. M.; Zaleski, K. L.; Solomon, E. I. *J. Am. Chem. Soc.* **2000**, *122*, 11703.
(147) Xue, G.; Wang, D.; Hont, R. D.; Fiedler, A. T.; Shan, X.; Munck, E.; Que, L. Jr. *Proc. Natl. Acad. Sci.* **2007**, *104*, 20713.
(148) Xue, G.; Pokutsa, A.; Que, L. *J. Am. Chem. Soc.* **2011**, *133*, 16657.
(149) Xue, G.; De Hont, R.; Münck, E.; Que, L. Jr. *Nature Chem.* **2010**, *2*, 400.
(150) Ménage, S.; Vincent, J. M.; Lambeaux, C.; Fontecave, M. *J. Mol. Catal. A: Chem.* **1996**, *113*, 61.
(151) Park, M. J.; Lee, J.; Suh, Y.; Kim, J.; Nam, W. *J. Am. Chem. Soc.* **2006**, *128*, 2630.
(152) Walling, C. *Acc. Chem. Res.* **175**, *8*, 125.
(153) Gozzo, F. *J. Mol.Catal. A: Chem.* **2001**, *171*.
(154) Patra, A. K.; Olmstead, M. M.; Mascharak, P. K. *Inorg. Chem.* **2002**, *41*, 5403.
(155) Holland, P. L.; Rodgers, K. R.; Tolman, W. B. *Angew. Chem. Int. Ed.* **1999**, *38*, 1139.
(156) Ryan, S.; Adams, H.; Fenton, D. E. *Inorg. Chem.* **1998**, *37*, 2134.
(157) Nam, W. *Acc. Chem. Res.* **2007**, *40*, 522.
(158) Perkins, M. J. *Chem. Soc. Rev.* **1996**, *25*, 229.
(159) Buxton, G. V.; Greenstock, C. L.; Helman, W. P.; Ross, A. B. *J. Phys. Chem. Ref. Data* **1988**, *17*, 513.
(160) MacFaul, P. A.; Ingold, K. U.; Wayner, D. D. M.; Que, L. *J. Am. Chem. Soc.* **1997**, *119*, 10594.
(161) Winkler, F. J. *Angew. Chem.* **1981**, *93*, 220.
(162) Nesheim, J. C.; Lipscomb, J. D. *Biochem.* **1996**, *35*, 10240.
(163) Cook, S. A.; Ziller, J. W.; Borovik, A. S. *Inorg. Chem.* **2014**, *53*, 11029.
(164) Johansson, A. J.; Blomberg, M. R. A.; Siegbahn, P. E. M. *J. Phys. Chem. C* **2007**, *111*, 12397.
(165) Manka, M. J.; Stein, S. E. *J. Phys. Chem.***1984**, *88*, 5914.
(166) Bell, S. R.; Groves, J. T. *J. Am. Chem. Soc.* **2009**, *131*, 9640.
(167) Cho, K.; Leeladee, P.; McGown, A. J.; DeBeer, S.; Goldberg, D. P. *J. Am. Chem. Soc.* **2012**, *134*, 7392.
(168) Prat, I.; Company, A.; Postils, V.; Ribas, X.; Que, L.; Luis, J. M.; Costas, M. *Chem. Eur. J.* **2013**, *19*, 6724.
(169) Barton, D. H. R.; Beck, A. H.; Taylor, D. K. *Tetrahedron* **1995**, *51*, 5245.
(170) Furukawa, S.; Hitomi, Y.; Shishido, T.; Tanaka, T. *Inorg. Chim. Acta* **2011**, *378*, 19.
(171) Chen, K.; Que Jr, L. *Chem. Commun.* **1999**, 1375.
(172) Kim, C.; Chen, K.; Kim, J.; Que, L. *J. Am. Chem. Soc.* **1997**, *119*, 5964.
(173) Kojima, T.; Leising, R. A.; Yan, S.; Que, L. *J. Am. Chem. Soc.* **1993**, *115*, 11328.
(174) Leising, R. A.; Norman, R. E.; Que, L. *Inorg. Chem.* **1990**, *29*, 2553.
(226) Barbour, C. J. C.; Winfield, J. H. *J. Chem. Soc., Dalton Trans* **1980**, 2001.
(227) Sharefkin, J. G. S. *Organic Syntheses, Coll.* **1973**, *5*, 658.

Chapter 4 – Spectroscopic Investigation into the Active Species Facilitating Hydrocarbon Oxidation Using C3

A vast range of mono-nuclear and di-nuclear Fe-oxygen model complexes have been isolated and spectroscopically characterised in the literature allowing for the compilation of a spectroscopic library. Model complexes can be grouped according to the structure of the Fe-oxygen core, *e.g.* Fe-OOH or Fe=O. Characteristic spectroscopic features of each category can be identified and compared to biological systems, aiding in the identification of active species formed during catalytic cycles of metalloenzymes, an otherwise difficult process due to the large protein environment enveloping the active site. Each category of Fe-oxygen compounds display preferences toward certain oxidative transformations. Identifying the relationship between active species and reactivity allows for the systematic development of bio-inspired catalysts to increase reactivity and/or selectivity toward a specific substrate. In this chapter, the species formed upon exposure of complex **C3** to PhIO, H_2O_2 and ^{t}BuOOH have been analysed by several spectroscopic techniques. Kinetic studies of the **C3**/PhIO system have been carried out in the absence and presence of DHA substrate. In the absence of DHA, spectroscopic studies of **C3**/PhIO uncovered the formation of a transient species, labelled **C7**, identified by a UV-Vis λ_{max} 430 nm, this species decayed to a di-ferric species labelled **C8**. In the presence of DHA, studies of **C3**/PhIO revealed the possible existence of two active species, differing in reactivity by a factor of 20. The lesser active species has been identified as the transient complex **C7**, while the structural identity of the more active species labelled **C**^{ox}, has remained elusive to variable temperature UV-Vis spectroscopy (-5 °C – 25 °C).

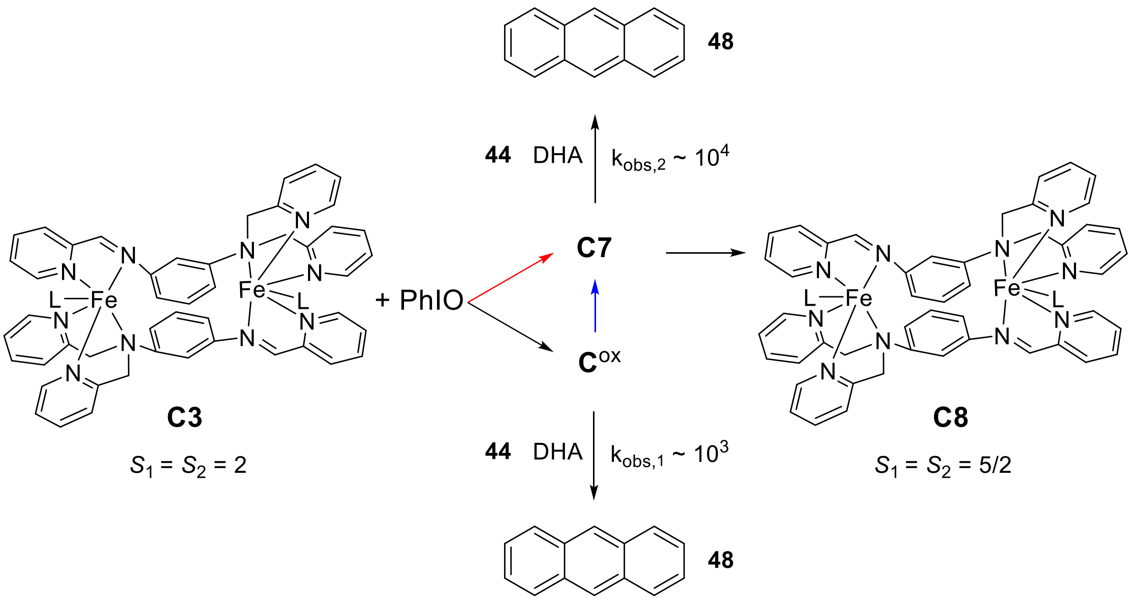

Scheme 34. Mechanistic Data Obtained in this Chapter during Oxidation of DHA by C3/PhIO.

4.1 Introduction

High-valent Fe-oxygen compounds have been unveiled as the active species for important biological oxidations.[111 - 113, 120, 175] For example, the active species of the versatile heme iron CP450 is a high-valent Fe^{IV}=O-($\mathbf{P}^{\cdot+}$ = oxidised porphyrin radical) **(32)**.[117 - 120] Extensive studies of the di-nuclear non-heme iron MMO active site has identified two active, interchangeable, oxygen bridged species; a (μ-1,2-peroxo)$Fe^{III}Fe^{III}$ species (commonly referred to as **P**) and the high valence $(\mu\text{-}O)_2Fe^{IV}Fe^{IV}$ species (commonly referred to as **Q**) **(10)**.[114, 122, 123, 176, 177] Studies of the Rieske dioxygenase catalytic cycle have identified an Fe^{III}-OOH species, but it is postulated that it isomerises to a more active high valence Fe^{V}=O(OH) species **(33)**.[126 - 129, 178] The generation and capabilities of each active species highlighted here is discussed in more detail in Chapter 3 – Oxidation of Hydrocarbons by Di-ferrous **C2** and **C3**. The study of model complexes has aided in the characterisation of active species in biological systems, an otherwise difficult feat due to the protein environment enveloping the active site. Information accrued from the highly active biological systems, in turn, allows for systematic design of bio-inspired catalysts.[133 - 137] Bio-inspired complexes displaying reactivity toward unactivated hydrocarbons have been isolated in many forms including; Fe^{III}-superoxo, Fe^{III}-peroxo, Fe^{IV}-oxo and $Fe_2(\mu\text{-}O)_2$ species. Isolation and characterisation of each of the various species allows for the compilation of a spectroscopic library. A brief overview of the spectroscopic characteristics for common Fe-oxygen categories will follow to provide insight to the data collected for **C3**.

4.1.1 Characteristic Spectroscopic Features of Bio-Inspired Mono-Nuclear Iron Model Complexes

Fe^{III}-OOH species have been synthetically generated upon addition of H_2O_2 to ferrous model complexes.[130, 178 - 180] The ferric ion of the synthetically produced species is most commonly found in the low-spin configuration, $S = 1/2$, in contrast to those of biological systems which are most commonly found in the high-spin, $S = 5/2$, configuration.[130, 178, 180] The synthetic low-spin Fe^{III}-OOH species can be categorised by several spectroscopic features;[148, 178 - 185]

- EPR signals of 2.2, 2.1 and 2.0.
- Mössbauer doublets typical of low-spin Fe^{III}; δ 0.17, ΔE_Q 2.0.
- Resonance Raman Fe-O and O-O vibrations at ~ 615 – 645 cm^{-1} and 780 – 806 cm^{-1}, respectively.
- A peroxo-Fe^{III} ligand to metal charge transfer (LMCT) band at ~ 540 nm in the absorption spectrum.

The features highlighted above have been assembled through the characterisation of a vast series of model complexes, however they are not exclusive. One example that deviates from the norm is based on the ligand scaffold TMC **(51)**. $[Fe^{III}(OOH)^{-}(TMC)]^{2+}$ has shown spectroscopic characteristics outside the typical ranges with a UV-Vis λ_{max} (ε M^{-1} cm^{-1}) at 500 nm (450), resonance

Raman bands at νFe-O 676 cm^{-1}, νO-O 870 cm^{-1} and Mössbauer parameters of δ 0.58, ΔE_Q 0.92 (Table 9, entry 5).[178] The spectroscopic ranges are therefore an aid to characterising novel species but are not definitive, ligand scaffold and other characteristics of the coordination sphere affect spectroscopy. The model hydroperoxo species can be synthetically inter-converted to their conjugate bases; side-on peroxo species (Scheme 35).[178, 182 - 186]

The side-on peroxo species, in contrast to their hydroperoxo counterparts, typically exist in the high-spin configuration, S = 5/2.[178, 183] A significant red shift in absorption spectra is observed after the conversion to side-on peroxo counterparts, consistent with the weaker basicity of the hydroperoxo mono-anion relative to the peroxo di-anion.[187] Characteristic resonance Raman Fe-O and O-O vibrations at 460 – 490 cm^{-1} and 816 – 850 cm^{-1}, respectively, alongside Mössbauer parameters typical of high-spin Fe^{III}, δ 0.61, ΔE_Q 1.11 can be used to identify side-on peroxo species (Scheme 35, Table 9).[178, 183 - 186] The side-on peroxo complex supported by TMC (**51**), $[Fe^{III}(O_2)^{2-}(TMC)]^+$, once again displays spectroscopic characteristics outside of the typical range with a λ_{max} (ε M^{-1} cm^{-1}) 835 nm (650) and Mössbauer parameters of δ 0.51, ΔE_Q 0.20 (Table 9, entry 6).[187]

The Fe^{IV}O species can be synthetically generated upon addition of single oxygen atom oxidants, such as PhIO and *meta*-chloroperbenzoic acid (*m*-CPBA), to ferrous model complexes.[116, 136, 178] As with Fe^{III}-OOH the iron ions in the synthetically produced complexes typically exist in the low-spin configuration, S = 1, in contrast to biological systems that most commonly exist in the high-spin, S = 2 configuration.[116, 136, 178] Synthetic low-spin Fe^{IV}O species can be categorised by several spectroscopic features;[178, 184, 185, 189]

- Mössbauer doublets typical of low-spin Fe^{II}; δ 0.01, ΔE_Q 0.90.
- Resonance Raman Fe-O vibration at ~ 750 – 850 cm^{-1}.
- Perhaps the most distinguishable feature; ligand field band at ~700 nm in the absorption spectrum.

Once again the Fe-oxo species supported by TMC (**51**), $[Fe^{IV}(O)^{2-}(TMC)(CH_3CN)]^{2+}$, exhibits spectroscopic characteristics outside of the typical range with a UV-Vis λ_{max} (ε M^{-1} cm^{-1}) at 820 nm (400) and Mössbauer parameters of δ 0.17, ΔE_Q 1.23 (Table 9, entry 11).[136, 178]

The Fe^{V}O species inferred as the active species in catalytic cycles of some synthetic and enzymatic systems have been more elusive toward characterisation due to their high reactivity and so low stability.

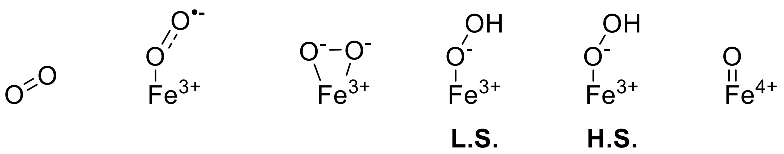

Type of Species	dioxygen	Fe-superoxo	Fe-peroxo Side-on	Fe-hydroperoxo		Fe-oxo
O-O Bond Order	2	1.5	1	1	1	0
O-O Av. Bond Length (A)	1.21	1.33	1.49			
υFe-O (cm^{-1})		530 - 580	460 - 490	615 - 645	500 - 620	750 - 850
$\Delta^{18}O$ (cm^{-1})		(-70)	(-40 - 48)	(-40 - 48)	(-48)	(-26 - 40)
υO-O (cm^{-1})	1580	1135 - 1150	816 - 850	780 - 806	830 - 850	
$\Delta^{18}O$ (cm^{-1})		(-25)	(-13 - 20)	(-13 - 20)	(-13 - 24)	

Scheme 35. Structural Characterisation of Model Mono-Nuclear Iron – Oxygen Species.[184, 185]

Table 9. Spectroscopic Characterisation of Model Mono-Nuclear Iron-Oxygen Species. [116, 136, 178, 181, 187]

Entry	Active Species	*S* of Fe	Absorption Spectroscopy	EPR	Vibration Spectroscopy		Mössbauer Spectroscopy	
			λ_{max} nm (ε M^{-1} cm^{-1})		νFe – O (cm^{-1})	νO – O (cm^{-1})	δ	ΔE_Q
1	$[Fe^{III}(OOH)^{-}(BLM)]^{2+}$	1/2		2.26, 2.17, 1.94			0.1	-3.0
2	$[Fe^{III}(OOH)^{-}(N4Py)]^{2+}$	1/2	547 (1300)	2.16, 2.12, 1.98	632	790	0.17	1.62
3	$[Fe^{III}(O_2)^{2-}(N4Py)]^{+}$	5/2	685 (520)	2.00, 2.00, 2.00	495	827	0.61	1.11
4	$[Fe^{III}(OOH)^{-}(TPA)]^{2+}$	1/2	538 (1050)	2.19, 2.15, 1.97	626	789		
5	$[Fe^{III}(OOH)^{-}(TMC)]^{2+}$	1/2	500 (450)	2.00, 2.00, 2.00	676	870	0.58	0.92
6	$[Fe^{III}(O_2)^{2-}(TMC)]^{+}$	5/2	835 (650)	2.06, 2.04, 2.01	493	826	0.51	0.20
7	$[Fe^{III}(OOH)^{-}(TPEN)]^{2+}$	1/2	541 (900)	2.22, 2.15, 1.97	617	796	0.17	2.07
8	$[Fe^{III}(O_2)^{2-}(TPEN)]^{+}$	5/2	755 (450)	2.00, 2.00, 2.00	470	817	0.63	1.12
9	$[Fe^{III}(OO^{t}Bu)^{-}(TPA)(H_2O)]^{2+}$	1/2	600 (2200)	1.98, 2.19, 2.14	696	796		
10	$[Fe^{III}(OO^{t}Bu)^{-}(6\text{-}MeTPA)(H_2O)]^{2+}$	1/2	598 (2000)	1.97, 2.20, 2.12	682	790		
		5/2		4.3	648	842, 878		
11	$[Fe^{III}(OO^{t}Bu)^{-}(6\text{-}Me_2TPA)(H_2O)]^{2+}$	5/2	552 (2000)	4.3	647	843, 881		
12	$[Fe^{IV}(O)^{2-}(N4Py)]^{2+}$	1	693 (400)		841		-0.04	0.93
13	$[Fe^{IV}(O)^{2-}(TPA)(CH_3CN)]^{2+}$	1	724 (300)				0.01	0.93
14	$[Fe^{IV}(O)^{2-}(TMC)(CH_3CN)]^{2+}$	1	820 (400)		834		0.17	1.23
15	$[Fe^{IV}(O)^{2-}(TPEN)]^{2+}$	1	730 (380)				0.01	0.87

4.1.2 Characteristic Spectroscopic Features of Bio-Inspired Di-Nuclear Iron Model Complexes

Di-nuclear model complexes most commonly exist as bridged Fe-O-Fe species. [123, 148, 150, 178, 190 - 193] They can contain one or more oxygen bridge which can take various forms; oxo di-anions (O^{2-}), peroxo di-anions (O_2^{2-}) or hydroxyl anions (OH^-) (Scheme 36, Table 10). The two iron ions can exist in the same oxidation state, typically III/III or IV/IV, but can also exist as a mixed valence species, typically III/IV. There are more factors to consider when characterising di-nuclear iron species, thus they are more complex to distinguish than mono-nuclear counterparts.

Raman spectroscopy is a powerful tool for divulging information about the structural conformation of di-iron oxygen bridged cores. Firstly, the presence of O-O vibrations can indicate a peroxo bridge over an oxo or hydroxyl bridge. Secondly, the energy of the Fe-O vibration correlates to the Fe-O-Fe angle, which can used to distinguish between a mono- or di-oxygen bridged species.[187] An Fe-O-Fe unit has two theoretical stretching vibrations arising from the two Fe-O bonds, the extent to which the two vibrations are coupled depends on the Fe-O-Fe angle. The strongest coupling is observed for linear Fe-O-Fe bridges, more common for mono-bridged species, with the symmetric combination ν_{sym}(Fe-O-Fe) observed in the Raman spectra at ~ 350 cm^{-1} and the asymmetric combination ν_{asym}(Fe-O-Fe) observed at ~ 850 cm^{-1} in the infrared (IR) spectra.[178] As the Fe-O-Fe angle becomes more acute, more common for di-bridged species due to steric hinderance, the coupling interaction weakens and the two vibrations start to converge to a common value, for example, complexes with $Fe_2(\mu\text{-}O^{2-})_2$ cores exhibit a prominent Raman peak at ~ 650 - 690 cm^{-1} (Table 10).[187] The presence of a second oxygen bridge does not equate to the observation of a second Raman Fe-O peak if the two iron ions are in the same oxidation state; the single Raman peak is representative of the entire tetra-atomic core. If, however, the III/IV mixed valence form is present, two peaks are observed in the Raman spectrum so Raman spectroscopy can thirdly be used to identify mixed valence di-nuclear species (Table 10, entry 2 and 7).

The inequivalent oxidation state of III/IV mixed valence di-nuclear complexes can also be observed using Mössbauer spectroscopy by the presence of two quadrupole doublets (Table 10, entry 5 and 9). However, in some cases when both iron cations exist in the low-spin configuration, a single quadrupole doublet of δ 0.14 mms^{-1} is observed due to valence delocalisation of the Fe^{III} Fe^{IV} centre (Table 10, entry 1, 2 and 7).[187]

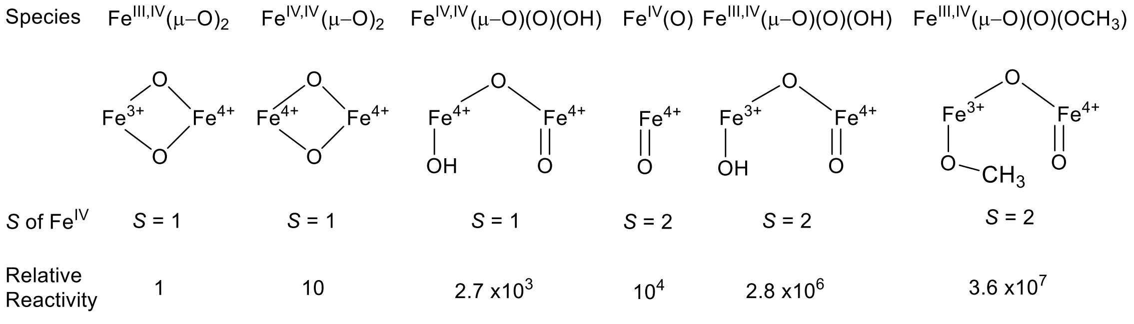

Scheme 36. Structural Comparison and Reactivity of Iron-Oxygen Species toward Unactivated Hydrocarbon Oxidation.[148]

Table 10. Spectroscopic Characterisation of Model Di-Nuclear Iron-Oxygen Species.[178, 191 - 196]

Entry	Active Species	Absorption Spectroscopy λ_{max} nm (ε M^{-1} cm^{-1})	Vibration Spectroscopy νFe – O (cm^{-1})	Mössbauer Spectroscopy	
				δ	ΔE_Q
1	$[Fe^{III},^{IV}(\mu\text{-}O^{2-})_2(TPA)_2]^{3+}$		666	0.13	0.5
2	$[Fe^{III},^{IV}(\mu\text{-}O^{2-})_2(5\text{-}Me_3\text{-}TPA)_2]^{3+}$	615 (5800)	656, 676	0.14	0.49
3	$[Fe^{III,III}(\mu\text{-}O^{2-})(\mu\text{-}OH^{-})(5\text{-}Me_3\text{-}TPA)_2]^{3+}$	550 (780)			
4	$[Fe^{III,III}(\mu\text{-}O^{2-})_2(6\text{-}Me_3\text{-}TPA)_2]^{2+}$			0.50	1.93
5	$[Fe^{III,IV}(\mu\text{-}O^{2-})_2(6\text{-}Me_3\text{-}TPA)_2]^{2+}$			0.10, 0.50	1.14, 1.30
6	$[Fe^{III,III}(\mu\text{-}O^{2-})(\mu\text{-}OH^{-})(6\text{-}Me_3\text{-}TPA)_2]^{3+}$	550 (670)		0.51	1.66
7	$[Fe^{III,IV}(\mu\text{-}O^{2-})_2(((CH_3)_2OCH_3)_3\text{-}TPA)_2]^{3+}$	620 (5300)	655, 667	0.11	0.44
8	$[Fe^{IV,IV}(\mu\text{-}O^{2-})_2(((CH_3)_2OCH_3)_3\text{-}TPA)_2]$	485 (9200) 875 (2200)	674	-0.04	2.06
9	$[Fe^{III,IV}(\mu\text{-}O^{2-})(O)(OH)(((CH_3)_2OCH_3)_3\text{-}TPA)_2]$	450		0.4, 0.09	0.6, 0.4
10	$[Fe^{IV,IV}(\mu\text{-}O^{2-})(O)(OH)(((CH_3)_2OCH_3)_3\text{-}TPA)_2]$			0.0, -0.03	1.96, 0.92
11	$[Fe^{III,III}(\mu\text{-}O^{2-})(OH^{-})(BPMEN)_2]^{3+}$	555 (700), 512 (540)			

Complex **C3** is di-nuclear, however, due to the large Fe···Fe distance it is unclear whether each iron site within the complex will react independently of the other during hydrocarbon oxidation, resembling two mono-nuclear sites in close proximity, or whether the sites will have an enhanced or impeding effect on reactivity. Comparisons of the spectroscopic data obtained for the **C3**/oxidant systems to literature trends are hoped to unveil information about the active species formed and in turn shed light on the dual site effect.

4.2 Reactivity of C3 with Common Oxidants at 298 K

Preliminary absorption and Raman spectroscopic studies were undertaken whereby complex **C3** was exposed to oxidants H_2O_2, ^tBuOOH and PhIO, in attempt to characterise the possible active species formed prior to hydrocarbon oxidation. Complex **C3** exhibits an MLCT band in the absorption spectrum at λ_{max} (ε M^{-1} cm^{-1}) 510 nm (1060 M^{-1} cm^{-1}) in CH_3CN. Upon addition of 2 eq. of H_2O_2, under an inert atmosphere in CH_3CN, the MLCT transition at 510 nm increased in absorbance, over a period of 10 min, to a plateau (~ 2000 M^{-1} cm^{-1}) with a slight red-shift to 521 nm (Figure 44, Left). A visible change of the solution from pink to deep red/purple was observed.

A trend between the number of coordinated pyridine units and the energy of the LMCT band of the Fe^{III}-OOH species has been established within literature.[183] Of a series of ligands investigated those with five coordinating pyridine units displayed an LMCT at 592 nm, four coordinating pyridine units at 548 nm and three coordinating pyridine units at 530 – 541 nm, while $[Fe^{III}(OOH)^{-}TMC]^{2+}$ with zero coordinating pyridine units gave the highest energy transition at 500 nm. This trend was proposed to be the result of the π-accepting power of pyridine which increases that of the

Fe^{III}. The transition of **C3**/H_2O_2 at 521 nm is close to the value given for three coordinated pyridine units to an Fe^{III}-OOH, so from the absorption data it is possible that a low spin, $S = 1/2$, Fe^{III}-OOH species is formed. However, the formation of the Fe^{III}-OOH species is not definitive. The change displayed in the UV-Vis spectra could also be a shift in the MLCT of complex **C3** due to other changes in the coordination sphere, but Fe^{III}-OOH formation can still be taken into consideration at this stage.

Fe^{III}-OO^{t}Bu species, generated upon addition of ^{t}BuOOH to ferrous model complexes, exhibit distinguishable absorption spectra with a peroxo-Fe^{III} LMCT band at ~ 600 nm.[183] Upon addition of 2 eq. ^{t}BuOOH to complex **C3**, under inert atmosphere in CH_3CN, no change in absorbance or energy of the **C3** CT band was observed by UV-Vis spectroscopy (Figure 44, Right). The only difference between the spectra was a slight broadening of the band around 450 – 500 nm in the latter (solid line *vs.* dashed line). The reaction was monitored by UV-Vis for a 10 min period in case the reaction was sluggish, but no further changes were observed. A visual change of the solution from pink to orange was observed. Based on the absorption data alone it is not possible to propose a possible structure for the species formed between **C3**/^{t}BuOOH. The formation of an Fe^{III}-OO^{t}Bu species seems unlikely as the characteristic LMCT band at ~ 600 nm is not observed, but cannot be wholly excluded based on UV-Vis data as there are exemptions to the typical ranges found in literature.

Fe^{IV}O species, generated upon addition of PhIO to ferrous model complexes, exhibit distinguishable absorption spectra with an ligand field band at ~ 700 nm of relatively weak intensity; ~ 400 M^{-1} cm^{-1}.[116, 157, 178, 189] Upon addition of 2 eq. of PhIO, under inert atmosphere in CH_3CN, the CT band of **C3** decreased slightly in intensity but without the observation of any NIR band. The reaction mixture had to stir for 10 min until complete dissolution of solid PhIO was achieved in CH_3CN and hence before a spectra could be recorded. It is a possibility that an Fe^{IV}O species formed may have been short lived and decayed within this 10 min period. The absorption spectrum of the reaction between **C3** and PhIO is studied in more depth in this chapter in Sections 4.3 and 4.4 and so no further analysis will ensue in this section but to state the ligand field band characteristic of Fe^{IV}O species was not observed under these conditions.

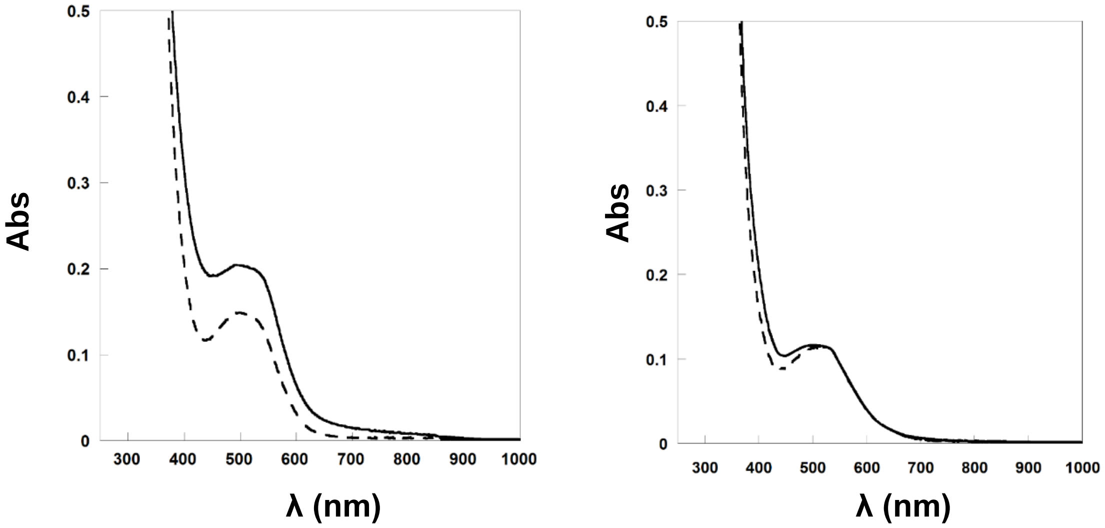

Figure 44. Left: Absorption Spectrum of C3 (1 ×10^{-4} M) (Dashed Line) and After Addition of 2H_2O_2 (Solid Line). Solvent = CH_3CN; 298 K. Right: Absorption Spectrum of C3 (1 ×10^{-4} M) (Dashed Line) and After Addition of 2^{t}BuOOH (Solid Line). Solvent = CH_3CN; 298 K.

Raman spectroscopy was employed to analyse the **C3**/H_2O_2, **C3**/^{t}BuOOH and **C3**/PhIO species. For all three **C3**/H_2O_2, **C3**/^{t}BuOOH and **C3**/PhIO species, the Raman spectra obtained exhibited weak peaks, which made it difficult to differentiate species peaks from background noise. Spectra of both solid and frozen solution states were collected at both 532 nm and 634 nm excitation wavelengths in attempt to obtain spectra exhibiting stronger peaks but to no success. The best spectra obtained can be found in the Appendix. For all three **C3**/H_2O_2, **C3**/^{t}BuOOH and **C3**/PhIO species a peak around 650 cm^{-1} could be distinguished from the background noise. A peak at this energy is consistent with the energy of Fe-O stretches suggesting the successful substitution of labile ligands to form Fe-O species'. The **C3**/PhIO species gave the strongest spectrum with a peak at 653 cm^{-1} evidently observed, a much lower energy than expected for an $Fe^{IV}O$ species with an Fe-oxygen double bond, typically observed in the range of 750 – 850 cm^{-1}.[178] The lower energy of the band could be indicative of a weaker Fe-O bond, possibly a single bond. No further analysis could be drawn due to the poor quality of the spectra.

Little information could be gleaned from these initial spectroscopic studies. It is possible that the reaction of complex **C3** with H_2O_2 forms an Fe^{III}-OOH species based on UV-Vis spectroscopy, while the formation of an Fe^{III}-OO^{t}Bu species upon addition of ^{t}BuOOH seems unlikely based on UV-Vis spectroscopy and the reaction of complex **C3** with PhIO under these conditions possibly forms a species with a single Fe-O bond based on Raman spectroscopy. These statements are presumptuous at this stage but are simply initial suggestions based on the little information collected thus far, and further analysis is required. The **C3**/PhIO system was chosen to be studied in more depth as reactivity studies from Chapter 3 suggested it was the most promising system for metal-centred oxidation, with degradation of H_2O_2 effecting the **C3**/H_2O_2 system and exceeding product yields suggesting the participation of radical-based reactions in the **C3**/^{t}BuOOH system or handling errors making data inaccurate.

4.3 Variable Temperature Absorption Spectroscopy of C3 with PhIO

As outlined in the previous section, the signature Fe^{IV}O transition at ~ 700 nm transition was not observed by absorption spectroscopy on reaction of PhIO with complex **C3** in CH_3CN at 25 °C. Literature studies have established that Fe^{IV}O species are often unstable at 25 °C, and indeed at temperatures above –40 °C, which has made characterisation of the species problematic. In an attempt to identify the existence of this high-valent species within our system, complex **C3** was reacted with PhIO in CH_3CN/CH_3OH solutions (10/1) at -5 °C and the reaction was monitored by absorption spectroscopy (Figure 45). The CH_3CN/CH_3OH (10/1) solvent mixture was chosen to ensure the complete dissolution of solid PhIO, which allows spectra to be recorded immediately after addition with no unmonitored reaction time. Complex **C3** displays two MLCT bands at λ_{max} nm (ε M^{-1} cm^{-1}) 528 (2430) and 578 (2150) in CH_3CN/CH_3OH (10/1). There was no change in the absorption spectrum of complex **C3** at -5 °C after addition of PhIO. The reaction was monitored at this temperature for 10 min with no further spectral changes observed (Figure 45, red spectrum). The reaction mixture was progressively warmed to 0 °C and monitored for 10 min. A small decrease in the absorbance of the MLCT bands were observed with an increase in absorbance at ~ 430 nm (Figure 45, blue spectrum). The reaction mixture was progressively warmed to 15 °C, the MLCT bands of **C3** decreased further in absorbance over the 10 min monitoring period with an increase in absorbance at ~ 430 nm (Figure 45, green spectrum). The reaction mixture was progressively warmed to 25 °C, the absorbance of the MLCT bands of **C3** depleted quickly at this temperature with an increase in absorbance at ~ 430 nm (Figure 45, black spectrum). At all temperatures studied we did not observe the formation of any NIR features, ~ 700 nm, commonly associated with Fe^{IV}O species.

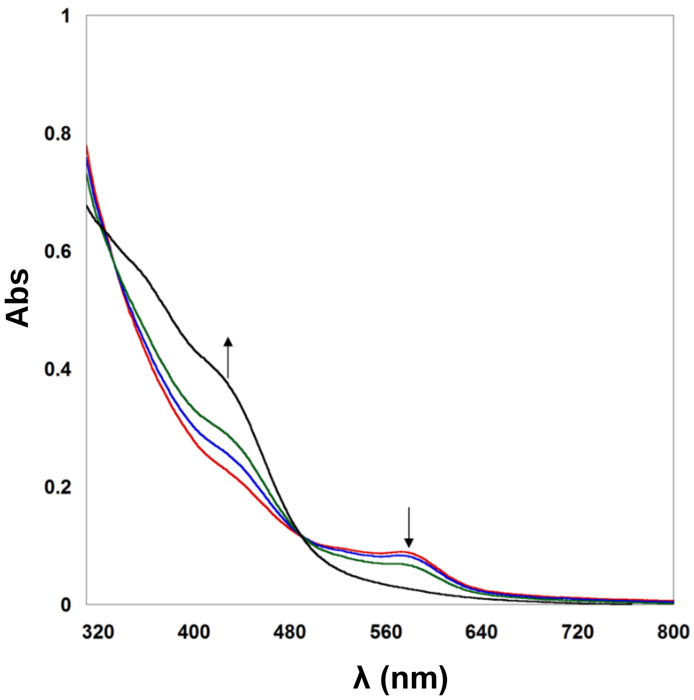

Figure 45. UV−Vis Spectroscopic Changes for the Reaction of C3 (4.7 ×10^{-5} M) with 25 eq. PhIO (1.2 ×10^{-3} M) at Varied Temperature (-5 °C – 25 °C; Red Trace = -5 °C, Blue Trace = 0 °C, Green Trace = 15 °C, Black Trace = 25 °C). Traces Represent Final Spectrum Taken After 10 min Monitoring Period at Each Temperature. Solvent = CH_3CN/CH_3OH (10/1).

The absence of the characteristic NIR band does not entirely exclude the possibility of $Fe^{IV}O$ formation. The initial formation of a short lived $Fe^{IV}O$ species has not been excluded. Britovsek and co-workers could not identify an $Fe^{IV}O$ species by absorption spectroscopy from the reaction between ferrous $[Fe(BPAbipy)(CH_3CN)](ClO_4)_2$ complex and PhIO at temperatures below 0 °C.[197] These findings echo our own during variable temperature experiments between **C3** and PhIO. At 0 °C and above, Britovsek and co-workers witnessed a rapid reaction between the ferrous complex and PhIO, resulting in the formation of the di-nuclear bridged species $[(Fe(BPAbipy))_2(\mu\text{-}O)]^{4+}$, which was isolated and characterised. Britovsek postulated the reaction between the ferrous complex and PhIO initially generated the high valence $[Fe^{IV}(O)(BPAbipy)]^{2+}$ species which is declared short lived due to its high reactivity, rapidly forming the isolated $[(Fe^{III}(BPAbipy))_2(\mu\text{-}O)]^{4+}$ species upon reaction with a second ferrous molecule.[197] Britovsek proposed the strong field BPAbipy ligand had a destabilising effect on the intermediate high valence $Fe^{IV}O$ species, leading to its short lifetime. Owing to the similarities between L^1 and BPAbipy, our ligand scaffold may have the same destabilising effect on an initially generated $Fe^{IV}O$ species, making characterisation challenging and leading our complex to also favour the formation of an Fe-O bridged species. Oxygen-bridged di-iron species have been isolated with a series of pentadentate ligand scaffolds similar to L^1 and BPAbipy suggesting the mono-bridged structure is favourable; $SBPy_3$, TPOEN and N4Py (Scheme 37). The μ-O bridged dimer formed by $SBPy_3$ exhibits strong, high energy transitions in the absorption spectrum; λ_{max} (ε M^{-1} cm^{-1}) = 366 (7220), 310 (11830),[79] as does the μ-O bridged dimer formed by TPOEN; λ_{max} (ε M^{-1} cm^{-1}) = 354 (10900),[80] and N4Py; λ_{max} (ε M^{-1} cm^{-1}) = 316 (14000).[81]

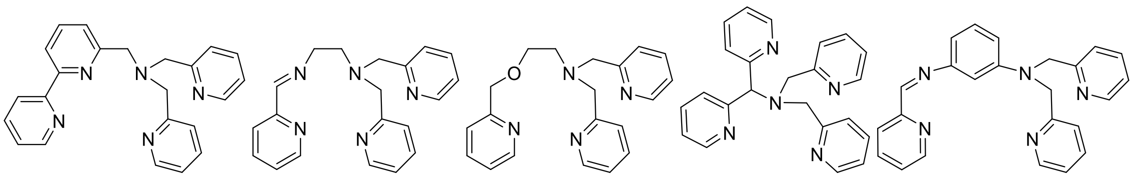

BPAbipy **26**

$SBPy_3$ **25**

TPOEN **27**

N4Py **36**

L^1 **21**

Scheme 37. Pentadentate Ligands with a Similar Scaffold to L^1 that Preferentially Form μ-O Bridged Species.

A short lived species is not the only explanation for the lack of an NIR band for an $Fe^{IV}O$ intermediate, if such as species is present. An example of a stable species with a terminal $Fe^{IV}O$ unit that does not exhibit the characteristic NIR band is the mixed valence species $[Fe^{III}Fe^{IV}(\mu\text{-}O^{2-})(O)(OH)(((CH_3)_2OCH_3)_3\text{-}TPA)_2]$, which exhibits a sole transition at 450 nm in the UV-Vis range.[187] $[Fe^{III}Fe^{IV}(\mu\text{-}O^{2-})(O)(OH)(((CH_3)_2OCH_3)_3\text{-}TPA)_2]$ has other distinguishing features including a μ-oxo bridge and an Fe^{III}-OH terminal unit and so the 450 nm feature cannot be compared directly to the 430 nm band exhibited by **C3**/PhIO, but the absence of ~ 700 nm band can be noted. In addition, several $[Fe^{III},Fe^{IV}O]$ and $[Fe^{II},Fe^{IV}O]$ intermediates characterised in bi-nuclear non-heme enzymes and synthetic compounds absorb solely in the UV-visible region (λ_{max} = 385 – 430 nm) without exhibiting an NIR band therefore the formation of a similar mixed valence species may also be possible with our system resulting in the absence of NIR bands.[116, 198] At this stage the formation of an $Fe^{IV}O$ species can be neither verified nor excluded.

4.4 Kinetic Studies of the Reaction of C3 with PhIO in the Absence of Substrate at 298 K

Britovsek's study of $[Fe(BPAbipy)(CH_3CN)](ClO_4)_2$ with PhIO determined the formation of the $Fe^{IV}O$ species as fleeting with intermolecular reactions occurring quickly in favour of further reactions with PhIO. To determine whether the 430 nm band, observed after addition of PhIO to complex **C3** by absorption spectroscopy, is the result of the formation of a secondary product after initial $Fe^{IV}O$ formation, as observed in the studies by Britovsek, the reaction between complex **C3** and PhIO was monitored at 25 °C over time at short time increments by absorption spectroscopy (Figure 46). The 430 nm transition grew in absorbance over a period of 8.5 min with no other distinguishable features noted in the absorbance spectrum. The 430 nm species, henceforth labelled **C7**, is stable for approximately 10 min, after which the 430 nm feature slowly decays over 13 h (Figure 47). The absorption spectrum of this decomposition product, henceforth labelled **C8**, is featureless in the visible region with transitions observed exclusively at higher energies than 350 nm

(Figure 50). Of the mono- and di-nuclear Fe-oxygen model complexes collated from literature studies in Tables 9 and 10, all exhibit transitions in the visible region between 830 nm and 450 nm and so the complete absence of transitions in the visible region suggest **C8** is unlikely to be an Fe-oxygen species. The slow rate of **C7** formation is dissimilar to the findings of Britovsek, in which intermolecular bridging was rapid, faster than the reaction between the ferrous complex with PhIO.[197] Complex **C7** formation data were unsuccessfully fit to both 1st and 2nd order reaction kinetic plots with both ln (Δ Abs @ 430 nm) and 1/(Δ Abs @ 430 nm) *vs.* time plots yielding curves (Figure 48 and Figure 49). The inability to obtain linear plots mean **C7** formation follows a more complicated reaction mechanism than for typical 1st and 2nd order reactions. Absorbance cannot be converted into concentration at this time as the identity and hence molar extinction coefficient of **C7** is unknown so the Beer-Lambert law cannot be applied. The Beer-Lambert law states absorbance and concentration are directly proportional when the path length is 1 cm and ε is constant, hence plotting functions of absorbance against time should identify the order of product formation if zero, first or second order just as concentration *vs.* time plots.

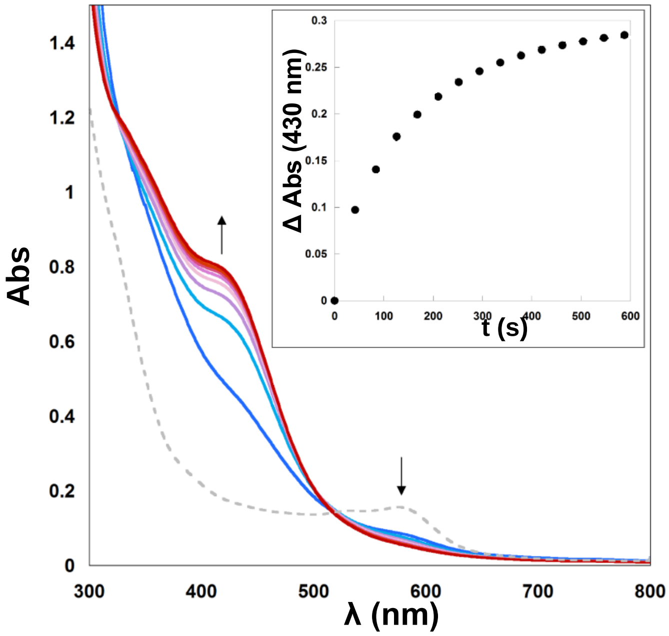

Figure 46. UV-Vis Spectroscopic Changes upon Addition of PhIO (3.3×10^{-3} M) to C3 (4.7×10^{-5} M) as Monitored Over 10 min. Grey Dashed Line Represents the Spectrum of C3 (4.7×10^{-5} M). Inset; Absorbance against time of C7 formation.

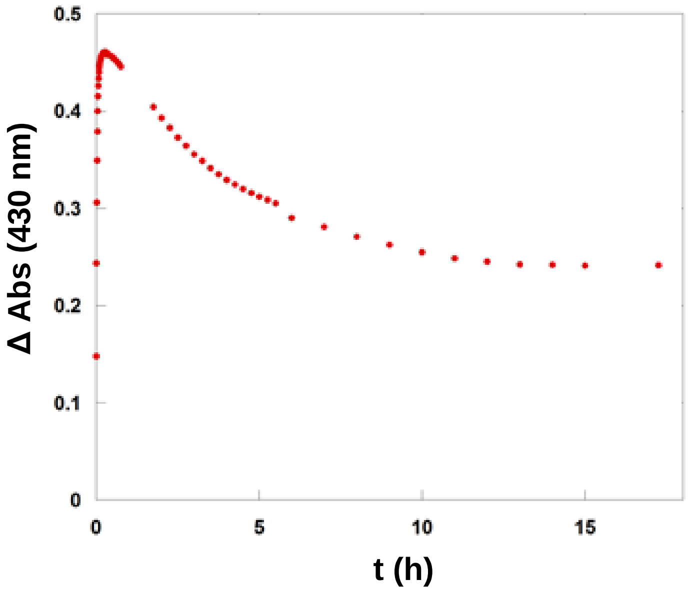

Figure 47. Spectral Changes at 430 nm over 15 h During the Reaction of C3 (4.7 ×10^{-5} M) with PhIO (3.3 ×10^{-3} M). Solvent = CH_3CN/CH_3OH (10/1); 298 K.

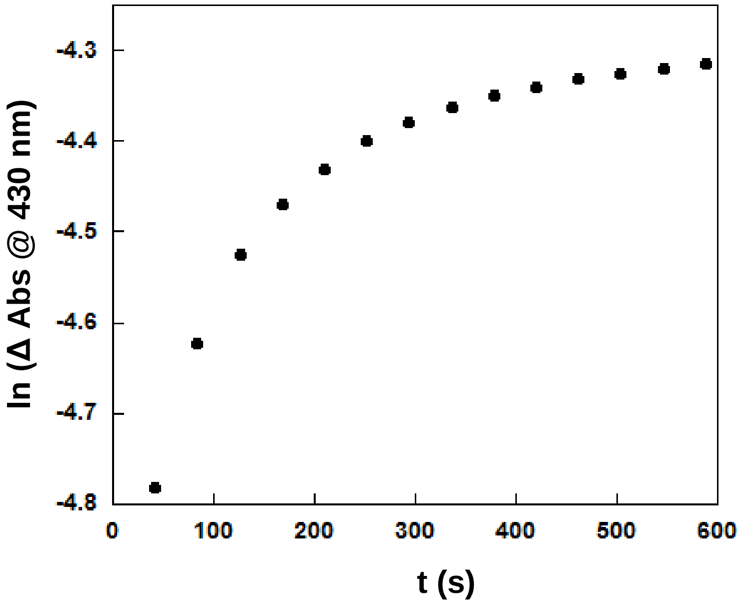

Figure 48. Ln(Δ Abs @ 430nm) *vs.* time (s) Plot of C7 Formation.

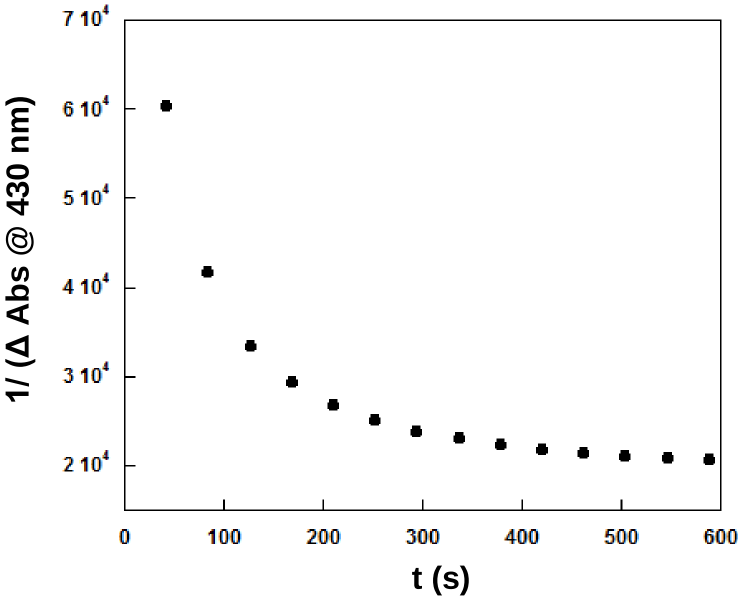

Figure 49. 1/(Δ Abs @ 430nm) *vs.* time (s) Plot of C7 Formation.

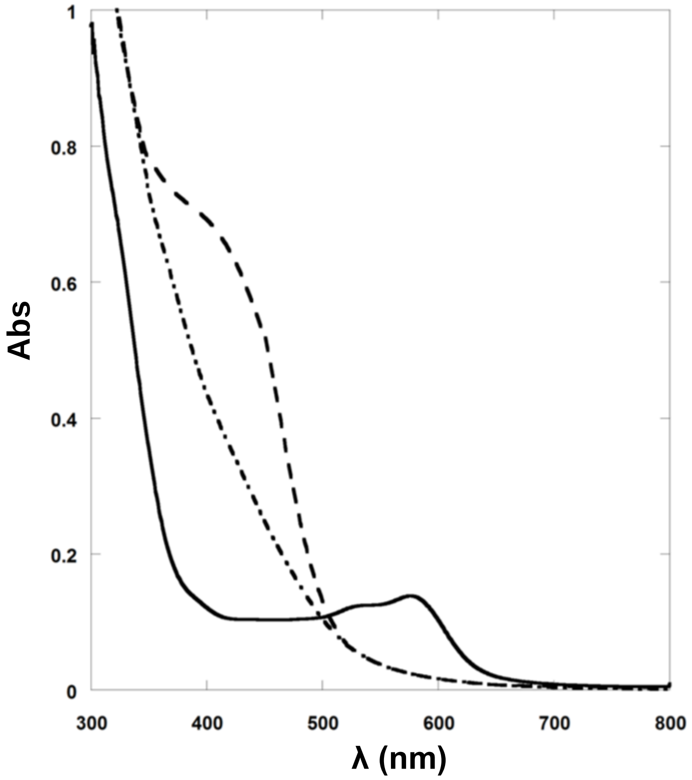

Figure 50. Absorption Spectra of C3 (4.7 x10^{-5} M) (Solid Line), C7 (Dashed Line) and C8 (Dot Dash Line). Solvent = CH_3CN/CH_3OH (10/1); 298 K.

The decomposition product, labelled **C8**, was analysed by Mössbauer spectroscopy (Figure 52). The Mössbauer spectrum exhibits a single quadrupole doublet, with isomer shift and quadrupole splitting values (δ = 0.48 mm s^{-1} and ΔE_Q= 0.80 mm s^{-1}) consistent with the presence of high-spin, S = 5/2, ferric ions. A single quadrupole doublet signifies both iron ions exist in an identical environment. The equivalency of the iron ions argues against the identity of **C8** as an oxygen bridged species between two **C3** molecules, which would result in two different iron environments; bridging and terminal as exemplified in Figure 51 with the bridging iron ions in red and the terminal iron ions in blue. The ΔE_Q value of 0.80 for complex **C8** is small in comparison to ΔE_Q values for literature $[Fe^{III}Fe^{III}(\mu\text{-}O^{2-})_2(L)_2]^{3+}$ complexes, exhibiting ΔE_Q values typically in the range of 1.5 – 2.0, again arguing against the presence of intermolecularly oxygen-bridged species (Table 10). Likewise the absence of any $Fe^{III}Fe^{III}(\mu\text{-}O^{2-})_2$ absorption bands from UV-Vis spectroscopy support this argument. The Mössbauer data of **C8** is more suggestive of a two-electron oxidised form of the ferrous compound **C3**; a di-ferric species (Scheme 38).

IR spectroscopic data were collected on **C8** to examine whether the oxidation of **C3** by PhIO results in modification of the L^1 backbone (Figure 53). The oxidation of α-diimine moieties to the corresponding amides and/or the hydroxylation of aromatic groups has been observed upon exposure of metal compounds containing ligand scaffolds similar to L^1, to various oxidants.[79, 155, 156] The lack of any discernible features in the region associated with C=O (1650 – 1760 cm^{-1}) or OH (3200 – 3600 cm^{-1}) stretches suggest the ligand scaffold remains unmodified. The imine bond, observed as the C=N stretch ~ 1690 cm^{-1}, is still intact after oxidation by PhIO so it is assumed the α-diimine group plays no role in oxidation.

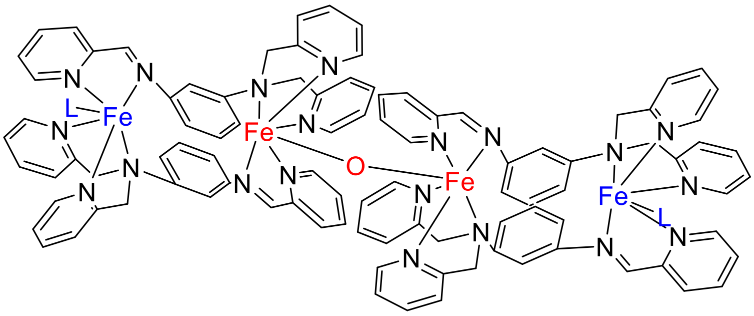

Figure 51. Exemplary Illustration of Intermolecular Oxygen Bridging of Two C3 Molecules with the Inequivalency of the Iron Ions Highlighted with the Bridging Iron Ions in Red and the Terminal Iron Ions in Blue.

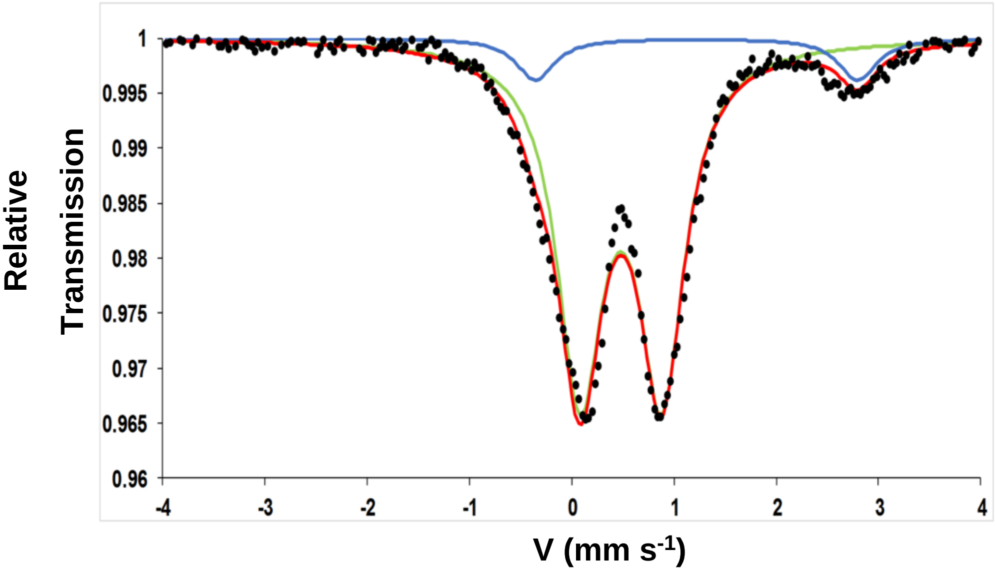

Figure 52. Zero-Field Mössbauer Spectrum (80 K) of C8. Experimental Data Shown as Solid Black Circles. The Primary Component (Solid Green Line) Affords δ (|ΔE_Q|): 0.48 (0.80) mm s^{-1}. The Combined Fit (Solid Red Line) Includes a Minor Impurity Present in the Solid Sample (Solid Blue Line, 9.41 %, δ (|ΔE_Q|): 1.22 mm s^{-1} (3.15 mm s^{-1})).

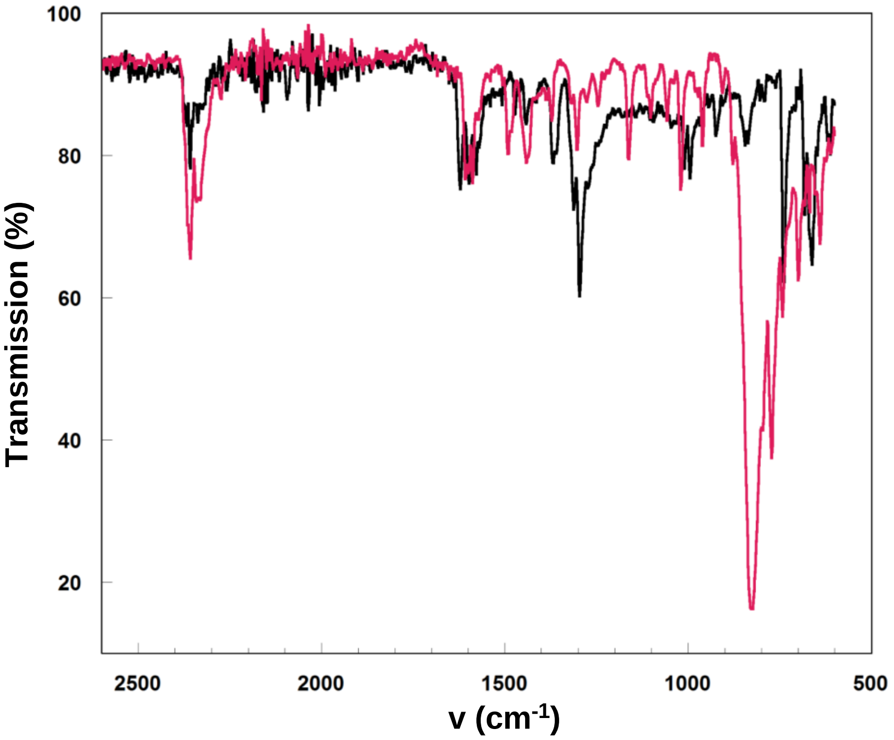

Figure 53. Infrared Spectrum of C3 (Red), and After Addition of Excess PhIO (Black) After 13 h Reaction Time.

From the information collated thus far we can establish the model shown in Scheme 38, where high-spin di-ferrous complex **C3** reacts with PhIO to form **C7**. Complex **C7** decays to the high-spin di-ferric **C8**, thought to be a di-ferric L^1 dimer.

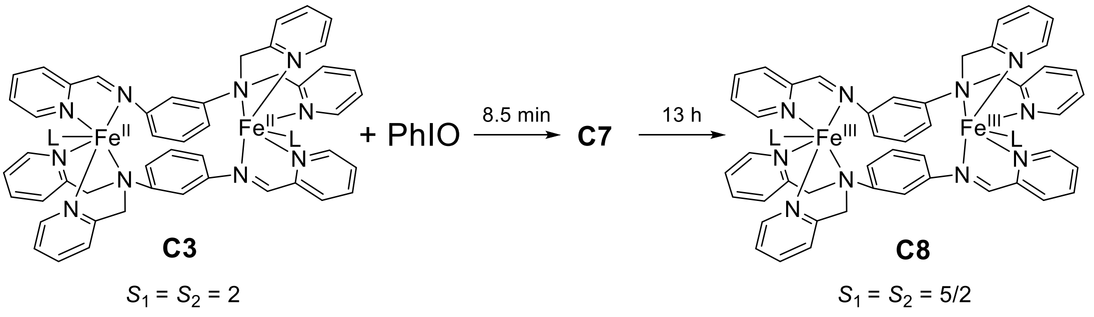

Scheme 38. Proposed Reaction of C3 with PhIO as Determined by Absorption Spectroscopy. L = CH_3CN for C3 while the Nature of L is Unknown for C8.

Mössbauer and IR data of complex **C7** are to be collected by existing members of the Hess group. Currently our collaborators in Max-Planck-Institut für Biochemie assess our samples by Mossbauer spectroscopy. It is unlikely the transient complex **C7** would remain stable long enough for transport between Durham University and Munich. The relocation of the Hess group to Munich will hopefully allow easier acquisition of this data with facilities in place to freeze samples in the glovebox avoiding any risk of exposure to oxygen.

4.5 Kinetic Studies of Reaction of C3 with PhIO in the Presence of DHA at 298 K

To uncover more information about the active species formed between **C3** and PhIO a kinetic study in the presence of substrate was undertaken, specifically with DHA. DHA was chosen as the substrate of study for two reasons; the oxidation to anthracene follows a relatively straightforward mechanistic pathway (two successive hydrogen abstractions with the first being energetically limiting) and secondly, anthracene provides a good spectroscopic handle that can be monitored by absorption spectroscopy (376 nm, 5880 M^{-1} cm^{-1}).

4.5.1 Dependence of DHA Oxidation on PhIO Concentration

The dependence of DHA oxidation by **C3**/PhIO on [PhIO] was examined. Reactions were carried out with varied concentrations of PhIO ($4.7 \times 10^{-5} - 9.4 \times 10^{-4}$ M), fixed [**C3**] (4.7×10^{-5} M) and fixed [DHA] (0.9×10^{-3} M; ≥ 20 eq. with respect to **C3**), under an inert atmosphere, over a 3 h reaction period (Figure 54). Product amounts were quantified by GC-MS. The amount of anthracene formed was found to be dependent on the concentration of PhIO when PhIO concentrations were < 5 eq., with respect to **C3**. When concentrations of PhIO were > 5 eq., with respect to **C3**, DHA oxidation was independent of PhIO. Therefore, 5 equivalents and more is considered an excess under these conditions.

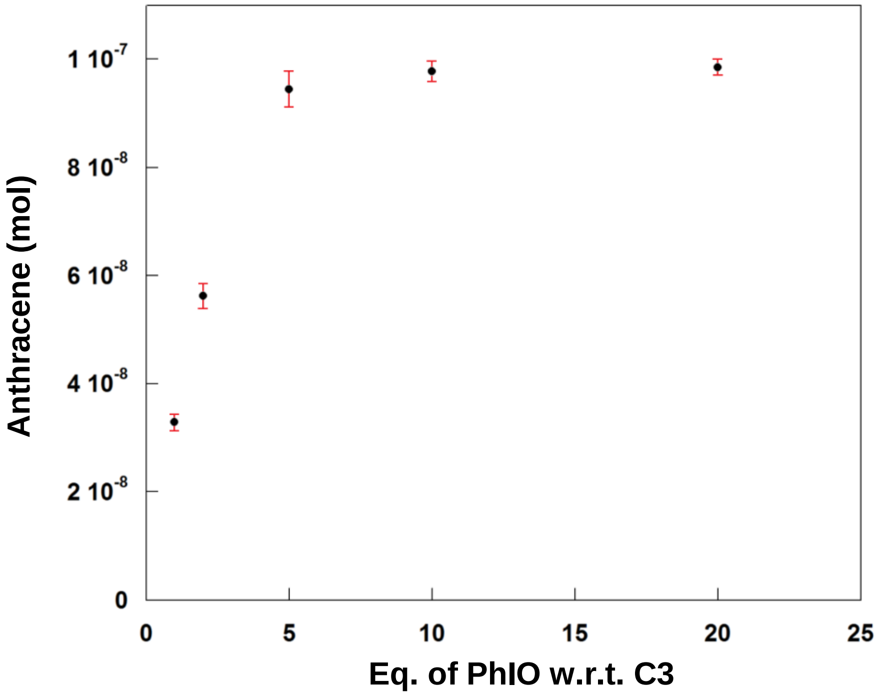

Figure 54. Amount of Anthracene (mol) For the Reaction of C3 (4.7 ×10^{-5} M) with DHA (0.9 ×10^{-3} M) at Varied Concentrations of PhIO (4.7 ×10^{-5} M – 9.4 ×10^{-4} M). Product Amounts as Determined by GC-MS After 3 h Reaction Period. Circles Represent Mean Value, Error Bars Represent One Standard Deviation Range.

4.5.2 Dependence of DHA Oxidation on C3 Concentration

The dependence of DHA oxidation by **C3**/PhIO on **[C3]** was examined. Reactions were carried out with varied concentrations of **C3** (0.02 ×10^{-3} M – 0.1 ×10^{-3} M), fixed [DHA] (10.3 ×10^{-3} M; ≥ 100 eq. with respect to **C3**) and fixed [PhIO] (3.3 ×10^{-3}; ≥ 33 eq. with respect to **C3**) under an inert atmosphere over a 3 h time period. Product amounts were quantified by absorption spectroscopy after removing any complexes present by filtering through Silica. As expected, increasing the amount of catalyst led to an increase in the final product amounts (Figure 55). Anthracene formation was found to be directly proportional to [**C3**]; $R^2 = 0.98$.

One possible identity of the **C3**/PhIO active species is an oxygen bridged species such as is exemplified in Figure 51 – although this type of species has already been excluded as the identity of decomposition product **C8**. If DHA is indeed oxidised by a bridged species an increase in complex concentration should increase reactivity. An increase in complex concentration would increase the likelihood of **C3** collision and hence bridged species formation, in turn increasing oxidative reactivity. The reactivity of **C3**/PhIO, in the form of turnover number (TON), appears to be independent of the concentration of **C3.** The reactivity of **C3** does not change upon increasing **C3** concentration (Figure 56). The lack of **[C3]** dependence therefore suggests the formation of an intermolecularly bridged species (such as in Figure 51) is not significant during DHA oxidation by

C3/PhIO. The lack of **C3** dependence on TON can otherwise be expected due to the large excess of substrate.

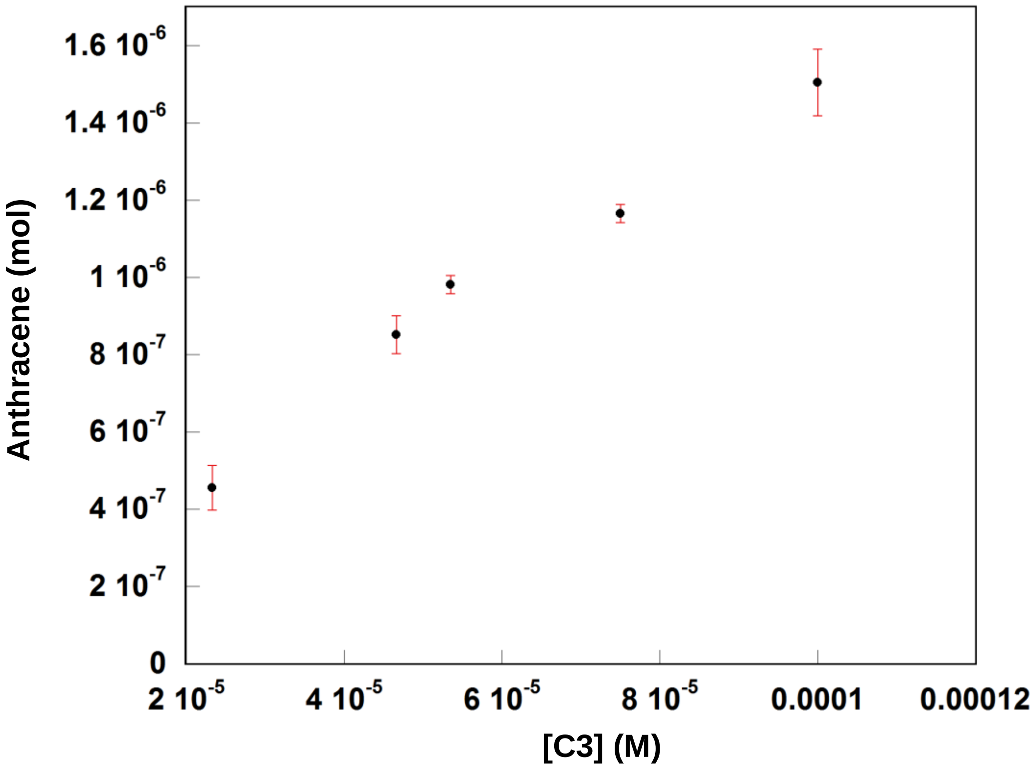

Figure 55. Amount of Anthracene (mol) for the Reaction of C3 with DHA (10.3 ×10^{-3} M) and PhIO (3.3 ×10^{-3} M), at Varied Concentrations of C3 (0.02 ×10^{-3} M – 0.1 ×10^{-3} M). Solvent = CH_3CN/CH_3OH (10/1); 298 K. Product Amounts as Determined Based on the Absorbance of Anthracene at 376 nm After 3 h Reaction Period. Circles Represent Mean Value, Error Bars Represent One Standard Deviation Range. Trend line; $y = 3.7721x + 2\times10^{-7}$

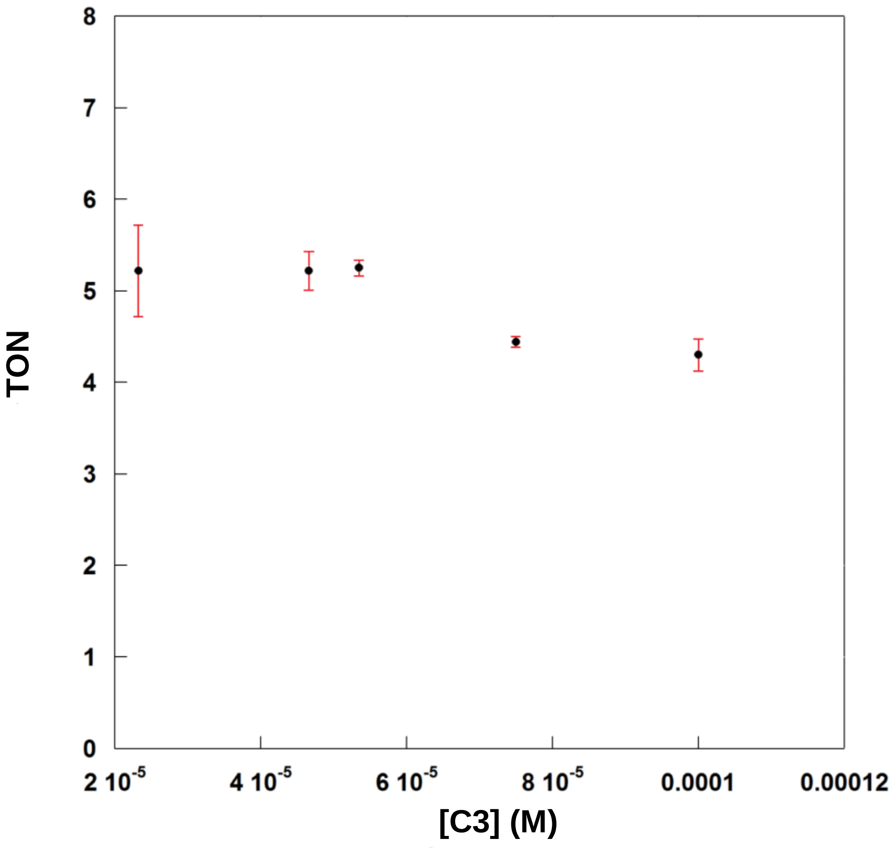

Figure 56. Turnover Numbers (TON) For the Reaction of C3 with DHA (10.3 ×10^{-3} M) and PhIO (3.3 ×10^{-3} M), At Varied Concentrations of C3 (0.02 ×10^{-3} M – 0.1 ×10^{-3} M). Solvent = CH_3CN/CH_3OH (10/1); 298 K. Product Amounts As Determined Based on the Absorbance of Anthracene at 376 nm After 3 h Reaction Period. Circles Represent Mean Value, Error Bars Represent One Standard Deviation Range. TON = Mol Product / Mol Catalyst.

4.5.3 Dependence of DHA Oxidation on DHA Concentration

The dependence of DHA oxidation by **C3**/PhIO on [DHA] was examined. Reactions were carried out with varied concentrations of DHA (0.9 – 4.0 ×10^{-3} M), fixed [**C3**] (4.7 ×10^{-5} M) and fixed [PhIO] (3.3 ×10^{-3} M; 70 eq. with respect to **C3**) under an inert atmosphere over a 3 h time period. Product amounts were quantified by absorption spectroscopy after removing any complexes present by filtering through Silica. Product formation was found to be directly proportional to initial DHA concentration; $R^2 = 0.998$ (

Figure 57). A slight contaminant is thought to co-exist alongside anthracene in solution as c is not equal to 0 in the linear fit of data in Figure 57.

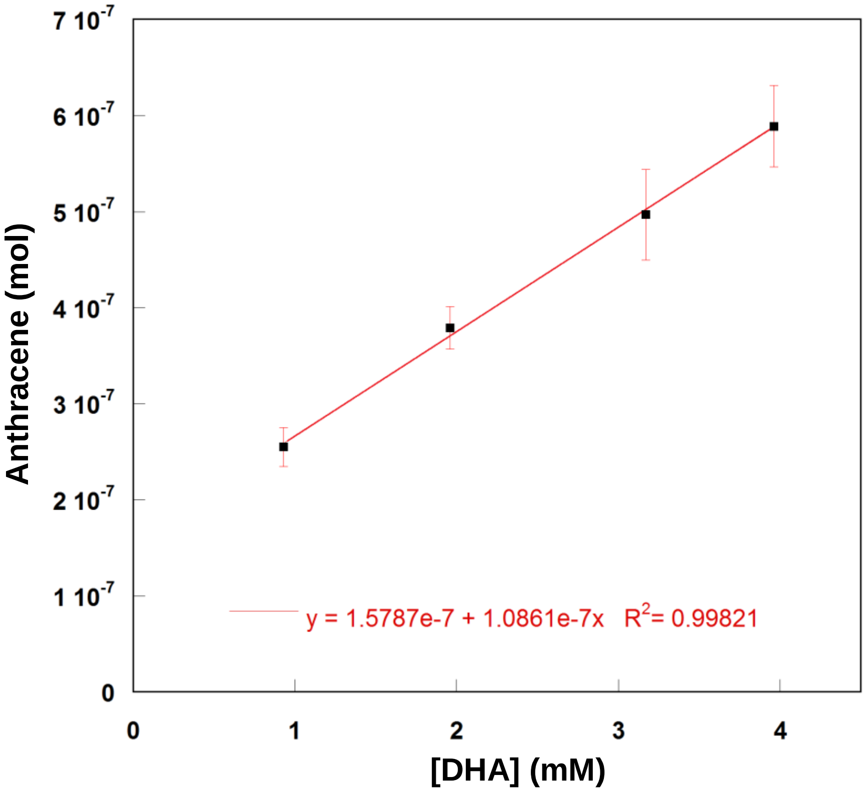

Figure 57. Amount of Anthracene Formed (mol) after 2.7 h Reaction Period, as Quantified by Absorption Spectroscopy; [C3] = 4.7 ×10^{-5} M, [PhIO] = 3.3 ×10^{-3} M, [DHA] = 0.9 ×10^{-3} - 4.0 ×10^{-3} M. Solvent = CH_3CN/CH_3OH (10/1); 298 K. Squares Represent Mean Value, Error Bars Represent One Standard Deviation Range.

Anthracene formation was then monitored at multiple time increments by UV-Vis absorbance spectroscopy. The characteristic absorbance of anthracene at λ_{max} = 376 nm provided a convenient spectroscopic handle to monitor DHA oxidation. Anthracene formation by **C3**/PhIO was monitored over a period of 2.7 h, at varied DHA concentrations (0.93 – 3.96 ×10^{-3} M) (Figure 62). Absorbance at 376 nm as converted into anthracene concentration using the Beer Lambert law and ε = 5880 M^{-1} cm^{-1} obtained from a calibration curve. Anthracene formation data collected were unsuccessfully fit to both 1st or 2nd order kinetic plots for all DHA concentrations studied resulting in an un-linear correlation for both plots suggesting a more complex mechanism of DHA oxidation is present (Figure 58 and Figure 59).

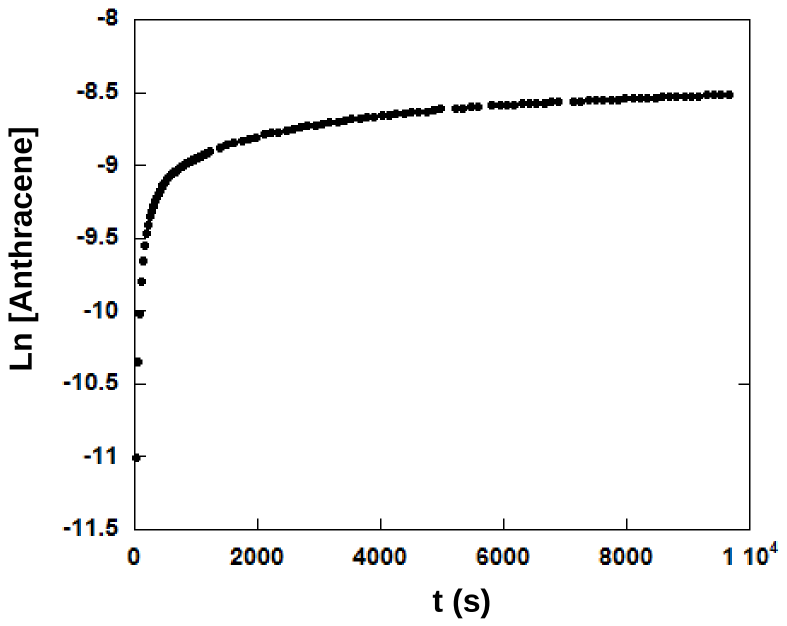

Figure 58. Ln[Anthracene] *vs.* time (s) of Anthracene Formation where $[DHA]_0 = 4.0 \times 10^{-3}$ M (the largest DHA concentration studied). A representative example, the same plot obtained for all DHA concentrations studied.

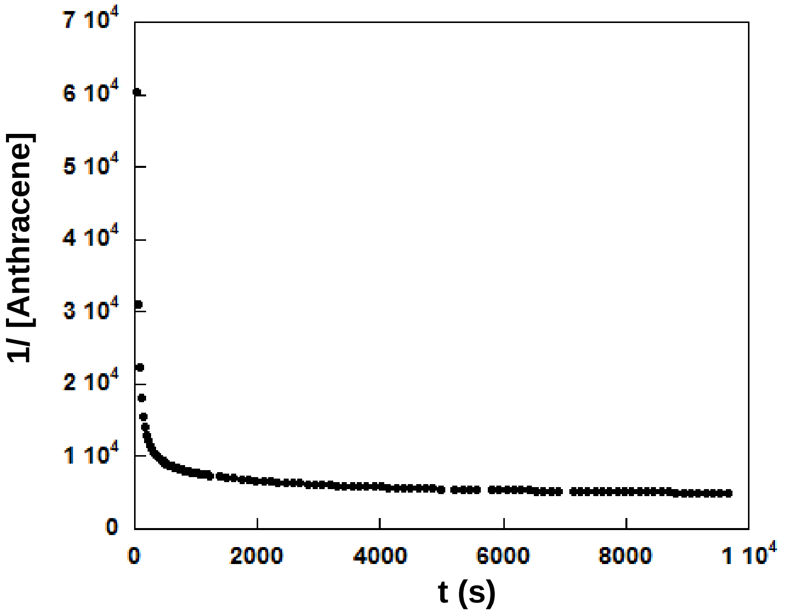

Figure 59. 1/[Anthracene] *vs.* time of Anthracene Formation where $[DHA]_0 = 4.0 \times 10^{-3}$ M (the largest DHA concentration studied). A representative example, the same plot obtained for all DHA concentrations studied.

The more complex mechanism may be explained through the means by which anthracene is produced from DHA oxidation. Anthracene is formed *via* two consecutive hydrogen abstraction steps each with different rates due to different C-H bond dissociation energies (Figure 60).

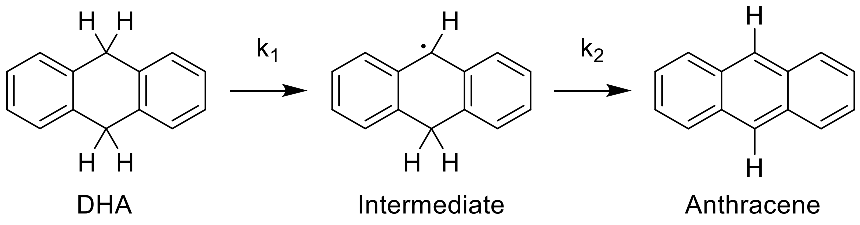

Figure 60. Two Step Mechanism of Anthracene Formation from DHA.

The intermediate species is consumed to form anthracene as quickly as it is produced, it is never detected in the reaction mixture, therefore k_2 has a negligible effect on the rate of product formation in comparison to k_1 and is represented by the following equation; $[\text{Anthracene}]_t = [\text{DHA}]_o(1-\exp(-k_1(t)))$.[188] Data should then fit to Equation 1 were k_1 is rate determining over k_2;

$$A_t = C_1(1-\exp(-k_1*t)).^{[188]}$$

Equation 1. Mono-exponential Rate Equation for Consecutive Reaction were k_2>k_1.

Data were unsuccessfully fit to equation 1 using the curve fitting software KaleidaGraph quantified by the large chi-squared value of 0.9 and an R^2 of 0.86 signifying a poor curve fit has been obtained. A representative attempted fit is shown in Figure 61.

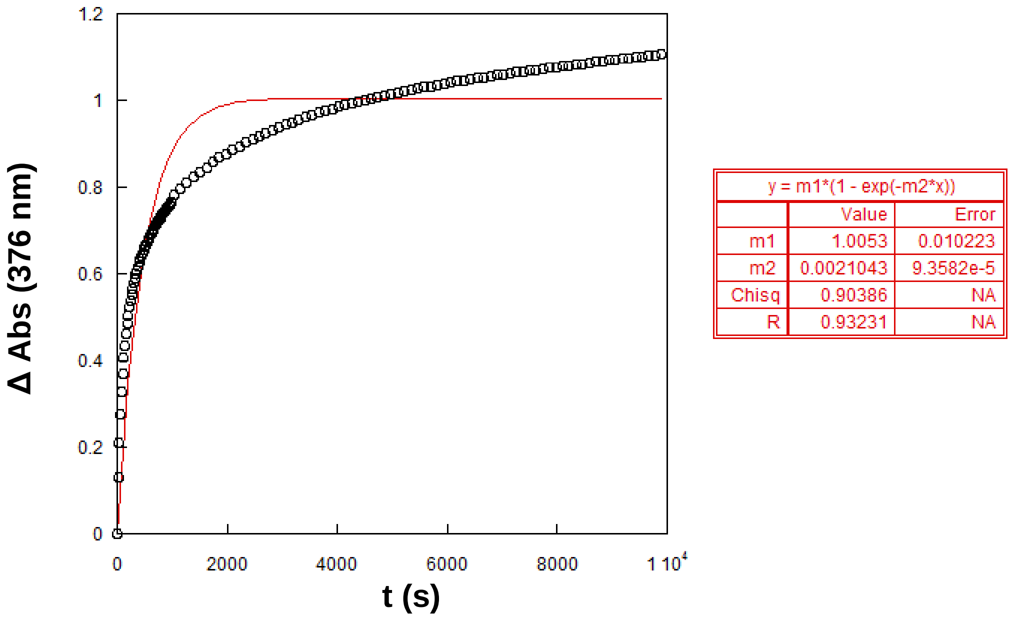

y = m1*(1 - exp(-m2*x))		
	Value	Error
m1	1.0053	0.010223
m2	0.0021043	9.3582e-5
Chisq	0.90386	NA
R	0.93231	NA

Figure 61. Mono-exponential Attempted Fit of Anthracene Formation where $[\text{DHA}]_0 = 4.0 \times 10^{-3}$ M (the largest DHA concentration studied). A representative example, the same plot obtained for all DHA concentrations studied.

The anthracene formation data were instead best fit to Equation 2, a bi-exponential equation with a very good agreement between data and fit found as signified by average R values of 0.99 and average chi-squared values of 0.01-0.02. One representative example at each DHA concentration is shown in Figure 62 with the raw data represented as hollow circles and the data fit as a solid line (triplicate runs for each DHA initial concentration).

$$A_t = C_1(1 - \exp(k_{obs,1}.t)) + C_2(1 - \exp(k_{obs,2}.t))$$

Equation 2. Bi-exponential Rate Equation to Which Data Were Fit.

A bi-exponential fit of the data is suggestive of two different processes occurring at two different rates. The bi-exponential fit obtained could be reasoned as the result of two reaction pathways forming anthracene product involving two active species reacting *via* parallel or consecutive pathways with different reactivity toward hydrocarbon oxidation. The bi-exponential fits yielded values in the range of $k_{obs,1} = 1.1 \times 10^{-2} - 5.6 \times 10^{-3}$ s^{-1} and $k_{obs,2} = 2.8 \times 10^{-4} - 5.5 \times 10^{-4}$ s^{-1} for the two apparent rate constants (Table 11). At all DHA concentrations examined, $k_{obs,1}$ was approximately 20-fold greater than $k_{obs,2}$ and the relative amplitudes of the two processes remained constant. Reactivity can be quantified by an initial burst in activity for the first 9 min, with turnover frequencies (TOFs) of 0.157, 0.202, 0.237 and 0.268 min^{-1} at [DHA] = 0.9, 2.0, 3.2 and 4.0 $\times 10^{-3}$ M, respectively. The activity significantly reduces from 9 min onwards. The second phase of activity results in turnover frequencies (TOFs) of 0.004, 0.007, 0.010 and 0.011 min^{-1} for [DHA] = 0.9 $\times 10^{-3}$, 2.0 $\times 10^{-3}$, 3.2 $\times 10^{-3}$ and 4.0 $\times 10^{-3}$ M respectively, 20 times less than the TOFs for phase 1. Overall TONs of 2.0, 3.0, 3.6 and 4.1 for [DHA] = 0.9 $\times 10^{-3}$, 2.0 $\times 10^{-3}$, 3.2 $\times 10^{-3}$ and 4.0 $\times 10^{-3}$ M, respectively, were observed over the entire 2.7 h period. More than half of the oxidative reactivity occurs during the first phase (71 %, 61 %, 59 % and 58 % at [DHA] = 0.9, 2.0, 3.2 and 4.0 $\times 10^{-3}$ M, respectively).

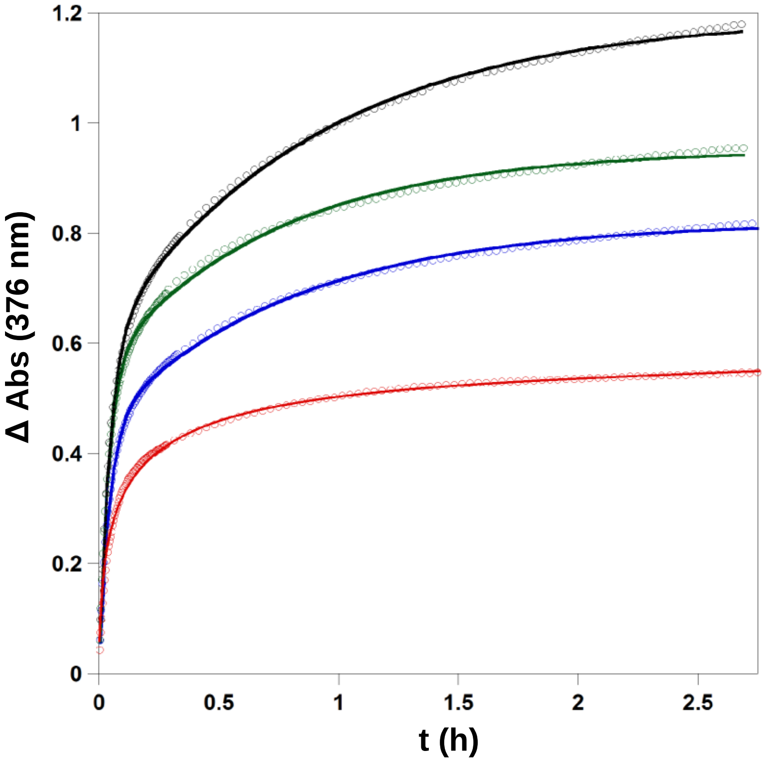

Figure 62. Product (Anthracene) Formation vs. Time, in the Reaction of C3 with PhIO and DHA, Monitored at 376 nm; [C3] = 4.7×10^{-5} M, [PhIO] = 3.3×10^{-3} M, [DHA] = 0.9×10^{-3} M – 4.0×10^{-3}. Solvent = CH_3CN/CH_3OH 10/1; 298 K. Circles Represent the Experimental Data and Solid Lines Represent the Fit of the Data to the Bi-exponential Rate Equation. Red: 0.9×10^{-3} M DHA, Blue: 2.0×10^{-3} M DHA, Green: 3.2×10^{-3} M DHA, Black: 4.0×10^{-3} M DHA.

Table 11. Parameters, with Errors, Obtained from the Bi-exponential fit of the Absorbance *vs.* Time Traces Monitoring Anthracene Formation (at 376 nm) by C3/PhIO over 2.7 h. Values Represent the Average Values from Five Identical Reactions. Data Were Fit to the Following Rate Equation: $A_t = C_1(1 - \exp(k_{obs,1}.t)) + C_2(1 - \exp(k_{obs,2}.t))$. [C3] = 4.7×10^{-5} M, [PhIO] = 3.3×10^{-3} M, [DHA] = 0.9×10^{-3} - 4.0×10^{-3} M. Solvent = CH_3CN/CH_3OH (10/1); 298 K.

[DHA] (mM)	Av. C_1 (error)	Av. $k_{obs,1}$ (error)	Av C_2 (error)	Av $k_{obs,2}$ (error)	Av R	Av Chi Sq.
3.96	0.60 (0.013)	5.6×10^{-3} (2.0×10^{-4})	0.53 (0.014)	2.8×10^{-4} (2.22×10^{-5})	0.999	0.020
3.17	0.55 (0.009)	5.3×10^{-3} (1.4×10^{-4})	0.48 (0.023)	2.7×10^{-4} (1.96×10^{-5})	0.999	0.015
1.96	0.44 (0.007)	6.3×10^{-3} (2.5×10^{-4})	0.36 (0.009)	3.0×10^{-4} (2.15×10^{-5})	0.999	0.007
0.93	0.34 (0.009)	1.1×10^{-2} (1.1×10^{-3})	0.19 (0.008)	5.5×10^{-4} (6.61×10^{-5})	0.995	0.011

The amount of anthracene formed during the DHA oxidation by **C3**/PhIO was verified by analysing aliquots of the reaction mixture at various time points by GC-MS. This verification was carried out to ensure that the changes in the absorbance at 376 nm could be attributed solely to anthracene formation, and that the formation of any Fe–oxygen species that might absorb in this region does not skew the data analysis. Anthracene formation determined from absorbance spectroscopy after 2.7 h gave slightly higher values than obtained by GC-MS attributed to a small co-existing contamination. (Figure 63). However, the product *vs.* time curves generated from the GC-MS data also fit well to bi-exponential rate Equation 2, and provided apparent rate constants that were comparable to those obtained from the absorption data ($k_{obs,1}$ = 1.9 ×10^{-3} (GC-MS); 5.6 ×10^{-3} (UV-Vis) and $k_{obs,2}$ = 2.5 ×10^{-4} (GC-MS); 2.8 ×10^{-4} (UV-Vis) from the respective data fits).

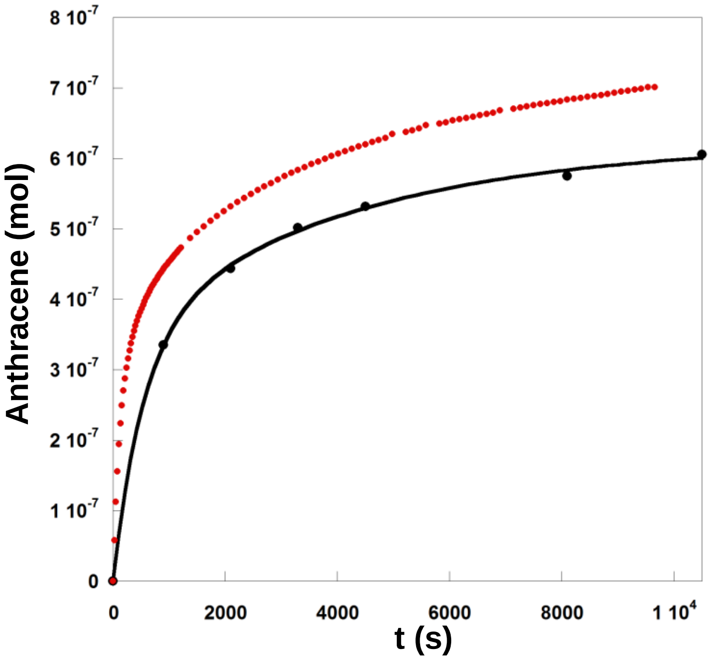

Figure 63. Comparison of the Amount of Anthracene (mol) Formed in the Reaction of C3/PhIO with DHA, as Determined by GC-MS (Black Data Points) and by Absorption Spectroscopy (Red Data Points), Based on ε = 5880 M^{-1} cm^{-1} for Anthracene at 376 nm (Determined by Calibration Curve), over 3 h Reaction Period; [C3] = 4.7 ×10^{-5} M, [PhIO] = 3.3 ×10^{-3} M, [DHA] = 4.0 ×10^{-3} M. Solvent = CH_3CN/CH_3OH (10/1); 298 K. GC-MS Data were Fit to a Bi-exponential Rate Equation: $A_t = C_1(1 - \exp(k_{obs,1}.t)) + C_2(1 - \exp(k_{obs,2}.t))$ (Black Line), Which Yielded $k_{obs,1}$ = 0.00185 s^{-1}, $k_{obs,2}$ = 0.000246 s^{-1}. One Representative Example, Repeated in Triplicate.

From the information collated by the study of DHA oxidation by **C3**/PhIO we can establish the model shown in Scheme 39. **C3**/PhIO is proposed to generate two active species which oxidise DHA to anthracene through either parallel pathways, depicted in Scheme 39 by the black and red arrows, or through a consecutive pathway, depicted in Scheme 39 by the black and blue arrows. The first species, depicted as $\mathbf{C}^{ox1}$ in Scheme 39, is short lived (~ 9 min) and more active by approximately 20 times than the second species depicted as $\mathbf{C}^{ox2}$ in Scheme 39.

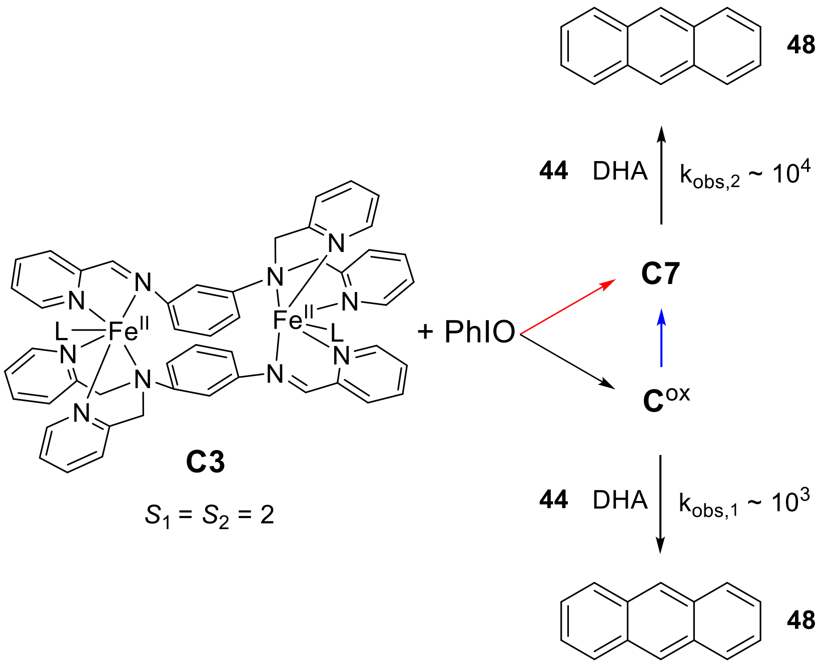

Scheme 39. Presence of Two Active Species Proposed Based On Studies of DHA Oxidation by C3/PhIO.

4.5.4 Incubation Reactions of C3 with PhIO Toward DHA Oxidation

The identities of the two active species, $\mathbf{C}^{\mathrm{ox1}}$ and $\mathbf{C}^{\mathrm{ox2}}$, were explored by evaluating the reactivity of complexes **C7** and **C8** to determine if either or both species are responsible for the oxidation of DHA. Alternate reactions were carried out in which complex **C3** and PhIO were incubated for either 8.5 min or 13 h, allowing for the formation of complexes **C7** or **C8** respectively, after which DHA (4.0×10^{-3} M) was added to the reaction mixture. Using Equation 1 a mono-exponential fit of anthracene formation was observed in the reaction of DHA with complex **C7** with good agreement between data and fit signified by a chi squared of 0.0014 and an R value of 0.995 (Figure 64). The value of the observed rate constant for **C7**/PhIO DHA oxidation was determined as $k_{\mathrm{obs,inc}} = 2.2 \times 10^{-4}$ s^{-1}, very similar to the slower apparent rate constant $k_{\mathrm{obs,2}} = 2.8 \times 10^{-4}$ s^{-1}, derived from data obtained under the standard reaction conditions for this concentration of DHA. Due to the similar rate of DHA oxidation the implication is that complex **C7** is generated even in the presence of DHA, and is the less active catalytic species, in the oxidation of DHA by the **C3**/PhIO system.

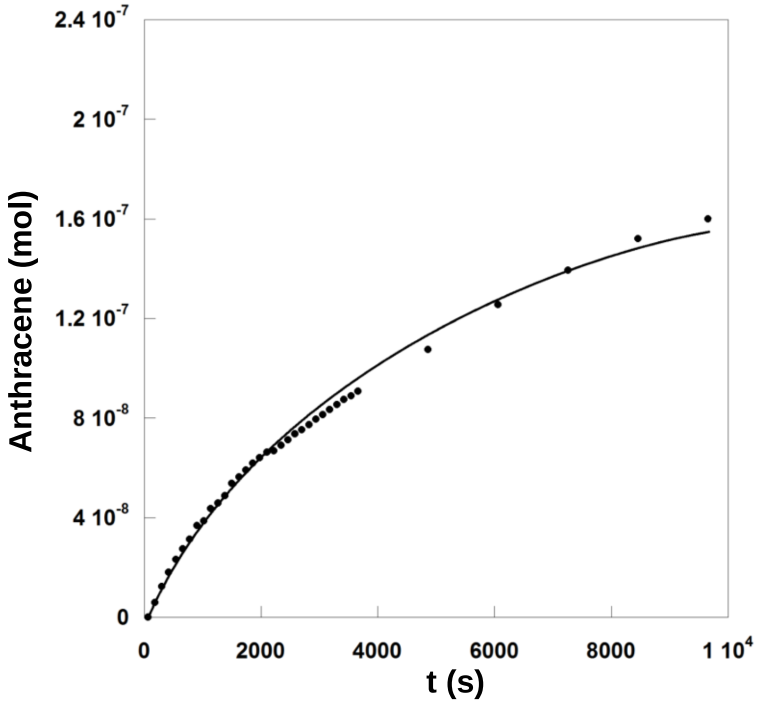

Figure 64. Amount of Anthracene Generated over Time in the Reaction of C7 with DHA as Determined by Absorption Spectroscopy, Based on ε = 5880 M^{-1} cm^{-1} for Anthracene at 376 nm (Determined by Calibration Curve); [C3] = 4.7 $\times10^{-5}$ M, [PhIO] = 3.3 $\times10^{-3}$ M, [DHA] = 4.0 $\times10^{-3}$ M. Solvent = CH_3CN/CH_3OH (10/1); 298 K. Data Points Fit to a Mono-exponential Equation: $A_t = C(1 - \exp(k_{obs,inc}.t))$, which yielded $k_{obs,inc} = 2.13 \times 10^{-4}$ s^{-1}. One Representative Example, Repeated in Triplicate.

Anthracene was not detected upon addition of DHA (4.0 $\times10^{-3}$ M) to a solution of complex **C8** after a continuous 3 h monitoring period. Several mono-nuclear non-heme ferric compounds, including bleomycin, carry out hydrocarbon oxidation reactions in the presence of H_2O_2. Since the Mössbauer data suggest complex **C8** is di-ferric, we went on to examine whether complex **C8** could be reactivated in the presence of H_2O_2. Anthracene was not generated by complex **C8** in the presence of H_2O_2 and therefore complex **C8** is inactive toward DHA oxidation.

Based on the combined results of absorption spectroscopy studies, our current model for the oxidation of DHA by **C3** is as depicted in Scheme 40. The reaction of **C3** with PhIO initially generates an active species, labelled **C**^{ox}, which reacts with DHA with an apparent rate constant in the order of 10^{-3}. The high activity of **C**^{ox} is traded off with low stability, which in turn leads to a short life time making characterisation elusive. **C3**/PhIO can generate a second active species, labelled **C7**, either through parallel pathways, depicted in Scheme 40 by the black and red arrows, or through a consecutive pathway, depicted in Scheme 40 by the black and blue arrows, which also is capable of H-atom abstraction, but exhibits a lower reactivity toward DHA oxidation with an apparent rate constant in the order of 10^{-4}. The inactive species **C8** represents the final decomposition product that cannot be restored to an active form upon addition of H_2O_2.

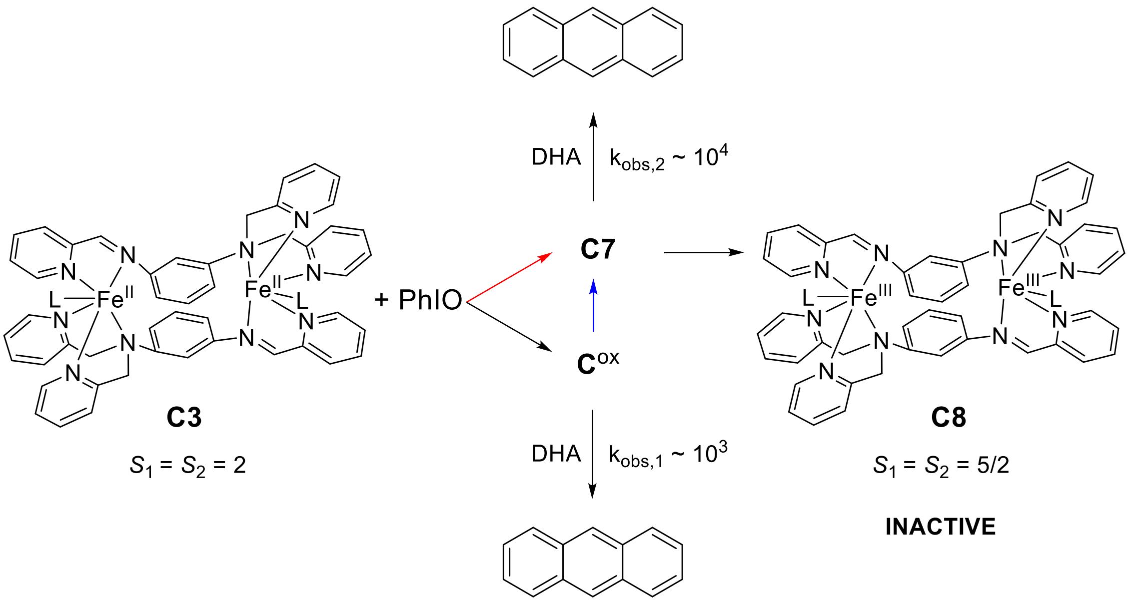

Scheme 40. Proposed Current Model for the Oxidation of DHA by C3 by Involvement of Two Active Species.

4.6 Conclusions

Initial spectroscopic studies of **C3** with H_2O_2, ^tBuOOH and PhIO did not glean significant structural information about the iron-oxygen species formed upon addition of oxidants to complex **C3** due to poor resonance Raman spectra and indecisive UV-Vis spectroscopy.

Under variable temperature conditions the **C3**/PhIO species exhibited a transition at 430 nm in the absorption spectrum rather than the distinguishing NIR features exhibited by most mono-nuclear non-heme Fe^{IV}- and Fe^{V}-oxo compounds in literature. Even with the absence of the NIR band we are not willing to entirely exclude the possibility of $Fe^{IV}O$ formation. The initial formation of a short lived $Fe^{IV}O$ species has not been excluded following the work by Britovsek and co-workers who witnessed a rapid reaction between their ferrous complex and PhIO, resulting in a di-nuclear bridged species, $[(Fe(BPAbipy))_2(\mu\text{-}O)]^{4+}$, postulated to form *via* an initial $Fe^{IV}O$ species. Further to this, several $[Fe^{III},Fe^{IV}O]$ and $[Fe^{II},Fe^{IV}O]$ intermediates characterised in bi-nuclear non-heme enzymes and synthetic compounds absorb solely in the UV-visible region (λ_{max} = 385 – 430 nm) without exhibiting an NIR band therefore the formation of a similar mixed valence species may also be possible with our system resulting in the absence of NIR bands.[116, 198]

Absorbance spectroscopy studies in the presence of DHA suggested DHA oxidation best fit to bi-exponential Equation 2, indicative of two rates of anthracene formation and hence two active species. Complex **C7** was identified as the second slower oxidant species based on the comparison of rate of anthracene formation after the incubation reaction compared to the normal DHA oxidation conditions. The more reactive initial species, $\mathbf{C}^{ox}$, has thus far remained elusive to characterisation by absorbance spectroscopy. Further absorbance spectroscopy studies with low temperature facilities available to the Hess group in Munich are planned in hope of obtaining successful characterisation of **C**^{ox}.

The reactivity of bi-nuclear non-heme enzymes and complexes toward C-H oxidation has been found to be highly dependent on the structure and valence form of the iron sites, within literature. The structural identity of the two active forms of **C3 (C7** and **C**^{ox}**)** may differ only with respect to metal oxidation states. For example, if the reaction of **C3** with PhIO were to initially yield an asymmetric [Fe^{II},Fe^{IV}O] species, one might envision rapid rearrangement of such an intermediate to other forms including a [Fe^{III},Fe^{III}] form (such as **C8**). Indeed, studies with the di-iron(II) compound, [$Fe_2(H_2Hbamb)_2(NMeIm)_2$] provide precedent for this scenario.[198, 199] The reaction of [$Fe_2(H_2Hbamb)_2(NMeIm)_2$] **(52)** with various oxidants, including Me_2PhIO, rapidly led to the formation of a mixed valence [Fe^{II}Fe^{IV}O] species containing a terminally bound oxo ligand at one metal site. This initial reaction intermediate converted, *via* a ligand reorganisation, to yet another [Fe^{II}Fe^{IV}] species, followed by its decay to a ferric di-iron compound. Both of the reported [Fe^{II}Fe^{IV}] species displayed absorption bands at ca. 440 nm, and the interconversion took place with an observed rate constant on the order of 10^{-1} s^{-1}. [198, 199] Mössbauer is an effective tool for identifying mixed valence species and the conversions between one and another, further work employing Mössbauer spectroscopy to monitor the DHA oxidation reaction by **C3**/PhIO is planned by the Hess group to determine if valence states play a key part in the reactivity of the **C3**/PhIO system.

It is reasoned that the reactivity of an intermoleculary bridged species (such as exemplified in Figure 51) would increase as the concentration of **C3** increases due to an increased likelihood of **C3** collision and hence bridged species formation, so the lack of dependence on the concentration of **C3** of DHA oxidation suggests the formation of an intermolecularly bridged species is not rate determining and is unlikely the identity of **C7** or **C**^{ox}.

Complex **C7** decays to the final di-ferric compound, **C8**, which was found to be inert toward DHA oxidation. The Mössbauer spectrum of **C8** excluded intermolecular bridging of two **C3** molecules in an end on manner, which would result in two different iron environments; bridging and terminal. The ΔE_Q value of 0.80 is small in comparison to [$Fe^{III}Fe^{III}(\mu\text{-}O^{2-})_2(L)_2$]$^{3+}$ complexes and the absence of any $Fe^{III}Fe^{III}(\mu\text{-}O^{2-})_2$ absorption bands likewise argues against its formation. Di-ferric complex **C8** is proposed to be the two electron oxidised analogue of **C3**.

As stated throughout this section, further studies are currently underway by the Hess group to unveil more information on the structural conformation of active species **C**^{ox} and **C7**. In addition to low temperature absorbtion spectroscopy and Mossbauer spectroscopy of isolated intermediates and reaction monitoring, a one electron metal-based mixed valence Fe^{II},Fe^{III} species has been isolated and reactivity studies are underway to compare to the reactvitity of **C3**/PhIO to investigate how oxidation state effects reactivity.

4.7 Experimental

Reaction of C3 with 2H_2O_2 at 298 K.

For absorption spectroscopy studies a solution of **C3** (1.0×10^{-4} M, 3.5 mL) in CH_3CN was added to a sealed cuvette under N_2. Degassed H_2O_2 (4.4 µL, 0.16 M) was syringed into the sealed cuvette and absorption spectral changes were monitored immediately over a 10 min period. For Raman spectroscopy studies 3.5 mg of **C3** was dissolved in 0.5 mL CH_3CN and H_2O_2 (2.8 µL, 1.6 M) was added. The solution was stirred for 10 min after which solvent was removed in *vacuo*. Raman spectroscopy was carried out using an excitation wavelength of 532 nm and 634 nm.

Reaction of C3 with 2^{t}BuOOH at 298 K.

For absorption spectroscopy a solution of **C3** (1.0×10^{-4} M, 3.5 mL) in CH_3CN was added to a sealed cuvette under N_2. Degassed ^{t}BuOOH (4.4 µL, 0.16 M) was syringed into the sealed cuvette and absorption spectral changes were monitored immediately over a 10 min period. For Raman spectroscopy studies 7.0 mg of **C3** was dissolved in 0.5 mL CH_3CN and ^{t}BuOOH (2.0 µL, 5.5 M) was added. The solution was stirred for 10 min after which solvent was removed in *vacuo*. Raman spectroscopy was carried out at an excitation wavelength of 532 nm and 634 nm.

Reaction of C3 with PhIO at 298 K.

For absorption spectroscopy a solution of **C3** (0.8×10^{-3} M, 0.2 mL) in CH_3CN was added to a cuvette under N_2. PhIO (1 mg) was added to the cuvette which was sealed and stirred for 20 min to ensure complete dissolution. Absorption spectra were taken after this time period. For Raman spectroscopy studies 10.0 mg of **C3** was dissolved in 0.5 mL CH_3CN and PhIO (3 mg) was added. The solution was stirred for 10 min after which solvent was removed in *vacuo*. Raman spectroscopy was carried out at an excitation wavelength of 532 nm and 634 nm.

Variable Temperature Reaction of C3 with PhIO.

A solution of PhIO (1.3×10^{-3} M, 3.3 mL) in CH_3CN/CH_3OH (10/1) was stirred for 20 min to ensure complete dissolution, then cooled to -5 °C using a cryostat attachment to the cell holder of Cary 100 UV-Vis spectrometer. Complex **C3** (0.8×10^{-3} M, 0.2 mL) was added to the cooled solution and absorption spectra were recorded consecutively for 10 min. The cell holder was progressively warmed to 0, 10 and 25 °C and absorption spectra were taken over a period of 10 min at each temperature.

Reaction of C3 with Excess PhIO at 298 K.

For absorption spectroscopy a solution of PhIO (2.5 mg, 3.3 mL) in CH_3CN/CH_3OH (10/1) was stirred for 20 min to ensure complete dissolution. Complex **C3** (0.8×10^{-3} M, 0.2 mL) was added to the cuvette and spectral changes were monitored immediately upon addition of the di-iron complex over a 17 h period. Samples for Mössbauer and IR spectroscopy were produced as follows: complex **C3** (35 mg, 0.02 mmol) was dissolved in CH_3CN/CH_3OH (10/1) (12 mL), PhIO (125 mg, 0.57 mmol) was added to the solution and stirred for 13 h, after which time the solvent was removed in *vacuo* and the solid analysed.

[PhIO] Dependence on DHA Oxidation by C3/PhIO at 298 K.

Assay mixtures (final volume of 3.3 mL, CH_3CN/CH_3OH (10/1)) containing PhIO (4.7×10^{-5} – 9.4×10^{-4} M) and DHA (0.9×10^{-3} M) were stirred for 20 min to ensure complete dissolution of PhIO. The reaction was subsequently initiated by addition of **C3** (4.7×10^{-5} M). All assays were carried out under N_2 at 25 °C. Product formation was monitored after a 2.7 h reaction. Products were identified by comparison to GC retention times and mass spectra of commercial samples. Products were quantified using a single point internal standard method, with fluorene as the standard.

$[L^1_2Fe_2(CH_3CN)_2](PF_6)_4]$ Dependence on DHA Oxidation by C3/PhIO at 298 K.

Assay mixtures (3.3 mL, CH_3CN/CH_3OH 10/1) containing PhIO (2.5 mg, 3.3×10^{-3} M) and DHA (6.5 mg, 10.3×10^{-3} M) were stirred for 20 min to ensure complete dissolution of PhIO. Assays were carried out under N_2, 25 °C, and reactions were initiated by addition of **C3** (0.02×10^{-3} M – 0.1×10^{-3} M). The reaction mixture was stirred for 3 h after which the reaction solution was passed over silica (60 Å) to remove any iron-containing materials and the organic products were eluted with CH_3CN. The product, anthracene, was quantified by absorption spectroscopy using the characteristic absorbance at 376 nm ($\varepsilon = 5880$ M^{-1} s^{-1}), or alternatively, by GC-MS.

[DHA] Dependence on DHA Oxidation by C3/PhIO at 298 K.

Assay mixtures (3.3 mL, CH_3CN/CH_3OH 10/1) containing PhIO (2.5 mg, 3.3×10^{-3} M) and DHA ($0.9 - 4.0 \times 10^{-3}$ M) were stirred for 20 min to ensure complete dissolution of PhIO. Assays were carried out under N_2, 25 °C, and reactions were initiated by addition of **C3** (4.7×10^{-5} M). The reaction mixture was stirred for 3 h after which the reaction solution was passed over silica (60 Å) to remove any iron-containing materials and the organic products were eluted with CH_3CN. The product, anthracene, was quantified by absorption spectroscopy using the characteristic absorbance at 376 nm ($\varepsilon = 5880$ M^{-1} s^{-1}).

Assay mixtures (final volume of 3.3 mL, CH_3CN/CH_3OH (10/1)) containing PhIO (2.5 mg, 3.3×10^{-3} M) and DHA (0.9×10^{-3} M – 4.0×10^{-3} M) were stirred for 20 min to ensure complete dissolution of PhIO. The reaction was subsequently initiated by addition of **C3** (0.2 mL, 0.8×10^{-3} M). All assays were carried out under N_2 at 25 °C. Product formation was monitored immediately after addition of the di-iron complex, by absorption spectroscopy, using the characteristic absorbance of anthracene at 376 nm ($\varepsilon = 5880$ M^{-1} s^{-1}), (spectra recorded at 20 s intervals for t < 15 min then at 2 min intervals until the end point at 2.7 h).

Alternatively, assay mixtures were stirred for a total of 3 h, and aliquots of the reaction mixture were removed at various time points and subjected to GC-MS analysis. Products were identified by comparison to GC retention times and mass spectra of commercial samples. Products were quantified using a single point internal standard method, with fluorene as the standard, as described above.

Assay of the Reactivity of C7 and C8 with DHA at 298 K.

PhIO (2.5 mg) was stirred in CH_3CN/CH_3OH (10/1) (3.1 mL) for 20 min to ensure complete dissolution. Complex **C3** (0.8×10^{-3} M, 0.2 mL) was added to the cuvette and the reaction was monitored by UV-vis absorption spectroscopy over a period of either 8.5 min or 13 h, after which DHA (2.5 mg, 0.2 mL) was added to the solution. Product formation was monitored immediately after addition of DHA, by absorption spectroscopy, using the characteristic absorbance of anthracene at 376 nm over 3 h subsequent to substrate addition.

4.8 References

(79) Patra A. K.; Olmstead M. M.; Mascharak P. K. *Inorg. Chem.* **2002**, *41*, 5403.

(80) Li, F.; Wang, M.; Ma, C.; Gao, A.; Chen, H.; Sun, L. *Dalton Trans.* **2006**, *20*, 2427.

(81) Roelfes, G.; Lubben, M.; Chen, K.; Ho, R. Y. N.; Meetsma, A.; Genseberger, S.; Hermant, R. M.; Hage, R.; Mandal, S. K.; Young, V. G. Jr.; Zang, Y.; Kooijman, H.; Spek, A. L.; Que, L. Jr.; Feringa B. L. *Inorg. Chem.* **1999**, *38*, 1929.

(111) Hess, C. R.; Welford, R. W. D.; Klinman, J. P.; Begley, T. P. In *Wiley Encyclopedia of Chemical Biology*; John Wiley & Sons, Inc.: 2007.

(112) Que, L.; Tolman, W. B. *Nature* **2008**, *455*, 333.

(113) Shilov, A. E.; Shul'pin, G. B. *Chem. Rev.* **1997**, *97*, 2879.

(114) Wallar, B. J.; Lipscomb, J. D. *Chem. Rev.* **1996**, *96*, 2625.

(116) McDonald, A. R.; Que, L. *Coord. Chem. Rev.* **2013**, *257*, 414.

(117) Montellano, P. R. In *Cytochrome P450: Structure, Mechanism and Biochemistry*; Kluwer Academic/Plenum Publishers, 2005.

(118) Schlichting, I.; Berendzen, J.; Chu, K.; Stock, A. M.; Maves, S. A.; Benson, D. E.; Sweet, R. M.; Ringe, D.; Petsko, G. A.; Sligar, S. G. *Science* **2000**, *287*, 1615.

(119) Denisov, I. G.; Makris, T. M.; Sligar, S. G.; Schlichting, I. *Chem. Rev.* **2005**, *105*, 2253.

(120) Sono, M.; Roach, M. P.; Coulter, E. D.; Dawson, J. H. *Chem. Rev.* **1996**, *96*, 2841.

(122) Elango, N.; Radhakrishnan, R.; Froland, W. A.; Wallar, B. J.; Earhart, C. A.; Lipscomb, J. D.; Ohlendorf, D. H. *Protein Sci.* **1997**, *6*, 556.

(123) Shu, L.; Nesheim, J. C.; Kauffmann, K.; Münck, E.; Lipscomb, J. D.; Que, L. *Science* **1997**, *275*, 515.

(126) Bruijnincx, P. C. A.; van Koten, G.; Klein Gebbink, R. J. M. *Chem. Soc. Rev.* **2008**, *37*, 2716.

(127) Gibson, D. T.; Resnick, S. M.; Lee, K.; Brand, J. M.; Torok, D. S.; Wackett, L. P.; Schocken, M. J.; Haigler, B. E. *J. Bacteriol* **1995**, *177*, 2615.

(128) Karlsson, A.; Parales, J. V.; Parales, R. E.; Gibson, D. T.; Eklund, H.; Ramaswamy, S. *Science* **2003**, *299*, 1039.

(129) Ferraro, D. J.; Gakhar, L.; Ramaswamy, S. *Biochem. Biophys. Res. Commun.* **2005**, *338*, 175.

(130) Roelfes, G.; Lubben, M.; Hage, R.; Que, L.; Feringa, B. L. *Chem. Eur. J.* **2000**, *6*, 2152.

(133) Jackson, T. A.; Rohde, J.-U.; Seo, M. S.; Sastri, C. V.; DeHont, R.; Stubna, A.; Ohta, T.; Kitagawa, T.; Münck, E.; Nam, W.; Que, L. *J. Am. Chem. Soc.* **2008**, *130*, 12394.

(134) Solomon, E. I.; Brunold, T. C.; Davis, M. I.; Kemsley, J. N.; Lee, S.-K.; Lehnert, N.; Neese, F.; Skulan, A. J.; Yang, Y.-S.; Zhou, J. *Chem. Rev.* **2000**, *100*, 235.

(136) de Visser, S. P.; Rohde, J.-U.; Lee, Y.-M.; Cho, J.; Nam, W. *Coord. Chem. Rev.* **2013**, *257*, 381.

(137) Chen, K.; Costas, M.; Que, J. L. *Dalton Trans.* **2002**, 672.

(148) Xue, G.; Pokutsa, A.; Que, L. *J. Am. Chem. Soc.* **2011**, *133*, 16657.

(149) Xue, G.; De Hont, R.; Münck, E.; Jr, L. Q. *Nature Chem.* **2010**, *2*, 400.

(150) Ménage, S.; Vincent, J.-M.; Lambeaux, C.; Fontecave, M. *J. Mol. Catal. A: Chem.* **1996**, *113*, 61.

(155) Holland, P. L.; Rodgers, K. R.; Tolman, W. B. *Angew. Chem. Int. Ed.* **1999**, *38*, 1139.

(156) Ryan, S.; Adams, H.; Fenton, D. E. *Inorg. Chem.* **1998**, *37*, 2134.

(157) Nam, W. *Acc. Chem. Res.* **2007**, *40*, 522.

(175) Stahl, S. S.; Lippard, S. J. In *Iron Metabolism*; Wiley-VCH Verlag: 1999, p 303.

(176) Rosenzweig, A. C.; Frederick, C. A.; Lippard, S. J.; Nordlund, P. *Nature* **1993**, *366*, 537.

(177) Lee, S.; Nesheim, J. C.; Lipscomb, J. D. *J. Biol. Chem.* **1993**, *268*, 21569.

(178) Costas, M.; Mehn, M. P.; Jensen, M. P.; L. Que, J. *Chem. Rev.* **2004**, *104*, 939.

(179) Park, M. J.; Lee, J.; Suh, Y.; Kim, J.; Nam, W. *J. Am. Chem. Soc.* **2006**, *128*, 2630.

(180) Cho, J.; Jeon, S.; Wilson, S. A.; Liu, L. V.; Kang, E. A.; Braymer, J. J.; Lim, M. L.; Hedman, B.; Hodgson, K. O.; Valentine, J. S.; Solomon, E. I.; Nam, W. *Nature* **2011**, *478*, 502.

(181) E. A. Duban, K. P. B., E. P. Talsi *Kinet. Catal.* **2008**, *49*, 379.

(182) Roelfes, G.; Vrajmasu, V.; Chen, K.; Ho, R. Y. N.; Rohde, J.-U.; Zondervan, C.; la Crois, R. M.; Schudde, E. P.; Lutz, M.; Spek, A. L.; Hage, R.; Feringa, B. L.; Münck, E.; Que, L. *Inorg. Chem.* **2003**, *42*, 2639.

(183) Meunier, B.; Girerd, J.-J.; Banse, F.; Simaan, A. In *Metal-Oxo and Metal-Peroxo Species in Catalytic Oxidations*; Springer Berlin Heidelberg: 2000; Vol. 97, p 145.

(184) Proshlyakov, D. A.; Henshaw, T. F.; Monterosso, G. R.; Ryle, M. J.; Hausinger, R. P. *J. Am. Chem. Soc.* **2004**, *126*, 1022.

(185) Vaska, L. *Acc. Chem. Res.* **1976**, *9*, 175.

(186) Horner, O.; Jeandey, C.; Oddou, J.-L.; Bonville, P.; McKenzie, Christine J.; Latour, J.-M. *Eur. J. Inorg. Chem.* **2002**, *2002*, 3278.

(187) Li, F.; Meier, K. K.; Cranswick, M. A.; Chakrabarti, M.; Van Heuvelen, K. M.; Münck, E.; Que, L. *J. Am. Chem. Soc.* **2011**, *133*, 7256.

(188) Atkins, P.; dePaula, J.; In *Atkins' Physical Chemistry 8th Edition*; Oxford University Press: 2006, 811 - 814.

(189) Wang, D.; Ray, K.; Collins, M. J.; Farquhar, E. R.; Frisch, J. R.; Gomez, L.; Jackson, T. A.; Kerscher, M.; Waleska, A.; Comba, P.; Costas, M.; Que, L. *Chem. Sci.* **2013**, *4*, 282.

(190) Do, L. H.; Xue, G.; Que, L.; Lippard, S. J. *Inorg. Chem.* **2012**, *51*, 2393.

(191) Dong, Y.; Fujii, H.; Hendrich, M. P.; Leising, R. A.; Pan, G.; Randall, C. R.; Wilkinson, E. C.; Zang, Y.; Que, L. *J. Am. Chem. Soc.* **1995**, *117*, 2778.

(192) Friedle, S.; Reisner, E.; Lippard, S. J. *Chem. Soc. Rev.* **2010**, *39*, 2768.

(193) Ghosh, A.; Almlöf, J.; Que, L. *Angew. Chem. Int. Ed.* **1996**, *35*, 770.

(194) Xue, G.; Wang, D.; Hont, R. D.; Fiedler, A. T.; Shan, X.; Munck, E.; Jr, L. Q. *Proc. Natl. Acad. Sci.* **2007**, *104*, 20713.

(195) Zang, Y.; Pan, G.; Que, L.; Fox, B. G.; Munck, E. *J. Am. Chem. Soc.* **1994**, *116*, 3653.

(196) Zang, Y.; Dong, Y.; Que, L.; Kauffmann, K.; Muenck, E. *J. Am. Chem. Soc.* **1995**, *117*, 1169.

(197) Wong, E.; Jeck, J.; Grau, M.; White, A. J. P.; Britovsek, G. J. P. *Catal. Sci. Tech.* **2013**, *3*, 1116.

(198) Rowe, G. T.; Rybak-Akimova, E. V.; Caradonna, J. P. *Inorg. Chem.* **2007**, *46*, 10594.

(199) Rowe, G. T.; Rybak-Akimova, E. V.; Caradonna, J. P. *Chem. Eur. J.* **2008**, *14*, 8303.

Chapter 5 – Synthesis of a New Generation Series of Aza-Macrobicyclic Ligand Scaffolds for use in Multi-electron Reactions

The synthesis of a new generation of aza-macrobicyclic ligand scaffolds for investigation as bi-metallic molecular catalysts is outlined in this chapter. The designed functionality of this new scaffold is similar to that outlined for ligand scaffold L^1 **(21)** (Chapter 1 and 2). The second generation ligand scaffold has been designed in the hope of addressing the short comings of the L^1 bi-metallic complexes that were that the structure was highly flexible with large M···M distances such that the original design of an asymmetric mixed valence complex could not be achieved with these structures. As with L^1, the design is such that two metal ions are intended to coordinate in distinctive pockets, one redox active and one redox innocent. The bis(imino)pyridine redox active group was chosen as it has an established two-electron redox series and evidence of facilitating multi-electron reactions. There is a wealth of evidence of the innocent 1,8-dimethyl-1,4,8,11-tetraazacyclotetradecane macrocycle **(53)** coordinating late first row transition metals within the macrocyclic cavity and so it was selected as the second coordination site. A series of five scaffolds have been designed with the same redox active and innocent units but with a different set of spacers varying in length; **C9** – **C13** (Figure 65). Altering the spacer allows for the investigation of M···M distance on magnetism and reactivity. The spacers incorporated are the aliphatic chains; ethyl, propyl and butyl and the aromatic benzyl group in *meta*- and *para*-substituted positions, which allows for the additional investigation of π-stacking contributions to metal interactions. In this Chapter the synthetic routes toward creating the bi-metallic catalysts, which are in the completion stages, are discussed. Density functional theory geometry optimisation calculations were conducted to gain insight into the final target structures and to determine how the series of spacers effect M···M distances.

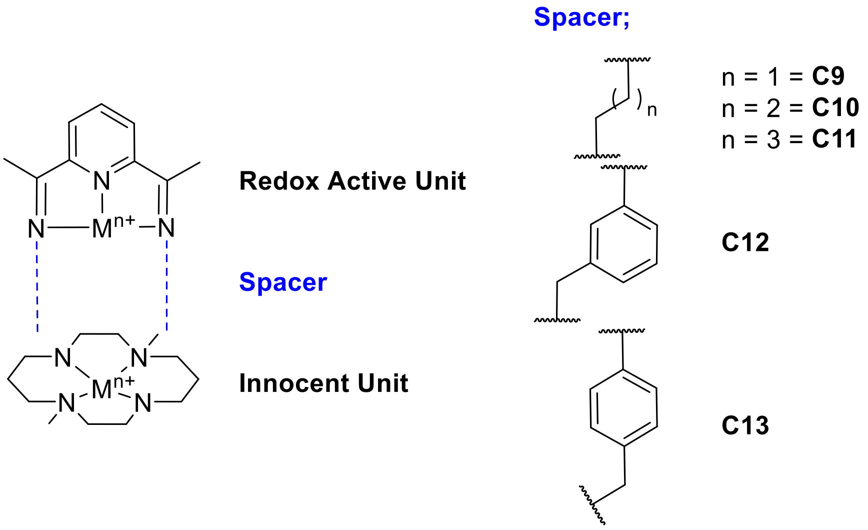

Figure 65. Structural Design of Aza-Macrobicyclic Ligand Scaffold with Various Spacers. M = 1st Row Transition Metal.

5.1 Introduction

The examination of L^1 as a bi-metallic catalyst scaffold uncovered several pitfalls, discussed in Chapter 2 - Conclusions, and so are only briefly readdressed herein. Firstly, L^1 is highly flexible preferentially forming an L^1 dimer for **C2**, **C3** and **C4** and forming some unexpected tri-metallic and tetra-metallic structures, as seen by other members of the Hess group investigating the coordination of different first row transition metals. The original design of an asymmetric mixed valence complex cannot be achieved with these structures. The second pitfall is the large M···M distances found for the bi-metallic complexes which are unable to hold the metal ions closely enough for processes such as hydrogen migration, required for proton reduction. Thirdly, from CV studies, only the one-electron reduced form of L^1, **C1**, **C2** and **C3** was accessible, thus bi-metallic complexes could not be used to generate a two-electron mixed valence state. And finally, stability of L^1 and subsequent bi-metallic complexes is problematic in aqueous and acidic media.

Therefore, to overcome the outlined issues a new ligand scaffold is required with increased rigidity to maintain the two distinct coordination sites. Several scaffolds should be investigated in attempt to fine tune to M···M. The redox active unit should have established access to the two electron reduction series to enable the formation of two electron mixed valence species. Overall stability of the molecule should be improved.

The redox active bis(imino)pyridine unit was chosen as it has established redox activity with the ability to accept up to three electrons (Scheme 41).[200] The first one-electron reduction results in the formation of a π-radical monoanion (S = 1/2). The second one-electron reduction results in the formation of a diradical dianion (with a triplet ground state), and a third one-electron reduction yields a trianion (S = 1/2).[200] The three-electron reduction has been achieved for a lithium complex,[201] but in more frequent cases coordination complexes only access the two-electron reduced form of the ligand.[200]

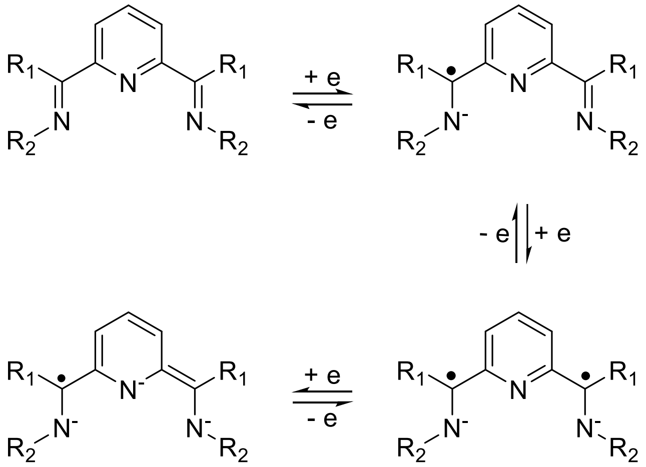

Scheme 41. Three Electron Redox Series Established for Bis(imino)pyridine.[200]

As described previously in Chapter 2 the PDI (pyridine diimine) ferrous complex has shown activity toward multi-electron reactions. Reduction of the ferrous $Fe^{II}(PDI)Cl_2$ with a sodium amalgam affords the di-radical species **(23)** capable of the [2+2] cycloaddition of dienes and terminal alkene hydrosilylation (Scheme 11).[51, 68, 71] The central iron ion remains in the ferrous oxidation state throughout the catalytic cycles with the charge localised on the PDI ligand.

Macrocycles are important ligands, abundant in transition metal coordination chemistry as they mimic the structure of important biological scaffolds, such as the porphyrins found in metalloenzymes. They provide thermodynamic and kinetic stabilities to subsequent metal complexes uncommon or unseen with ligand scaffolds of linear structure. 1,8-Dimethyl-1,4,8,11-tetraazacyclotetradecane (**53**) was chosen as the innocent coordination unit to provide increased stability and rigidity to the overall scaffold. There is a wealth of evidence on the ability of cyclam to coordinate late first row transition metals within the macrocyclic cavity; $[Fe(TMC)]^{2+}$ **(51)** is a benchmark molecular catalyst for C-H oxidation highlighted in Chapter 3 – Oxidation of Hydrocarbons by Di-ferrous C2 and C3. The four equatorial *N*-donors allow for a range of coordination geometries to be accommodated whilst discouraging dimerisation by encapsulating the ion.

The design of the new series of ligand scaffolds is such that the redox active and innocent units are connected in a cyclic fashion rather than *via* a singular bridge, as in L^1, to ensure the preservation of the two distinctive coordination sites. The two units are bridged in a cross-linked manner by *trans* *N*-donors of dimethylcyclam to increase chances that the two metal ions will be held in close proximity. The formation of the second macrocycle makes the structure macrobicyclic and places it within the group of macropolycycles. Macropolycycles are of research interest due to their ability to introduce separate cavities into one molecule structure called crypts. As the macrocyclic effect increases stability so does the cryptate effect. Some macropolycyclic structures are shown in Figure 66.[202]

Structure A (Figure 59) illustrates a singular macrocycle. Structure B is macrobicycle now with two cavities. Structures C and D are both macrotricyclic, but with very different structures; C is cylindrical forming three separate cavities, while D is spheroidal with one three-dimensional cavity. Macropolycycles have the ability to form inclusion complexes, which trap substrates within the molecular structure.[202]

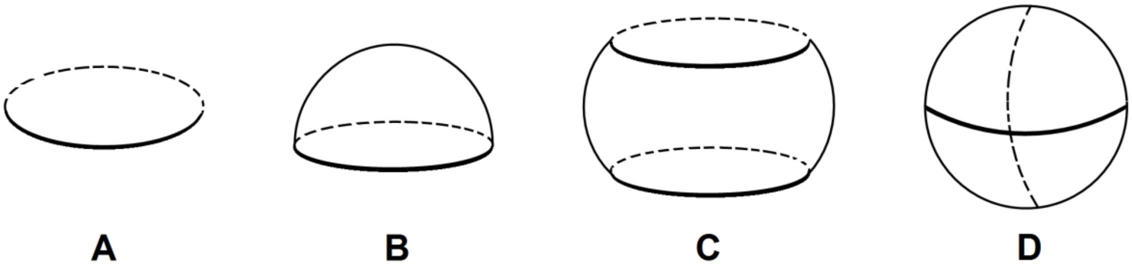

Figure 66. A Selection of Different Variations on Macropolycycles.

Bi-metallic transition-metal complexes of macropolycyclic ligands have been studied as they can serve as models of some metalloenzyme sites potentially activating small molecules such as O_2, CO and N_2. A notable example of the small molecule activation is the four electron reduction of O_2 catalysed by Co derivatives of face-to-face porphyrins, as in structure C.[203] Bi-metallic complexes where the ions are separated by a distance of 4 – 6 Å are particularly interesting because the substrate inside the cavity should be able to interact simultaneously with both metal ions.

The design of the new scaffold discussed in this chapter takes the form of macrobicyclic structure B and is represented in Figure 67 where the bridge head unit is redox-active bis(imino)pyridine and the base unit dimethylcyclam (**53**). A series of five spacers were chosen increasing in atomic length. The spacer group is altered to investigate the effect on M···M interactions, magnetism and reactivity. The spacers incorporated are the aliphatic chains ethyl, propyl and butyl, and the aromatic benzyl group in the *meta*- and *para*-substituted positions, which allows for the additional investigation of π-stacking contribution to metal interactions. The synthetic routes developed for the synthesis of the five macrobicycles are described herein.

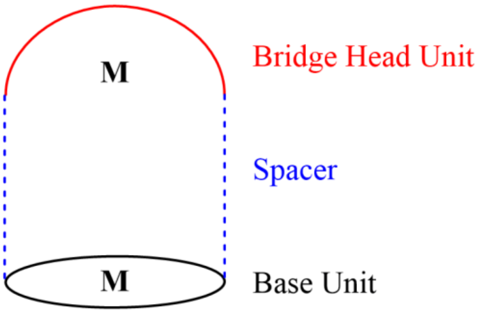

Figure 67. Macrobicyclic Structure Representation of Molecules Studied in this Chapter.

5.2 Synthesis of Diamine Species for Schiff Base Condensations

Schiff-base macrocycles are generally prepared by condensation of a dicarbonyl unit with a diamine unit.[204] The strategy toward creating the five target macrobicycles was therefore to create diamines of the different spacers trans-substituted on the dimethylcyclam base unit, then to react with diacetylpyridine to create the redox active unit and complete the macrobicycle.

5.2.1 Synthetic Studies Toward Diamine 56 – Ethyl Spacer

The first step toward achieving **56** was the addition of the pendant spacer groups onto the base dimethylcyclam unit, **(53)**. An *N*-tosylaziridine ring opening and subsequent deprotection was envisioned. *N*-Tosylaziridine **(54)** was added to compound **53** in CH_3CN at 90 °C (Scheme 42). This reaction was reported by Comba and co-workers, but no spectroscopic data were collected on the *N*-tosyl-protected product.[205] The ^1H NMR spectrum obtained after a 6 h reaction period were suggestive that the desired product had been formed; there was no literature data to compare to, the crude residue was therefore carried forward into the next step.

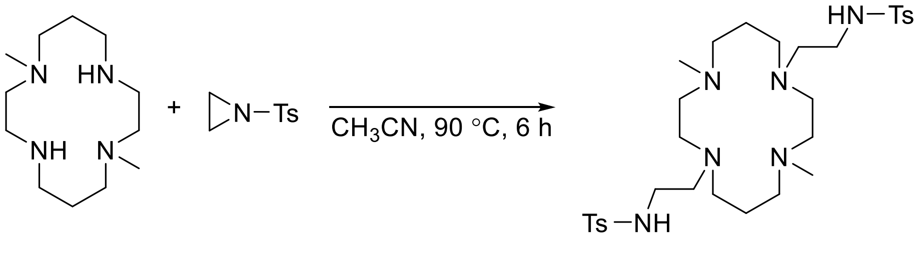

53 **54** **55**

Scheme 42. *N*-Alkylation of Dimethylcyclam 53 *via* Ring Opening of *N*-Tosylaziridine to Form 55.

N-Tosyl deprotection was conducted with concentrated H_2SO_4 at 100 °C as per literature procedure (Scheme 43).[205] After 8 h the disappearance of the *N*-tosyl aromatic signals in the ^1H NMR spectrum were observed alongside peaks in the aliphatic region suggesting the desired product was formed however purity was an issue throughout this route. An alternative synthetic route was therefore sought.

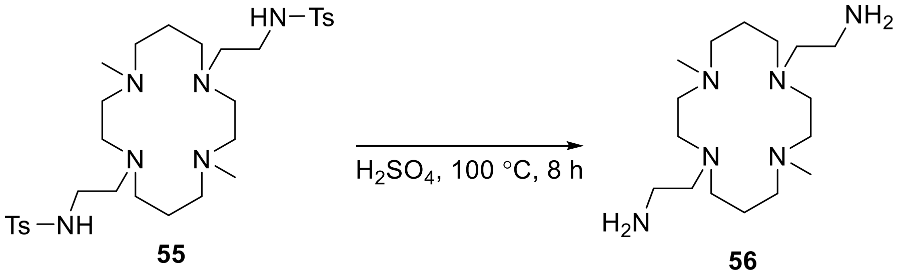

55 **56**

Scheme 43. *N*-Tosyl Deprotection of 55 to Form Diamine 56

A Strecker reaction with compound **53**, NaCN and formaldehyde in H_2O gave, after a 12 h reaction period at room temperature, product **57** in quantitative yield (99 %) (as determined by ^{1}H NMR spectroscopy) (Scheme 44).

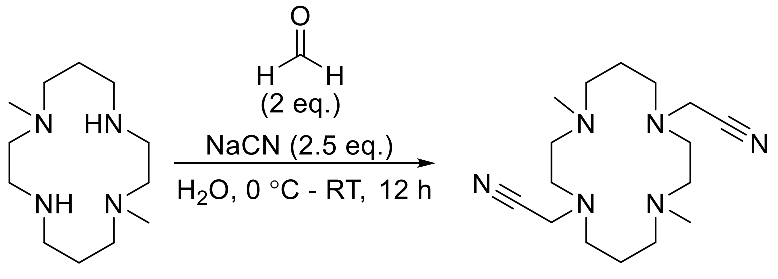

53 **57**

99 %

Scheme 44. *N*-Alkylation of Dimethylcyclam 53 *via* Strecker Reaction to Form 57.

To reduce the pendant nitrile groups on compound **57** to the corresponding primary amines, **56**, several reduction methods were investigated with reductants such as $LiAlH_4$ and $Ni^0/NaBH_4$, these methods provided the desired product in typically poor conversion and in most cases showed complex crude mixtures (as determined by ^{1}H NMR spectroscopy). Pleasingly, the nitrile substituents were successfully reduced with the use of BH_3.DMS in THF at 80 °C for 72 h, proceeded by the addition of H_2O and HCl at 120 °C for 2 h, to produce the **56**.6HCl salt. The **56**.6HCl salt was made alkaline and extracted to yield the free amine **56** (32 % isolated yield after recrystallisation) (Scheme 45). Despite the long reaction time this procedure proved to be an improvement on that reported by Kaden and co-workers who applied a Raney Ni/H_2 and ammonia reaction conducted in a high pressure autoclave with a reaction time of 1 week.[206] Subsequent reactions described by Kaden and co-workers commenced from the **56**.6HCl salt, the free amine was never isolated. Compound **56** was found to be inherently unstable at room temperature, however, the compound can be stored at −10 °C for at least three months under an inert atmosphere without decomposition (determined by ^{1}H NMR spectroscopy).

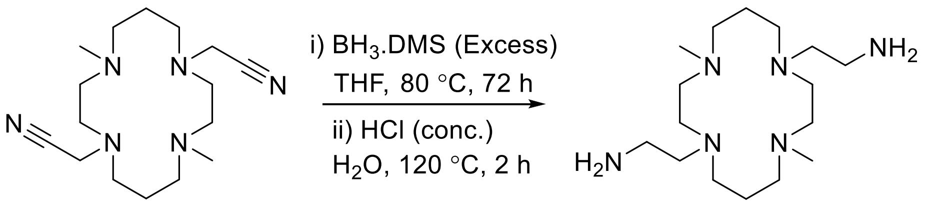

57

56

32 %

Scheme 45. BH_3.DMS Reduction of 57 to Form Free Diamine 56.

5.2.2 Synthetic Studies Toward Amine 59 – Propyl Spacer

The synthesis of compound **59** was pursued to extend the distance between coordination sites to favour the coordination of two metal ions. The first step in the synthesis of **59** is the addition of the pendant spacer groups to the base unit **53** with the *trans* alkylation of the secondary amines in the N(4) and N(11) positions. Compound **58** was synthesised in 75 % yield by a Michael addition using acrylonitrile (Scheme 46). The reaction proceeded readily at room temperature.

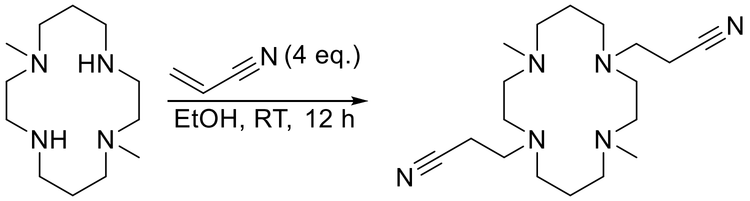

53

58

75 %

Scheme 46. Michael Addition of 53 with Acrylonitrile to Form 58.

Compound **58** was reduced to the corresponding primary amine using the same synthetic route as was employed for **57** (Scheme 47). Reaction durations were kept the same which again yielded complete reduction of **58** (41 % isolated yield after recrystallisation). As with **56, 59** was found to be inherently unstable at room temperature, however, the compound can be stored at −10 °C for at least three months under an inert atmosphere without decomposition (determined by ^{1}H NMR spectroscopy).

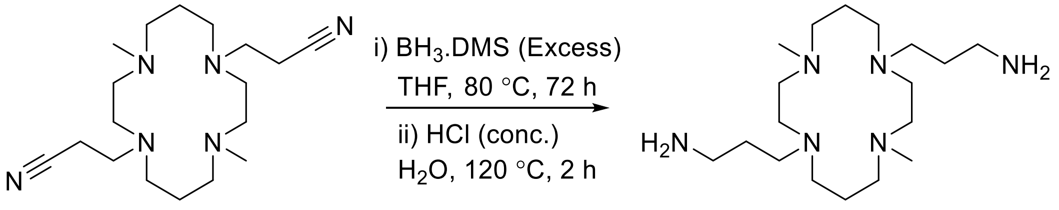

58 **59** 41 %

Scheme 47. BH$_3$.DMS Reduction of 58 to Form Free Diamine 59.

The ring-opening addition of *N*-tosylaziridine to compound **53** was similarly attempted in the synthesis of **61** using *N*-tosylazetidine **(60)**. However, this reaction gave a complex product mixture, as observed by ^{1}H NMR spectroscopy (Scheme 48). The product obtained after deprotection with H_2SO_4 again gave rise to broad peaks in the ^{1}H NMR spectrum suggesting purity is once again an issue for this route and so it was not pursued no further.

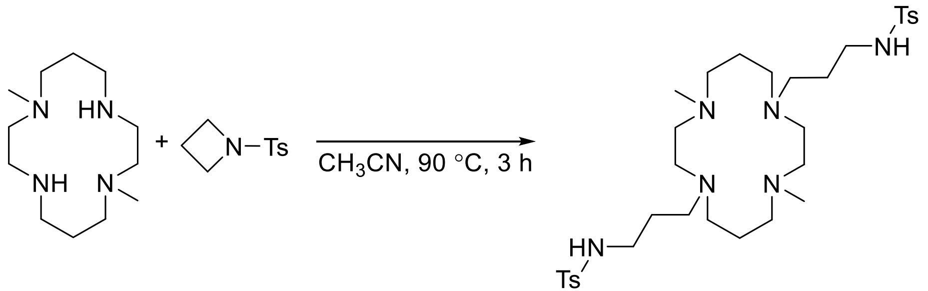

53 **60** **61**

Scheme 48. *N*-Alkylation of Dimethylcyclam 53 *via* Ring Opening of *N*-Tosylazetidine to Form 61.

5.2.3 Synthetic Studies Toward Diamine 63- Butyl Spacer

The spacer length was increased again by one atom to investigate M···M distance effects on magnetism and reactivity. The first step toward achieving **63** was the addition of the pendant spacer groups to compound **53** with the *trans* alkylation of the secondary amines in the N(4) and N(11) positions. The S$_N$2 reaction between **53** and 4-chlorobutyronitrile in the presence of K_2CO_3 and KI in CH_3CN at 80 °C gave, after 72 h, the desired product **62** in 76 % yield (Scheme 49).

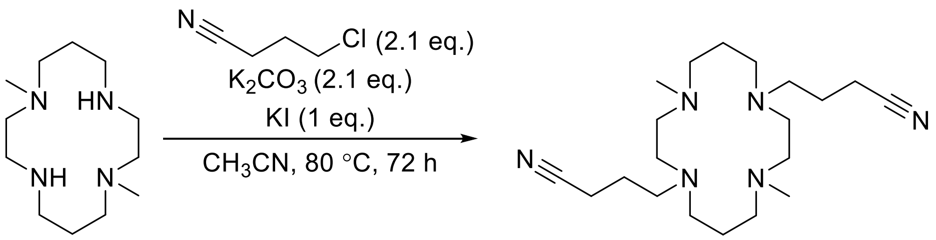

53 **62** 76 %

Scheme 49. *N*-Alkylation of Dimethylcyclam 53 *via* S$_N$2 to form 62.

Compound **62** was reduced to the corresponding primary amine using the same BH_3.DMS procedure employed previously for **57** and **58** providing product **63** in 58 % yield (Scheme 50). As with **56** and **59**, **63** was found to be inherently unstable at room temperature, however, the compound can be stored at −10 °C for at least three months under an inert atmosphere without decomposition (determined by ^{1}H NMR spectroscopy).

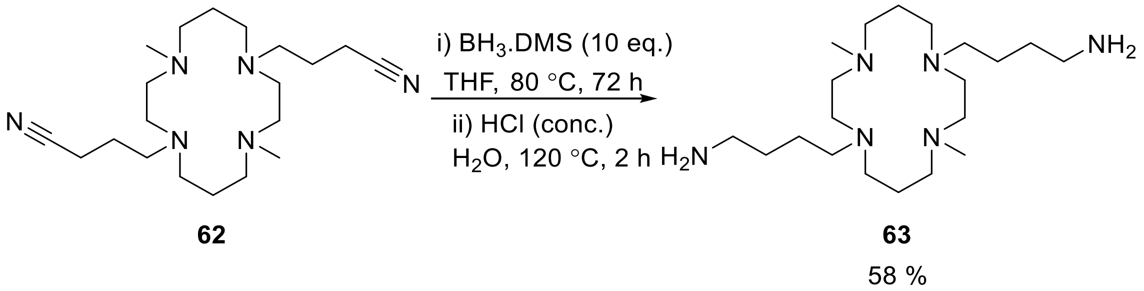

Scheme 50. BH_3.DMS Reduction of 62 to Form Free Diamine 63.

5.2.4 Synthetic Studies Toward Diamine 72 – *m*-Benzyl Spacer

With the synthesis of a range of alkyl spacers varying in chain length achieved it was next attempted to synthesise analogues containing aryl spacer units which would allow an investigation into the effects that extra ligand rigidity and π-stacking interactions may have on the properties of the corresponding bi-metallic complexes. Starting from commercially available 3-aminobenzyl alcohol **(64)** the amine group was protected with BOC anhydride giving **65** in an excellent 92 % isolated yield (Scheme 51).

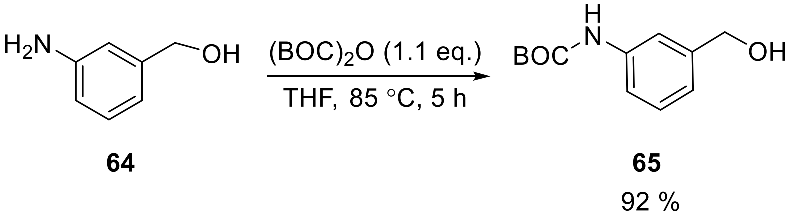

Scheme 51. BOC protection of 64 to Form 65.

The alcohol group was substituted with bromide *via* a modified Appel reaction (Scheme 52). Treatment of alcohol **65** with PPh_3 and NBS in CH_2Cl_2 at room temperature gave, after 2h, benzyl bromide **66** in a moderate 59 % yield.

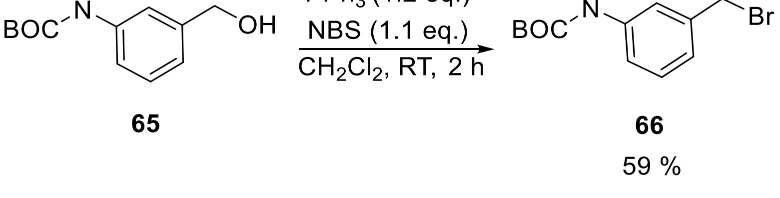

Scheme 52. Modified Appel Reaction of 65 to Form 66.

Next, compound **66** was attached to dimethylcyclam **53** *via* the S_N2 reaction applied previously for **62** (Scheme 49). Reaction of **53** with **66**, K_2CO_3, KI in CH_3CN at 80 °C produced a complex mixture of products. There was no observation of the desired product **67**. Therefore an alternative synthetic route was sought.

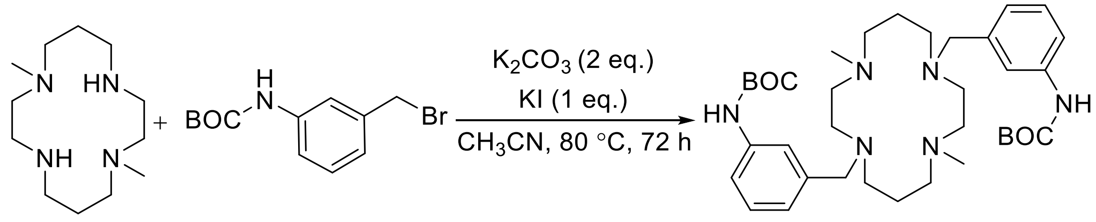

53 **66** **67**

Scheme 53. Proposed S_N2 Substitution to Dimethylcyclam 53 to Form 67.

The amine group of 3-aminobenzyl alcohol **64** was instead protected with phthalic anhydride **(68)** to form phthalimide benzyl alcohol **69** in an isolated 74 % yield (Scheme 54).

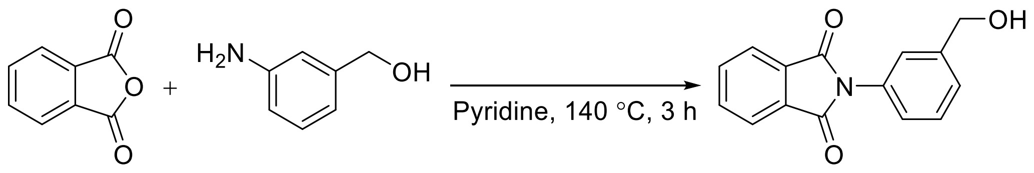

68 **64** **69**

74 %

Scheme 54. Amine Protection of 64 by Phthalic Anhydride to Form 69.

The alcohol group was substituted with a bromine *via* an Appel reaction (Scheme 55). Reaction of benzyl alcohol **69** with PPh_3 and CBr_4 in CH_2Cl_2 gave the desired benzyl bromide **70** in a relatively low 30 % yield.

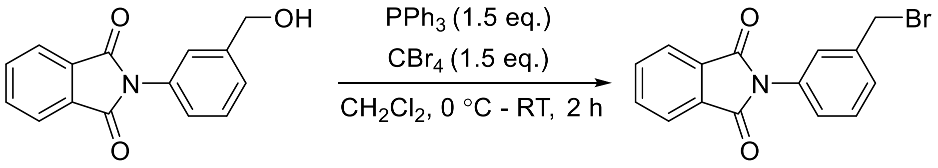

69 **70**

30 %

Scheme 55. Appel Reaction of 69 to Form 70.

The *m*-benzyl fragment **70** was attached to dimethylcyclam **53** *via* a S_N2 reaction under basic conditions, as was employed with the formation of **59** (Scheme 56). The reaction was run for 72 h, the ^1H NMR spectrum after this time period showed dominant peaks of the target molecule with some impurities (~ 5:1). Column chromatographic purification resulted in the recovery of a very poor 3 % yield of the target molecule. The poor yield is likely due to the instability of compound **71** to silica-based column chromatography. Alternatively, **71** was extracted from the crude mixture into ethyl acetate, the solution was evaporated to dryness and the yellow solid was washed with CH_3CN resulting in a white solid. This alternative purification of **71** increased final yields considerably from 3 % to 67 %.

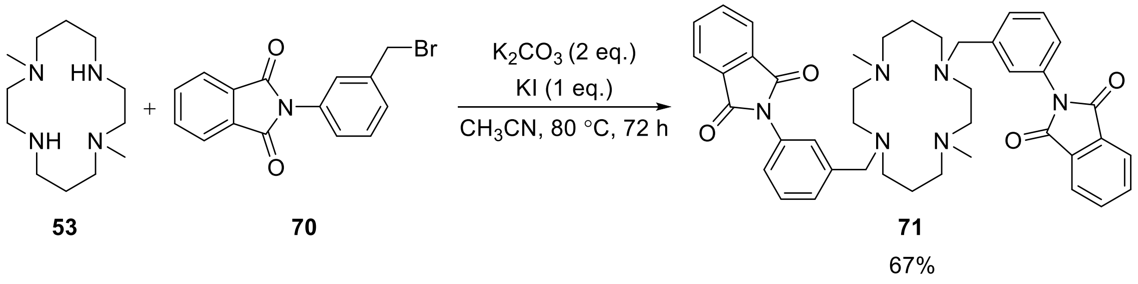

Scheme 56. S_N2 Substitution with Dimethylcyclam 53 to Form 71.

The phthalimide group was then removed using a procedure analogous to that found in a Gabriel reaction (Scheme 57). Treatment of **71** with $N_2H_4.H_2O$ in EtOH at 80 °C provided the desired product, **72**, in quantitative isolated yield.

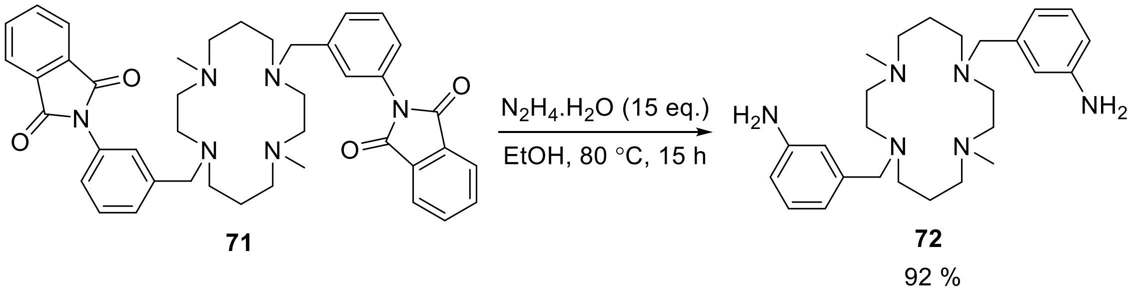

Scheme 57. Deprotection of 71 with Hydrazine Monohydrate to Form Diamine 72.

5.2.5 Synthetic Studies Toward Diamine 76- *p*-Benzyl Spacer

The para-substituted benzyl spacer was synthesised to increase the M···M distance further. Starting from commercially available 4-aminobenzyl alcohol **73**, the amine group was protected with phthalic anhydride **(68)** as with **64** to form a phthalimide **74**. The reaction proceeded readily giving **74** in a reasonable 48 % yield (Scheme 58).

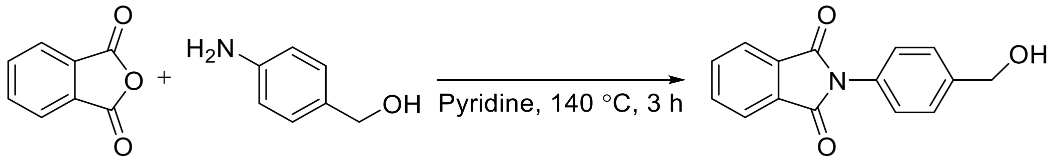

68 **73** **74**

48 %

Scheme 58. Amine Protection by Phthalic Anhydride of 73 to Form 74.

The alcohol group was substituted with a bromine *via* an Appel reaction (Scheme 59). Reaction of para-substituted benzyl alcohol **74** with PPh_3, CBr_4 in CH_2Cl_2 gave, after 2 h, product **75** in a low 22 % yield.

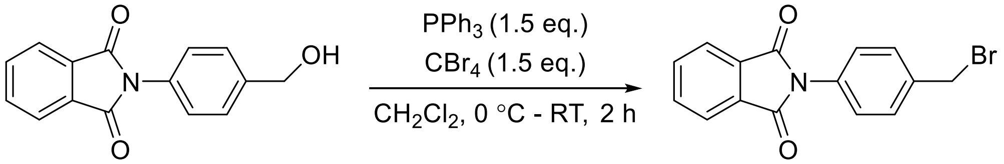

74 **75**

22 %

Scheme 59. Appel reaction of 74 to Form 75.

The *p*-benzyl spacer was proposed to be attached to dimethylcyclam *via* a S_N2 reaction under basic conditions and in the same manner as described for **71** (Scheme **60**). The same alternative purification for **71**; extraction into ethyl acetate proceeded by washing with CH_3CN, resulted in product **76** with an isolated yield of 59 %. The alternative purification increased the isolated yield considerably from 5 % to 59 % over column chromatographic purification, as was originally examined again suggesting an instability of **76** on silica.

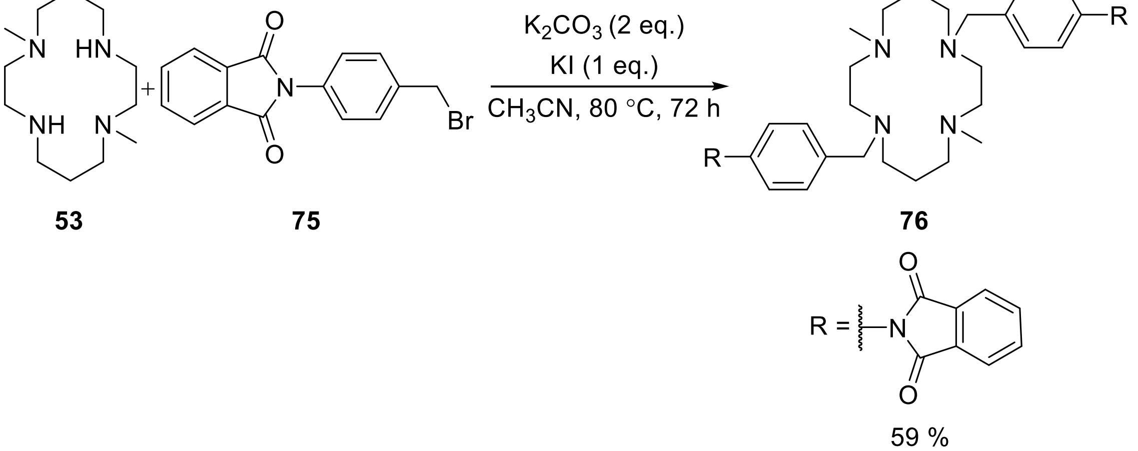

53 **75** **76**

59 %

Scheme 60. Proposed SN2 Substitution with Dimethylcyclam 53 to Form 76.

5.3 Schiff Base Dual Condensation Reactions

A dual Schiff base condensation was required to create the diimine head unit and complete the aza-macrobicycle. This is typically difficult to achieve due to the high likelihood of polymerisation versus that of the desired cyclisation. Schiff-base macrocycles are generally prepared by the metal-templated reaction of a dicarbonyl head unit and diamine unit.[204] The presence of the metal ion promotes the cyclisation reaction in several ways. Firstly, by acting as a Lewis acid enhancing the polarisation of the carbonyl bond thereby increasing the electrophilicity. Secondly, it can induce a kinetic template effect by bringing the reactive sites closer increasing the likelihood of reaction. Finally, a thermodynamic template effect stabilises the macrocycle as the metal complex.[204]

Template reaction conditions between diacetylpyridine and compound **56** were investigated in attempt to form the macrobicycle. $ZnNO_3$, $MnCl_4.4H_2O$, $FeCl_2$ and $[Fe(CH_3CN)_6](PF_6)_2$ were all investigated as the metal template with the latter giving the most promising results hopefully yielding desired macrobicycle **C9** (Scheme 61). The reaction of $[Fe(CH_3CN)_6](PF_6)_2$ with diacetylpyridine formed a pink complex typical of ferrous bound diacetylpyridine; $[Fe(\text{diacetylpyridine})(CH_3CN)_2]^{2+}$ **(77)**. Addition of compound **56** at high dilution at 80 °C resulted in a persistent purple suspension after a 12 h reaction period. Filtration of the crude mixture resulted in a purple solid and a pale yellow solution. Recrystallisation of the purple solid has not yet yielded single crystals suitable for X-ray diffraction. The IR spectrum of the purple solid provided evidence a condensation reaction successfully occurred due to the absence of the distinctive carbonyl band of diacetylpyridine observed at 1696 cm^{-1} and the presence of the bis(imino)pyridine νC=N observed at 1616 cm^{-1} typically found between 1610 – 1630 cm^{-1}.[207] ^1H NMR spectrum of the purple solid in DMF-*d*7 did not exhibit any peaks between 16 and -3 ppm high frequency peaks, suggesting the purple solid is a paramagnetic compound, the iron ion is not held in the low-spin configuration.

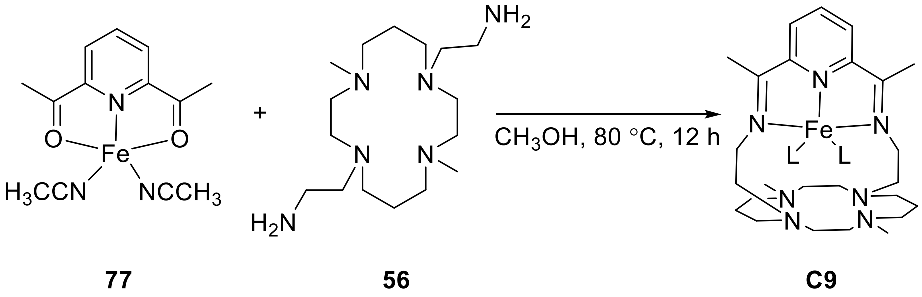

Scheme 61. Proposed Template Reaction to Form C9 where L = CH_3CN written as L for Clarity.

The addition of the second metal ion, hoped to be coordinated within the dimethylcyclam base unit, was attempted by reacting the crude templation purple solid with $CuCl_2$, $CoCl_2$, $FeCl_2$ and $[Fe(CH_3CN)_6](PF_6)_2$. Recrystallisation of the crude mixture after the addition of $[Fe(CH_3CN)_6](PF_6)_2$ yielded only $[Fe(CH_3CN)_6](PF_6)_2$. It was unclear whether the recovery of unreacted $[Fe(CH_3CN)_6](PF_6)_2$ was because no reaction took place or because an excess of

$[Fe(CH_3CN)_6](PF_6)_2$ was unintentionally used as the purple solid was yet to be confirmed as solely **C9**.

The same template conditions, employing $[Fe(CH_3CN)_6](PF_6)_2$, as was used in attempt to synthesise ferrous macrobicycle **C9** were also used in the synthesis of **C10** and **C11** (Scheme 62). In both cases a transient peach suspension was followed by the formation of a persistent purple suspension. Recrystallisation of each of the purple solids has not yet yielded single crystals suitable for X-ray diffraction. The IR spectra of both the purple solids provided evidence a successful condensation reaction occurred due to the absence of the distinctive carbonyl bands of diacetylpyridine and the presence of the bis(imino)pyridine νC=N observed at 1652 cm^{-1} for **C10** and 1632 cm^{-1} for **C11**. Again as with **C9**, the ^1H NMR spectroscopy of the purple solids in DMF-*d*7 exhibited broad, high frequency peaks, suggesting both purple solids are paramagnetic compounds, the iron ions are not held in the low-spin configuration.

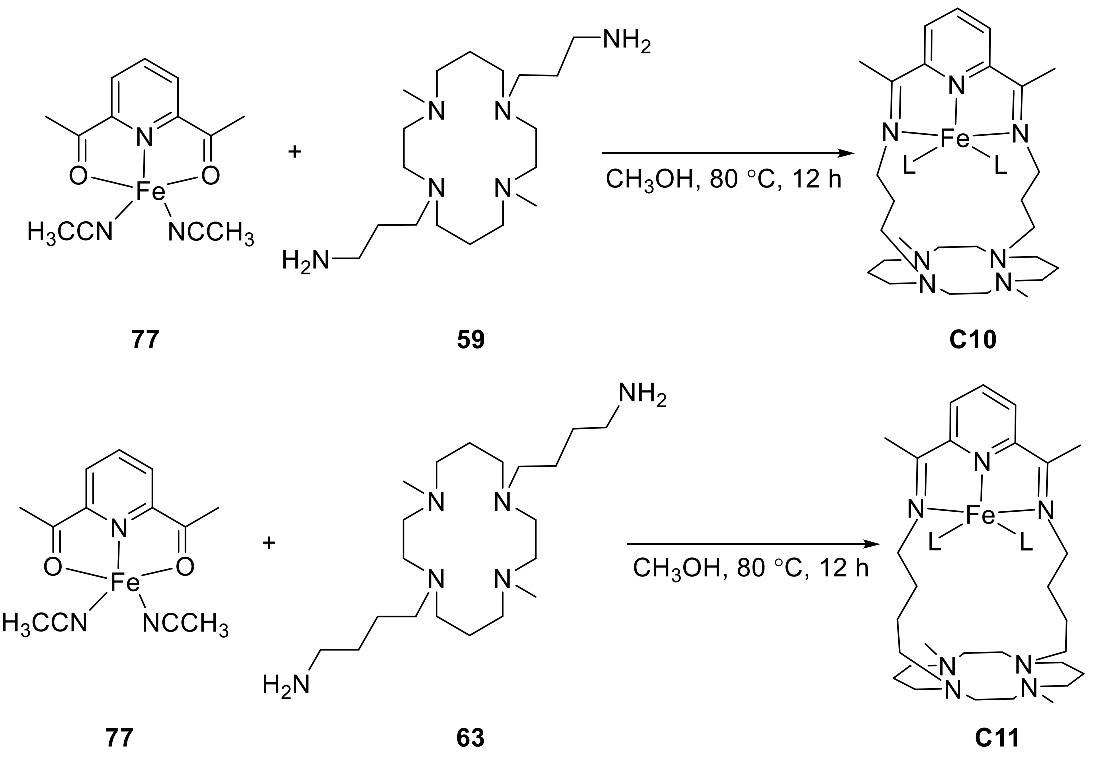

77 **59** **C10**

77 **63** **C11**

Scheme 62. Top: Proposed Template Reaction to Form C10 where L = CH_3CN Written as L for Clarity. Bottom: Proposed Template Reaction to Form C11 where L = CH_3CN Written as L for Clarity.

The template stage was not reached for the benzyl spacers due to time constraints so the project was handed over to remaining members of the Hess group. The same template conditions are being used with the remaining diamines and are hoped to give the target structures shown in Scheme 63.

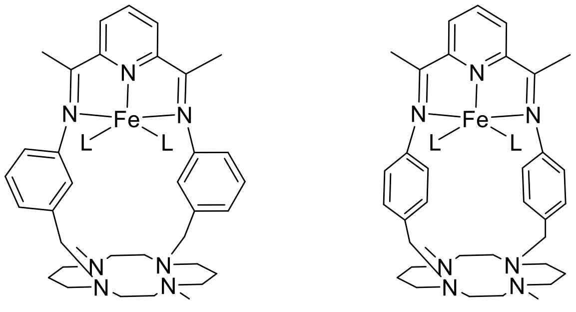

C12 **C13**

Scheme 63. Target Benzyl-substituted Spacer Macrobicycles C12 and C13 where L = CH_3CN Written as L for Clarity.

5.4 DFT Geometry Optimisations of Macrobicycles C9 – C13

Geometry optimisation calculations (B3LYP) were conducted to determine the structure of **C9**. The geometry optimised structure is shown from two viewpoints in Figure 68. The ferrous ion from the template reaction is bound by both the bis(imino)pyridine group and the dimethylcyclam base unit **(53)**. The spacer allows the bis(imino)pyridine group to fold down (76 ° to the plane of **53**) and bind the ferrous ion to two *cis-N* of **53**. The ethyl spacer (2.795 – 3.280 Å) does not allow a molecular arrangement such that a second metal ion can be coordinated. The addition of one CH_3CN molecule completes the distorted octahedral coordination geometry of the ferrous ion. The DFT-optimised geometry provides rational for the lack of reaction between the purple solid **C9** and a second metal salt.

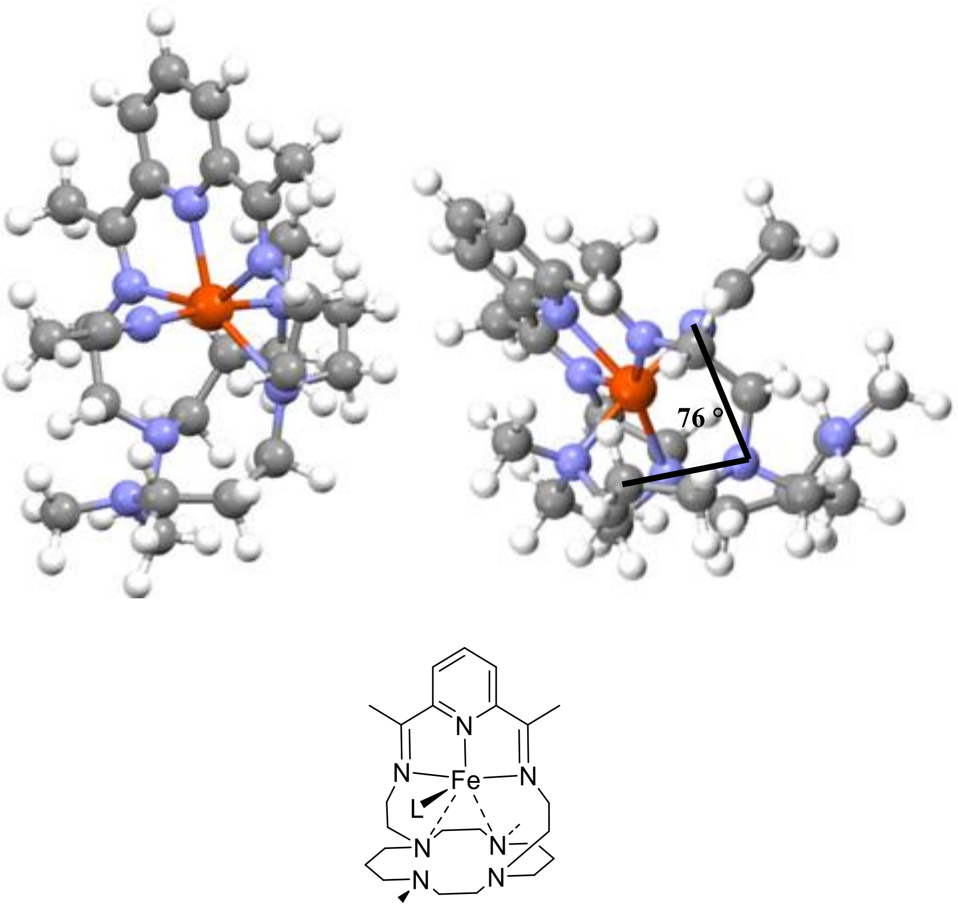

Figure 68. Top: Geometry Optimised Structure of C9 as Calculated by DFT using B3LYP at Two Viewpoints. Bottom: Molecular Representation of Optimised Structure where L = CH_3CN Written as L for Clarity.

Geometry optimisation calculations (BP86) were conducted to determine the structures of **C10**, **C11, C12** and **C13**. The geometry optimised structure of **C10** is shown from two viewpoints in Figure 69. The two coordination sites designed for the aza-macrobicycles are accessible for this structure; the ferrous ion from the template reaction is bound solely by the bis(imino)pyridine group leaving the dimethylcyclam base unit vacant. The ferrous ion is five coordinate; the bis(imino)pyridine group is tridentate and planar, two facially opposing labile CH_3CN ligands make up the coordination sphere. This geometry is typical of ferrous bis(imino)pyridine complexes.[84, 208, 207] The spacer distance between *N* atoms is calculated as 4.892 – 4.930 Å. The calculated distance between the ferrous ion and the centre of the vacant dimethylcyclam base unit is ~ 4.7 Å. This distance would allow bridging of diatomic species such as CN^-, as found by Holm and co-workers, but not monoatomic species such as OH^- which required shorter M$\cdots$M distances between 3.697 – 3.873 Å.[209]

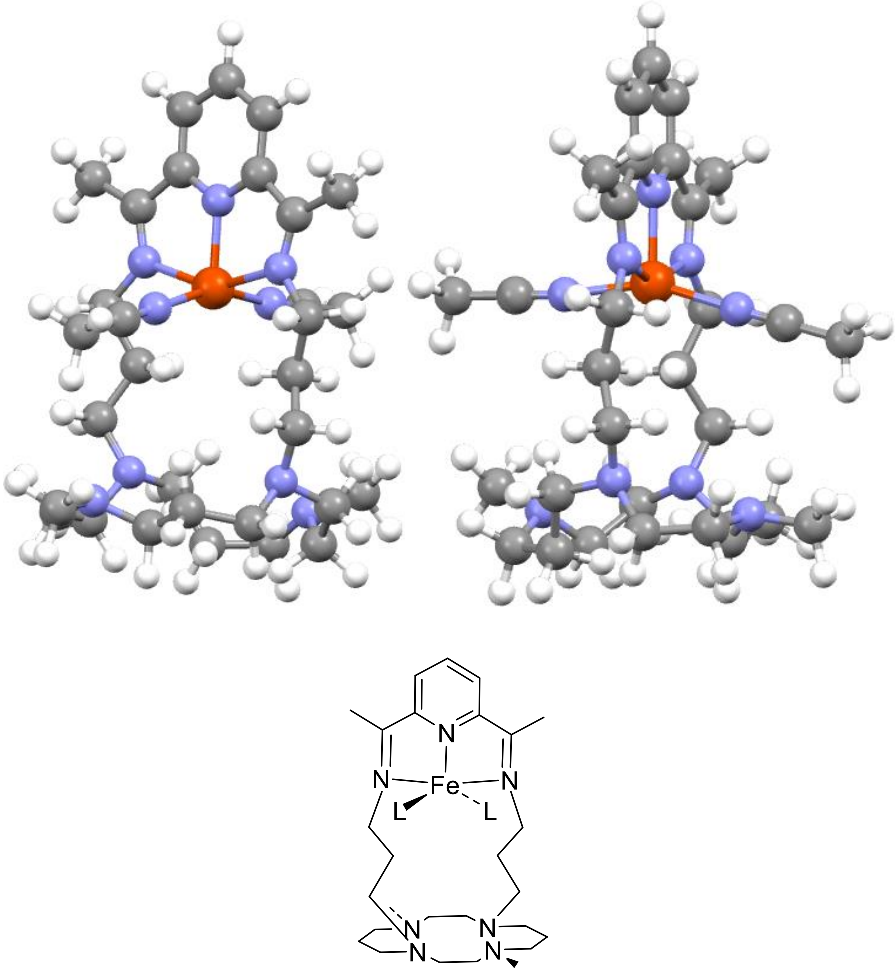

Figure 69. Top: Geometry Optimised Structure of C10 as Calculated by DFT using BP86 at Two Viewpoints. Bottom: Molecular Representation of Optimised Structure where L = CH_3CN Written as L for Clarity.

The two coordination sites designed for the aza-macrobicycles were found to be accessible for all further macrobicyclic structures examined, with the ferrous ion being solely bound by the bis(imino)pyridine group leaving the dimethylcyclam base unit vacant. The ferrous ion was always calculated as in a five coordinate geometry with two facially opposing labile CH_3CN ligands completing the coordination sphere. A trend between atomic spacer length and predicted M···M distance was observed. For **C11**, the spacer distance between *N* atoms is extended compared to **C10** to 5.553 – 5.602 Å. The calculated distance between the ferrous ion and the centre of the vacant dimethylcyclam base unit also is extended to ~ 5.1 Å. This distance may still permit bridging of diatomic molecules, as was found by Holm and co-workers, but is very unlikely to bridge small molecules like OH^-.[209] The spacer distance between *N* atoms for **C12** is comparable to **C11,** calculated as 5.422 – 5.583 Å. The calculated distance between the ferrous ion and the centre of the vacant dimethylcyclam base unit for **C12** ~ 5.3 Å. At this M···M distance Holm and co-workers found no bridging of bi-metallic complexes but instead each metal has separate terminal chlorine ligands (M···M = 5.315 Å).[209] The phenyl groups are facing 90 ° to one another and the horizontal planes are perpendicular to one another discouraging π-stacking interactions from contributing to the M-M interactions. The spacer distance between *N* atoms of **C13** is extended compared to **C12** at the longest length of 6.133 – 6.366 Å. The calculated distance between the ferrous ion and the centre of the vacant dimethylcyclam base unit is also at the furthest distance of ~ 5.7 Å. As for **C12**, this distance discourages the bridging of small molecules and is more likely that the metal ions will have terminal labile ligands.[209] Unlike **C12** the benzene rings of **C13** are facing toward one another, although slipped, suggesting possible π-stacking interactions which could increase M-M interactions.

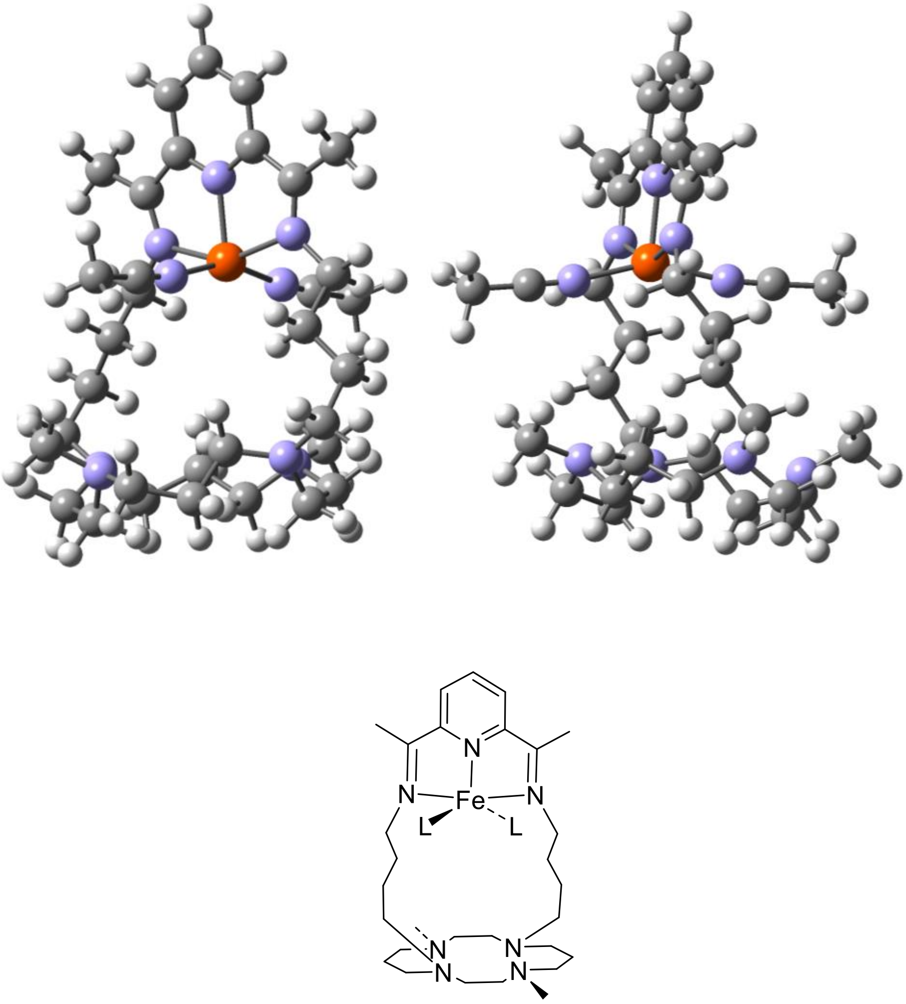

Figure 70. Top: Geometry Optimised Structure of C11 as Calculated by DFT using BP86 at Two Viewpoints. Bottom: Molecular Representation of Optimised Structure where L = CH_3CN Written as L for Clarity.

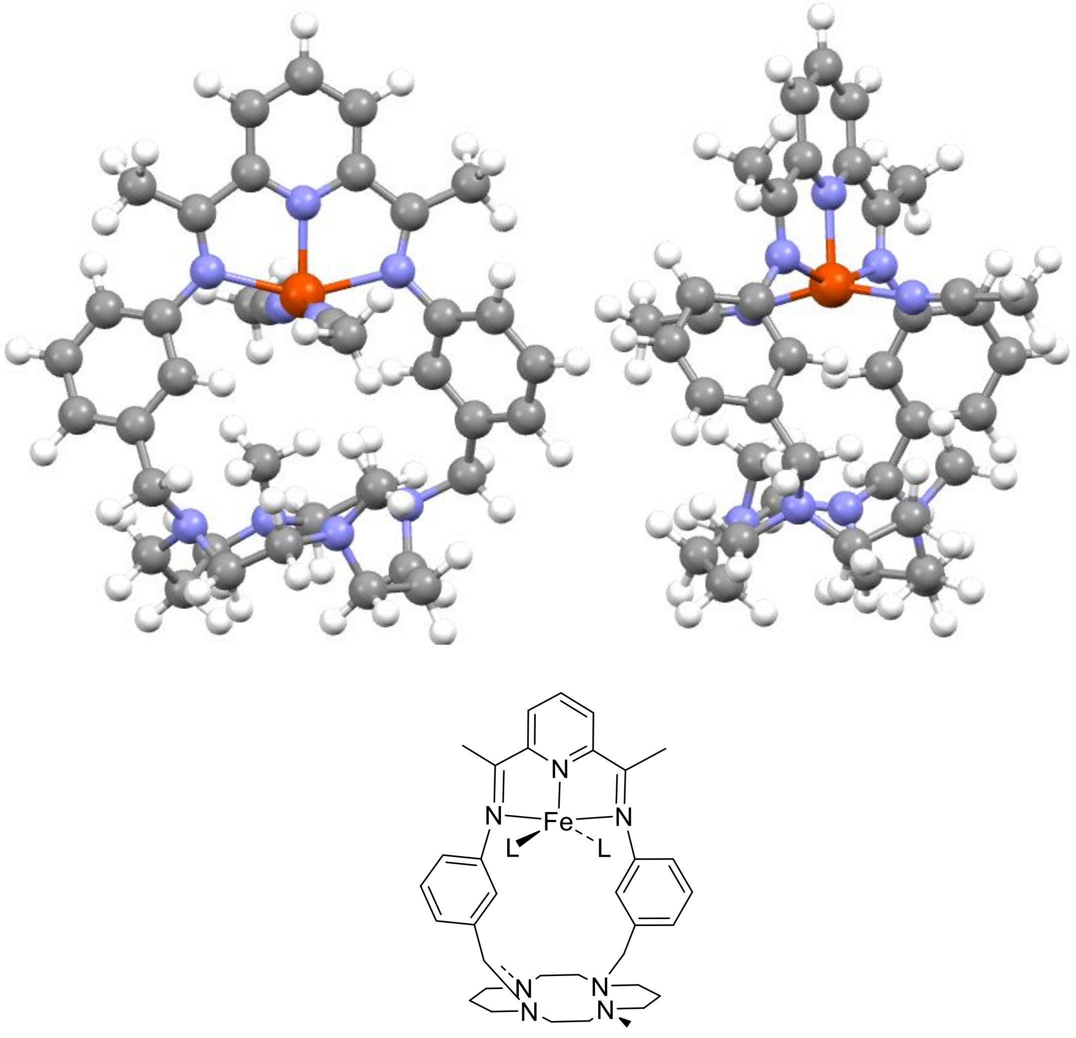

Figure 71. Top: Geometry Optimised Structure of C12 as Calculated by DFT using BP86 at Two Viewpoints. Bottom: Molecular Representation of Optimised Structure where L = CH_3CN Written as L for Clarity.

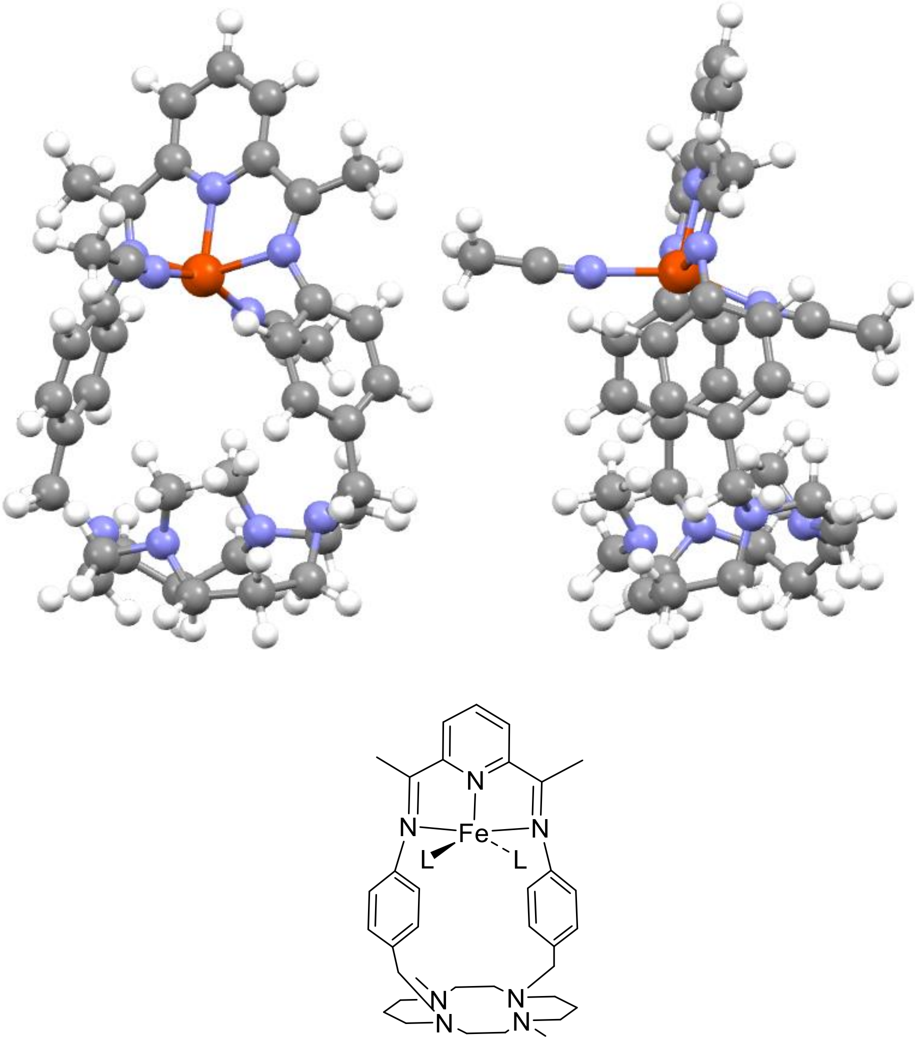

Figure 72. Top: Geometry Optimised Structure of C13 as Determined by DFT at Two Viewpoints. Bottom: Molecular Representation of Optimised Structure where L = CH_3CN Written as L for Clarity.

5.5 Conclusions and Further Work

Synthetic routes have been developed for the formation of a series of five new aza-macrobicyclic ligand scaffolds, of varying spacer length. The macrobicycles define two different coordination sites; one ion is enveloped by the redox-active bis(imino)pyridine and the second ion is encapsulated by the innocent dimethylcyclam. A series of spacers have been incorporated to allow the investigation of M···M distance on magnetism and reactivity. The scaffolds incorporating the aliphatic chain spacers; ethyl propyl and butyl, have shown promising results for the ferrous templated Schiff base condensation displaying a νC=N stretch in the IR spectra typical for bis(imino)pyridine in conjunction with the absence of distinctive carbonyl bands of diacetylpyridine. ^{1}H NMR analysis of the condensation products gave paramagnetic signals indicating the ferrous ion is not in the low spin configuration. The condensation reactions for the benzyl spacers are currently being investigated by other members of the Hess group.

DFT geometry optimisation calculations were conducted to model the mono-metallic ferrous structures and preliminarily investigate the effect of spacer length on the scaffold structure. For macrobicycle **C9** the ethyl spacer was not long enough to define two coordination sites; the ferrous ion is bound by both the bis(imino)pyridine head group and by one side of the dimethylcyclam. This echoes experimental findings during which the addition of a second ion was deemed unsuccessful due to the recovery of starting material. Extending the spacer by one carbon atom, **C10**, was enough to allow the definition of two coordination sites; the ferrous ion was bound by the bis(imino)pyridine unit with two CH_3CN molecules completing the five coordinate ferrous configuration. The five coordinate geometry with two facially opposing labile ligands is common for ferrous bound bis(imino)pyridine demonstrated by $[Fe(PDI)]^{2+}$ with two chlorine ligands, two nitrogen ligands or two CH_3CN ligands and was determined for all further spacers. The M···M distance calculated for **C10**, with the incorporation of the propyl spacer, suggests the bridging of small molecules is possible between the metal sites. Extending to the butyl spacer, **C11**, increases the internuclear distance between metal sites but it is still within the reach of bridging ligands. **C12** with the metabenzyl substituted spacer is of comparable length to the butyl spacer, the incorporation of which again leads to metal sites within the reach of bridging ligands. Reactivity comparison between **C11** and **C12** will provide an interesting insight into the rigidity effect of the phenyl ring as this is the only disparity. **C13**, with the *p*-benzyl substituted spacer has the largest distance between ferrous ion and dimethylcyclam cavity of ~ 5.7 Å, a distance at which similar scaffolds presented two metal sites with terminal ligands, no bridging.[209] The advantage of the parabenzyl spacer over the meta- is that the phenyl rings are face to face, although slipped, which should encourage π-stacking interactions and could encourage electronic interactions between metal sites. The phenyl groups of **C12** are facing 90 ° to one another facing in perpendicular directions discouraging interactions.

Immediate further studies include the completion of the template Schiff base condensation reactions and the characterisation of products thereof. The growth of single crystals suitable for X-ray diffraction is the only definitive way of assuring the formation of the target ferrous bis(imino)pyridine complexes over larger macrocycles incorporating multiple bis(imino)pyridine and dimethylcyclam units. The addition of the second metal ion to the dimethylcyclam base unit may encourage crystal formation and products thereof should be analysed by magnetic susceptibility to begin to uncover the magnetic properties and interactions of the bi-metallic scaffold and future reactivity implications. Electrochemical studies should be employed to divulge the nature of the redox processes available to **C9** – **C13**. Chemical reductions should be carried out to determine if stable mixed valence complexes can be obtained. Hetero bi-metallic complex synthesis should be attempted taking into consideration the Irving-Williams series which yielded promising hetero bi-metallic complex absorption spectra data. Initial reactivity studies in acidic medium should then be carried out to determine to ability of **C9** – **C13** to serve as a proton electron catalysts.

5.6 Experimental

4,11-Dimethyl-1,4,8,11-tetraazacycloatetradecane-1,8-diethan(*N*-tosyl)amine (55).

Dimethylcyclam **(53)** (1.4 g, 1.5 mL, 6.1 mmol) was dissolved in dry CH_3CN (30 mL) and brought to reflux at 87 °C under inert atmosphere. *N*-tosylaziridine **(54)** (2.6 g, mL, 13.2 mmol) was dissolved in dry CH_3CN (30 mL) and added dropwise to the refluxing solution of **53**. The mixture was left to reflux under inert atmosphere for a further 6 h. The suspension was filtered to obtain a white solid. The reaction was carried out per literature instructions.[205] ^1H NMR ($CDCl_3$); δ 8.94 (br s, $\nu_{1/2}$ = 19.0 Hz, 2H), 7.72 (d, *J* = 8.3 Hz, 4H), 7.24 (d, *J* = 8.3 Hz, 4H), 2.88 (t, *J* = 4.8 Hz, 4H), 2.53 – 2.26 (m, 26H), 2.24 (s, 6H), 1.70 – 1.60 (m, 4H). The same quality of spectra as literature was not obtained.

4,11-Dimethyl-1,4,8,11-tetraazacycloatetradecane-1,8-diethanamine (56).

Compound **56** (0.4 g, 0.6 mmol) was dissolved in 3 mL HCl (12 M) and heated to 100 °C for 48 h. The solution was added dropwise to diethylether forming a grey solid. The solid was collected and washed with diethylether. The grey solid was dissolved in D.I. H_2O (20 mL) and 3 M NaOH added until the pH reached 14. The product was extracted with chloroform (3 x 15 mL). The reaction was carried out per literature instructions.[205] An alternative reaction route was sought as clean spectra could not be obtained. Major peaks in ^1H NMR ($CDCl_3$); δ 2.70 (t, *J* = 5.8 Hz, 4H), 2.56 – 2.48 (m, 8H), 2.46 – 2.40 (m, 12H), 2.18 (s, 6H), 1.60 (quin, *J* = 6.8 Hz, 4H). The same quality of spectra as literature was not obtained.

4,11-Dimethyl-1,4,8,11-tetraazacycloatetradecane-1,8-diacetonitrile (57).

Dimethylcyclam **(53)** (1.5 g, 1.6 mL, 6.7 mmol) and formaldehyde aq. solution (1.0 mL, 12.7 M, 13.1 mmol) were added to 100 mL RBF in air with 15 mL D.I. H_2O. The solution was cooled to 0 °C in NaCl/ice bath. NaCN (0.8 g, 16.3 mmol) was suspended in 15 mL D.I. H_2O and added dropwise to solution at 0 °C. After complete addition the mixture was warmed to RT and left to stir overnight. By the next morning a cloudy white suspension persisted. The suspension was transferred to 250 mL RBF and 100 mL, 2 M NaOH aq. was added. A white suspension persisted. The product was extracted with DCM (3 x 50 mL), dried $MgSO_4$ and solvent was removed in *vacuo* to a white solid, **57** (2.0 g, 6.5 mmol, 99 %). **CAUTION:** NaCN is fatal on contact with skin, inhalation and ingestion so wear double gloves, weigh and use in fume hood. ^1H NMR ($CDCl_3$); δ 3.62 (s, 4H), 2.65 – 2.59 (m, 8H), 2.43 (t, *J* = 5.6 Hz, 4H), 2.39 (t, *J* = 6.8 Hz, 4H), 2.18 (s, 6H), 1.60 (quin, *J* = 6.7 Hz, 4H). ^{13}C NMR ($CDCl_3$); δ 115, 54, 53, 51, 50, 43, 42, 25. ASAP-MS; 307.3 M+1. IR; 2944 (w), 2796 (m), 2772 (m), 2034 (w), 1452 (m), 1278 (m), 1148 (s), 1132 (s), 1122(s), 1050 (m), 940 (m), 906 (m), 848 (m), 808 (m), 794 (m), 748 (m), 638(m). Anal Calcd for $C_{16}H_{30}N_6$: C, 62.71; H, 9.87; N, 27.42. Found: C, 61.77; H, 9.81; N, 26.59. The ^1H NMR data obtained is in agreement with that reported in literature.[206]

4,11-Dimethyl-1,4,8,11-tetraazacycloatetradecane-1,8-diethanamine (56).

Compound **57** (1.1 g, 3.6 mmol), was added to 100 mL RBF under inert atmosphere. Dry THF (60 mL) was added resulting in a clear colourless solution. 30 mL BH_3.DMS (2.0 M THF) was added under inert atmosphere. After a few minutes the solution changed to a white suspension. The suspension was heated to reflux at 80 °C under N_2 for 72 h. The white suspension was transferred to a 250 mL flask and 50 mL D.I. H_2O was added gradually to quench excess BH_3.DMS. 30 mL, 12 M HCl (conc.) was added to suspension and heated at reflux at 120 °C for 2 h in air. When the mixture reached >100 °C the white suspension changed to a colourless solution. After 2 h solvent was removed in *vacuo* resulting in a white solid. The white solid was treated with 50 mL, 2.5 M NaOH aq. (pH = 14). The product was extracted with DCM (4 x 50 mL), dried with $MgSO_4$ and solvent was removed in *vacuo* to a white solid which was recrystallised from hexane (0.36 g, 1.1 mmol, 32 %). ^1H NMR ($CDCl_3$); δ 2.80 (t, *J* = 6.0 Hz, 4H), 2.63 – 2.55 (m, 22H), 2.48 – 2.42 (m, 4H), 2.20 (s, 6H), 1.62 (quin, *J* = 6.7 Hz, 4H). ^{13}C NMR ($CDCl_3$); δ. 63, 55, 55, 52, 43, 39, 25, 14. ASAP-MS; 315.3 M+1. IR; 2926 (w), 2792 (m), 2778 (m), 2368 (w), 1618 (m), 1596 (m), 1450 (s), 1350 (m), 1296 (s), 1282 (s), 1120 (s), 1078 (s), 1048 (m), 924 (m), 808 (s), 784 (m), 726 (m), 632 (m).

4,11-Dimethyl-1,4,8,11-tetraazacycloatetradecane-1,8-dipropanenitrile (58).

Dimethylcyclam **(53)** (1.0g, 1.1 mL, 4.4 mmol) and acrylonitrile (0.9 g, 1.1 mL, 17.0 mmol) were added to 50 mL RBF under inert atmosphere. 20 mL dry ethanol was added and the orange solution was left to stir at RT overnight. Solvent was removed in *vacuo* resulting in an orange oil. The orange oil was recrystallised from hexane to give a white solid, **58** (1.1 g, 3.3 mmol, 75 %). ^1H NMR ($CDCl_3$); δ 2.79 (t, *J* = 7.0 Hz, 4H), 2.60 – 2.56 (m, 8H), 2.46 – 2.42 (m, 12H), 2.19 (s, 6H), 1.60 (quin, *J* = 6.7 Hz, 4H). ^{13}C NMR ($CDCl_3$); δ 120, 55, 54, 52, 51, 50, 44, 25, 16. ASAP-MS; 335.3 M+1. IR; 2946 (m), 2836 (m), 2790 (s), 2244 (w), 1464 (m), 1454 (m), 1372 (m), 1338 (m), 1316 (m), 1236 (m), 1140 (s), 1102 (s), 1056 (s), 1042 (s), 1022 (m), 962 (m), 776 (m), 738 (m), 628 (m). Anal Calcd for $C_{18}H_{34}N_6$: C, 64.63; H, 10.25; N, 25.12. Found: C, 61.12; H, 9.91; N, 23.48. The ^1H NMR data obtained is in agreement with that reported in literature.[206]

4,11-Dimethyl-1,4,8,11-tetraazacycloatetradecane-1,8-dipropanamine (59).

Compound **58** (1.1 g, 3.3 mmol), was added to 100 mL RBF under an inert atmosphere. 60 mL dry THF added forming a clear colourless solution. 30 mL BH_3.DMS (2.0 M THF, 60.0 mmol) was added under inert atmosphere. Immediately after addition the colourless solution turned to a white suspension. The suspension was heated to reflux at 80 °C under N_2 for 72 h. The white suspension was then transferred to a 250 mL flask and 50 mL D.I. H_2O was added gradually to quench excess BH_3.DMS. 30 mL, 12 M HCl (conc.) was added to suspension and heated to reflux at 120 °C for 2 h in air. When suspension reached >100°C suspension turned to colourless solution. After 2 h solvent was removed in *vacuo* resulting in a white solid. The white solid was treated with 50 mL, 2.5 M NaOH aq. (pH = 14). The product was extracted with DCM (4 x 50 mL), dried with $MgSO_4$ and solvent removed in *vacuo* to white solid which was recrystallised from hexane (0.46 g, 1.3 mmol, 41 %). ^{1}H NMR ($CDCl_3$); δ 2.76 (t, *J* = 6.7 Hz, 4H), 2.53 (t, *J* = 5.4 Hz, 4H), 2.48 – 2.38 (m, 16H), 2.22 (s, 6H), 1.85 (br s, $\nu_{1/2}$ = 57.2 Hz, 4H), 1.66 (quin, *J* = 7.1 Hz, 4H), 1.60 (quin, *J* = 6.7 Hz, 4H). ^{13}C NMR ($CDCl_3$); δ 54, 52, 51, 44, 40, 32, 30, 24. ASAP-MS; 343.3 M+1. IR; 2958 (w), 2784 (m), 1598 (m), 1458 (m), 1318 (m), 1286 (m), 1260 (s), 1078 (s), 1058 (s), 1014 (s), 794 (s), 718 (m).

4,11-Dimethyl-1,4,8,11-tetraazacycloatetradecane-1,8-dipropan(*N*-tosyl)amine (61).

Dimethylcyclam **(53)** (0.3 g, 0.32 mL, 1.3 mmol) was dissolved in dry CH_3CN (30 mL) and brought to reflux at 87 °C under inert atmosphere. *N*- tosylazetidine **(60)** (0.63 g, 3.0 mmol) was dissolved in dry CH_3CN (30 mL) and added dropwise to a solution of dimethylcyclam at reflux. The mixture was left at reflux under an inert atmosphere for a further 6 h. The suspension formed was filtered to obtain a white solid.

4,11-Dimethyl-1,4,8,11-tetraazacycloatetradecane-1,8-dibutanenitrile (62).

Dimethylcyclam **(53)** (1.3 g, 1.4 mL, 5.7 mmol), 4-chlorobutyronitrile (1.2 g, 1.1 mL, 12.0 mmol), K_2CO_3 (1.7 g, 12.0 mmol), and KI (1.0 g, 5.7 mmol) were added to 250 mL RBF under inert atmosphere. 120 mL dry MeCN was added to form a pale yellow suspension. The mixture was heated to reflux at 80 °C under N_2 for 72 h. A pale orange suspension persisted. The mixture was vacuum filtered to obtain an orange solution and white solid. The solvent was removed in *vacuo* resulting in a brown oil. The brown oil was recrystallised from DCM/Hexane to a pale yellow sticky solid, **62** (1.6 g, 4.3 mmol, 76 %). ^{1}H NMR ($CDCl_3$); δ 2.46 – 2.38 (m, 16H), 2.36 – 2.29 (m, 8H), 2.11 (s, 6H), 1.67 (quin, *J* = 6.7 Hz, 4H), 1.52 (quin, *J* = 6.7 Hz, 4H). ^{13}C NMR ($CDCl_3$); δ 120, 55, 54, 52, 51, 50, 43, 25, 23, 15. ASAP-MS; 363.3 M+1. IR; 2942 (m), 2790 (s), 2360 (m), 2334 (m), 2234(w), 2012(w), 1662 (w), 1458 (s), 1364 (m), 1288 (s), 1146 (s), 1120 (s), 1038 (m), 1016 (m), 920 (m), 802 (m), 720 (m), 624 (w). Anal Calcd for $C_{20}H_{38}N_6$: C, 66.26; H, 10.56; N, 23.18. Found: C, 63.28; H, 10.23; N, 21.28.

4,11-Dimethyl-1,4,8,11-tetraazacycloatetradecane-1,8-dibutanamine (63).

Compound **62** (0.1 g, 0.28 mmol), was added to 50 mL RBF under inert atmosphere. 10 mL dry THF added forming a clear colourless solution. 3 mL BH_3.DMS (2.0 M THF, 6.0 mmol) was added under inert atmosphere. Immediately after addition the colourless solution turned to a white suspension. The suspension was heated to reflux at 80 °C under N_2 for 72 h. The white suspension was then transferred to a 250 mL flask and 10 mL D.I. H_2O was added gradually to quench excess BH_3.DMS. 3 mL, 12 M HCl (conc.) was added to suspension and heated at reflux at 120 °C for 2 h in air. When suspension reached >100°C suspension turned to colourless solution. After 2 h solvent was removed in *vacuo* giving a white solid. The white solid was treated with 5 mL, 2.5 M NaOH aq. (pH = 14). The product was extracted with DCM (4 x 10 mL), dried with $MgSO_4$ and solvent was removed in *vacuo* to a white oil which was recrystallised from hexane resulting in colourless crystals with a sticky texture, **63** (0.06 g, 0.16 mmol, 58 %). ^{1}H NMR ($CDCl_3$); δ 2.60 (t, *J* = 6.6 Hz, 4H), 2.51 – 2.43 (m, 12H), 2.38 – 2.28 (m, 8H), 2.12 (s, 6H), 1.78 (quin, *J* = 6.9 Hz, 4H), 1.61 (quin, *J* = 7.5 Hz, 4H), 1.55 (quin, *J* = 5.8 Hz, 4H). ASAP-MS; 371.4 M+1. IR; 2942 (m), 2806 (m), 1642 (w), 1466 (m), 1174 (m), 1112 (s), 1056 (s), 1011 (s), 688 (m), 612 (m).

Tert-butyl *N*-[3-(hydroxymethyl)phenyl]carbamate (65).

3-Aminobenzylalcohol **(64)** (4.0 g, 32.5 mmol) and BOC anhydride (7.5 g, 34.4 mmol) was added to 100 mL RBF. 50 mL THF was added and the orange solution was heated at reflux at 85 °C for 5 h. Solvent was removed in *vacuo* resulting in an orange oil. The orange oil was purified by flash Si column chromatography using 1:2 EtOAc/pet ether. The fractions containing product were isolated resulting in a yellow oil. The yellow oil was sonicated in hexane for 10 min, which resulted in a white solid, **65** (6.7 g, 30.0 mmol, 92 %). ^{1}H NMR ($CDCl_3$); 7.48 (s, 1H), 7.32 – 7.23 (m, 2H), 7.05 (d, *J* = 7.3 Hz, 2H), 6.52 (br s, $\nu_{1/2}$ = 9.0 Hz, 1H), 4.69 (s, 2H), 1.75 (s, 1H), 1.55 (s, 9H). The ^{1}H NMR data obtained is in agreement with that reported in literature.[210]

Tert-butyl *N*-[3-(bromomethyl)phenyl]carbamate (66).

Compound **65** (2.7 g, 12.1 mmol), PPh_3 (3.8 g, 14.5 mmol) and *N*-bromosuccinimide (2.4 g, 13.5 mmol) was added to 100 mL RBF under inert atmosphere. 25 mL dry DCM was added resulting in an orange solution. The solution was left to stir at RT under N_2 for 2 h. 160 mL hexane was added to the orange solution which gave a white precipitate which was removed by filtration. The orange solution was purified by Si column using 5:1 Pet ether/EtOAc, Rf = 0.24. Product was collected and evaporated to dryness which gave a pale yellow oil which solidified on standing, **66** (2.0 g, 7.0 mmol, 59 %). ^{1}H NMR ($CDCl_3$); 7.51 (s, 1H), 7.28 – 7.18 (m, 2H), 7.06 (dt, *J* = 7.4, 1.5 Hz, 1H), 6.48 (br s, $\nu_{1/2}$ = 11.0 Hz, 1H), 4.46 (s, 2H), 1.52 (s, 9H). The ^{1}H NMR data obtained is in agreement with that reported in literature.[211]

4,11-Dimethyl-1,8-diamino(Boc-protected)metabenzyl cyclam (67).

Compound **66** (0.8 g, 2.8 mmol), K_2CO_3 (0.4 g, 2.9 mmol) and KI (0.2 g, 1.3 mmol) was added to 250 mL RBF under inert atmosphere. 80 mL dry MeCN was added followed by dimethylcyclam **(53)** (0.3 g, 0.3 mL, 1.3 mmol). Mixture was heated at reflux at 80 °C under N_2 for 72 h. The mixture was vacuum filtered to obtain a pale yellow solution and white solid. The solvent was removed in *vacuo* resulting in a white oil. Reaction considered failed.

2-[3-(hydroxymethyl)phenyl]-2,3-dihydroisoindol-1,3-dione (69).

Phthalic anhydride **(68)** (2.4 g, 16.2 mmol) and 3-aminobenzyl alcohol **(64)** (2.0 g, 16.2 mmol) were added to 250 mL RBF under an inert atmosphere. 80 mL pyridine was added and the solution was heated to 140 ºC under N_2 for 3 h. After 3 h the solution was cooled to RT. 200 mL DCM was added and the mixture was washed with brine (50 mL) and H_2O (3 x 50 mL). The organic layer was collected and dried with $MgSO_4$, solvent was removed in *vacuo* to an off-white solid, **69** (3.0 g, 12.0 mmol, 74 %). ^{1}H NMR ($CDCl_3$); δ 7.95 (dd, *J* = 5.5, 3.1 Hz, 2H), 7.80 (dd, *J* = 5.5, 3.1 Hz, 2H), 7.50 (t, *J* = 7.8 Hz, 1H), 7.46 – 7.39 (m, 2H), 7.35 (d, *J* = 7.8 Hz, 1H), 4.77 (s, 2H). The ^{1}H NMR data obtained is in agreement with that reported in literature.[212]

2-[3-(bromomethyl)phenyl]-2,3-dihydroisoindol-1,3-dione (70).

Compound **69** (2.0g, 7.9 mmol) and PPh_3 (3.1 g, 11.8 mmol) were suspended in 20 mL dry DCM under inert atmosphere. The brown solution was cooled to 0 ºC in NaCl/ice bath. CBr_4 (3.9 g, 11.8 mmol) was dissolved in 20 mL dry DCM under inert atmosphere and added dropwise to cooled solution. The solution turned yellow on addition. The mixture was left to stir at 0 ºC for 2 h under N_2. After 2 h the solution was allowed to warm to RT. 25 mL EtOAc was added resulting in a yellow suspension which was then washed with brine (4 x 10 mL). The organic layer (pale yellow solution) was dried with $MgSO_4$ and solvent removed in *vacuo* resulting in a light brown solid. The ^{1}H NMR spectrum was dominated mostly by $OPPh_3$. The product was purified by flash Si column chromatography using DCM as eluent. Rf = 0.35. The product was recovered as a white solid, **70** (0.75g, 2.4 mmol, 30 %). ^{1}H NMR ($CDCl_3$); δ 7.97 (dd, *J* = 5.5, 3.1 Hz, 2H), 7.81 (dd, *J* = 5.5, 3.1 Hz, 2H), 7.54 – 7.47 (m, 2H), 7.46 – 7.38 (m, 2H), 4.54 (s, 2H). The ^{1}H NMR data obtained is in agreement with that reported in literature.[209]

1,8-Dimethyl,-4,11-diamino(Tosylprotect)metabenzyl cyclam (71).

Compound **70** (1.8 g, 5.7 mmol), K_2CO_3 (0.8 g, 5.7 mmol) and KI (0.5 g, 3.0 mmol) was added to 250 mL RBF under inert atmosphere. 150 mL dry MeCN was added followed by dimethylcyclam **(53)** (0.7 g, 0.7 mL, 3.0 mmol). Mixture was heated at reflux at 80 ºC under N_2 for 72 h. The mixture was vacuum filtered to obtain a pale yellow solution and white solid. The pale yellow solution was evaporated to dryness resulting in a light brown solid (2.0 g). Crude product was purified by Si column chromatography using 85/25/2.5 $CHCl_3$/MeOH/NH_4OH (35% aq.). Obtained 0.1 g product (0.1 mmol, 3 %). Alternative purification was to extract product from crude mixture into EtOAc, solvent was removed in *vacuo* to give a yellow solid. Yellow solid was washed with CH_3CN which resulted in a white solid, **71** (1.4 g, 2.0 mmol, 67 %). ^{1}H NMR ($CDCl_3$); δ 7.94 (dd, *J* = 5.5, 3.1 Hz, 4H), 7.78 (dd, *J* = 5.5, 3.1 Hz, 4H), 7.45 – 7.35 (m, 6H), 7.30 – 7.26 (m, 2H), 3.61 (s, 4H), 2.62 – 2.54 (m, 8H), 2.52 – 2.39 (m, 8H), 2.11 (s, 6H), 1.64 (quin, *J* = 6.7 Hz, 4H). ^{13}C NMR ($CDCl_3$); δ 167, 135, 132, 131, 129, 128, 127, 125, 124, 116, 59, 55, 54, 51, 51, 43, 24. ASAP-MS; 699.38 M+1.

1,8-Dimethyl,-4,11-diaminometabenzyl cyclam (72).

Compound **71** (0.1 g, 0.14 mmol) was dissolved in 5 mL of dry THF/1.5 mL dry ethanol and heated to 60 °C. $N_2H_4{\cdot}H_2O$ (0.1 g, 1.5 mmol) was added under an inert atmosphere. The mixture was heated to reflux at 80 °C for 15 h, which resulted in a white suspension. A further 5 mL of ethanol was added, and the mixture was filtered. Solvent was removed in *vacuo* to a pale yellow oil, which solidified on standing, **72** (0.057 g, 0.13 mmol, 92 %). ^{1}H NMR ($CDCl_3$); 7.08 (t, *J* = 7.4 Hz, 2H), 6.75 – 6.70 (m, 4H), 6.56 (d, *J* = 8.2 Hz, 2H), 3.62 (br s, $\nu_{1/2}$ = 8.0 Hz, 4H), 2.62 – 2.55 (m, 8H), 2.51 – 2.43 (m, 8H), 2.13 (s, 6H), 1.66 (quin, *J* = 6.7 Hz, 4H). ^{13}C NMR ($CDCl_3$); δ 146, 141, 129, 120, 116, 114, 60, 55, 54, 51, 51, 43, 30. ASAP-MS; 439.76 M+1. The ^{1}H NMR data obtained is in agreement with that reported in literature.[209]

2-[4-(hydroxymethyl)phenyl]-2,3-dihydroisoindol-1,3-dione (74).

Phthalic anhydride **(68)** (2.4 g, 16.2 mmol) and 4-aminobenzyl alcohol **(73)** (2.0 g, 16.2 mmol) were added to 250 mL RBF under inert atmosphere. 80 mL pyridine added and the solution was heated to 140 °C under N_2 for 3 h. After 3 h the solution was cooled to RT. 200 mL DCM was added and the mixture was washed with brine (50 mL) and H_2O (3 x 50 mL). Organic layer (yellow soln) was dried with $MgSO_4$ and solvent removed in *vacuo* (2.0 g, 48 %). ^{1}H NMR ($CDCl_3$); 7.96 (dd, *J* = 5.5, 3.1 Hz, 2H), 7.80 (dd, *J* = 5.5, 3.1 Hz, 2H), 7.53 (d, *J* = 8.9 Hz, 2H), 7.44 (d, *J* = 8.9 Hz, 2H), 4.77 (s, 2H). The ^{1}H NMR data obtained is in agreement with that reported in literature.[212]

2-[4-(bromomethyl)phenyl]-2,3-dihydroisoindol-1,3-dione (75).

Compound **74** (5 g, 19.7 mmol) and PPh_3 (7.7 g, 29.6 mmol) were suspended in 5 mL dry DCM under inert atmosphere. The brown solution was cooled to 0 °C in NaCl/ice bath. CBr_4 (9.8 g, 30.0 mmol) was dissolved in 5 mL dry DCM under inert atmosphere and added dropwise to cooled solution. The solution turned yellow on addition. The mixture was left to stir at 0 °C for 2 h under N_2. After 2 h the solution was allowed to warm to RT. 250 mL EtOAc was added resulting in a yellow suspension which was washed with brine (4 x 10 mL). The organic layer (pale yellow solution) was dried with $MgSO_4$ and solvent removed in *vacuo* resulting in a light brown solid. The ^{1}H NMR spectrum was dominated by $POPh_3$. Product was purified by flash Si column chromatography using DCM as eluent. Rf = 0.35. Product was white solid, **75** (1.4 g, 4.4 mmol, 22 %). ^{1}H NMR ($CDCl_3$); 7.97 (dd, *J* = 5.5, 3.1 Hz, 2H), 7.81 (dd, *J* = 5.5, 3.1 Hz, 2H), 7.54 (d, *J* = 8.9 Hz, 2H), 7.45 (d, *J* = 8.9 Hz, 2H), 4.55 (s, 2H). The ^{1}H NMR data obtained is in agreement with that reported in literature.[213]

Dimethyl, diamino(Tosylprotect)parabenzyl cyclam (76).

Compound **75** (0.9 g, 2.8 mmol), K_2CO_3 (0.4 g, 2.8 mmol) and KI (0.2 g, 1.4 mmol) was added to 500 mL RBF under inert atmosphere. 225 mL dry MeCN was added followed by dimethylcyclam **(53)** (0.3 g, 0.3 mL, 1.4 mmol). Mixture was heated to reflux at 80 °C under N_2 for 72 h. The mixture was vacuum filtered to obtain a pale yellow solution and white solid. Solvent was removed in *vacuo* resulting in a yellow solid. Yellow solid was purified by Si column chromatography using 85/25/2.5 $CHCl_3$/MeOH/NH_4OH (35% aq.). Obtained 0.05 g product (0.07 mmol, 5 %). Alternative purification was to extract product from crude mixture into EtOAc, solvent was removed in *vacuo* to give a yellow solid. Yellow solid was washed with CH_3CN which resulted in a white solid, **75** (0.54 g, 0.77 mmol, 59 %). ^1H NMR ($CDCl_3$); 7.95 (dd, *J* = 5.5, 3.1 Hz, 4H), 7.79 (dd, *J* = 5.5, 3.1 Hz, 4H), 7.52 (d, *J* = 8.5 Hz, 4H), 7.37 (d, *J* = 8.5 Hz, 4H), 3.55 (s, 4H), 2.69 – 2.61 (m, 8H), 2.51 – 2.45 (m, 8H), 2.20 (s, 6H), 1.65 (quin, *J* = 6.2 Hz, 4H).

All Template Reactions (C9 – C13).

Diacetylpyridine (0.05 g, 0.03 mmol) was dissolved in dry CH_3OH (3 mL) and added to a Schlenk flask under inert atmosphere. $[Fe(CH_3CN)_6](PF_6)_2$ was dissolved in dry CH_3OH (3 mL) and was added to the same schlenk flask which resulted in a raspberry pink solution **(77)**. An equimolar amount of diamine was dissolved in CH_3OH/$CHCl_3$ (1:5) (6 mL) under an inert atmosphere. Dry CH_3OH (30 mL) was added to a 2-neck RBF under inert atmosphere and heated to reflux at 70 °C. The Fe/diacetylpyridine and diamine solutions were added dropwise to the RBF over an 8 h period. After addition the mixture was left to reflux for a further 12 h. A purple suspension persisted. The solution was filtered under inert atmosphere to obtain a pale yellow solution and purple solid.

Template Schiff Base Condensation in Attempt to Form C9

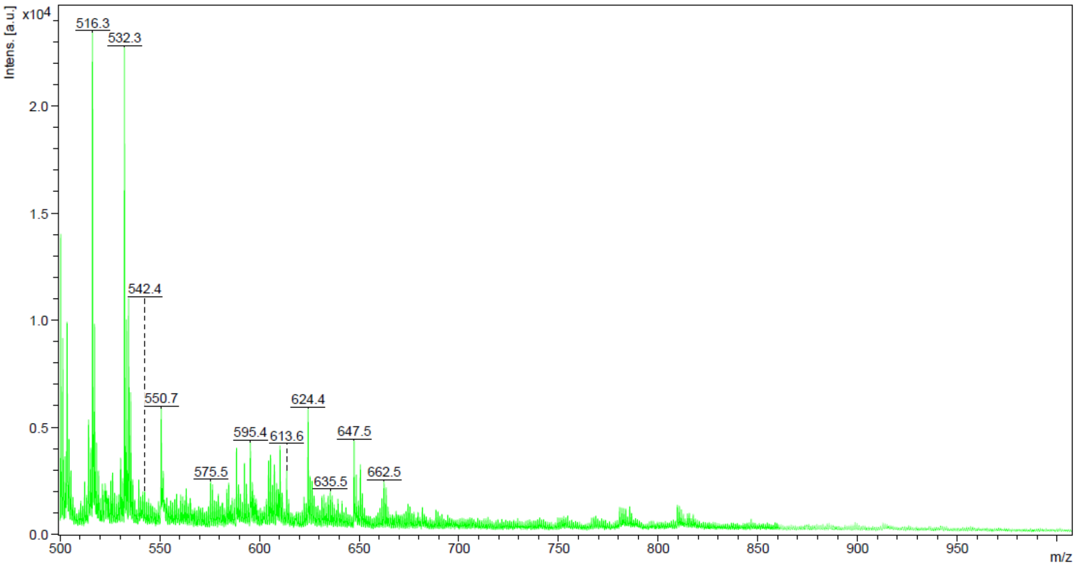

Figure 73. MALDI Mass Spectrum of Purple Precipitate Obtained after Template Schiff Base Condensation of 77 with Diamine 56 in Attempt to Form C9.

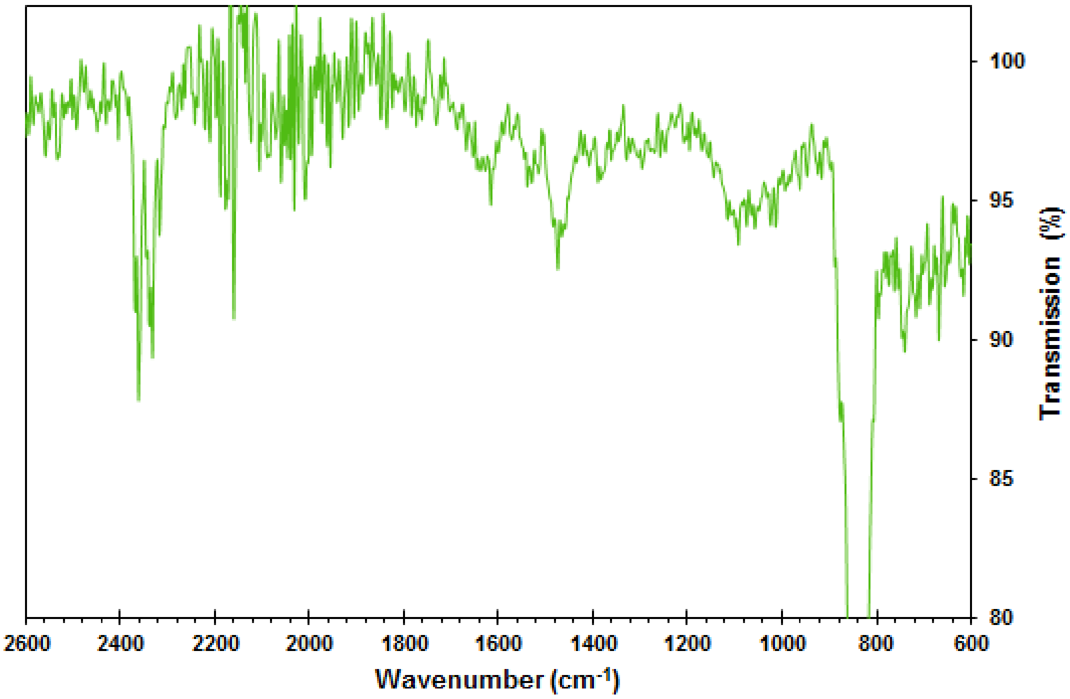

Figure 74. Infrared Spectrum of Purple Precipitate Obtained after Template Schiff Base Condensation of 77 with Diamine 56 in Attempt to Form C9. The Infrared Spectra Were Collected using a Diamond ATR (Attenuated Total Reflection) Accessory (Golden Gate) for Solids; No Sample Preparation was Required. Dominated by PF_6 Stretch ~ 840 cm^{-1} So Cut Off Spectra.

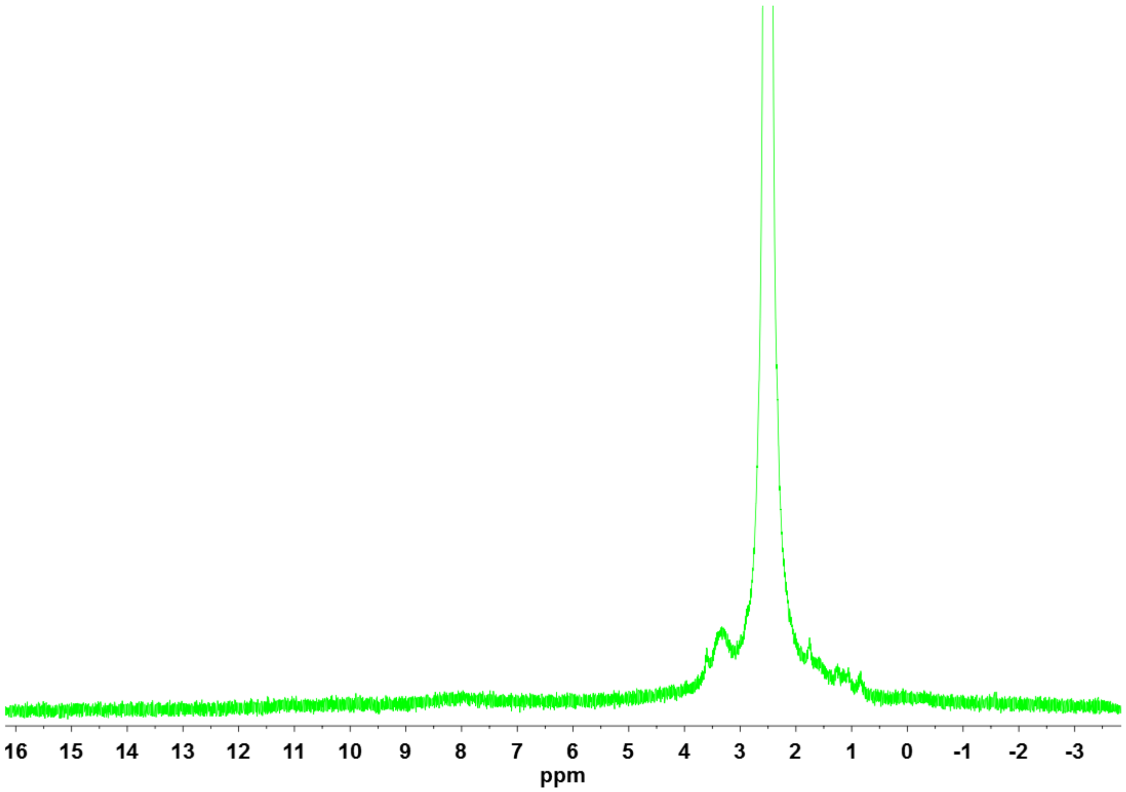

Figure 75. ^{1}H NMR Spectrum of Purple Precipitate Obtained after Template Schiff Base Condensation of 77 with Diamine 56 in Attempt to Form C9 in C_2D_6OS.

Template Schiff Base Condensation in Attempt to Form C10

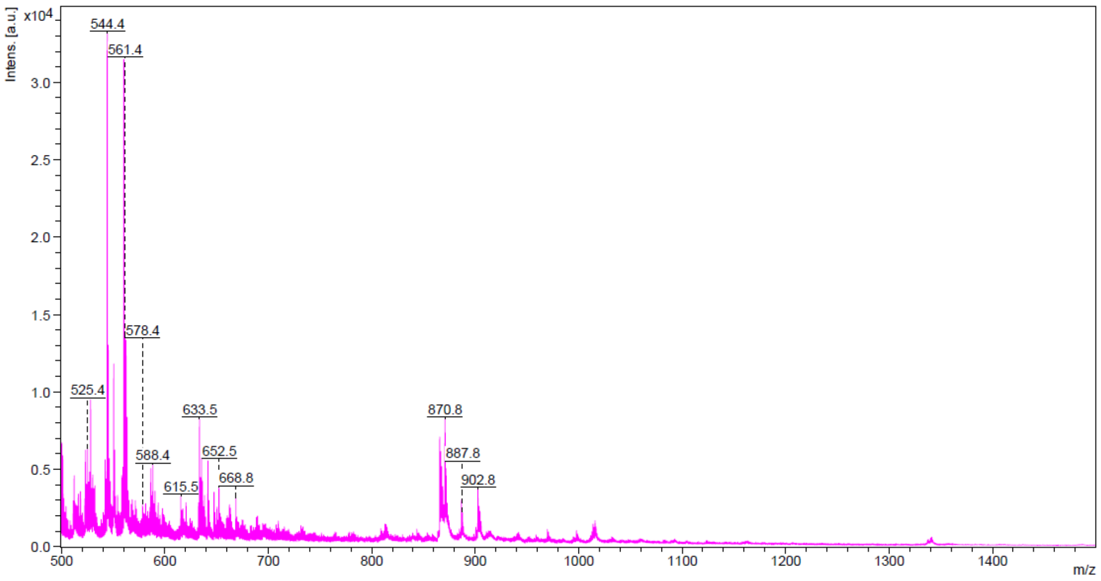

Figure 76. MALDI Mass Spectrum of Purple Precipitate Obtained after Template Schiff Base Condensation of 77 with Diamine 59 in Attempt to Form C10.

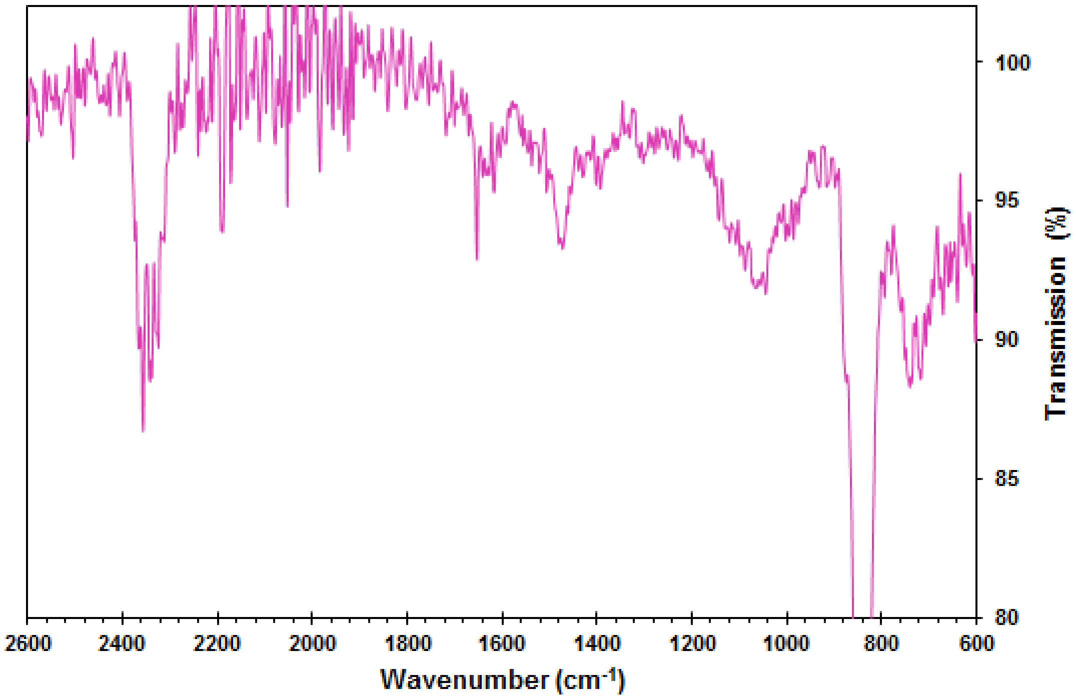

Figure 77. Infrared Spectrum of Purple Precipitate Obtained after Template Schiff Base Condensation of 77 with Diamine 59 in Attempt to Form C10. The Infrared Spectra Were Collected using a Diamond ATR (Attenuated Total Reflection) Accessory (Golden Gate) for Solids; No Sample Preparation was Required. Dominated by PF_6 Stretch ~ 840 cm^{-1} So Cut Off Spectra.

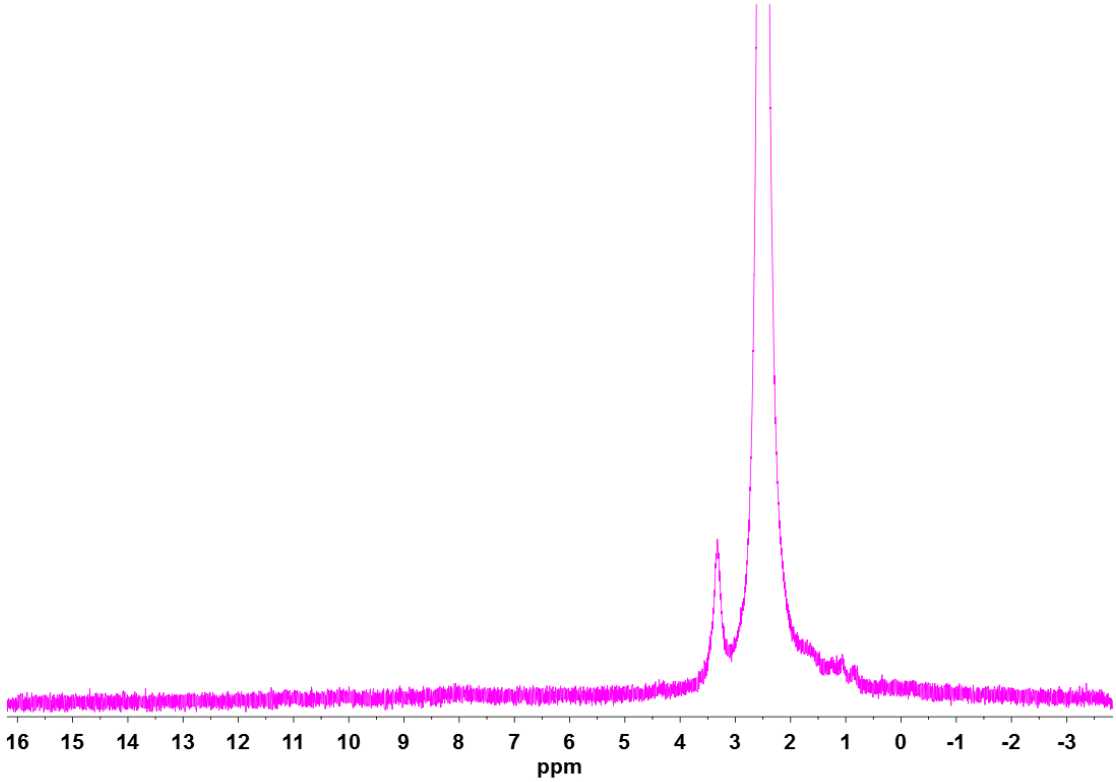

Figure 78. ^{1}H NMR Spectrum of Purple Precipitate Obtained after Template Schiff Base Condensation of 77 with Diamine 59 in Attempt to Form C10 in C_2D_6OS.

Template Schiff Base Condensation in Attempt to Form C11

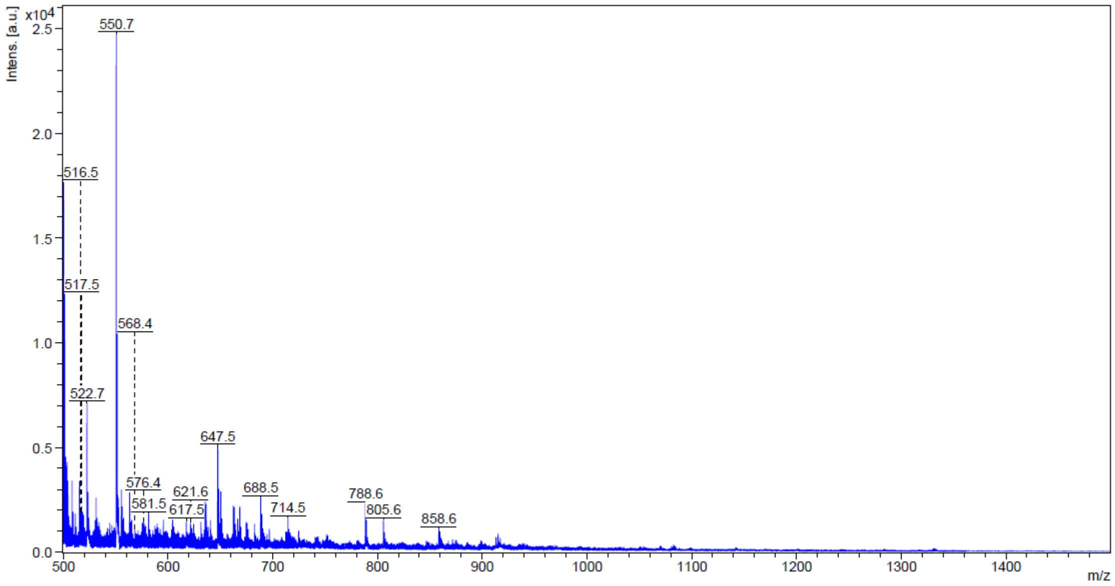

Figure 79. MALDI Mass Spectrum of Purple Precipitate Obtained after Template Schiff Base Condensation of 77 with Diamine 63 in Attempt to Form C11.

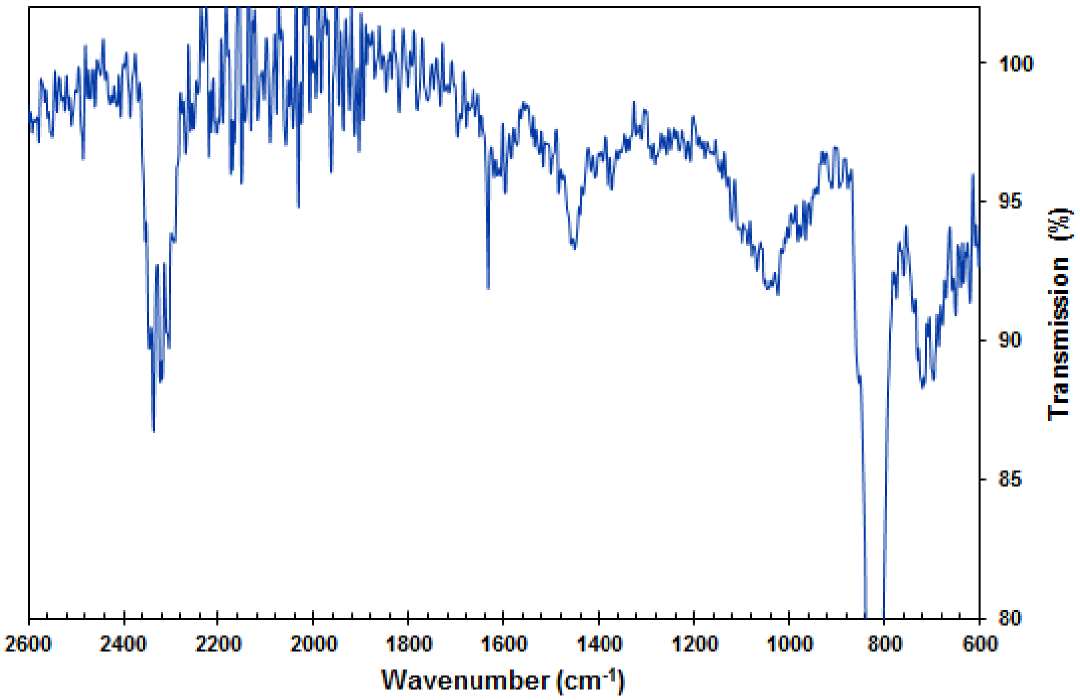

Figure 80. Infrared Spectrum of Purple Precipitate Obtained after Template Schiff Base Condensation of 77 with Diamine 63 in Attempt to Form C11. The Infrared Spectra Were Collected using a Diamond ATR (Attenuated Total Reflection) Accessory (Golden Gate) for Solids; No Sample Preparation was Required. Dominated by PF_6 Stretch ~ 840 cm^{-1} So Cut Off Spectra.

5.7 References

(51) Praneeth, V. K. K.; Ringenberg, M. R.; Ward, T. R. *Angew. Chem. Int. Ed.* **2012**, *51*, 10228.

(68) Bouwkamp, M. W.; Bowman, A. C.; Lobkovsky, E.; Chirik, P. J. *J. Am. Chem. Soc.* **2006**, *128*, 13340.

(71) Tondreau, A. M.; Atienza, C. C. H.; Weller, K. J.; Nye, S. A.; Lewis, K. M.; Delis, J. G. P.; Chirik, P. J. *Science* **2012**, *335*, 567.

(84) Britovsek, G. J. P.; Gibson, V. C.; Spitzmesser, S. K.; Tellmann, K. P.; White, A. J. P.; Williams, D. J. *J. Chem. Soc., Dalton Trans.* **2002**, 1159.

(200) Ghosh, M.; Weyhermuller, T.; Wieghardt, K. *Dalton Trans.* **2010**, *39*, 1996.

(201) Enright, D.; Gambarotta, S.; Yap, G. P. A.; Budzelaar, P. H. M. *Angew. Chem. Int. Ed.* **2002**, *41*, 3873.

(202) Lehn, J. M. *Acc. Chem. Res.* **1978**, *11*, 49.

(203) Fukuzumi, S.; Okamoto, K.; Gros, C. P.; Guilard, R. *J. Am. Chem. Soc.* **2004**, *126*, 10441.

(204) Beckmann, U.; Brooker, S. *Coord. Chem. Rev.* **2003**, *245*, 17.

(205) Comba, P.; Gahan, L. R.; Hanson, G. R.; Mereacre, V.; Noble, C. J.; Powell, A. K.; Prisecaru, I.; Schenk, G.; Zajaczkowski-Fischer, M. *Chem. Eur. J.* **2012**, *18*, 1700.

(206) Comparone, A.; Kaden, T. A. *Helv. Chim. Acta* **1998**, *81*, 1765.

(207) Britovsek, G. J. P.; England, J.; Spitzmesser, S. K.; White, A. J. P.; Williams, D. J. *Dalton Trans.* **2005**, 945.

(208) Bart, S. C.; Lobkovsky, E.; Bill, E.; Wieghardt, K.; Chirik, P. J. *Inorg. Chem.* **2007**, *46*, 7055.

(209) Zhang, X.; Huang, D.; Chen, Y.-S.; Holm, R. H. *Inorg. Chem.* **2012**, *51*, 11017.

(210) Bobek, M.; An, S. H.; Skrincosky, D.; De Clercq, E.; Bernacki, R. J. *J. Med. Chem.* **1989**, *32*, 799.

(211) Metherell, A. J.; Ward, M. D. *RSC Adv.* **2013**, *3*, 14281.

(212) dos Santos, J. L.; Lanaro, C.; Lima, L. M.; Gambero, S.; Franco-Penteado, C. F.; Alexandre-Moreira, M. S.; Wade, M.; Yerigenahally, S.; Kutlar, A.; Meiler, S. E.; Costa, F. F.; Chung, M. *J. Med. Chem.* **2011**, *54*, 5811.

(213) Pingali, S. R. K.; Upadhyay, S. K.; Jursic, B. S. *Green Chem.* **2011**, *13*, 928.

APPENDIX

General Experimental Procedures

Unless otherwise mentioned, reagents were used as received from commercial suppliers (Alfa Aesar, Fischer Scientific, Sigma Aldrich and Strem). Solvents used were laboratory grade. Dry solvents were obtained from Durham University SPS and were stored with molecular sieves in. Molecular sieves, 3 Å 1-2mm beads, were purchased from Alfa Aesar and were activated at 250 °C under vacuum and stored in the dry nitrogen Glovebox. Air and water sensitive reactions were carried out under an atmosphere of dry argon on the Schlenk line or an atmosphere of dry nitrogen in the Glovebox. Glassware was oven dried (120 °C) as required and cooled under a positive pressure of argon or nitrogen. Reactions monitored by TLC analysis employed POLTFRAM® SIL G/UV254 (40 x 80 mm) TLC plates. Column chromatography was carried out using Silica purchased from Sigma-Aldrich (230-400 mesh, 40-63 μm, 60 Å) and was monitored by TLC analysis. Risk assessments were carried out before any experimental work was undertaken according to COSHH procedures.

Physical Measurements

NMR spectra were recorded on a Bruker Avance-400 (400 MHz ^{1}H, 100 MHz ^{13}C, 376 MHz ^{19}F) or a Varian VNMRS-700 (700 MHz ^{1}H, 176 MHz ^{13}C) spectrometer. Spectra were recorded in commercially available deuterated solvents and internally referenced to residual solvent signals. Electronic spectra were recorded on a Perkin-Elmer Lambda 900 spectrophotometer, Cary 100 and Cary 5000 spectrophotometers. Mass spectra were measured using a diamond ATR (attenuated total reflection) accessory (Golden Gate) for solids on a Perkin Elmer Paragon 1000 FT-IR Spectrometer. Waters TQD instrument for ESI (1 μL of a ~1 mg/mL sample in methanol or acetonitrile injected into a flow (0.2 mL/min) of methanol or acetonitrile; capillary voltage 3000 V, cone voltage 30 V) or on a *Xevo QToF* for high-resolution spectra (atmospheric pressure solids analysis probe ionization experiments (ASAP)). Infrared spectra were recorded using Microanalyses were carried out in the Chemistry Department at Durham University. Electrochemical measurements were carried out using an Autolab PG-STAT 30 potentiostat using a three-electrode cell equipped with a Pt working electrode and Pt wire counter and reference electrodes. Potentials are reported with reference to an internal standard of ferrocenium/ferrocene ($Fc^{+/0}$). Magnetic susceptibility data (2–290 K) were recorded using a SQUID magnetometer (MPMS7, Quantum Design) in a 1 T external field. Data were corrected for underlying diamagnetism using tabulated Pascal's constants and fit using julX (Dr. E. Bill). Mössbauer data were recorded on an alternating constant-acceleration spectrometer. The minimum experimental line width was 0.24 mm s^{-1} (full width at half-height). Sample temperature was maintained constant in an Oxford Instruments Variox or an Oxford Instruments Mössbauer-Spectromag 2000 cryostat, which is a split pair superconducting magnet system for applied fields (up to 8 T). The field at the sample is oriented perpendicular to the γ-beam. The ^{57}Co/Rh source (1.8 GBq) was positioned at room temperature inside the gap of the magnet system at a zero-field position. Isomer shifts are quoted relative to iron metal at 300 K; data were simulated using mfit (Dr. E. Bill). Multifrequency EPR measurements were carried out at the EPSRC National UK EPR Facility and Service in the Photon Science Institute at The University of Manchester. X-Band spectra were collected using a Bruker EMX Micro spectrometer, K-band spectra with a Bruker E580 spectrometer, and Q-band spectra on a Bruker EMX spectrometer. Simulations were performed using Bruker's Xsophe software package.[214]

Crystallography

Structure determinations were carried out from single-crystal X-ray diffraction data collected at 100 K using Cu Kα radiation (λ = 1.54178 Å) on a Bruker Pt135-CCD Proteum diffractometer with multilayer focusing optics or at 120 K using Mo Kα radiation (λ = 0.71073 Å) on a Bruker SMART 6K-CCD diffractometer. The sample temperature was controlled and maintained using a Cryostream (Oxford Cryosystems) open-flow N_2 cooling device.[215] A series of narrow φ and/or ω scans (0.5° or 0.3°) was performed at various setting angles to maximize data coverage. Unit cell parameters were determined and refined inside the APEX software suite, and raw data were integrated using the SAINT program. The structures were solved, refined and publication material produced using the OLEX2[216] and SHELXTL[217] suites of programs. All structures presented were affected, to variable degrees, by low-resolution data being achievable, due to crystal size and quality. This was also coupled in many cases with solvent and/or ligand disorder (further details are included in the crystallographic information files). In particular, the small size of **C1** and the low crystal symmetry (*P*-1), coupled to the orientation of the sample, limited the completeness of the diffraction data for C1 at high resolution. In spite of the less than ideal completeness, diffraction data were collected to a θ_{max} of 68.33° with Cu Kα radiation, giving a data to parameter ratio of 4179/316. Lower than optimal completeness to high angle does marginally affect the accuracy of the derived parameters but is correctly reflected in the standard uncertainties recorded in the crystallographic information file and reported parameters herein. The structure determinations were carried out from single crystal X-ray diffraction data collected at 120.0(2) K using graphite monochromated Mo Kα radiation (λ = 0.71073 Å) and contains severely disordered PF_6 counter-ions and solvent molecules.

Density Functional Theory (DFT) Calculations

All DFT calculations were performed with the ORCA program package.[218] The geometry optimisations of the complexes were performed at the B3LYP or BP86 [219, 220, 221] level of DFT. The all-electron Gaussian basis sets were those developed by the Ahlrichs group.[222, 223] Triple-ζ quality basis sets TZV(P) with one set of polarization functions on the metals and on the atoms directly coordinated to the metal centre were used.[223] For the carbon and hydrogen atoms, slightly smaller polarised split-valence SV(P) basis sets were used, that were of double-ζ quality in the valence region and contained a polarizing set of d-functions on the non-hydrogen atoms.[222] Auxiliary basis sets used to expand the electron density in the resolution-of-the-identity (RI) approach were chosen,[224], [225] where applicable, to match the orbital basis. The SCF calculations were tightly converged (1×10^{-8} E_h in energy, 1×10^{-7} E_h in the density change, and 1×10^{-7} in maximum element of the DIIS error vector). The geometry optimizations for all complexes were carried out in redundant internal coordinates without imposing symmetry constraints. In all cases the geometries were considered converged after the energy change was less than 5×10^{-6} E_h, the gradient norm and maximum gradient element were smaller than 1×10^{-4} E_h Bohr^{-1} and 3×10^{-4} E_h Bohr^{-1}, respectively, and the root-mean square and maximum displacements of all atoms were smaller than 2×10^{-3} Bohr and 4×10^{-3} Bohr, respectively.

Appendix 1. Crystallographic Information for C1

Empirical formula	$C_{24}H_{21}Cl_4N_5Zn_2$
Formula weight	652.00
Temperature/K	
Crystal system	Triclinic
Space group	P-1
a/Å	7.1827(2)
b/Å	9.4410(2)
c/Å	20.2740(4)
α/°	77.8560(10)
β/°	87.9490(10)
γ/°	72.3700(10)
Volume/Å^3	1280.35(5)
Z	2
ρ_{calc}mg/mm^3	1.691
m/mm^{-1}	6.338
F(000)	
Crystal size/mm^3	0.13 × 0.07 × 0.05
2Θ range for data collection	
Index ranges	
Reflections collected	
Independent reflections	
Data/restraints/parameters	4179/0/316
Goodness-of-fit on F^2	1.058
Final R indexes [I>=2σ (I)]	0.0241
Final R indexes [all data]	0.0638
Largest diff. peak/hole / e Å^{-3}	–0.31, 0.34

Appendix 2. Crystallographic Information for C2

Empirical formula	$C_{62}H_{57}N_{15}O_{12}F_{12}S_4Fe_2$
Formula weight	1672.17
Temperature/K	100
Crystal system	triclinic
Space group	P-1
a/Å	10.6568(2)
b/Å	12.9150(2)
c/Å	15.0100(3)
α/°	106.9800(10)
β/°	109.4480(10)
γ/°	97.5000(10)
Volume/Å^3	1802.68(6)
Z	1
ρ_{calc}mg/mm^3	1.540
m/mm^{-1}	5.198
F(000)	854.0
Crystal size/mm^3	0.12 × 0.11 × 0.07
2Θ range for data collection	6.7 to 135.06°
Index ranges	$-12 \leq h \leq 12$, $-15 \leq k \leq 15$, $-16 \leq l \leq 17$
Reflections collected	16924
Independent reflections	5831[R(int) = 0.0393]
Data/restraints/parameters	5831/23/523
Goodness-of-fit on F^2	1.095
Final R indexes [I>=2σ (I)]	$R_1 = 0.0527$, $wR_2 = 0.1554$
Final R indexes [all data]	$R_1 = 0.0557$, $wR_2 = 0.1607$
Largest diff. peak/hole / e Å^{-3}	0.58/-0.71

Appendix 3. Crystallographic Information for C3

Empirical formula	$C_{56}H_{54}N_{14}F_{24}P_4Fe_2$
Formula weight	1614.71
Temperature/K	120
Crystal system	triclinic
Space group	P-1
a/Å	12.7381(5)
b/Å	12.8678(5)
c/Å	13.2029(6)
α/°	109.8380(10)
β/°	94.7080(10)
γ/°	116.9190(10)
Volume/Å^3	1741.95(12)
Z	1
ρ_{calc}mg/mm^3	1.539
m/mm^{-1}	0.620
F(000)	816.0
Crystal size/mm^3	0.32 × 0.31 × 0.28
2Θ range for data collection	3.42 to 61.04°
Index ranges	$-18 \le h \le 18$, $-18 \le k \le 18$, $-18 \le l \le 18$
Reflections collected	24019
Independent reflections	10569[R(int) = 0.0186]
Data/restraints/parameters	10569/52/454
Goodness-of-fit on F^2	1.042
Final R indexes [I>=2σ (I)]	$R_1 = 0.0884$, $wR_2 = 0.2476$
Final R indexes [all data]	$R_1 = 0.0962$, $wR_2 = 0.2570$
Largest diff. peak/hole / e Å^{-3}	1.60/-1.79

Appendix 4. Crystallographic Information for C4

Empirical formula	$C_{52}H_{42}N_{10}O_{12}F_{12}S_4Cu_2$
Formula weight	1482.28
Temperature/K	100
Crystal system	monoclinic
Space group	C2/c
a/Å	42.0617(8)
b/Å	10.7977(2)
c/Å	28.7341(5)
α/°	90.00
β/°	97.1390(10)
γ/°	90.00
Volume/Å^3	12949.0(4)
Z	8
ρ_{calc}mg/mm^3	1.521
m/mm^{-1}	2.896
F(000)	6000.0
Crystal size/mm^3	0.16 × 0.12 × 0.06
2Θ range for data collection	3.1 to 126.86°
Index ranges	$-45 \le h \le 45$, $-11 \le k \le 12$, $-29 \le l \le 32$
Reflections collected	51265
Independent reflections	10141[R(int) = 0.0523]
Data/restraints/parameters	10141/20/849
Goodness-of-fit on F^2	1.082
Final R indexes [I>=2σ (I)]	R_1 = 0.0592, wR_2 = 0.1729
Final R indexes [all data]	R_1 = 0.0686, wR_2 = 0.1793
Largest diff. peak/hole / e Å^{-3}	1.44/-0.92

Appendix 5. Evans ^{1}H NMR Equations

Evans method ^{1}H NMR experiments were employed to determine the electronic configuration of the iron cations. The effective magnetic moment was determined using Equation 1 - Equation 5.

$$X_g = 3\Delta f/4\pi fm + \chi_0 + \chi_0(d_0 - d_s)/m$$

Equation 1. Evans ^{1}H NMR Mass Susceptibility Equation where; X_g = Mass Susceptibility in cm^3 g^{-1}, Δf = Observed Frequency Difference in Hz, F = Spectrometer Frequency in Hz, m = Mass of Paramagnetic Substance in g cm^{-3}, χ_0 = Mass Susceptibility of Solvent in cm^3 g^{-1}, d_0 = Density of Solvent in g cm^{-3} and d_s = Density of Solution in g cm^{-3}.

$$\chi_{mol} = M\chi_g$$

Equation 2. Molar Susceptibility Equation where M = Molecular Weight of the Compound in g mol^{-1}. If Two Metal Ions present 0.5 × Molecular Weight as $\chi_{mol,}$ this Calculates Spin per Metal Ion.

$$\chi_{mol(corr)} = \chi_{mol} + \chi_{mol\text{-}dia}$$

Equation 3. Diamagnetic Susceptibility Correction of Molar Susceptibility where $\chi_{mol\text{-}dia}$ is Calculated using Pascal Constants.

$$\mu_{eff} = \sqrt{\ }\chi_{mol\text{-}corr}\,T$$

Equation 4. Effective Magnetic Moment Equation where T = Temperature in K.

$$\mu_{eff} = 2\sqrt{S(S+1)}$$

Equation 5. Theoretical Effective Magnetic Moment Equation where S = Spin (Number of Unpaired Electrons / 2).

Table 12. Theoretical Effective Magnetic Moment Values.

Number unpaired Electrons	S	μ_{eff}
1	1/2	1.73
2	1	2.83
3	3/2	3.87
4	2	4.90
5	5/2	5.92

Appendix 6. ^{19}F NMR of C2 – Dynamic Equilibrium between Coordinated OTf$^-$ and CH_3CN Solvent Molecules.

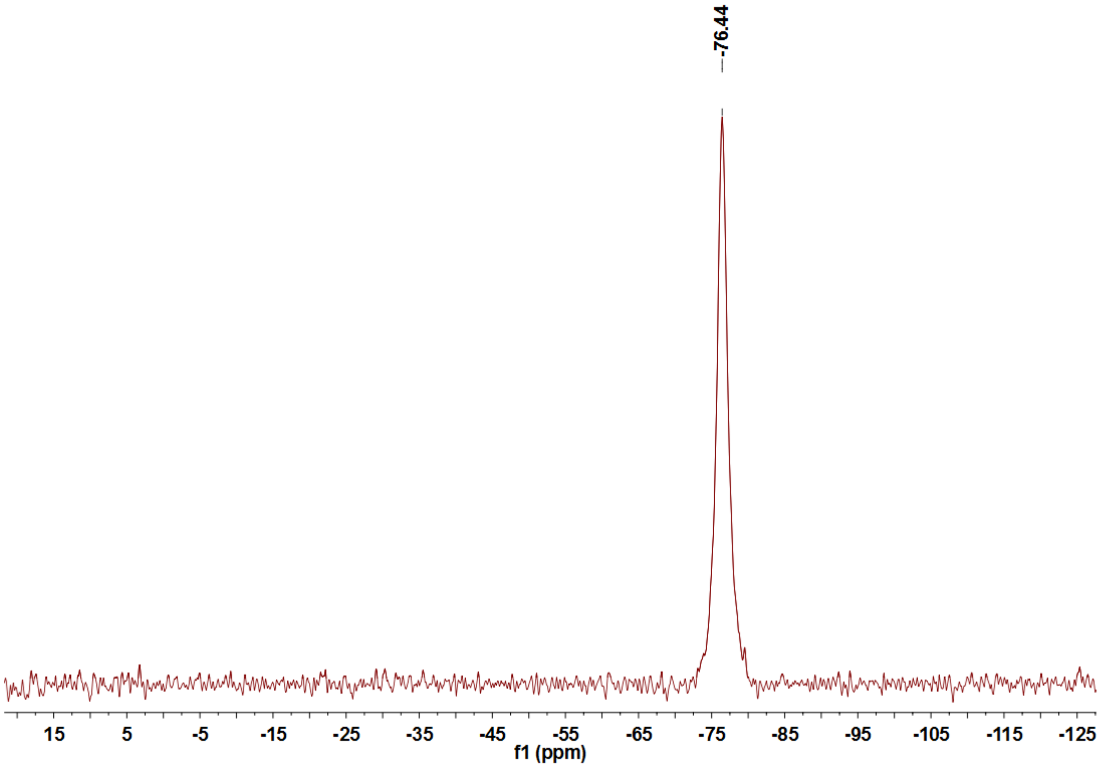

Appendix 7. Catalytic Oxidation of Cyclohexene by $[Fe(CH_3CN)_6](PF_6)_2$ at 298 K as Quantified by GC-MS.^{a}

Entry	Oxidant	Atm.	Mol Epoxide^b (+/-)^e	Mol En-ol^b (+/-)^e	Mol En-one^b (+/-)^e	TON^c	TOF^d (min^{-1})
1	PhIO	Ar	6.58×10^{-7}	4.64×10^{-8}	5.31×10^{-8}	0.23	0.008
			(4.53×10^{-7})	(2.84×10^{-8})	(3.47×10^{-8})		
2	H_2O_2	Ar	0	1.53×10^{-6}	3.95×10^{-7}	0.59	0.020
			(-)	(2.40×10^{-7})	(5.20×10^{-8})		
3	^{t}BuOOH	Ar	0	3.24×10^{-8}	7.37×10^{-8}	0.03	0.001
			(-)	(3.70×10^{-9})	(5.00×10^{-10})		

[a] Cat./Oxidant/Cyclohexene = 1:10:300. Mol Cat = 3.24×10^{-6}. Solvent = CH_3CN. [b] Epoxide Denotes Cyclohexene Oxide; En-ol, 2-Cyclohexen-1-ol; En-one, 2-Cyclohexen-1-one. [c] Turnover Number (TON) = Total Moles of Oxidised Products / Moles of Catalyst. [d] Turnover Frequency (TOF) = (Total Moles of Oxidised Product / Moles of Catalyst) / 30. [e] Error = Standard Deviation of Duplicate Runs.

Appendix 8. EPR Data Collect on C4 by Collaborator Dr. Stephen Sproules.

The spectral profile is dominated by a large *g*-splitting synonymous with Cu^{II} plus the addition of the minuscule exchange coupling gives rise to a poorly resolved 7-line hyperfine pattern in the $g_{||}$ region characteristic of coupled ^{63,65}Cu ($I = {}^3/_2$, 100 % abundant) nuclei. This pattern is more clearly displayed at K-band frequency (~24 GHz) where the enhanced Zeeman interaction separates the parallel component centred on $g_{||} = 2.196$ from the broad perpendicular feature at $g_\perp \sim 2.08$ that is devoid of hyperfine splitting. The inset in shows a half-field feature arising from the forbidden "$\Delta M_S = 2$" transition of the spin-triplet ($S = 1$) formed by coupling of the two Cu^{II} ions. The 7-line pattern is poorly resolved as its intensity is proportional to the magnitude of *D*,[86, 104] and therefore substantially higher power (63 mW) was required to expose this feature. Simulation of both the X- and K-band spectrum was achieved with the same spin-Hamiltonian parameters: $g = (2.081, 2.088, 2.196)$ and $A = (0, 40, 156) \times 10^{-4}$ cm^{-1}. The spin-spin interaction was included in the simulation using a *J* interaction matrix, which incorporates both exchange and dipolar coupling elements. The best fit was achieved for $J = -0.2$ cm^{-1} (fixed from magnetic susceptibility) for an interspin distance (*r*) of 6.9 Å retrieved from the crystal structure, and is consistent with very weakly coupled Cu^{II} ions.

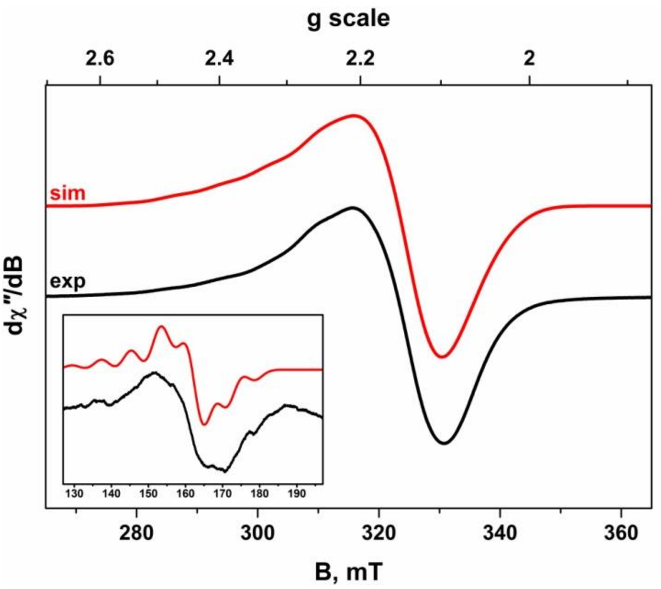

X-Band EPR Spectrum of C4 Recorded in CH_3CN/CH_2Cl_2 at 10 K (Experimental Conditions: Frequency, 9.4740 GHz; Modulation, 0.2 mT; Power, 0.2 mW). Experimental Spectrum Shown in Black and Simulation Depicted by the Red Trace: g = (2.081, 2.088, 2.196); A = (0, 40, 156) × 10^{-4} cm^{-1}; J = -0.2 cm^{-1}; $d_{Cu\cdots Cu}$ = 6.9 Å; χ = 34°; ρ = 7°. Inset Shows Experimental and Simulated EPR Spectra in the Half-Field Region (Conditions: Frequency, 9.4741 GHz; Modulation, 1.0 mT; Power, 63 mW).

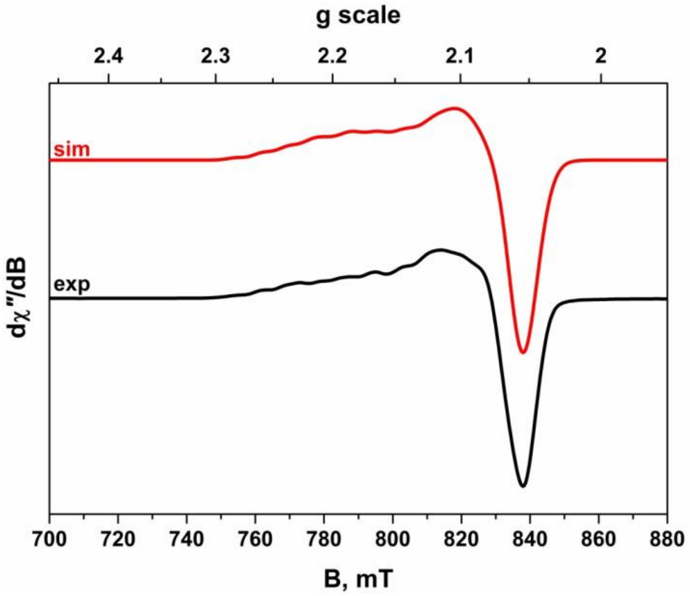

K-Band EPR Spectrum of C4 Recorded in CH_3CN/CH_2Cl_2 at 50 K (Conditions: Frequency, 24.093 GHz; Modulation, 0.5 mT; Power, 0.3 mW). Experimental Spectrum Shown in Black and Simulation Depicted by the Red Trace.

Appendix 9. Raman Data Collected on C3/PhIO, C3/H_2O_2 and C3/^{t}BuOOH

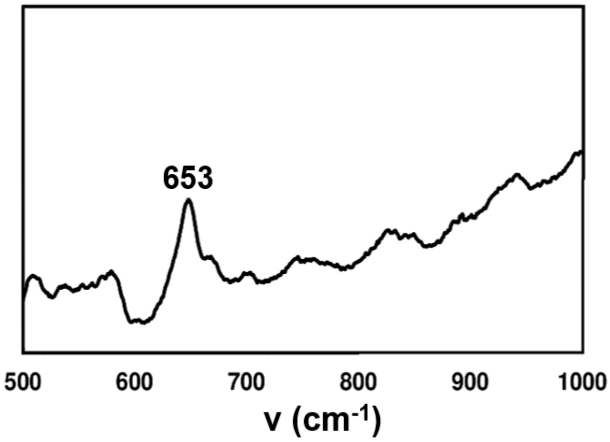

C3 + PhIO

Excitation wavelength 534 nm

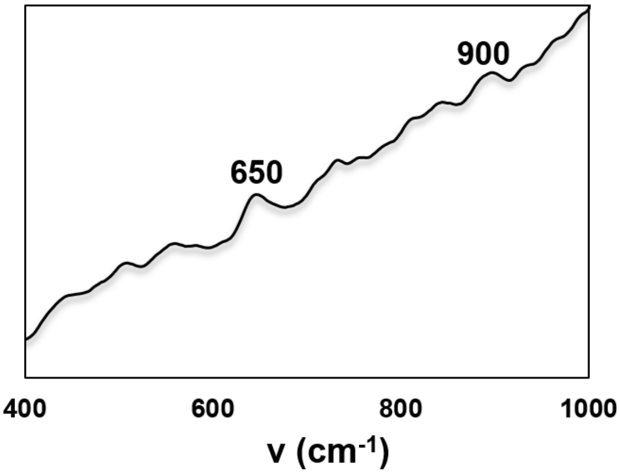

C3 + H_2O_2

Excitation wavelength 534 nm

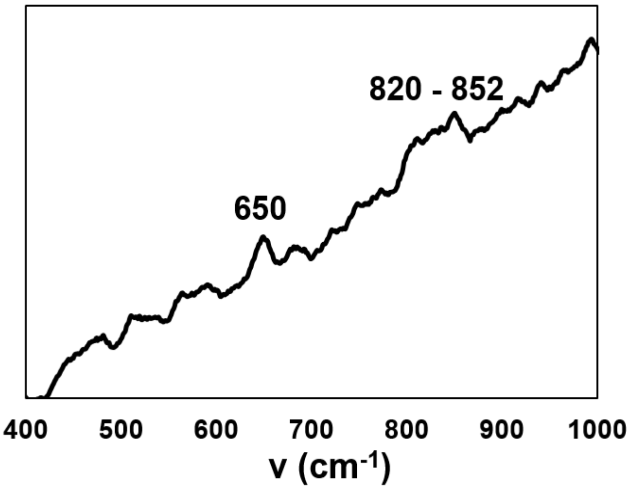

C3 + ^{t}BuOOH

Excitation wavelength 534 nm